The Dissertation Committee for Jianying Cui Atkisson
certifies that this is the approved version of the following dissertation:

Models for Acoustically Driven Bubbles in Channels

Committee:

Mark F. Hamilton, Supervisor

Preston S. Wilson, Supervisor

Ronald E. Barr

Stanislav Y. Emelianov

Ronald L. Panton

Models for Acoustically Driven Bubbles in Channels

by

Jianying Cui Atkisson, B.A., B.S., M.S.

DISSERTATION

Presented to the Faculty of the Graduate School of

The University of Texas at Austin

in Partial Fulfillment

of the Requirements

for the Degree of

DOCTOR OF PHILOSOPHY

THE UNIVERSITY OF TEXAS AT AUSTIN

August 2008

Dedicated to my family, and to Ting and Frances Yuan.

Acknowledgments

The completion of this dissertation would not have been possible without the guidance of my supervisors and the support from my family and friends. Many years of solving puzzle after puzzle is a trying and alienating experience. First and foremost deserving of thanks is my wonderful husband, Eric N. Atkisson. Thank you for putting up with a disgruntled and weary wife for all these years and thanks for all your patience and support.

Many thanks also go to my supervisor, Dr. Mark F. Hamilton. His ardent enthusiasm in research was the initial ignition of my interest in research. His curiosity and insight in this problem have led to the depth of this research, and his thorough guidance over the years has made the progress and completion of this work possible. Dr. Hamilton's faith in me has been the constant drive for me to accomplish this work. I believe his scientific attitude and philosophy of perfection will influence me for many years to come.

Dr. Preston S. Wilson, my co-supervisor, is thanked for his constant encouragement and all the constructive advice on a wide range of topics. Dr. Wilson, thanks for all the valuable suggestions and contributions to my dissertation writing and its presentation. Thanks to Dr. Hamilton and Dr. Wilson for their financial support during my Ph.D. study. I also express my sincere gratitude to Dr. Yurii A. Ilinskii for his important contributions in conquering all the difficulties I experienced in the

course of this work. I am thankful to Dr. Elmer L. Hixson for giving me the chance to pursue a Ph.D. at The University of Texas at Austin. Many thanks also go to the professors on my committee, Dr. Ronald E. Barr, Dr. Stanislav Y. Emelianov, and Dr. Ronald L. Panton for their interesting insights into the work.

I also feel grateful to my fellow acoustics students; thanks for all the helpful tips and discussions.

I would also like to thank my parents, Hong Cui and Aiqing Liang, for their help during their short stay in the United States and for their lifelong love and support. Special thanks go to Ting and Frances Yuan, who provided financial support in the initial years of my Ph.D. studies, and over the years they provided encouragement and substantial help in every aspect. Thanks to my mother-in-law, Jean Atkisson, for all her support and help during this trying period. Finally, thanks to my daughter, Sophie Lian Atkisson, for keeping me sane. This work is dedicated to all my family and to Mr. and Mrs. Yuan.

August 2008

Models for Acoustically Driven Bubbles in Channels

Jianying Cui Atkisson, Ph.D.
The University of Texas at Austin, 2008

Supervisors: Mark F. Hamilton
                    Preston S. Wilson

A model is developed for the dynamics of an acoustically driven bubble in a channel. The bubble is assumed to be smaller than the transverse dimension of the channel and spherical in shape. The channels considered are infinite in length and formed by either parallel planes or tubes with triangular, rectangular, or hexagonal cross sections. For surfaces that are rigid or pressure release, the boundary conditions on the channel walls in each of these geometries can be satisfied using the method of images. Effects due to confinement by the channel walls are thus determined by an analysis of coupled bubble interactions in line and plane arrays. An existing model for the coupled dynamics of spherical bubbles provides the basis for the model. Liquid compressibility is an essential feature of the model, both in terms of radiation damping and the finite propagation speed of acoustic waves radiated by the bubble. Solutions for the frequency response are obtained analytically by perturbation for low drive amplitudes and weak nonlinearity, and by numerical solution for high drive amplitudes and strong nonlinearity. The perturbation solutions for the radial motion

at the drive frequency and its second harmonic are obtained in closed form for a bubble between parallel planes. The response of a bubble between rigid parallel planes is found to be mass controlled, whereas for a rigid tube it is found to be radiation damping controlled. The dynamics of a bubble located near the center of a tube are found to depend on the area but not the specific geometry of the cross section. At drive amplitudes below which subharmonic generation occurs, the numerical solutions for high drive amplitudes reveal the same general properties as the perturbation solutions for low drive amplitudes. All of the solutions can be extended to tubes with arbitrary wall impedance if the radiation impedance on the bubble is known, for example calculated by normal mode expansion.

Table of Contents

List of Tables

List of Figures

xiv

xvi

Chapter 1

Introduction

This dissertation investigates the linear and nonlinear responses and radiation impedance of acoustically driven bubbles in channels. Channels formed by two parallel plates and tubes of triangular, square, rectangular and hexagonal cross sections are chosen because they are the only geometries for which the method of images can be used to satisfy the boundary conditions. The main goal of this work is to understand the effect of boundaries on the dynamics of bubbles, and the method of images permits us to use well-established theories for the nonlinear dynamics of interacting bubbles.

The motivation for this work was the modeling of bubble dynamics in confined spaces when ultrasound is present. Medical applications such as use of microbubbles as contrast agents in ultrasound imaging, their development for drug and gene delivery, and their role in shock wave lithotripsy all involve bubbles in constrained media. Some fluid-handling microdevices also involve bubble cavitation in confined spaces where the bubble size is comparable to the surrounding environment [1]. Our first step was to model the simplest geometry of two parallel plates with an intention to provide benchmarks for more advanced analysis. The methodology and solutions developed for plates were extended to tubes with cross sections that can tessellate two-dimensional space, i.e., triangular, square, rectangular, and hexagonal, with the

last being the closest approximation to a circle. The radiation impedance of a bubble in a tube was derived using the method of images and was compared with the radiation impedance obtained from a normal mode expansion by Morse and Ingard [2]. It shows that the expression for the linear and nonlinear frequency responses obtained via the method of images can be extended to tubes of other cross sections, including a cylindrical tube, and arbitrary wall impedance can be addressed.

1.1 Motivation and Background

Bubbles in liquid have been associated with many interesting phenomena: the babbling of a brook, the cavitation damage to ship propellers and the fragmentation of kidney stones. Research on bubbles interacting with sound thus has a long history. Minnaert [3] in 1933 was interested in finding the origin of "the murmur of the brook, the roar of the cataract, or the humming of the sea." He treated bubbles in liquid as simple harmonic pulsators and examined how such oscillations gave rise to natural acoustic emissions. The role bubbles play in cavitation damage was recognized in the late 19th century. In 1894 in England [4], a test was made to examine why ships could not reach their design speed at the trial runs of a high speed marine propeller, and cavitation phenomena were discovered to be one of the factors preventing improvement in the performance of hydraulic machinery. Rayleigh [5] in 1917 studied theoretically the motion of an empty spherical cavity in an infinite inviscid and incompressible liquid and derived an expression for the pressure developed in the liquid upon collapse of the cavity, following the formulation presented by Besant in 1859 [6]. These pioneering works were followed by thousands of papers and several books [7–

12] focusing on cavitation and bubble dynamics research. Various aspects of bubble dynamics have been considered at length under different simplifying assumptions for a bubble in an unbounded liquid.

In the last two decades, ultrasound contrast agents (UCAs)[1] were investigated for diagnostic and therapeutic ultrasound applications [13, 14]. A bubble has a significant acoustic response due to the impedance mismatch between the gas inside and the surrounding liquid medium, and an even greater response when excited at its resonance frequency. At resonance, a bubble scatters and absorbs much more acoustic power than one would expect from its cross-sectional area. For diagnostic applications the resonant scattering properties of contrast agents are used to improve imaging, as the harmonic and subharmonic responses of the bubbles assist in distinguishing the acoustic scattering of blood from that of the surrounding tissue. It is reported [15] that the image intensity of blood containing UCAs is as much as 40 dB higher than UCA-free blood. Microbubbles can also be used as delivery vehicles for drugs or genes, and targeted drug delivery can reduce the systemic toxicity and improve the efficacy. Ultrasound-mediated delivery of medicine and DNA using encapsulated microbubbles has been demonstrated *in vitro* [16–19]. Low amplitude ultrasound pulses are administrated to control the travel of microbubbles in the bloodstream to the target site, where the bubbles are ruptured by fragmenting ultrasound pulses, and drugs and DNA are released. Bubble cavitation effects are used in ultrasonic fragmentation and emulsification [20–24]. When high amplitude ultrasound or a shock wave is

---

[1]Ultrasound contrast agents (UCAs) are encapsulated microbubbles that are filled with air or gas such as nitrogen, or a perfluorocarbon to act as echo-enhancers.

applied to a liquid medium, cavitation bubbles form (or the pre-existing cavities or nuclei grow explosively) as the local pressure drops. The bubbles grow and with each collapse release strong forces to fragment and disintegrate stones. High intensity focused ultrasound (HIFU) is a treatment used to cause localized cell necrosis. The heat generated by the bubble oscillation can enhance localized heating, which is applied in noninvasive ablation. HIFU can also cause coagulative necrosis by increasing the local temperature above the threshold level of protein denaturation. Applying ultrasound in this manner is extremely appealing as it offers an opportunity for treatment without mechanically penetrating the target organ while preserving healthy tissue and nerve structures [25, 26].

Optimization of these medical applications requires accurate mathematical models of bubble dynamics in blood vessels and other confined spaces. In the contrast-enhanced ultrasound imaging and the ultrasound-mediated microbubble drug delivery applications, it is essential to predict the resonance frequency and the damping of microbubbles in constrained media. Shock wave lithotripsy (SWL) has been routinely used to treat kidney stones [27], yet stone comminution can be accompanied by damage to surrounding tissue. Experimental studies both *in vitro* and *in vivo* indicate vascular injuries can result from both localized drug and gene delivery and SWL [28, 29]. In gas-rich organs such as the lungs and the intestine, bubble activities can cause microscopic hemorrhage [29–31]. It is important to understand the mechanism responsible for enhancing vascular permeability and vascular injuries and the interaction between bubbles and tissues in lithotripsy to minimize any permanent damage to blood vessels and tissues and to optimize treatment. Predictive models

of bubble oscillation in confined space could be used to enhance the efficacy of medical treatments and could increase the efficiency and performance of the industrial applications.

1.2 Review of the Literature

There is an extensive literature on modeling a single bubble in an unbounded liquid. A comprehensive review is provided by Timothy Leighton's book *The Acoustic Bubble*, which contains references to over 1,400 cited works [11]. For bubbles confined in narrow spaces the literature is far less rich. Only recently has research been reported in the literature that concentrates on the mathematical modeling of a bubble in constrained environments [15, 27, 32–38]. The present review will focus on the mathematical modeling of bubbles in confined spaces, and the related modeling of arrays of bubbles in unbounded liquid.

1.2.1 Models of Bubbles in Constrained Media
1.2.1.1 Approximate Analytical Model

Prosperetti and co-workers [1, 39] pioneered development of a model for a bubble in short liquid-filled tubes. Motivated by the applications of gas bubbles as actuators in small fluid-handling systems, Oğuz and Prosperetti [1] performed a numerical study of the natural frequencies of gas bubbles in rigid tubes of finite length and obtained approximate analytical solutions. When bubble radii are not small compared with the radius of the tube, the gas bubble was assumed to occupy the entire cross section of the tube. The two columns of incompressible liquid on

either side of the bubble were modeled as lumped, finite masses.

Sassaroli and Hynynen [33, 35] extended the model by Oğuz and Prosperetti to include thermal and viscous damping. They performed parametric studies of the natural frequency, damping coefficient, and forced frequency responses of a gas microbubble in blood capillaries. Their justification for assuming rigid capillaries was that they considered capillaries which are embedded in rather rigid tissue.

1.2.1.2   Numerical Models

Finite Length Tube Models

Ye and Bull developed fluid-structure interaction models to study unsteady microbubble expansion in rigid [40] and flexible [41] tubes in order to assess the risk of vessel damage from acoustic droplet vaporization in a potential gas embolotherapy technique for the treatment of tumors. Their models used a fixed grid, multi-domain, interface tracking, direct numerical simulation method that treated all interfaces and boundaries as sharp discontinuities. The tube in their model has an aspect ratio of 7:1, liquid compressibility was neglected, and the tube end conditions were assumed to be pressure release. They obtained numerical results that in 2006 required more than 400 CPU hours per simulation of each set of parameter values.

Qin and Ferrara [15, 37] developed a lumped-parameter model to study the acoustic response of a microbubble in a microvessel. In Ref. [37], they performed a numerical study of the circumferential stress of blood vessels with compliant walls, predicting the vascular permeability to be enhanced in the presence of ultrasound contrast agents. In Ref. [38] their work focused on the natural frequency of the

nonlinear oscillation of a microbubble in blood vessels with three types of wall conditions: rigid vessels, compliant vessels, and vessels with increasing stiffness that could correspond to tumor vasculature. Their results showed that the natural frequency of oscillation of a bubble in a compliant vessel increased with decreasing vessel size and decreased with increasing values of vessel rigidity. This finding may be useful for choosing the transmitted frequency in ultrasound contrast imaging and drug delivery. Their models were also based on a finite length tube, and liquid compressibility was not included.

For the models mentioned above, the finite effective tube lengths ensure that the mechanical impedance at the bubble wall due to inertia of the liquid is finite, even though the liquid in the channel is assumed to be incompressible. For tubes of infinite length, Oğuz and Prosperetti [1] pointed out that "volume changes of the bubble would only be possible in a compressible fluid."

Infinite Channels

Krasovitski and Kimmel [42] developed a numerical model for bubble pulsation in an infinite planar liquid layer bounded by two rigid walls. The evolution of the bubble shape was calculated using the boundary integral method. Hu et al. [27] analyzed the constrained oscillations of a bubble inside a blood vessel that is modeled as a rigid tube of infinite length. They attempted to evaluate the non-spherical bubble shape due to the bubble-vessel interaction using a perturbation approach. In these two papers the liquid was assumed to be incompressible.

Models Including Liquid Compressibility

There are two papers by Leighton in which liquid compressibility was included for modeling a bubble in a tube and in a rectangular tank. Using a Green's function approach to derive the acoustic radiation impedance of a pulsating sphere, and thus accounting for compressibility of the liquid, Leighton et al. [43] developed an approximate expression for the resonance frequency shift of a bubble in an infinite cylindrical pipe. Calculations are presented for a pipe with diameter so large, more than 100 times the bubble radius, that the shift in resonance frequency due to constraint of the flow by the pipe is negligible. In contrast, our emphasis is on relatively narrow channels, with wall separations of order 10 times the bubble radius, for which the corresponding resonance frequency shift can be substantial.

A subsequent paper by Leighton et al. [44] extends the earlier analysis of a bubble in a cylindrical pipe [43] to a bubble in a rectangular tank. Using a Green's function solution and the method of images, they obtained results for the acoustic radiation impedance of the bubble, and thus for the resonance frequency and damping factor. Their focus was on radiation damping of a bubble in a large tank, and no results for the resonance frequency were presented.

1.2.2 Our Models

We derive analytical models describing bubble dynamics in channels and obtain analytical or semi-analytical solutions for the resonance frequency, quality factor, radiation impedance and frequency responses. The advantage of an analytical model is that it can provide insights into the underlying physics of the systems that are diffi-

cult to gain from numerical solutions. In addition, solving analytical model equations numerically is less computationally intensive than obtaining solutions from purely numerical models. Our model includes liquid compressibility and focuses on its role in the dynamics of a bubble in channels. Infinite parallel plates and tubes are used in the present work to permit use of the method of images.

1.2.3 Literature on Bubble Interactions in Arrays

When the method of images is applied to satisfy the boundary conditions on the channel walls, the bubble and its images form an array, a line array for a bubble between two parallel plates, and a plane array for a bubble in a tube with triangular, square, rectangular, or hexagonal cross section. The method of images works for these geometries because they possess shapes that individually tessellate a planar surface. No other cross-sectional shapes can be solved by the image method.

The interactions in bubble arrays were investigated previously for various purposes [45–51]. Zabolotskaya [46] derived a system of nonlinear dynamical equations for two interacting gas bubbles. She investigated the normal modes of the system and determined the Bjerknes force between the bubbles. Twersky [45] studied a pair of symmetrically excited monopole scatterers using a self-consistent integral equation approach and obtained the scattered intensity and phase. His method was later extended by Weston [47] to a line and plane array of identical bubbles. Weston was the first to derive a mathematical model for acoustic scattering from an infinite line array of bubbles that accounts for multiple scattering between the bubbles. In other words, the bubbles were considered to be dynamically coupled. His analysis was restricted

to bubble separations that are small on the scale of a wavelength, and therefore free-field results are not recovered for large bubble separations. Tolstoy and Tolstoy [48] provided improved models of line and plane bubble arrays, using a method similar to that of Weston, but were able to eliminate the restriction to small bubble separation. Their results and discussion described the scattering amplitude as a function of the propagation direction of a plane sound wave incident on the line array. They did not investigate bubble resonance frequency or damping. In general, while the papers by Weston and subsequently Tolstoy and Tolstoy provided models that are relevant to our problem at hand, their focus on target strength entails theoretical formulations that are not well suited to the study of bubble dynamics.

Feuillade [49] investigated acoustic scattering from schools of fish at frequencies near the swim bladder resonance. He performed an exhaustive analysis of resonances and damping associated with pairs and triplets of acoustically excited bubbles. Both in-phase and antiphase pulsations were considered. The results for in-phase excitation displayed trends that were similar to those found in the present work for a bubble between parallel plates. Feuillade's paper concluded with a solution for excitation of an infinite line array. The discussion of this case was brief and focused on acoustic scattering. The solution was used to illustrate the limiting target strength as the number of bubbles in a line array was increased. Solutions were not presented by Feuillade for the resonance frequency or damping.

Nonlinear models of clusters of interacting bubbles in three-dimensional space were developed recently [50, 52, 53]. The mathematical models in the present work are based on a model developed by Hamilton et al. [52] in which liquid compressibility

10

was included. This model was subsequently extended to include bubble translation by Ilinskii et al. [53]. A model by Doinikov [50] included translation as well as pulsation, but not time delays associated with liquid compressibility. Later Doinikov et al. [51] modeled a two-bubble system and a bubble chain containing up to 16 equispaced bubbles to illustrate that time delays caused by liquid compressibility can considerably change the damping constants of free oscillations of coupled gas bubbles. Analytical solutions were obtained for the two-bubble system, and numerical solutions were obtained for a line array of up to 16 equispaced bubbles. By comparing the numerical data with measurements, they showed that allowing for time delays considerably improved agreement between theory and experiment. The focus of their work was not on modeling a bubble in confined spaces.

1.3 Outline of Dissertation

Chapter 2 reviews mathematical models for a single bubble and a cluster of bubbles in unbounded liquid that form the basis of our model equations. The method of images is used to account for the reverberant field due to reflections from the boundaries. Channels formed by parallel plates and tubes of triangular, square, rectangular, and hexagonal cross sections are considered. Through use of the image method, the study of the boundary effects on a bubble becomes a study of bubble interactions in a two-dimensional cluster formed by the bubble and its images.

The linearized models and their solutions are discussed in Chapter 3. The frequency response of a bubble between two parallel rigid plates is presented first, and explicit expressions for the resonance frequency, the quality factor, and the fre-

quency response are provided. These results have been published previously by the author [54]. Next the frequency responses of bubbles confined in tubes with different cross sections are compared. Special cases of finite wall impedance (including pressure-release walls) are investigated for certain channels.

In Chapter 4 the radiation impedances of a bubble between plates and in square and rectangular tubes are derived. The radiation resistances and reactances of a bubble in free space, between two parallel plates, and in a square tube are compared and the different behavior in parallel plates and tubes is discussed. Results of radiation impedance obtained using the method of images are compared to those derived by Morse and Ingard [2] using normal mode theory. An expression for the frequency response in terms of the radiation impedance is presented.

As the drive amplitude increases, nonlinearity must be taken into account. Chapters 5 and 6 are devoted to the nonlinear frequency response of the bubble. Chapter 5 covers the weakly nonlinear regime, where the drive amplitudes are moderate (acoustic pressure amplitudes less than about 5% of atmospheric pressure) and harmonics are generated. The nonlinearity in this regime is investigated by keeping only quadratic nonlinear terms. Coupled systems of equations for the hamonic amplitudes are presented and generalized to include tubes of other cross-sections. The frequency responses of the first five harmonics are discussed. The perturbation solutions derived for the second harmonic and dc component were published previously by the author [55].

The strongly nonlinear regime is associated with high drive amplitudes (acoustic pressure amplitudes up to atmospheric pressure, i.e., 1 bar) and violent bubble

responses. A hybrid time-frequency domain method was developed to solve the model equations with their full nonlinearity. Frequency responses for the first five harmonics are investigated in Chapter 6, and the limitation of the hybrid method is discussed. Chapter 7 provides a summary of the work and suggestions for future work. Finally, several appendices are included with supporting material.

Chapter 2

Basic Equations

In this chapter we review the equations for single and coupled bubble dynamics that form the bases for our analyses in subsequent chapters of bubbles in channels. We then show how we adapt an existing bubble cluster model to describe the dynamics of a bubble confined in channels via the method of images. The channels studied in this dissertation are liquid-filled and formed by two infinite parallel plates, or by infinite length tubes with square, hexagonal and triangular cross sections.

2.1 Rayleigh-Plesset Equation

We begin with the Rayleigh-Plesset equation describing the motion of the bubble wall [11, 56] in an unbounded incompressible liquid:

$$R\ddot{R} + \frac{3}{2}\dot{R}^2 = \frac{P_L - P_\infty(t)}{\rho_0}, \tag{2.1}$$

where R is the instantaneous bubble radius, the dots indicate time derivatives, ρ_0 is the liquid density, P_L is the pressure in the liquid immediately outside the bubble wall, and $P_\infty(t)$ is the pressure an infinite distance away. With the gas in the bubble assumed to obey a polytropic law, P_L is given by

$$P_L = \left(P_0 + \frac{2\sigma}{R} - P_v\right)\left(\frac{R_0}{R}\right)^{3\gamma} + P_v - \frac{2\sigma}{R} - 4\mu\frac{\dot{R}}{R}. \tag{2.2}$$

The term $(P_0 + 2\sigma/R - P_v)(R_0/R)^{3\gamma}$ is the gas pressure within the bubble, which is a function of the bubble radius, and γ is the ratio of specific heats. The ambient pressure is denoted by P_0, P_v is the vapor pressure, μ denotes the kinematic viscosity of the liquid, and σ is the surface tension. For acoustic excitation one lets $P_\infty(t) = P_0 + p_{ac}(t)$ in Eq. (2.1), where $p_{ac}(t)$ is the applied acoustic pressure. Equation (2.1) was derived under the assumption that the bubble remains spherical at all times, its radius is small compared with the acoustic wavelength, and that the surrounding liquid is incompressible. Also inherent in the derivation, the gas content of the bubble is assumed to be constant and the physical conditions in the bubble are assumed to be spatially uniform. No body forces (e.g., gravitational) are included.

2.2   Liquid Compressibility

The Rayleigh-Plesset model works very well in many situations, but the assumption of liquid incompressibility implies that the speed of sound is infinite. Therefore the equation becomes inaccurate as the bubble wall velocity approaches the sound speed, and it also cannot account for radiation damping even for moderate bubble wall velocities. Many modifications of the Rayleigh-Plesset equation have been proposed to include liquid compressibility. The correction for compressibility used in the present work, and which is incorporated in our model equations for a bubble in constrained media, is the new term included in the following augmentation of the Rayleigh-Plesset equation developed by Ilinskii and Zabolotskaya [57]:

$$R\ddot{R} + \frac{3}{2}\dot{R}^2 = \frac{P_L - P_\infty}{\rho_0} + \frac{\dddot{V}}{4\pi c_0}, \tag{2.3}$$

15

where $V = \frac{4}{3}\pi R^3$ is the bubble volume, and c_0 is the sound speed in the liquid. Equation (2.3) includes liquid compressibility to $O(1/c_0)$. Ilinskii and Zabolotskaya thus described the effect of liquid compressibility on a single bubble in an unbounded liquid in terms of the bubble volume rather than bubble radius. One can express $\dddot{V}$ in terms of bubble radius as $\dddot{V} = 4\pi(R^2\dddot{R} + 6R\dot{R}\ddot{R} + 2\dot{R}^3)$, and Eq. (2.3) becomes

$$R\ddot{R} + \frac{3}{2}\dot{R}^2 - \frac{1}{c_0}(R^2\dddot{R} + 6R\dot{R}\ddot{R} + 2\dot{R}^3) = \frac{P_L - P_\infty}{\rho_0}. \tag{2.4}$$

Equation (2.4) was derived previously by Prosperetti [58].

Augmentations of the Rayleigh-Plesset equation that include a correction for liquid compressibility are more commonly expressed as equations that are only second order in the time derivative. One reason for this is the practical matter of numerical calculation. Since the terms with third derivatives in Eqs. (2.3) and (2.4) are small in relation to the terms with second derivatives, numerical solutions of these equations are inherently unstable. We now show that Eq. (2.3) is consistent with second-order formulations that are more commonly encountered in the literature. First write Eq. (2.3) as

$$R\ddot{R} + \frac{3}{2}\dot{R}^2 = \frac{P_L - P_\infty}{\rho_0} + O(1/c_0), \tag{2.5}$$

and then $\dddot{V}/4\pi c_0$ as

$$\frac{\dddot{V}}{4\pi c_0} = \frac{1}{3c_0}\frac{d^3 R^3}{dt^3} = \frac{1}{c_0}\frac{d}{dt}[R(R\ddot{R} + 2\dot{R}^2)]. \tag{2.6}$$

Substituting Eq. (2.5) into Eq. (2.6) yields at $O(1/c_0)$

$$\frac{\dddot{V}}{4\pi c_0} = \frac{1}{2c_0}\dot{R}^3 + \frac{1}{c_0}R\dot{R}\ddot{R} + \frac{1}{\rho_0 c_0}\frac{d}{dt}[R(P_L - P_\infty)]. \tag{2.7}$$

16

Now substitution of Eq. (2.7) into Eq. (2.3) along with reorganization yields

$$\left(1 - \frac{\dot{R}}{c_0}\right) R\ddot{R} + \frac{3}{2}\left(1 - \frac{\dot{R}}{3c_0}\right)\dot{R}^2 = \frac{1}{\rho_0}\left(1 + \frac{\dot{R}}{c_0} + \frac{R}{c_0}\frac{d}{dt}\right)(P_L - P_\infty). \qquad (2.8)$$

Equation (2.8) is equivalent to the Keller-Miksis equation [59] at $O(1/c_0)$. The difference is in how the term containing P_∞ is expressed in the two equations, but this difference is at $O(1/c_0^2)$. The Keller-Miksis equation is a frequently used model equation for bubble dynamics when liquid compressibility is included. In the present work, Eq. (2.3) is used because the term $\dddot{V}/4\pi c_0$ has a physical origin that is easy to understand [57], in addition to being the most compact correction for liquid compressibility.

2.3 Models of Interacting Bubbles

When a bubble is part of a cluster (see Fig. 2.1), an additional term is needed in Eq. (2.3) to account for the pressure on that bubble due to acoustic radiation from all of the other bubbles in the cluster. The acoustic pressure radiated from a monopole is [60]

$$p = \frac{\rho_0\dot{Q}(t - r/c_0)}{4\pi r}, \qquad (2.9)$$

where r is the distance from the monopole to any arbitrary point in space, and Q is the volume velocity of the monopole. Since $\dot{Q} = \ddot{V}$, the total pressure on bubble i due to radiation from the neighboring bubbles is

$$p_i = \frac{\rho_0}{4\pi}\sum_j \frac{1}{d_{ij}}\ddot{V}(t - d_{ij}/c_0), \qquad (2.10)$$

where d_{ij} is the distance between bubble i and bubble j. Ilinskii and Zabolotskaya [57] have shown, by other means, that Eq. (2.10) is not a linear approximation. Adding

17
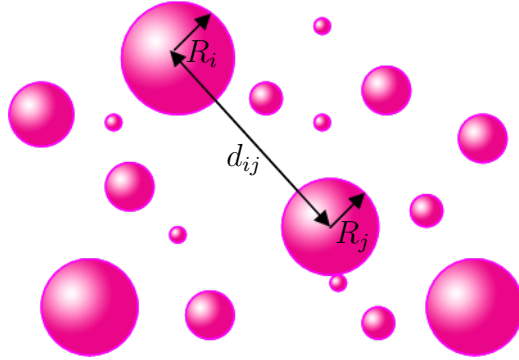
Figure 2.1: Bubble cluster.

this acoustic pressure to Eq. (2.3), we obtain the following model equation for a bubble cluster as an augmented version of Eq. (2.3):

$$R_i\ddot{R}_i + \frac{3}{2}\dot{R}_i^{\;2} = \frac{P_L(R_i) - P_\infty(t)}{\rho_0} + \frac{\dddot{V}_i}{4\pi c_0} - \frac{1}{4\pi}\sum_j \frac{1}{d_{ij}}\ddot{V}_j\left(t - \frac{d_{ij}}{c_0}\right). \qquad (2.11)$$

The term d_{ij}/c_0 accounts for the finite time it takes for sound to propagate from bubble j to bubble i. In most of this dissertation, the vapor pressure and effects of surface tension and viscosity are omitted in Eq. (2.2) to focus on effects of liquid compressibility, in which case we have

$$P_L(R_i) = P_0\left(\frac{R_{i0}}{R_i}\right)^{3\gamma} \qquad (2.12)$$

in Eq. (2.11).[1] Equation (2.11) is the model equation developed by Hamilton et al. [52, Eq. (2)] for a bubble cluster including the liquid compressibility, and it forms the basis of our model for a bubble in a channel.

---

[1]In Chapters 5 and 6, viscosity is taken into account by including the term $4\mu\dot{R}_i/R_i$ in Eq. (2.12).
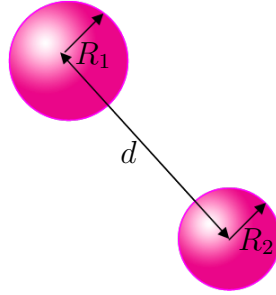
Figure 2.2: Two interacting bubbles in unbounded incompressible liquid.

If only two bubbles are involved and the liquid is assumed to be incompressible, in which case $c_0 = \infty$, Eq. (2.11) reduces to the following two coupled equations for bubbles with radii $R_1(t)$ and $R_2(t)$:

$$R_1 \ddot{R}_1 + \frac{3}{2} \dot{R}_1^2 + \frac{R_2}{d}(R_2 \ddot{R}_2 + 2\dot{R}_2^2) = \frac{P_L(R_1) - P_\infty(t)}{\rho_0}, \qquad (2.13)$$

$$R_2 \ddot{R}_2 + \frac{3}{2} \dot{R}_2^2 + \frac{R_1}{d}(R_1 \ddot{R}_1 + 2\dot{R}_1^2) = \frac{P_L(R_2) - P_\infty(t)}{\rho_0}, \qquad (2.14)$$

where d is the separation between the two bubbles (see Fig. 2.2). Note that $\ddot{V}_j/4\pi = R_j(R_j \ddot{R}_j + 2\dot{R}_j^2)$. Equation (2.14) was derived previously by Zabolotskaya [46].

2.4 Model of a Bubble Confined in a Channel

Liquid-filled channels formed by two infinite parallel plates, and by infinite length tubes of triangular, rectangular, square and hexagonal cross-sections, were studied. These geometries were chosen since they are the only geometries where the method of images can be applied, owing to the fact that their cross sections tessellate two-dimensional space.

2.4.1 Method of Images

The method of images is a basic tool used in acoustics and electromagnetics to satisfy the boundary conditions of a problem by replacing certain elements of the original system with images. An example that illustrates the idea is shown in Fig. 2.3. A simple source radiating sound omnidirectionally is located a distance h below a rigid plate. The sound pressure at an arbitrary location below the plate consists of a direct arrival from the source and a reflected arrival from the boundary. We can account for this by removing the rigid plate and replacing it with an image located at distance h above the plate so the normal particle velocity vanishes in the plane originally occupied by the plate. This boundary condition requires the image to be identical to the source. As indicated in the figure, the image and the source are in phase. This example can be extended to another situation where the rigid plate is replaced with a pressure release surface, such as a water-air interface. Since the pressure must vanish at $y = 0$, the image must be identical to the source but of the opposite phase.

2.4.2 Bubble between Two Parallel Rigid Plates

The geometry of a channel formed by two parallel plates is shown in Fig 2.4. The plates are assumed to be rigid and extend to infinity, and the channel is filled with liquid. The two plates are separated by distance d, and a spherical bubble of equilibrium radius R_0 is in the middle of the channel. The bubble is assumed to be spherical at all times. Viscous effects are neglected here along with the effect of heat conduction and surface tension in order to focus on the effect of the liquid
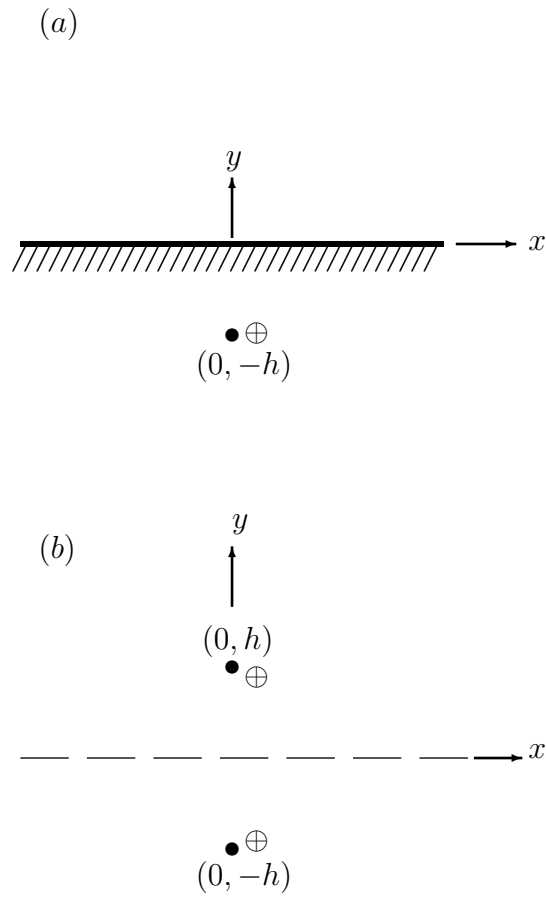
Figure 2.3: Illustration of the method of images. (a) The initial system: a simple sound source located a distance h from a rigid wall; (b) a mathematically equivalent system: the rigid plate is replaced by an identical image source.
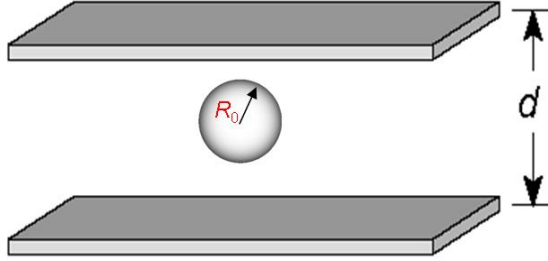
Figure 2.4: Geometry of a bubble located midway in a channel formed by two parallel plates.

compressibility. The initial pressure in the liquid and inside the bubble is assumed to be uniform and equal to P_0. The gas inside the bubble is assumed to behave adiabatically, with its pressure given by $P_g = P_0(R_0/R)^{3\gamma}$, where R is the instantaneous radius of the bubble and γ is the ratio of specific heats. An acoustic pressure $p_{ac}(t)$ is applied to the liquid.

We remove the channel walls and extend the liquid-filled space between the plates to infinity. For the two plates, a pair of images will be needed, I_1 and I_{-1}. Then pairs of images of I_1 and I_{-1} will be needed, and so on until an infinite line array of bubbles is created with separation d in both directions. The geometry is shown in Fig. 2.5.

Equation (2.11) can be applied directly to the geometry of the infinite line array of the bubble and its images. All images are at distances that are integer multiples of d away from the bubble. For the mth image, $d_m = md$, where $-\infty \leq m \leq \infty$ ($m \neq 0$) and m is an integer. The time delays to be considered here are therefore in the explicit form $t - md/c_0$. Noticing the symmetry inherent in the infinite line

22
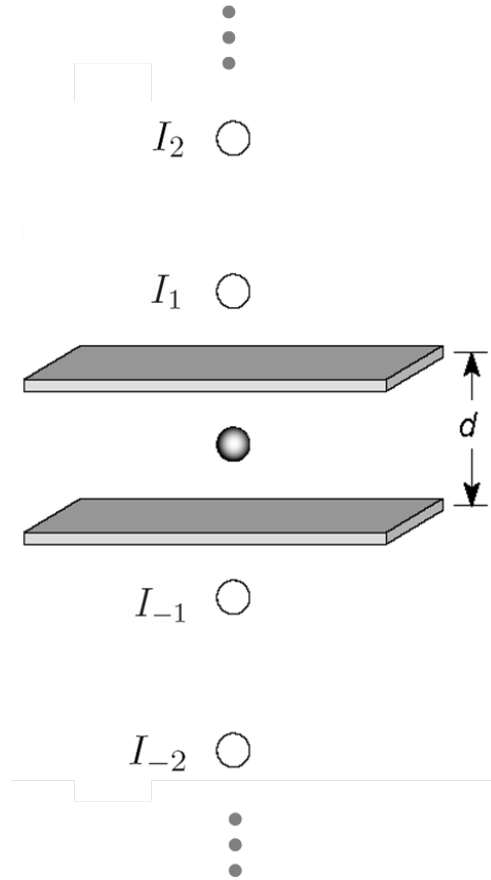
Figure 2.5: The geometry of the infinite line array is shown. The image bubbles are indicated with open circles and labeled I_m. They are separated by distance d and are shown extending indefinitely in both directions. Although the plates are no longer part of the model, they are shown in their original positions for convenience.

array, we will only need one model equation for one bubble to represent the whole system. Thus instead of the coupled model equations, Eq. (2.11), we now have the single equation

$$R\ddot{R} + \frac{3}{2}\dot{R}^2 = \frac{1}{\rho_0}\left[P_0\left(\frac{R_0}{R}\right)^{3\gamma} - P_0 - p_{\text{ac}}(t)\right] + \frac{\dddot{V}}{4\pi c_0} - \frac{1}{2\pi d}\sum_{m=1}^{\infty}\frac{1}{m}\ddot{V}\left(t - \frac{md}{c_0}\right).$$

(2.15)

The summation accounts for the interaction of the bubble with all of its images. For image m at distance md from the bubble, it takes time md/c_0 for the sound to arrive, so its effect is evaluated at the delayed time $t - md/c_0$. The summation accounts for the boundary effects of the plates, namely, for the pressure acting on the bubble due to successive reflections from the plates. The linear form of Eq. (2.15) becomes similar to Eqs. (2) of Doinikov et al. [51] when the latter are applied to the geometry depicted in Fig. 2.5 and the external sound field is taken into account. The linear form may also be obtained from Eqs. (7) of Feuillade [49] under the same conditions.

2.4.3 Bubble in a Tube

The geometries of channels formed by rigid infinite tubes with different cross-sections are shown in Fig. 2.6. Bubbles of initial radius R_0 are assumed to be at the center of the channels. The same assumptions used in Sec. 2.4.2 are also used here. Viscosity, surface tension and thermal conductivity are neglected. The bubble is assumed to be spherical at all times, and the liquid is compressible.

For the cross-sectional geometries in Fig. 2.6 we can again apply the method of images to satisfy the boundary conditions on the rigid surfaces. The layouts of the bubble and its images for triangular, square and hexagonal tubes are shown in
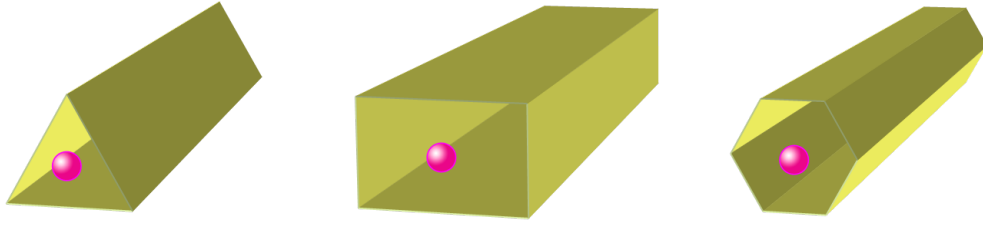
Figure 2.6: The three tube cross sections considered in the present study.

Figs. 2.7, 2.8 and 2.9, respectively. The bubbles and the tube cross sections are shown with dark lines, while the image bubbles and the image tube cross sections are shown in gray. As can be seen, for the shapes of triangle, square and hexagon, they tessellate the two-dimensional space. The bubble and its images form infinite plane arrays for these three cross sections.

To account for the reflections of sound waves from the tube walls, we need to account for the collective effects of the interactions between the bubble and all its images. It becomes critical how we count the images. We do not want to count any image twice or miss counting any of them. In other words, we need strategies to index the images for Figs. 2.7, 2.8 and 2.9. The counting techniques we developed for different geometries may be found in Appendix A. To generalize, we use r_{lm} to indicate the distance between the bubble and its images identified by the indices (l, m). The time delays are expressed as $t - r_{lm}/c_0$. A 3-fold (or a 4-fold, or a 6-fold) symmetry is used for a triangular (or a square, or a hexagonal) tube. Only the images in one of the symmetric regions are summed over, and the result is multiplied by 3 (or 4, or 6) to obtain the total contribution from all the images (see Appendix A).
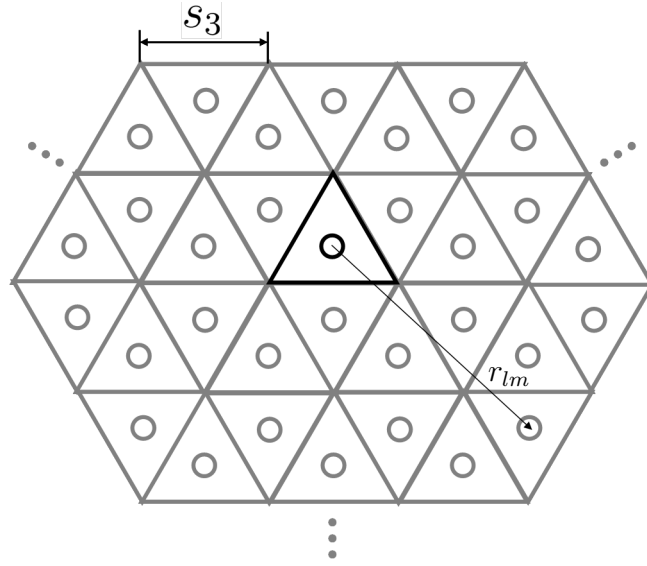
Figure 2.7: Plane array of bubble images for a triangular tube.
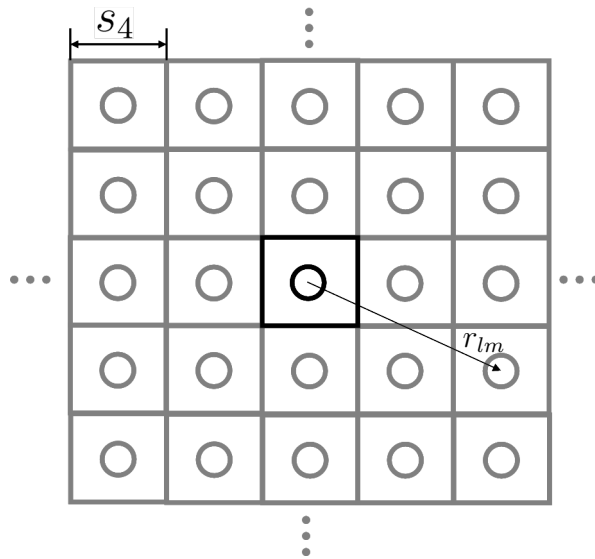
Figure 2.8: Plane array of bubble images for a square tube.
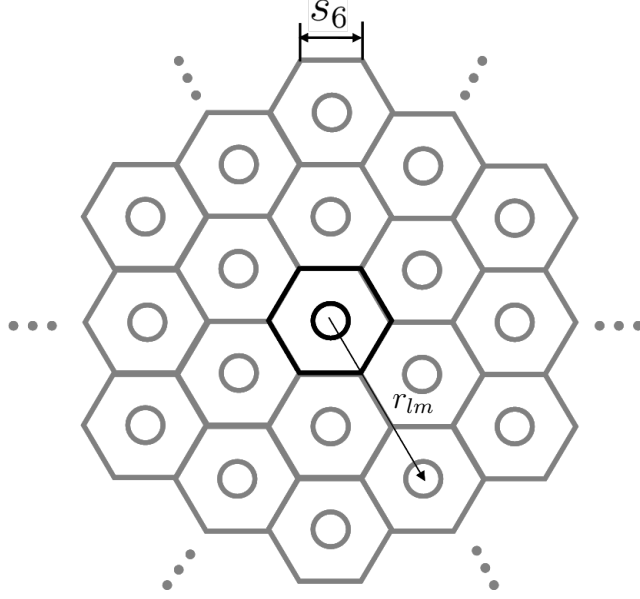
Figure 2.9: Plane array of bubble images for a hexagonal tube.

Extending Eq. (2.15) to the planar arrays of images yields

$$R\ddot{R} + \frac{3}{2}\dot{R}^2 = \frac{1}{\rho_0}\left[P_0\left(\frac{R_0}{R}\right)^{3\gamma} - P_0 - p_{\text{ac}}(t)\right] + \frac{\dddot{V}}{4\pi c_0} - \frac{1}{4\pi}\sum_{l,m}\frac{1}{r_{lm}}\ddot{V}\left(t - \frac{r_{lm}}{c_0}\right).$$

(2.16)

Use of Eq. (2.16) is restricted to the tube cross sections that are triangular, rect-angular, square or hexagonal. Although images of a centered bubble are shown in Figs. 2.5, 2.7, 2.8, and 2.9, Eq. (2.16) can be used for an arbitrary bubble position, as long as the terms r_{lm} are correctly accounted for. Off-centered bubble positions are considered for a square tube in later chapters. Also note that while Eq. (2.15) is only applicable to a bubble centered between parallel plates, it too can be modified for use with off-centered bubble positions, as discussed in Chapter 3.

The method of images cannot be applied to a cylindrical tube, which is the

27

case of most practical interest. With the progression from triangle to square to hexagon we may illustrate the transition to circular tubes, with the hexagon being the closest approximation to a circle. A different approach, normal mode expansion, was recently developed by others in our group for studying the dynamics of a bubble in a cylindrical tube [61], and the results from the two approaches will be compared. Rigid walls are implied in both Eqs. (2.15) and (2.16), but modifications can be made to the summations to accommodate deviation from the rigid wall assumption. In Chapter 3, pressure release walls are investigated for two parallel plates and a square tube. The effect of finite wall impedance is also studied for the parallel plates in Chapter 3.

Chapter 3

Linear Solutions

In this chapter we present solutions of Eqs. (2.15) and (2.16) in the linear approximation. The essential role of liquid compressibility for a bubble in an infinite channel with rigid walls is discussed in detail. For the case of parallel plates, analytic expressions for the frequency response, resonance frequency and quality factor are derived. For tubes, numerical summation over the images is required. A simplification of the summation is investigated for a square tube. Pressure release walls are considered for the parallel plates and a square tube. Finite wall impedance is considered for a bubble between two widely spaced plates.

3.1 Channels Formed by Parallel Plates

If we express the bubble radius as $R(t) = R_0 + \xi(t)$, where ξ is the perturbation of the bubble radius, and linearize Eq. (2.15) with respect to ξ we obtain the following model equation for an acoustically driven bubble between two rigid parallel plates:

$$\ddot{\xi}(t) + \omega_0^2 \xi(t) = \frac{R_0}{c_0}\dddot{\xi}(t) - 2\frac{R_0}{d}\sum_{m=1}^{\infty}\frac{1}{m}\ddot{\xi}(t - md/c_0) - \frac{p_{\text{ac}}(t)}{\rho_0 R_0}, \qquad (3.1)$$

where $\omega_0 = (3\gamma P_0/\rho_0 R_0^2)^{1/2}$ is the natural (Minnaert) angular frequency for a bubble in an unbounded liquid. Equation (3.1) forms the basis for the analyses in Secs. 3.1.1–

3.1.5. It is modified slightly in the frequency domain to describe parallel plate channels with pressure release walls in Sec. 3.1.6.

3.1.1 Liquid Compressibility Revisited

As pointed out in Chapter 2, compressibility of the liquid is taken into account by the term with three time derivatives in Eq. (3.1), corresponding to radiation damping, and by the time delays appearing in the summation. The time delays are due to the finite sound speed in compressible liquid. For an incompressible liquid and therefore infinite sound speed, Eq. (3.1) reduces to

$$\left(1 + 2\frac{R_0}{d}\sum_{m=1}^{\infty}\frac{1}{m}\right)\ddot{\xi}(t) + \omega_0^2\xi(t) = -\frac{p_{\rm ac}(t)}{\rho_0 R_0^2}, \quad c_0 \to \infty. \tag{3.2}$$

The expression multiplying $\ddot{\xi}$ represents the effective inertia of the liquid in contact with the bubble wall. Since the summation over $1/m$ diverges, the effective inertia is infinite, and there is no dynamical solution of Eq. (3.2). The infinite mechanical impedance at the bubble wall is produced by pressure waves arriving simultaneously, and therefore in phase, from the infinity of reflections between the plates.

In the context of incompressible flow in a rigid channel, a physical explanation of the aforementioned infinite impedance is readily appreciated on the basis of energy considerations. In free space, the total kinetic energy surrounding a spherical bubble whose wall moves radially with velocity $\dot{\xi}(t)$ is $2\pi\rho_0 R_0^3\dot{\xi}^2(t)$, a finite quantity [11]. Now consider the same bubble in the channel depicted in Fig. 2.4. Far from the bubble, where the streamlines are parallel to the walls and the flow is uniform across the channel (see Fig. 3.1), the velocity of the liquid at distance r from the bubble

30

is proportional to $\dot{\xi}(t)/r$ on account of cylindrical divergence, such that the kinetic energy per unit volume is proportional to $1/r^2$. The kinetic energy in a thin cylindrical shell of volume $d \times 2\pi r\, dr$ is thus proportional to dr/r, the integral of which between inner radius r_i and outer radius r_o yields $\ln(r_o/r_i)$ for a shell of finite thickness. The total kinetic energy in a liquid constrained by rigid plates of infinite extent, $r_o = \infty$, is therefore infinite. Unlike spherical divergence of the flow in an unconstrained liquid, cylindrical divergence is insufficient for the kinetic energy to be finite. The bubble must perform infinite work to change its volume in the channel, however small that change may be, and therefore radial motion of the bubble wall is prohibited. The same argument applies to a bubble in an infinite rigid tube with constant cross section, for which there is no divergence of the flow far from the bubble, and the kinetic energy increases linearly with distance, rather than logarithmically. Equation (3.1) is free of this shortcoming associated with incompressible flow.
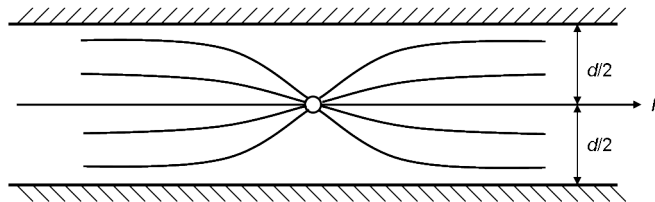
Figure 3.1: View of streamlines of the flow emanating from a bubble between two parallel rigid plates.

We emphasize that the essential role of compressibility discussed above is a consequence of assuming that the channel has infinite length and rigid walls. Relaxing either of these assumptions permits dynamical solutions to be obtained without accounting for compressibility. Models of bubble dynamics in incompressible

31

liquid constrained by a rigid but finite tube have been developed by Oğuz and Prosperetti [1]. An approximate approach to modeling bubble dynamics in incompressible liquid constrained by parallel plates with walls having finite impedance is described in Sec. 3.1.4. For tubes of finite length that are sufficiently long, or having walls with finite but not sufficiently large impedance, compressibility of the liquid competes with and eventually dominates these other mechanisms for reducing the effective inertia of the flow.

3.1.2 Frequency Response

The summation in Eq. (3.1) is history dependent, and therefore to solve Eq. (3.1) in the time domain requires storage of $\ddot{\xi}(t - md/c_0)$ at the delayed times $t - md/c_0$ at every time step. However, a closed-form solution can be obtained in the frequency domain. For harmonic excitation by an externally applied sound pressure $p_{\mathrm{ac}}(t) = p_0 e^{j\omega t}$, the response takes the form $\xi(t) = \Xi(\omega)e^{j\omega t}$, and substitution in Eq. (3.1) yields

$$\left[1 - \left(1 + 2\frac{R_0}{d} \sum_{m=1}^{\infty} \frac{e^{-jmkd}}{m} \right) \frac{\omega^2}{\omega_0^2} + jk_0 R_0 \frac{\omega^3}{\omega_0^3} \right] \frac{\Xi(\omega)}{R_0} = -\frac{p_0}{3\gamma P_0}, \qquad (3.3)$$

where $k = \omega/c_0$ and $k_0 = \omega_0/c_0$. The third derivative $\dddot{\xi}$ manifests itself as the term containing ω^3, and the time delays appear as the phase shifts e^{-jmkd}. The summation may be evaluated in closed form as follows [62]:

$$\sum_{m=1}^{\infty} \frac{e^{-jmkd}}{m} = -\ln(1 - e^{-jkd}), \quad \text{for all } kd, \qquad (3.4)$$

$$= -\ln\left(2\sin\frac{kd}{2} \right) - \frac{j}{2}(\pi - kd), \quad 0 < kd < 2\pi. \qquad (3.5)$$

Use of Eq. (3.4) in (3.3) yields

$$\left\{1 - \left[1 - 2\frac{R_0}{d}\ln(1 - e^{-jkd})\right]\frac{\omega^2}{\omega_0^2} + jk_0R_0\frac{\omega^3}{\omega_0^3}\right\}\frac{\Xi(\omega)}{R_0} = -\frac{p_0}{3\gamma P_0}, \qquad (3.6)$$

which we rewrite as

$$\frac{\Xi(\omega)}{\Xi(0)} = \left\{1 - \left[1 - 2\frac{R_0}{d}\ln(1 - e^{-jkd})\right]\frac{\omega^2}{\omega_0^2} + jk_0R_0\frac{\omega^3}{\omega_0^3}\right\}^{-1}, \qquad (3.7)$$

where $\Xi(0) = -(p_0/3\gamma P_0)R_0$ is the response at zero frequency.
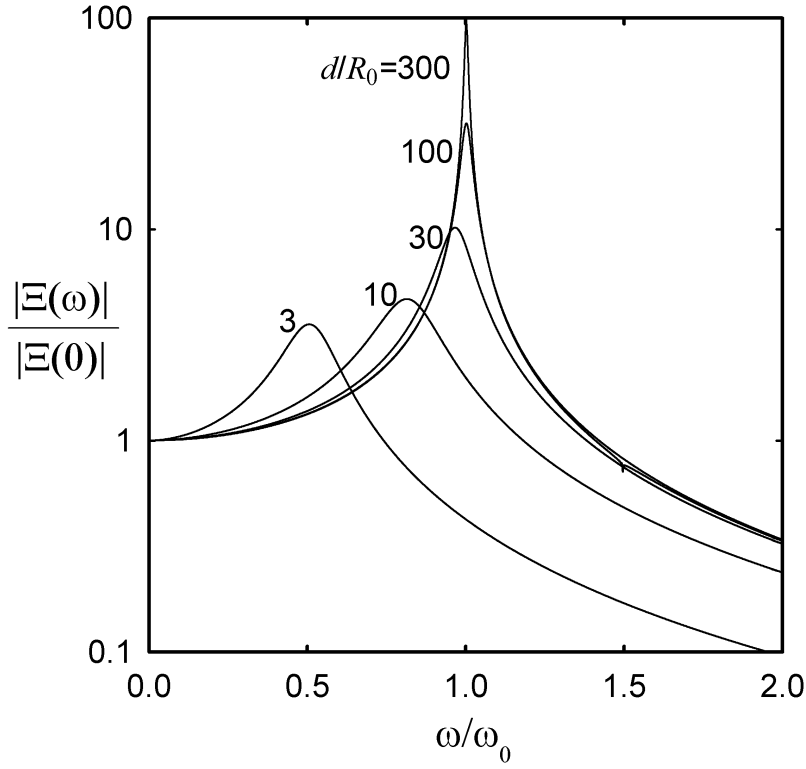
Figure 3.2: Frequency response of a bubble between two parallel rigid plates for different dimensionless plate separations d/R_0.

The effect of the plate separation d/R_0 on the frequency response of a bubble centered between the plates is shown in Fig. 3.2 for an air bubble in water, for which $k_0 R_0 = (3\gamma P_0/\rho_0 c_0^2)^{1/2} = 0.014$. It is seen that as the plate separation is reduced, the resonance frequency decreases from its value of ω_0 in a free field and the radiation damping increases. When the plates are far apart the response is effectively the same as that in the free field. The same behavior was observed by Weston [47] and Feuillade [49] in connection with line arrays of bubbles.

3.1.3 Resonance Frequency and Quality Factor

Explicit expressions for the resonance frequency and quality factor may be obtained using the relation given by Eq. (3.5). Although restricted to $0 < kd < 2\pi$, it permits separation of the real and imaginary parts of the solution. This relation may be used for all values of kd by understanding that it represents just one cycle of a function that is periodic in 2π. When Eq. (3.5) is substituted in Eq. (3.3), the term $jkd/2$ in the former cancels the term $jk_0 R_0 \omega^3/\omega_0^3$ in the latter, and the result is

$$\frac{\Xi(\omega)}{\Xi(0)} = \left\{ 1 - \left[1 - 2\frac{R_0}{d} \ln\left(2\sin\frac{kd}{2} \right) \right] \frac{\omega^2}{\omega_0^2} + j\pi\frac{R_0}{d}\frac{\omega^2}{\omega_0^2} \right\}^{-1}, \quad kd < 2\pi. \quad (3.8)$$

The restriction $kd < 2\pi$ is equivalent to $d < \lambda$. For $kd \to 0$ (incompressible liquid) and $kd \to 2\pi$ (for which arrivals from all images are in phase with radiation from the bubble), it is seen that $\Xi(\omega) \to 0$, corresponding to the absence of a response due to the infinite effective inertia discussed in connection with Eq. (3.2).

The resonance frequency ω_r is defined by setting the real part of the expression within the braces in Eq. (3.8) to zero, which yields the following transcendental

34

relation:

$$\omega_r = \frac{\omega_0}{\sqrt{1 - 2(R_0/d)\ln|2\sin(\omega_r d/2c_0)|}}. \tag{3.9}$$

While Eq. (3.8) is restricted to $kd < 2\pi$, Eq. (3.9) has been rendered valid for all kd by taking the absolute value of the sine function to account for the periodicity of Eqs. (3.4) and (3.5). Equation (3.9) also follows from the expression for the resonance frequency in a tank given by Eq. (42) of Leighton et al. [44], when the latter is evaluated for the geometry in Fig. 2.4 together with rigid boundary conditions, and the relation in Eq. (3.5) is used. [We note that the subscript 0 was omitted from the wavenumber k in their Eq. (42), corresponding to omitting the subscript r on the right side of our Eq. (3.9). Leighton et al. do not present solutions of their Eq. (42).]

The solution of Eq. (3.9) is shown in Fig. 3.3(a), which reveals the resonance frequency shift to be significant for plate separations less than about 10 bubble diameters, $d/R_0 \lesssim 20$. Resonance frequency is decreased because the plates prohibit the ideal radial expansion of flow that occurs in an unbounded liquid, thus increasing the effective fluid inertia. Figure 3.3(a) is qualitatively the same as Fig. 3 of Feuillade [49] for arrays of two and three bubbles. Quantitatively, the resonance frequency shift depicted in Fig. 3.3(a) is about twice that which is predicted for three bubbles separated by distance d.
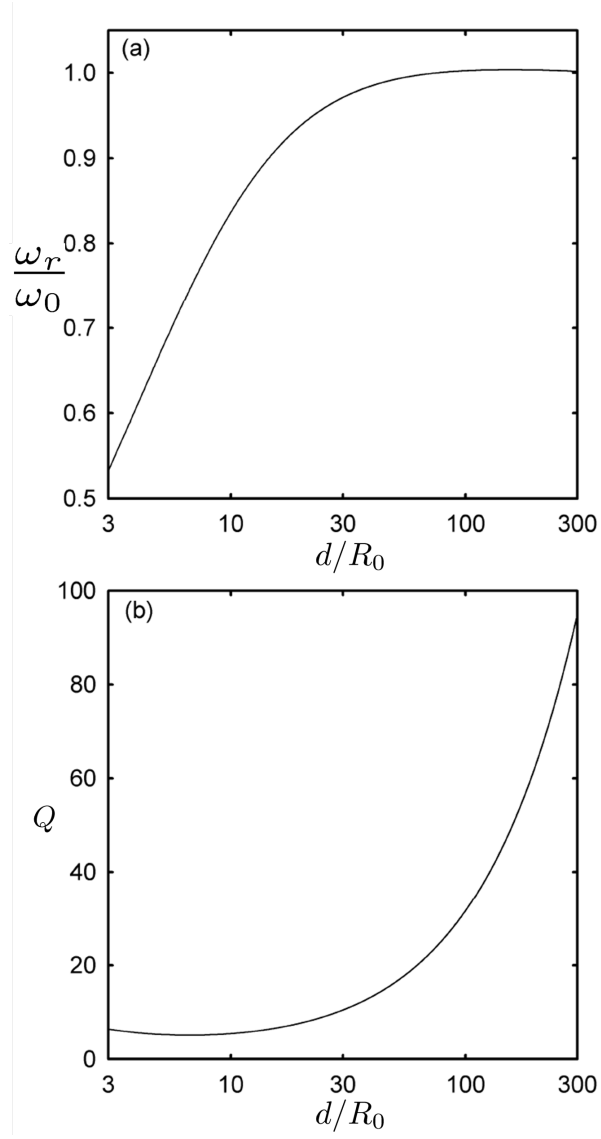
Figure 3.3: (a) Resonance frequency and (b) quality factor as functions of plate separation for an air bubble in water.

The quality factor is defined by the relation $Q = |\Xi(\omega_r)/\Xi(0)|$, such that

$$Q = \frac{\omega_0^2}{\omega_r^2} \frac{d}{\pi R_0}, \quad k_0 d < 2\pi, \tag{3.10}$$

$$\simeq \frac{d}{\pi R_0}, \quad \frac{d}{R_0} \gg 1, \quad k_0 d < 2\pi, \tag{3.11}$$

$$= \frac{1}{k_0 R_0}, \quad k_0 d \to \infty. \tag{3.12}$$

Equations (3.10) and (3.11) follow from (3.8), and Eq. (3.12) follows from (3.7). The dependence of Q on d/R_0 is shown in Fig. 3.3(b). Since losses due to viscosity and heat conduction are not included in the analysis, damping associated with the quality factor is due entirely to compressibility. The limiting value for a channel of infinite width, $Q \sim 1/k_0 R_0$, corresponds to radiation damping in an unbounded liquid. The transition to this limiting value, $Q \sim 72$ for an air bubble in water, is illustrated in Fig. 3.4, where $\lambda_0 = 2\pi/k_0$ is the acoustic wavelength in the liquid at the natural frequency of the bubble when the liquid is unbounded, and the periodic structure is due to the sawtooth behavior connected with the term $j(\pi - kd)/2$ in Eq. (3.5). For comparison, the value $d/\lambda_0 = 1$ in Fig. 3.4 corresponds to $d/R_0 = 450$ in Fig. 3.3(b).

3.1.4 Finite Wall Impedance

We consider here the effect of channel walls having finite acoustic impedance, whether due to the transmission of sound outside the channel, or due to wall compliance or inertia. A solution of this problem for arbitrary wall impedance is difficult, but solutions under certain restricted conditions suggest the dynamic response of a bubble that may be expected under more general conditions. In the limit of geomet-

37
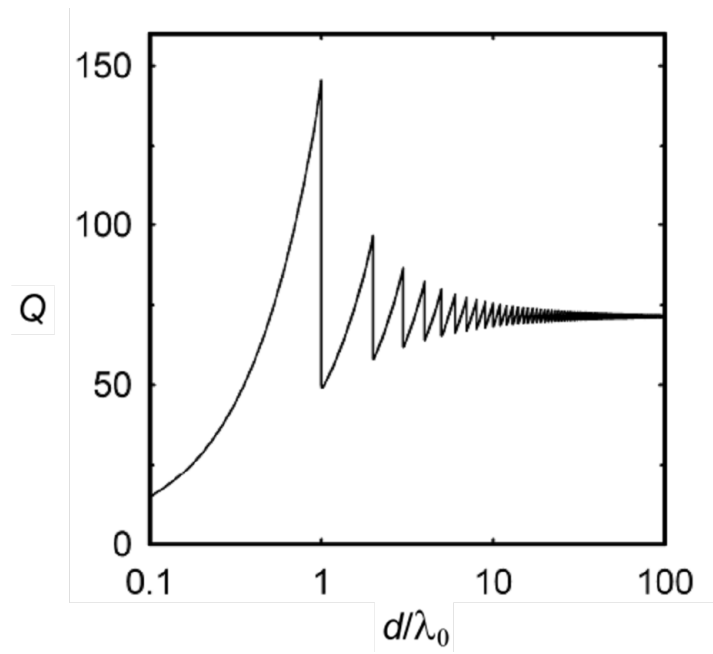
Figure 3.4: Convergence of the quality factor to its value of $1/k_0 R_0$ for a bubble in an unbounded liquid as plate separation is increased indefinitely.

rical acoustics (high frequencies), waves radiated by the bubble and reflected from the channel walls back toward the bubble follow ray paths that are approximately perpendicular to the channel walls. The characteristic impedance of the wave is $\rho_0 c_0$ in this limit, and use of the plane-wave reflection coefficient for normal incidence on the channel wall is then appropriate. The necessary condition for these assumptions to be reasonable is that wavenumber times the radius of curvature of the wavefront incident on the wall is large compared to unity. In our case this corresponds to $kd \gg 1$, or $d \gtrsim \lambda$.

If we assume that the surface of the wall is locally reacting, then for $kd \gg 1$ finite wall impedance can be taken into account by introducing a pressure reflection coefficient β in the summation in Eq. (3.3) as follows:

$$\sum_{m=1}^{\infty} \frac{e^{-jmkd}}{m} \rightarrow \sum_{m=1}^{\infty} \beta^m \frac{e^{-jmkd}}{m}, \quad kd \gg 1. \tag{3.13}$$

The quantity β is applied once for every reflection. Writing $\beta^m = e^{m \ln \beta}$, we can achieve the same result by replacing the real wavenumber $k = \omega/c_0$ in either Eq. (3.3) or (3.7) by the complex wavenumber

$$\tilde{k} = \frac{\omega}{c_0} + j\frac{\ln \beta}{d}. \tag{3.14}$$

This substitution cannot be made directly in Eq. (3.8); instead, it must be made one step earlier, in Eq. (3.5), because of how terms were combined to obtain Eq. (3.8).

For example, in Eq. (3.7) one obtains

$$\ln(1 - e^{-j\tilde{k}d}) = \ln(1 - |\beta|e^{-j(kd-\phi)}), \tag{3.15}$$

$$= \ln(1 - |\beta|e^{j\phi}), \quad c_0 \rightarrow \infty, \tag{3.16}$$

39

where the reflection coefficient has been expressed in polar form as $\beta = |\beta|e^{j\phi}$. For an arbitrary specific acoustic wall impedance z_w the reflection coefficient is

$$\beta = \frac{z_w - \rho_0 c_0}{z_w + \rho_0 c_0}. \tag{3.17}$$

The wall impedance may now be expressed as $z_w = r_w + jx_w$, where the real part r_w accounts for the loss of acoustic energy in the channel due to transmission through the walls, and the imaginary part x_w is the reactance associated with inertia and compliance of the walls. Since $|\beta| < 1$ for any finite value of r_w, and $\phi \neq 0$ for any finite value of x_w, the expression in Eq. (3.16) is bounded in either case. This is to say, the problem with the prediction of infinite inertia resulting from the assumption of an incompressible liquid in an infinite channel with rigid walls is avoided by allowing for finite wall impedance.

As indicated in Eq. (3.13), our analysis of finite wall impedance is restricted to channels having widths greater than about one wavelength. However, the implication of the underlying physics is clear. Change in bubble volume is possible in a constrained incompressible liquid only if the channel walls have finite impedance, allowing them to move in order to accommodate the liquid displaced by motion of the bubble wall.

We note that an alternative use of a complex wavenumber is to account for the attenuation of sound in the liquid.

3.1.5 Bubble Off-Center

When the bubble is off center, say an arbitrary distance b from one plate as shown in Fig. 3.5, simplicity is lost because of the asymmetric distribution of the

images required to satisfy the boundary conditions. The solution in this case is given by Eq. (3.3) after replacing the summation as follows:

$$\sum_{m=1}^{\infty} \frac{e^{-jmkd}}{m} \rightarrow \frac{1}{4} \sum_{m=1}^{\infty} \left(\frac{2}{m} + \frac{e^{j2kb}}{m - b/d} + \frac{e^{j2k(d-b)}}{m - 1 + b/d} \right) e^{-j2mkd}. \qquad (3.18)$$

The two summations are equivalent for a bubble in the midplane, $b = d/2$. For a bubble off center, the summation no the right longer admits a closed form as in Eqs. (3.4) and (3.5). Dependence of the pulsation amplitude on the position of the bubble in the channel is shown in Fig. 3.6 for $d/R_0 = 30$. Resonance frequency is decreased, and the amplitude response is slightly increased, as the bubble is moved closer to the wall.
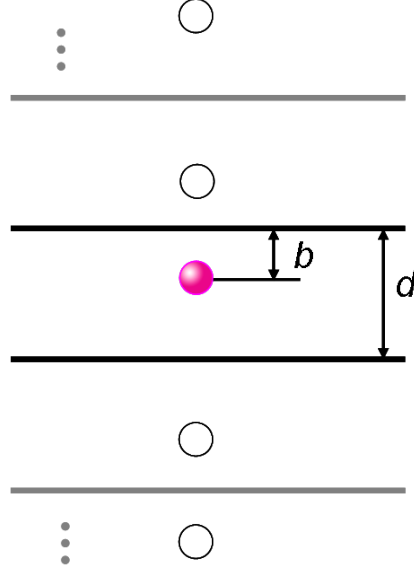
Figure 3.5: Geometry of a bubble located off-center in a channel formed by two parallel plates.
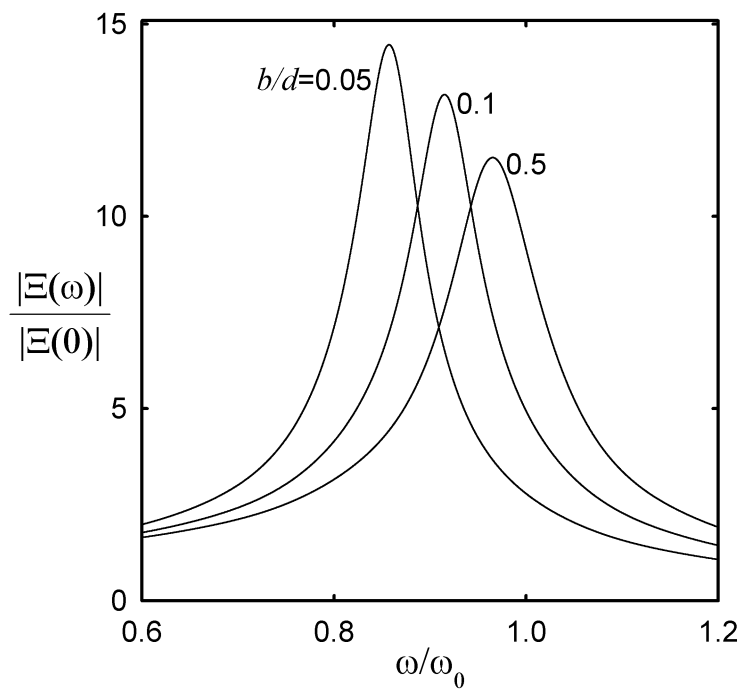
Figure 3.6: Dependence of amplitude response on distance b of bubble from channel wall, for $d/R_0 = 30$.

3.1.6 Pressure Release Walls

Equation (3.1) is easily modified to describe parallel plate channels with pressure release walls. The boundary condition is that the pressure at the interface is zero, which requires the first image to be in antiphase (differing by π radians, or opposite sign) with the bubble. For parallel surfaces, the images and the bubble form an infinite line array extending in both directions, with alternating phase from image to image. The summation accounting for radiation from the images in Eq. (3.3) becomes $\sum_{m=1}^{\infty}(-1)^m e^{-jmkd}/m$. The closed forms for the series, corresponding to Eqs. (3.4) and (3.5), are

$$\sum_{m=1}^{\infty}(-1)^m \frac{e^{-jmkd}}{m} = -\ln(1 + e^{-jkd}), \quad \text{for all } kd, \tag{3.19}$$

$$= -\ln\left(2\cos\frac{kd}{2}\right) + j\frac{kd}{2}, \quad -\pi < kd < \pi. \tag{3.20}$$

Alternatively, Eq. (3.19) can be obtained by setting $\beta = -1 = e^{j\pi}$ in Eq. (3.13), but Eq. (3.19) is free of the restriction $kd \gg 1$. Equation (3.19) is substituted in Eq. (3.3) to obtain

$$\frac{\Xi(\omega)}{\Xi(0)} = \left\{1 - \left[1 - 2\frac{R_0}{d}\ln(1 + e^{-jkd})\right]\frac{\omega^2}{\omega_0^2} + jk_0 R_0\frac{\omega^3}{\omega_0^3}\right\}^{-1}. \tag{3.21}$$

The magnitude of this frequency response is plotted in Fig. 3.7. From Fig. 3.7 we see that as the plate separation decreases, the resonance frequency increases. Since the path of least resistance for the liquid confined between two free surfaces is toward the free surfaces, when the channel becomes narrower less mass is in motion, the inertance decreases, and therefore the resonance frequency increases. This is in contrast to the rigid plates, for which the resonance frequency decreases as the

43
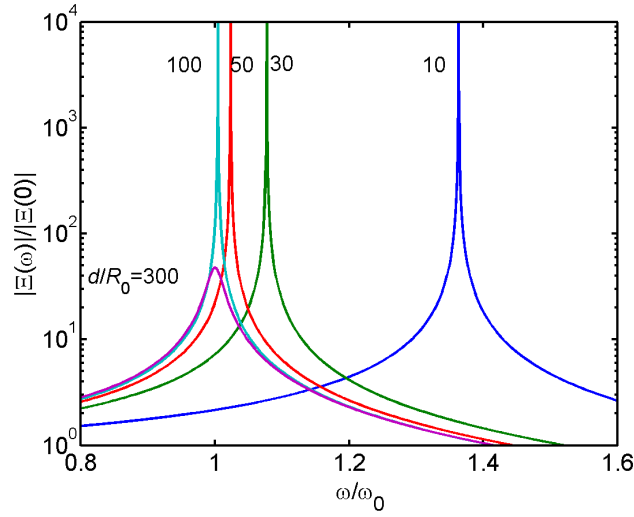
Figure 3.7: Frequency response of a bubble between two pressure release plates.

plate separation decreases owing to the increase in inertia (see Fig. 3.2). We also notice that the amplitudes at resonance are infinite for $d/R_0 \leq 100$. The reason for this is that, unlike a channel with rigid walls, a channel formed by free surfaces cannot support propagation at arbitrarily low frequencies. Consequently, there can be no radiation loss, and the quality factor is infinite, at frequencies below the cut-on frequency for the lowest propagating mode. The first propagating mode excited by the bubble cuts on at $kd = \pi$. Since $kd = k_0 R_0 (\omega/\omega_0)(d/R_0)$, for an air bubble in water and $\omega = \omega_0$ the first excited higher-order mode cuts on at $d/R_0 = 224$. Thus only when $d/R_0 > 224$ (half wavelength) can sound propagate, and only then will the bubble experience radiation loss. This explains the finite quality factor observed for $d/R_0 = 300$.

Explicit expressions for the resonance frequency and quality factor are obtained

44

by substituting Eq. (3.20) in Eq. (3.3), which yields

$$\frac{\Xi(\omega)}{\Xi(0)} = \left\{ 1 - \left[1 - 2\frac{R_0}{d} \ln\left(2\cos\frac{kd}{2} \right) \right] \frac{\omega^2}{\omega_0^2} \right\}^{-1}, \quad kd < \pi.$$ (3.22)

Setting the real part of the expression within the braces in Eq. (3.22) to zero, we obtain

$$\omega_r^{\mathrm{PR}} = \frac{\omega_0}{\sqrt{1 - 2(R_0/d)\ln|2\cos(\omega_r^{\mathrm{PR}}d/2c_0)|}}.$$ (3.23)

Using the relation $Q^{\mathrm{PR}} = |\Xi(\omega_r^{\mathrm{PR}})/\Xi(0)|$, we have for the quality factor

$$Q^{\mathrm{PR}} = \infty, \quad k_0 d < \pi,$$ (3.24)

$$= \frac{1}{k_0 R_0}, \quad k_0 d \to \infty.$$ (3.25)

Equation (3.24) follows from (3.22), and Eq. (3.25) follows from (3.21). The solution
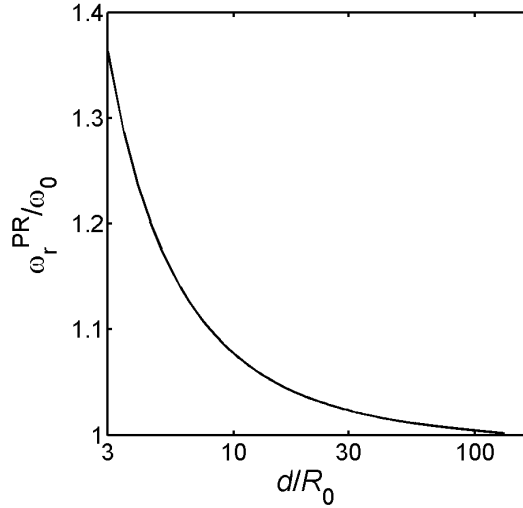
Figure 3.8: Resonance frequency of a bubble centered between two pressure release plates.

of Eq. (3.23) is shown in Fig. 3.8, which confirms what we observe in Fig. 3.7(a),

that the resonance frequency increases from its value of ω_0 in a free field as the plate separation is reduced.

3.2 Channels Formed by Tubes

The model equation for a bubble confined in a rigid tube, Eq. (2.16), can be linearized to obtain

$$\ddot{\xi}(t) + \omega_0^2 \xi(t) = \frac{R_0}{c_0}\dddot{\xi}(t) - R_0 \sum_{l,m} \frac{1}{r_{lm}}\ddot{\xi}\left(t - \frac{r_{lm}}{c_0}\right) - \frac{p_{ac}(t)}{\rho_0 R_0}, \tag{3.26}$$

where r_{lm} is the distance from the bubble to its image designated by the index pair (l, m), as shown in Figs. 2.7, 2.8 and 2.9.

3.2.1 Frequency Response

Again, time-harmonic excitation by an externally applied sound pressure is assumed. With $p_{ac}(t) = p_0 e^{j\omega t}$, the response takes the form $\xi(t) = \Xi(\omega)e^{j\omega t}$, and substitution of $p_{ac}(t)$ and $\xi(t)$ in Eq. (3.26) yields

$$\left[1 - \left(1 + R_0 \sum_{l,m} \frac{e^{-jkr_{lm}}}{r_{lm}}\right)\frac{\omega^2}{\omega_0^2} + jk_0 R_0 \frac{\omega^3}{\omega_0^3}\right]\frac{\Xi(\omega)}{R_0} = -\frac{p_0}{3\gamma P_0}, \tag{3.27}$$

or

$$\frac{\Xi(\omega)}{\Xi(0)} = \left[1 - \left(1 + R_0 \sum_{l,m} \frac{e^{-jkr_{lm}}}{r_{lm}}\right)\frac{\omega^2}{\omega_0^2} + jk_0 R_0 \frac{\omega^3}{\omega_0^3}\right]^{-1}. \tag{3.28}$$

Explicit expressions for r_{lm} when the bubble is in the center of a tube with a square, rectangular, or hexagonal cross section are

$$r_{lm} = (l^2 + m^2)^{1/2} s_4 \qquad\qquad \text{square tube,} \qquad\qquad (3.29)$$

$$= \sqrt{3}(l^2 + lm + m^2)^{1/2} s_6 \qquad \text{hexagonal tube,} \qquad\qquad (3.30)$$

$$= [(lb)^2 + (md)^2]^{1/2} \qquad\qquad \text{rectangular tube.} \qquad\qquad (3.31)$$

Here s_4 and s_6 are the lengths of the sides for the square and hexagon, respectively, and b and d are the breadth and height of the rectangle, respectively. For triangular cross section, no explicit expression was obtained for r_{lm}, and the method we used to calculate r_{lm} is given in Appendix A. An expression for d_{lm} for a bubble off center in a rectangular (square) tube was also obtained. Figure 3.9 shows an arbitrary position (x_s, y_s) of a bubble in a rectangular tube. The map of the images for an off-center bubble in a rectangular tube is shown in Fig. 3.10. The distance between the bubble
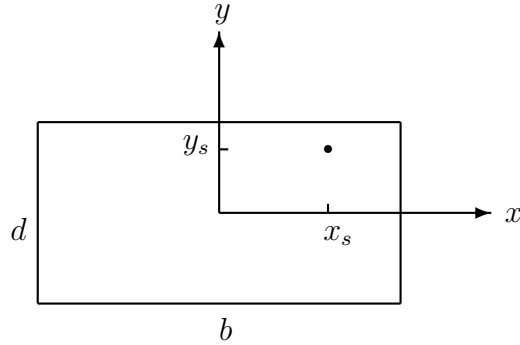
Figure 3.9: The coordinate system for an off-center bubble in a rectangular tube.
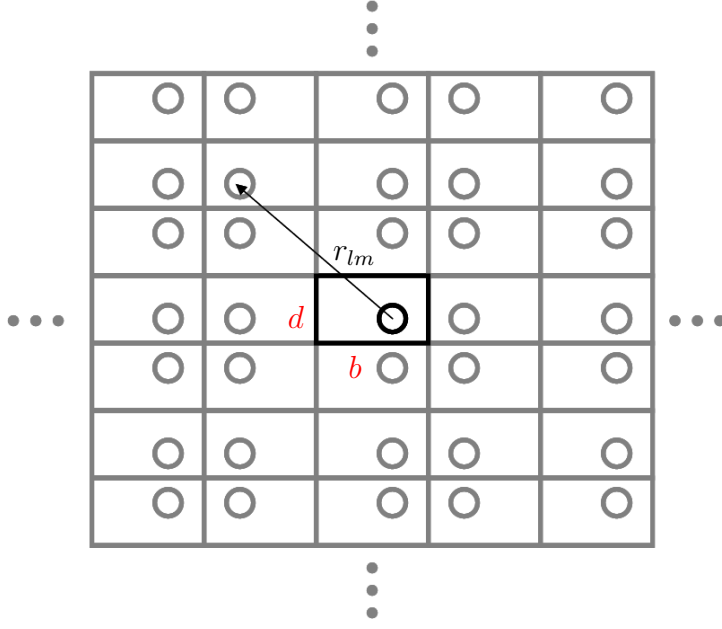
Figure 3.10: Image map for a bubble located off-center in a rectangular tube.

and any image with indices l, m is

$$r_{lm} = \sqrt{x_l^2 + y_m^2},$$

where

$$x_l = lb \qquad l \text{ even} \qquad\qquad (3.32)$$

$$= lb - 2x_s \qquad l \text{ odd}$$

$$y_m = md \qquad m \text{ even}$$

$$= md - 2y_s \qquad m \text{ odd}.$$

When $b = d = s_4$, Eq. (3.32) applies to an off-center bubble in a square tube. When $x_s = y_s = 0$, Eq. (3.31) is recovered.

48

We focus first on the case of a bubble located in the center of the tube. The frequency response is obtained from Eq. (3.28) for different tube geometries. Two questions are addressed: How does the shape of the tube cross section affect the bubble dynamics, and how does the width of the tube affect the bubble response? To address the first question, we normalize the three cross-sectional areas (triangular, square, and hexagonal) using the following relations to make them equal:

$$\frac{3^{1/4}}{2}s_3 = s_4 = \frac{3^{3/4}}{2^{1/2}}s_6, \tag{3.33}$$

where s_3, s_4 and s_6 refer to the side length of a triangle, square, and hexagon, respectively. To address the second question, we vary the normalized tube size $\sqrt{S}/R_0$ to see how the responses are affected. Thus for each tube size $\sqrt{S}/R_0$, a group of three curves corresponding to the three geometries is plotted together.

The double summation over the images is taken out to a circle of radius Ns_4. For a square tube, the relation $l^2 + m^2 \leq N^2$ ensures that the images included fall within the circular region. For triangular and hexagonal tubes, the images outside the circle were excluded from the summation. Details are provided in Appendix A. In our calculations, N was taken to be 1000.

Figure 3.11(a) shows five groups of frequency responses corresponding to five different cross-sectional areas, with each group containing three different tube geometries. For the range of $\sqrt{S}/R_0$ considered, 10 to 100, this would correspond to bubbles of radii 1 μm to 5 μm in tubes of radii from 10 μm to 500 μm (e.g., corresponding to contrast agents in blood vessels).

In Fig. 3.11(a) we see that the curves for the three different geometries overlap.

The cross-sectional shape of an infinite rigid tube thus has little effect on the bubble dynamics provided the cross-sectional areas are the same. This can be explained in terms of the number of images being summed. In any ring of radius r and thickness dr, since the number of images per unit area is the same (asymptotically) when the cross-sectional areas are the same, the number of images in any given ring is the same for all three geometries. We may also expect that Fig. 3.11(a) applies to cylindrical tubes when the tube areas match those of the three geometries considered. The frequency response of a bubble in a cylindrical tube will be investigated in Chapter 4 using a normal mode expansion. The ripples in the curves for $\sqrt{S}/R_0 = 10$ at very small values of ω/ω_0 result from numerical truncation error in the calculation of the summation. The more terms that are included in the summation, the less pronounced are the ripples. Figure 3.11(b) is an expanded view of the ripples, distinguishing the three different curves.

Notice also that as the cross-sectional area becomes smaller the damping increases, similar to what occurs for a bubble between rigid parallel plates. For $\sqrt{S}/R_0 = 20$ and below the resonance peaks disappear completely. For $\sqrt{S}/R_0 = 100$, the response is nearly the same as that in a free field. As will be discussed in more detail in the context of radiation impedance in Secs. 4.1.2 and 4.2.1, the radiation in a rigid tube couples with the plane wave mode, resulting in large radiation loss and leading to greater damping than for a bubble between rigid plates. The dynamics of a bubble in a rigid tube is controlled by the damping of the system, and the resonance peaks shift to lower frequencies as a result of the higher damping. This is different from the dynamics of a bubble between rigid plates, where the effect of mass loading

on the bubble is the dominant effect.

The trend of decreasing resonance frequency with decreasing tube diameter was also observed by Sassaroli and Hynynen [33–35] and Qin and Ferrara [15]. In their numerical study of the resonance frequency of a bubble in a blood vessel, Sassaroli and Hynynen [35] found that for a 2 μm bubble in a vessel with radius of 6 μm, the resonance frequency is 20% of its value in a free field. In their investigations a short tube model was used, where the length of the tube is much smaller than the wavelength of sound in the liquid (see Fig. 3.12, where L/a is small). The short tube approximation permits the liquid to be treated as incompressible in their study. Similarly, a short tube model is also the basis of the analysis by Oğuz and Prosperetti [1] and Ye and Bull [40, 41]. Ye and Bull [40, 41] performed a numerical simulation of the stresses on a short tube wall ($L/a = 7$) induced by a bubble expanding inside the tube. Both rigid and compliant tube walls were investigated.

The geometries of the finite-length tubes considered by Oğuz and Prosperetti [1] are shown in Fig. 3.13. They performed a numerical study of the natural frequencies of the systems and an approximate analytical solution was obtained.[1] They approximated the bubble as a cylindrical mass of gas spanning the cross section of the tube to obtain

$$\frac{f_{\text{tube}}}{f_0} = \frac{a}{\sqrt{R_0 L}}, \tag{3.34}$$

where f_{tube} is the natural frequency of a bubble located in the middle of the tube, f_0 is the natural frequency in a free field, a is the tube radius, R_0 is the equilibrium

---

[1]The approximate solution works very well except when the bubble radius is much smaller than that of the tube, for which an alternative approximate solution was developed.
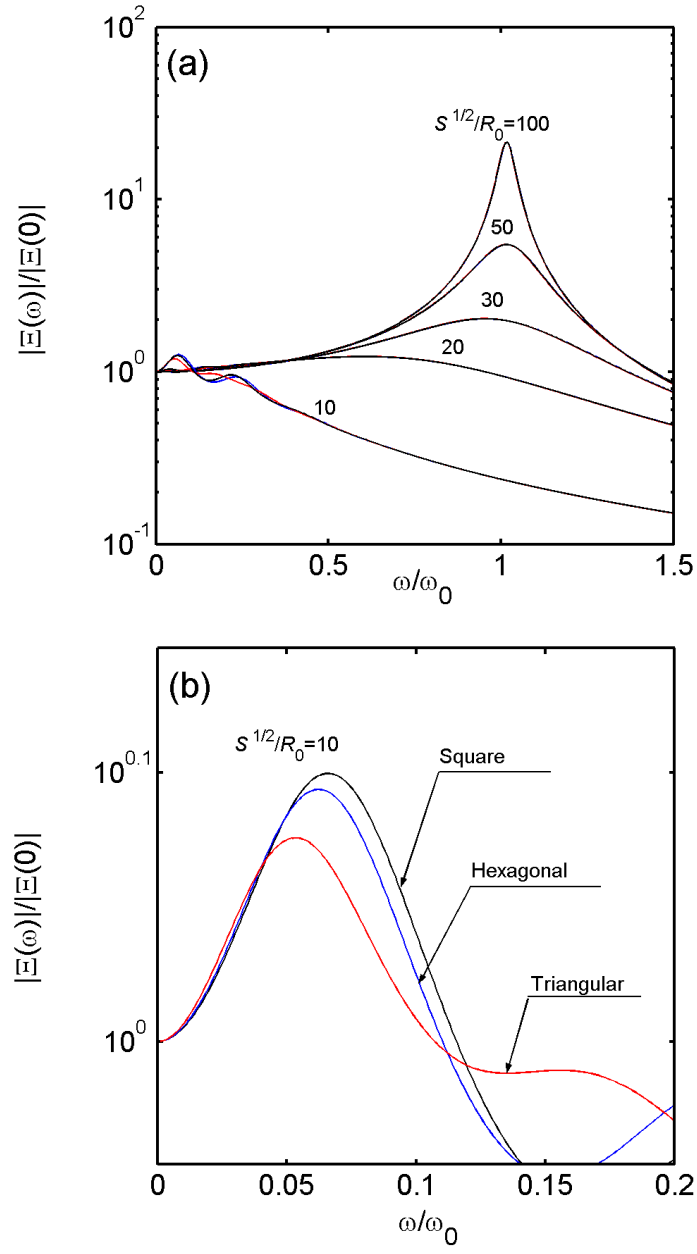
Figure 3.11: (a) Frequency responses for different tube cross-sections. The term $\sqrt{S}/R_0$ is the effective tube diameter normalized by the bubble radius. (b) Expanded view of the three curves for square, hexagonal and triangular tubes for $\sqrt{S}/R_0 = 10$.
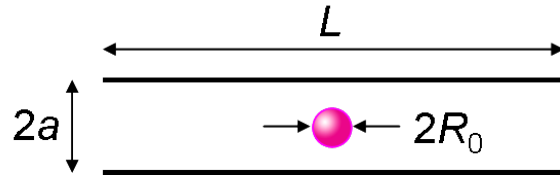
Figure 3.12: Bubble in a short tube.
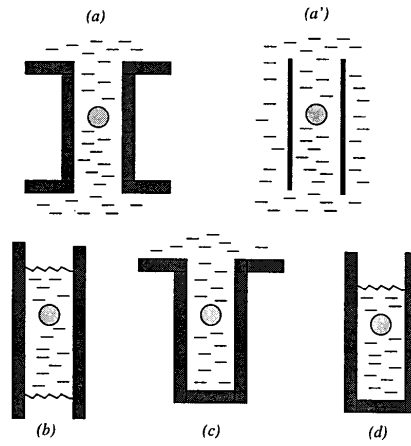
Figure 3.13: Geometries of tubes investigated by Oğuz and Prosperetti [1].

radius of the bubble, and L stands for the tube length with end corrections.

The physical interpretation of Eq. (3.34) is rather simple. Resonance frequency is proportional to the square root of the ratio of an effective stiffness to an effective mass. For both a bubble in a free field and a bubble in a rigid tube the effective stiffness is the same, being determined for an incompressible liquid only by the compressibility of the gas inside the bubble. The frequency ratio in Eq. (3.34) may thus be written as $f_{\text{tube}}/f_0 = (m_0/m_{\text{tube}})^{1/2}$, where m_0 is the effective mass in the free field, and m_{tube} is the effective mass in the presence of the tube. The former is given by $m_0 = 4\pi\rho_0 R_0^3$, the well known result for mass loading on a small pulsating sphere (equal to three times the mass of liquid displaced by the sphere). To estimate m_{tube} we assume that the inertia of the liquid is associated primarily with the liquid inside the tube, and that the inertia of the rapidly diverging flow fields at the ends of the tube is negligible in comparison. Begin by calculating the velocity v of the liquid in the tube assuming plug flow throughout the tube to the left and right of the bubble (recall Fig. 3.1), with $R_0 \ll a$. Considering, e.g., the right half of the tube, equate the volume velocity on the right half of the bubble wall, $2\pi R_0^2\dot{\xi}$, with the volume velocity in the tube, $\pi a^2 v$, to obtain $v = 2(R_0^2/a^2)\dot{\xi}$. The kinetic energy of the liquid in the entire tube is thus $\text{KE}_{\text{tube}} = \frac{1}{2}(\pi a^2 L\rho_0)v^2$, which after substitution for v may be written $\text{KE}_{\text{tube}} = \frac{1}{2}m_{\text{tube}}\dot{\xi}^2$, and one thus identifies $m_{\text{tube}} = 4\pi\rho_0 LR_0^4/a^2$ as the effective mass loading concentrated at the bubble wall. Substitution of the expressions for the effective masses in $(m_0/m_{\text{tube}})^{1/2}$ yields the right-hand side of Eq. (3.34) exactly.

For $L \to \infty$ one sees that $f_{\text{tube}} \to 0$, meaning that in this model there can

54

be no bubble pulsation due to the infinite inertia, which on the surface would seem to be consistent with our interpretation of bubble pulsation between infinite parallel plates. However, the assumption of incompressibility must be abandoned for long rigid tubes. Indeed, as noted in the discussion of Fig. 3.11(a) and analyzed in greater detail in Sec. 4.2.1, when compressibility of the liquid is taken into account for infinite rigid tubes it is radiation damping, not inertia, that reduces the resonance frequency below its value in a free field.

3.2.2 Square Tube

The square tube is a special case for which approximate analytical results can be obtained. For a bubble centered in a square tube with sides of length a, the summation in Eq. (3.27) can be written explicitly using the relation given in Eq. (3.29):

$$\left[1 - \left(1 + 4\frac{R_0}{a}\sum_{l=0}^{\infty}\sum_{m=1}^{\infty}\frac{e^{-j(l^2+m^2)^{1/2}ka}}{(l^2+m^2)^{1/2}}\right)\frac{\omega^2}{\omega_0^2} + jk_0R_0\frac{\omega^3}{\omega_0^3}\right]\frac{\Xi(\omega)}{R_0} = -\frac{p_0}{3\gamma P_0}. \quad (3.35)$$

A simplification of the summation is determined as follows. Use of $e^{jx} = \cos x + j \sin x$ leads to

$$\sum_{l=0}^{\infty}\sum_{m=1}^{\infty}\frac{e^{-j(l^2+m^2)^{1/2}ka}}{(l^2+m^2)^{1/2}} = \sum_{l=0}^{\infty}\sum_{m=1}^{\infty}\frac{\cos ka(l^2+m^2)^{1/2}}{(l^2+m^2)^{1/2}}$$
$$- j\sum_{l=0}^{\infty}\sum_{m=1}^{\infty}\frac{\sin ka(l^2+m^2)^{1/2}}{(l^2+m^2)^{1/2}}. \quad (3.36)$$

Tolstoy and Tolstoy [48] obtained the following closed-form expression for the sine series:

$$\sum_{l=0}^{\infty}\sum_{m=1}^{\infty}\frac{\sin ka(l^2+m^2)^{1/2}}{(l^2+m^2)^{1/2}} = \frac{\pi}{2}\frac{1}{ka} - \frac{ka}{4}, \quad 0 < ka < 2\pi. \quad (3.37)$$

55

For the cosine series, we show the numerical results for $N = 1000$ in Fig. 3.14(a). From Fig. 3.14(b) it can be seen that the asymptote of the cosine series is approximately -1 for $ka/\pi < 1$, and we can thus write

$$\sum_{l=0}^{\infty} \sum_{m=1}^{\infty} \frac{\cos ka(l^2 + m^2)^{1/2}}{(l^2 + m^2)^{1/2}} \simeq -1, \quad ka < \pi. \tag{3.38}$$

To generalize to tubes with other cross sections, we replace side a with $\sqrt{S}$, and the following approximate analytical result for the frequency response is obtained:

$$\frac{\Xi(\omega)}{\Xi(0)} = \left[1 - \left\{ 1 - 4\frac{R_0}{\sqrt{S}} \left[1 + j \left(\frac{\pi}{2} \frac{1}{k\sqrt{S}} - \frac{k\sqrt{S}}{4} \right) \right] \right\} \frac{\omega^2}{\omega_0^2} + jk_0 R_0 \frac{\omega^3}{\omega_0^3} \right]^{-1},$$

$$k\sqrt{S} < \pi. \tag{3.39}$$

Comparisons of numerical results obtained from the complete solution given by Eq. (3.35) (red curves) and the approximate analytical result given by Eq. (3.39) (blue curves) are shown in Fig. 3.15. Given that the admissible values of $k\sqrt{S}$ must be less than π for the approximation in Eq. (3.38) to be valid, and that for an air bubble in water $k_0 R_0 = 0.014$, the admissible values of $\sqrt{S}/R_0$ are less than $224/(\omega/\omega_0)$, or $\sqrt{S}/R_0 \lesssim 150$ for $\omega/\omega_0 < 1.5$, which is indeed satisfied in Fig. 3.15. The analytical approximation is seen to provide reasonable agreement with the complete solution for the frequency response. Approximately 4 million terms needed to be summed in Eq. (3.35) to achieve convergence.

One benefit of having an analytical approximation such as Eq. (3.39) is that it permits us to estimate the quality factor Q. We restrict our attention to values of $\sqrt{S}/R_0 \gtrsim 30$ in order to have an identifiable peak in the frequency response. As
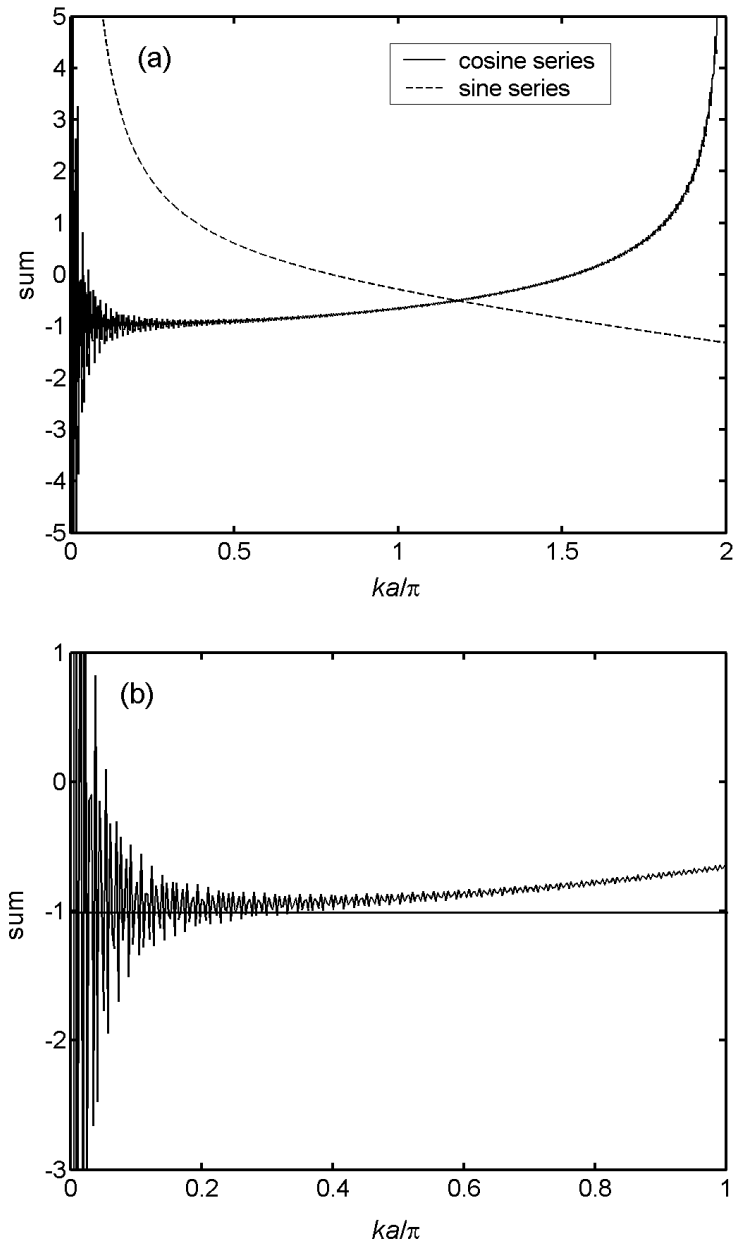
Figure 3.14: Summation results for a square tube. (a) Numerical summation of sine and cosine series in Eq. (3.35). (b) Expanded view of summation of cosine series.

57
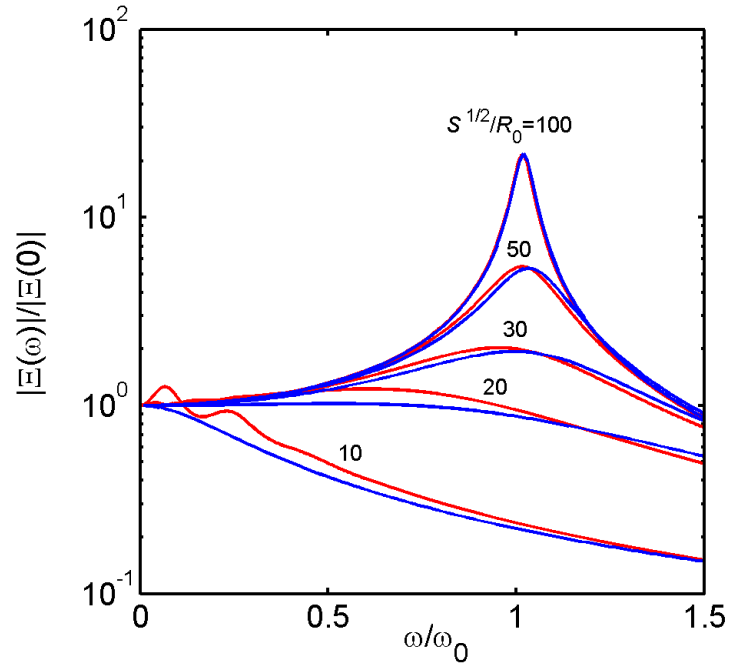
Figure 3.15: Comparison of the complete solution in Eq. (3.35) for a square tube with the approximate analytical solution in Eq. (3.39).

at the end of Sec. 3.1.3, define the quality factor by $Q = |\Xi(\omega_r)/\Xi(0)|$ in Eq. (3.39), approximating ω_r by ω_0 to obtain

$$Q \simeq \frac{k_0 R_0}{2\pi} \left(\frac{\sqrt{S}}{R_0} \right)^2 , \tag{3.40a}$$

$$= 2.23 \times 10^{-3} \left(\frac{\sqrt{S}}{R_0} \right)^2 . \tag{3.40b}$$

To obtain Eq. (3.40b) the value $k_0 R_0 = 0.014$ for an air bubble in water was used. From Eq. (3.40b) we see that the dependence of Q on $\sqrt{S}/R_0$ is quadratic. A plot of Eq. (3.40b) is shown in Fig. 3.16. The behavior shown in Fig. 3.16 is qualitatively
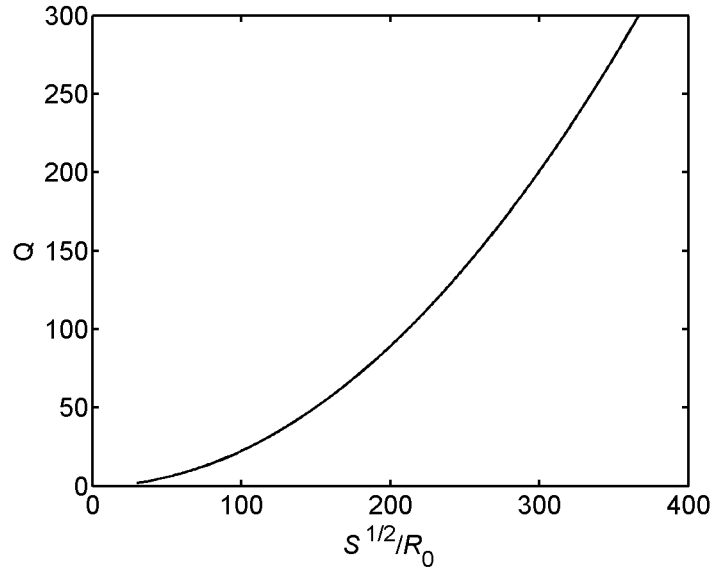
Figure 3.16: Quality factor based on the approximate result given by Eq. (3.40).

the same as shown in Fig. 3.3(b) for a bubble between rigid parallel plates. We remind the reader that the quality factors plotted in Figs. 3.3(b) and 3.13 account for loss associated only with radiation, and for wide tubes the quality factor will be

59

dominated by losses due to viscosity and heat conduction.

If the tube walls are instead pressure release, as for pressure release parallel plates the images will alternate phase. The summation in Eq. (3.27) becomes, for a square tube,

$$\sum_{l,m} \frac{e^{-jkr_{lm}}}{r_{lm}} = \frac{4}{a} \sum_{l=0}^{\infty} \sum_{m=1}^{\infty} (-1)^{l+m} \frac{e^{-j(l^2+m^2)^{1/2}ka}}{(l^2+m^2)^{1/2}}, \tag{3.41}$$

and the frequency response is obtained from an obvious modification of Eq. (3.35). Figure 3.17 shows the frequency responses of a bubble in square tubes of different sizes. For $a/R_0 \leq 30$, the nearby presence of the free surfaces requires less liquid to be in motion, thus causing the inertia to decrease and therefore the resonance frequency to increase. The trend of increasing natural frequency of oscillation of a bubble with decreasing compliant tube size was also observed by Qin and Ferrara [15]. For tubes sizes $a/R_0 \leq 100$ and drive frequencies shown in Fig. 3.17 there is no propagating mode in the tube. Consequently there is no radiation loss and the quality factor is infinite. For $\sqrt{S}/R_0 \geq 317$ the first propagating mode excited by the bubble produces radiation damping and thus the resonance amplitude is bounded (as shown in Fig. 3.17 for $a/R_0 = 450$). For sufficiently wide tubes the free field value of the quality factor is recovered.

Pressure release triangular and hexagonal tubes are not investigated here. Instead, a pressure release cylindrical tube will be studied, but this analysis is postponed to Chapter 4, where a normal mode expansion is used to study the problem.
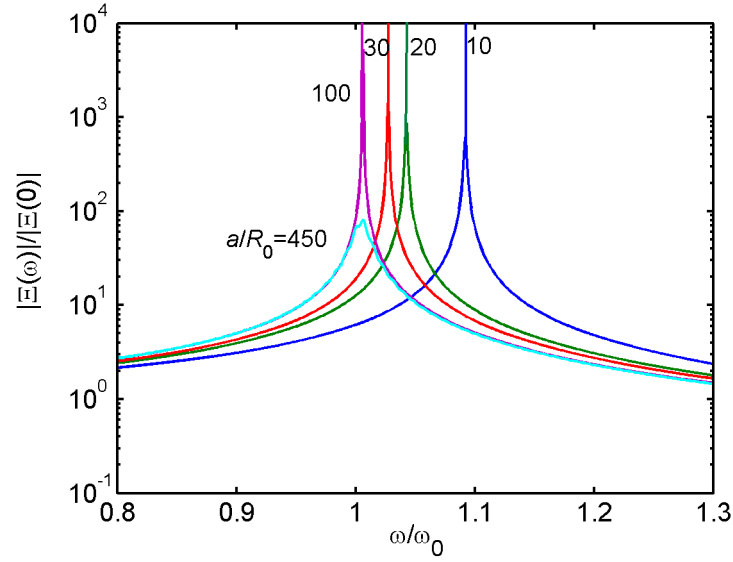
Figure 3.17: Frequency response of a bubble in the center of a square tube with pressure release walls. The tube walls have side length a.

3.2.3 Bubble in a Rectangular Tube

In this section we focus on the frequency response of a bubble centered in a rectangular tube. We are interested in showing the transition from a square tube to a rectangular tube to parallel plates as the aspect ratio of the sides of the rectangular tube are varied from unity to infinity. Let the rectangular cross-section have breadth b and height d, such that $r_{lm} = [(lb)^2 + (md)^2]^{1/2}$. The frequency response is then obtained by substituting this relation into Eq. (3.27). We show in Fig. 3.18 the resonance curves for a bubble centered in rectangular tubes with fixed side $d/R_0 = 30$ and ratios b/d ranging from 1 (square) to 100 (approximating infinite parallel plates). Along with the curves for the rectangular tube (black curves), we also plotted the frequency response for bubbles in a parallel-plate channel (red curves) and a square

61

tube (blue curves). The parallel-plate channel has a normalized separation of $d/R_0 = 30$, corresponding to the same ratio for the rectangular tube. The square tube has a cross-sectional area equal to that of the rectangle, such that each of its sides has length $a = \sqrt{bd}$.

For reference, the only curve that does not vary in Fig. 3.18 is the red line for the parallel plates (taking into account that the scale on the vertical axis may change), because the relative plate separation $d/R_0 = 30$ is fixed. As b/d is increased, the black curve for the rectangular tube moves away from the blue curve for the square tube and toward the red curve for the parallel plates. It can be seen that the rectangular tube approximates the parallel plates for $b/d > 20$.

The red curves in Fig. 3.18 correspond to the curve with $d/R_0 = 30$ in Fig. 3.2, where the confinement by the plates results in a suppressed resonance peak and a lower resonance frequency compared to free field values. The black and blue curves in Fig. 3.18(a) correspond to the curve for $\sqrt{S}/R_0 = 30$ in Fig. 3.11. As discussed in Sec. 3.2.1, the response of a bubble in a rigid duct is much more damped than between rigid plates due to coupling with the plane wave mode in the tube. As the rectangular tube becomes wider, it becomes more like two parallel plates. This transition can be seem from Fig. 3.18(a) to (f). In Fig. 3.18(f), the curves for the rectangular tube and parallel plates overlap, and the curve for the square tube corresponds to the response in a free field, with $a/R_0 = 300$.
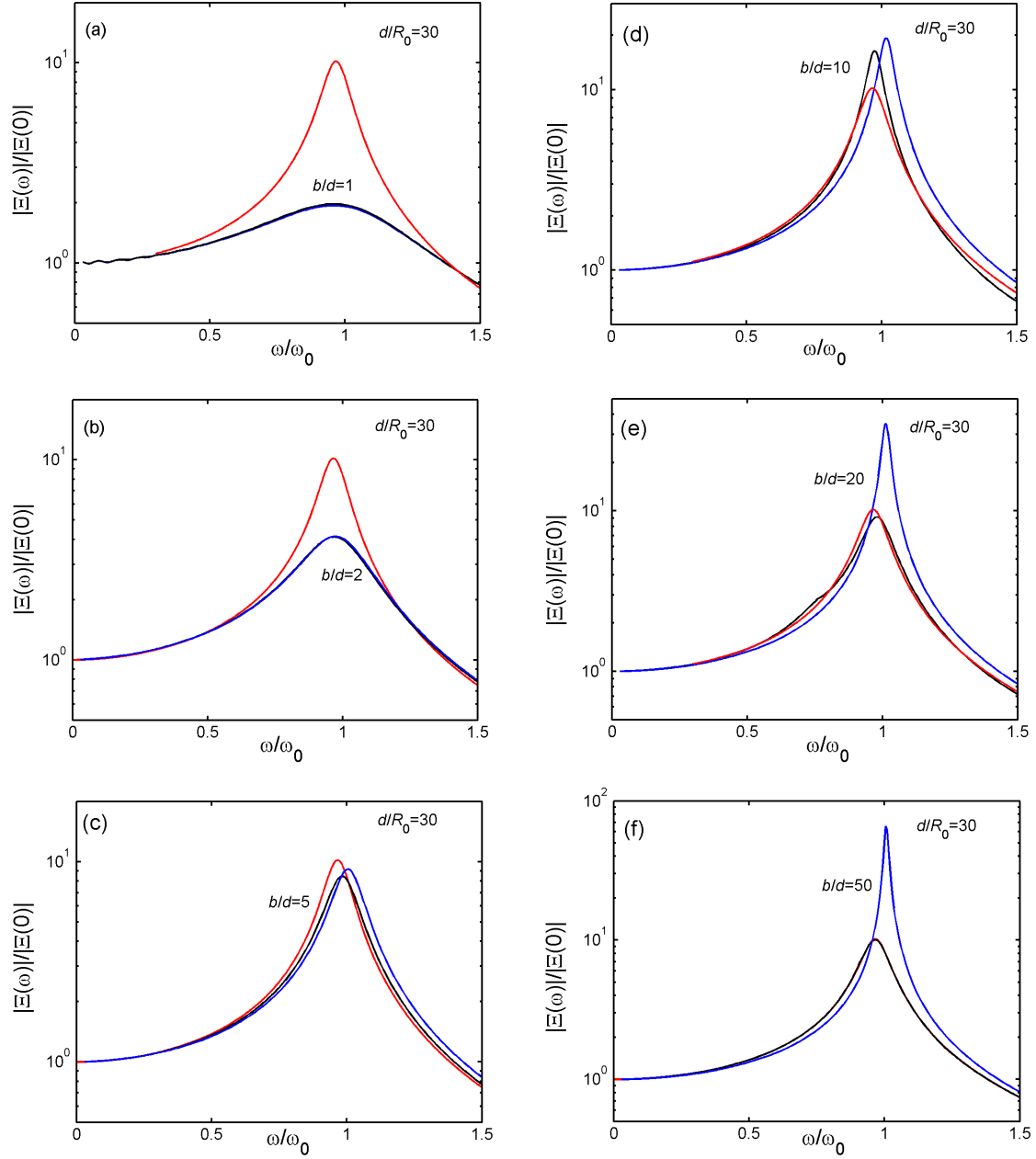
Figure 3.18: Transition of the frequency response of a bubble centered in a rigid rectangular tube. Black lines: bubble in a rectangular tube with width d ($d/R_0 = 30$) and varying height b ($d \leq b \leq 50d$). Blue lines: bubble centered in a rigid square tube with same cross-sectional area as the rectangle. Red lines: bubble centered between two rigid parallel plates with $d/R_0 = 30$.

63

3.2.4   Bubble Off-Center in a Square Tube

We also studied how the position of a bubble in a square tube affects the frequency response of the bubble. The geometry of a bubble off-center is shown in Fig. 3.9, and the expression for the bubble separation r_{lm} is given by Eq. (3.32) when $b = d = s_4$. The frequency response is obtained by substituting Eq. (3.32) into (3.27). Plots of the influence of the bubble position on the frequency response are shown in Fig. 3.19. Similar observations can be made as for a bubble off-center in the parallel plate channel shown in Fig. 3.6. Resonance frequency is decreased, and amplitude response is slightly increased, as the bubble is moved away from the center.
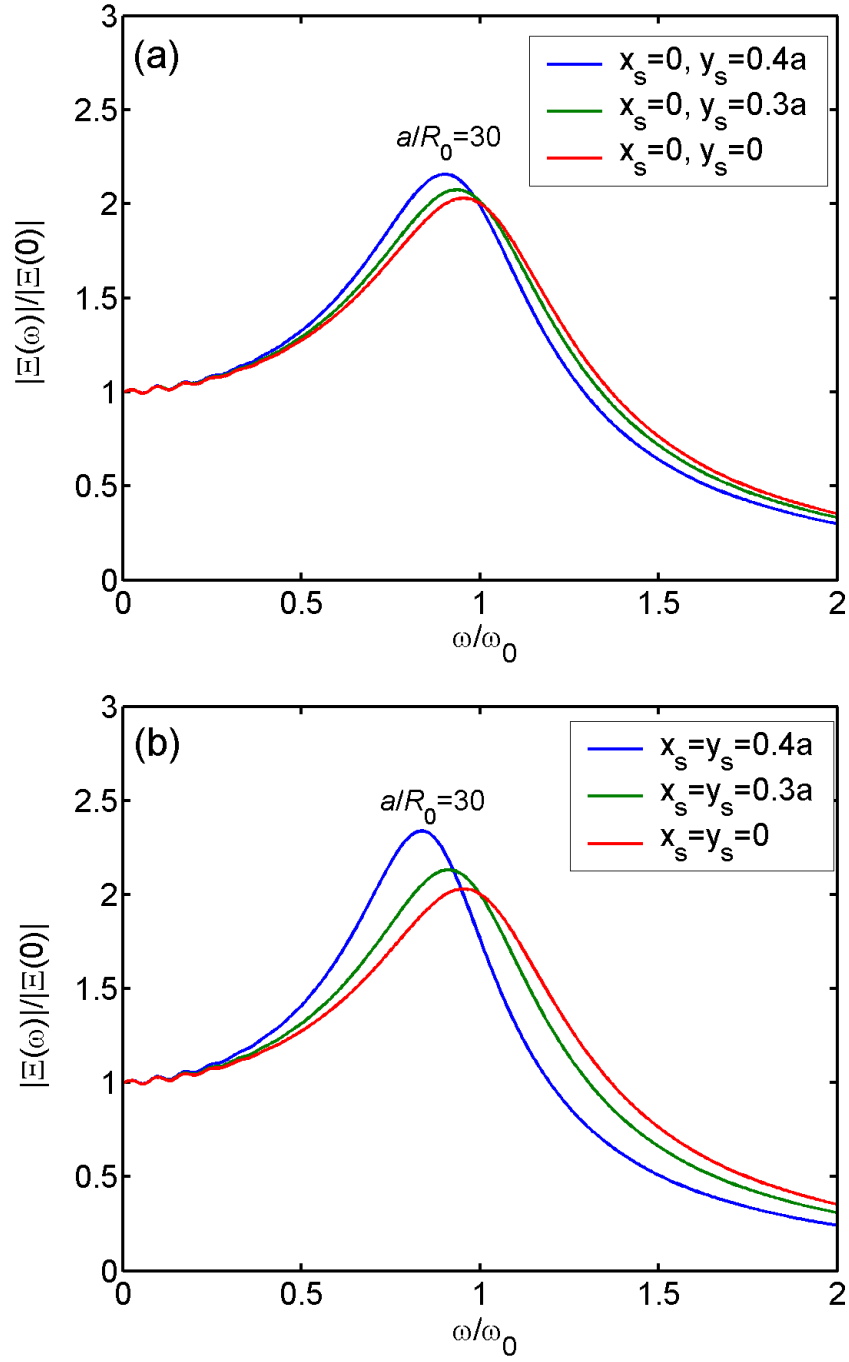
Figure 3.19: Frequency response of a bubble off-center in a square tube.

Chapter 4

Radiation Impedance

In the linear approximation, the radiation impedance of the bubble is the single most important property determining the dynamics of bubble pulsation in response to an applied sound field. The imaginary part of the radiation impedance, or reactance, influences the natural frequency, and the real part, or radiation resistance, influences the damping. Moreover, when recast as a function of radiation impedance, the frequency response of the bubble pulsation is easily related to existing analytical descriptions of simple sources in confined spaces created by ducts or cavities. In particular, following physical interpretation of the radiation impedance of bubbles in channels, we compare our expressions based on the method of images with Morse and Ingard's normal mode theory [2] for the radiation impedance of a simple source in a waveguide. The two approaches are found to be entirely consistent.

4.1   Radiation Impedance Based on Method of Images

We begin by deriving a general form of the frequency response given by Eq. (3.7) for parallel plates and Eq. (3.28) for tubes as a function of radiation impedance. As before, effects of viscosity, heat conduction, and surface tension are not considered here, and the frequencies under consideration are presumed to be such

that bubble radius is small in comparison with the acoustic wavelength.

The gas inside the bubble is assumed to behave adiabatically such that its pressure is $P_{\text{gas}} = P_0(R_0/R)^{3\gamma}$, where P_0 is atmospheric pressure, $R(t)$ the instantaneous bubble radius, and γ the ratio of specific heats. In the linear approximation this becomes, with $R(t) = R_0 + \xi(t)$,

$$P_{\text{gas}}(t) = P_0 - (3\gamma P_0/R_0)\xi(t)\,. \tag{4.1}$$

The gas pressure must equal the pressure P_{liq} in the liquid at the bubble wall. The latter is expressed as

$$P_{\text{liq}}(t) = P_0 + p_{\text{ac}}(t) + p_{\text{rad}}(t)\,, \tag{4.2}$$

where p_{ac} is the externally applied acoustic pressure, and p_{rad} is the acoustic pressure due to radiation from the bubble. Setting $P_{\text{gas}} = P_{\text{liq}}$ thus yields

$$-(3\gamma P_0/R_0)\xi(t) = p_{\text{ac}}(t) + p_{\text{rad}}(t)\,. \tag{4.3}$$

For harmonic excitation by an externally applied sound pressure $p_{\text{ac}}(t) = p_0 e^{j\omega t}$ the response takes the form $\xi(t) = \Xi(\omega)e^{j\omega t}$, and the acoustic pressure at the bubble wall may be expressed as $p_{\text{rad}}(t) = j\omega \Xi(\omega)e^{j\omega t}z_{\text{rad}}(\omega)$, where $j\omega \Xi(\omega)e^{j\omega t} = \dot\xi(t)$ is the radial particle velocity in the liquid at the bubble wall and $z_{\text{rad}}(\omega)$ is the acoustic radiation impedance. Making these substitutions in Eq. (4.3) one obtains

$$\left(1 + \frac{j\omega R_0 z_{\text{rad}}}{3\gamma P_0}\right)\Xi(\omega) = -\frac{p_0 R_0}{3\gamma P_0} \tag{4.4}$$

or, recognizing that $\Xi(0) = -p_0 R_0/3\gamma P_0$,

$$\frac{\Xi(\omega)}{\Xi(0)} = \left(1 + \frac{j\omega R_0 z_{\text{rad}}}{3\gamma P_0}\right)^{-1}\,. \tag{4.5}$$

67

Finally, it is convenient for our purposes to recast the previous equation as

$$\frac{\Xi(\omega)}{\Xi(0)} = \left[1 - \left(\frac{1}{jk_0R_0}\right)\left(\frac{z_{\text{rad}}}{\rho_0c_0}\right)\frac{\omega}{\omega_0}\right]^{-1}, \tag{4.6}$$

where $\omega_0 = (3\gamma P_0/\rho_0R_0^2)^{1/2}$ is again the natural angular frequency of a bubble in an unbounded liquid, $k_0 = \omega_0/c_0$ is the associated acoustic wavenumber in the liquid, and as noted previously for an air bubble in water $k_0R_0 = 0.014$.

In an unbounded fluid, the acoustic radiation impedance of a sphere with arbitrary radius R_0 is, in dimensionless form [60],

$$\frac{z_{\text{rad}}}{\rho_0c_0} = \frac{jkR_0}{1 + jkR_0}. \tag{4.7}$$

For $kR_0 \ll 1$ the expression reduces to $z_{\text{rad}}/\rho_0c_0 \simeq jkR_0$ at leading order, and the right-hand side of Eq. (4.6) becomes $(1 - \omega^2/\omega_0^2)^{-1}$, which is the classical result for a bubble in an unbounded incompressible liquid.

We now apply Eq. (4.6) to specific geometries.

4.1.1 Bubble between Parallel Plates

For a bubble centered between parallel plates, comparison of Eqs. (3.7) and (4.6) reveals that

$$\frac{z_{\text{rad}}}{\rho_0c_0} = jkR_0 + (kR_0)^2 - j2kR_0\frac{R_0}{d}\ln(1 - e^{-jkd}) \tag{4.8}$$

or equivalently

$$\frac{z_{\text{rad}}}{\rho_0c_0} = jkR_0 + (kR_0)^2 + j2kR_0\frac{R_0}{d}\sum_{m=1}^{\infty}\frac{e^{-jmkd}}{m}. \tag{4.9}$$

68

The first two terms in these expressions are the first two terms in the expansion of Eq. (4.7) for small kR_0. The first term thus accounts for mass loading in a free field, the second for radiation damping in a free field. The real and imaginary parts of the third term in Eqs. (4.8) and (4.9) are likewise the contributions to radiation damping and mass loading, respectively, due to the presence of the plates. To make the different contributions more clear, real and imaginary terms in Eq. (4.9) may be separated and regrouped as follows:

$$\frac{z_{\text{rad}}}{\rho_0 c_0} = jkR_0\left(1 + 2\frac{R_0}{d}\sum_{m=1}^{\infty}\frac{\cos mkd}{m}\right) + (kR_0)^2\left(1 + \frac{2}{kd}\sum_{m=1}^{\infty}\frac{\sin mkd}{m}\right), \quad (4.10)$$

or, making use of Eq. (3.4) for $kd < 2\pi$,

$$\frac{z_{\text{rad}}}{\rho_0 c_0} = jkR_0\left[1 - 2\frac{R_0}{d}\ln\left(2\sin\frac{kd}{2}\right)\right] + \pi kR_0\frac{R_0}{d}, \qquad kd < 2\pi. \quad (4.11)$$

The real and imaginary parts of Eq. (4.8), corresponding to the radiation resistance and radiation reactance, repeatedly are plotted in Fig. 4.1 for $d/R_0 = 30$. The dashed lines in Fig. 4.1, corresponding to the first two terms in Eq. (4.8), are included for comparison with the results for an unbounded liquid. From Fig. 4.1(a) we see that for $kd/\pi < 1$ the radiation resistance of a bubble centered between two parallel plates is larger than that of a bubble in a free field. This in turn corresponds to higher damping and lower quality factor for $d/R_0 \leq 100$, as shown in Fig. 3.2. The maximum value of kd, which occurs for $d/R_0 = 100$, can be calculated as $kd = (\omega/\omega_0)(d/R_0)(k_0R_0) = 2 \times 100 \times 0.014 = 2.8$ for the drive frequency range $\omega/\omega_0 \leq 2$, and so we have $kd/\pi < 1$ over this entire frequency range of d/R_0 under consideration. Similarly, from Fig. 4.1(c) we notice that the radiation reactance of a bubble between

69

Figure 4.1: Radiation impedance of a bubble in the middle between two parallel rigid plates for $d/R_0 = 30$, obtained from Eq. (4.8). (a) Radiation resistance, (b) radiation reactance, (c) expanded view of radiation reactance for $kd/\pi < 0.4$. Solid lines: bubble between two parallel rigid plates. Dashed lines: bubble in free space.

plates is slightly larger than that in a free field for $kd/\pi < 0.33$. This corresponds to higher mass loading and results in lower resonance frequencies for $d/R_0 \leq 30$, as observed in Fig. 3.2. Also for $d/R_0 \leq 30$, we have $kd/\pi < 0.3$ over the entire range of the drive frequency.

The crossover points in Fig. 4.1 at $kd/\pi = 1$ for the radiation resistance and $kd/\pi = 0.33$ for the radiation reactance can be calculated as follows. Equating the second terms in Eqs. (4.8) and (4.11) yields $kd = \pi$ for the crossover point for the resistance, independent of d/R_0. Likewise, equating the first terms yields $kd = 2\arcsin(0.5) = \pi/3$, or $kd/\pi = 0.33$, for the reactance, again independent of d/R_0.
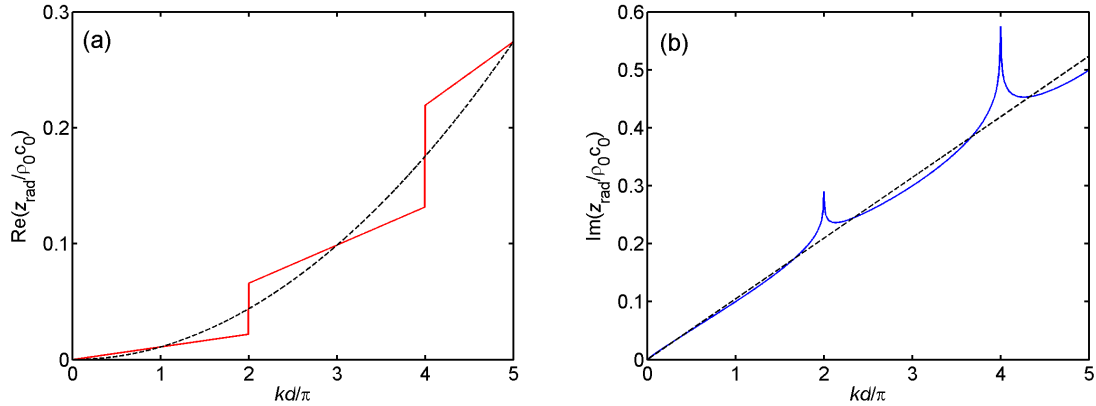
Figure 4.2: Radiation impedance of a bubble in the middle between two parallel rigid plates and the resonance pattern for $d/R_0 = 30$, obtained from Eq. (4.8). (a) Radiation resistance, (b) radiation reactance. Solid lines: bubble between two parallel rigid plates. Dashed lines: bubble in free space.

The radiation resistance and reactance are plotted up to $kd = 5\pi$ in Fig. 4.2 to show the resonance pattern. As kd (or the drive frequency) increases, both the
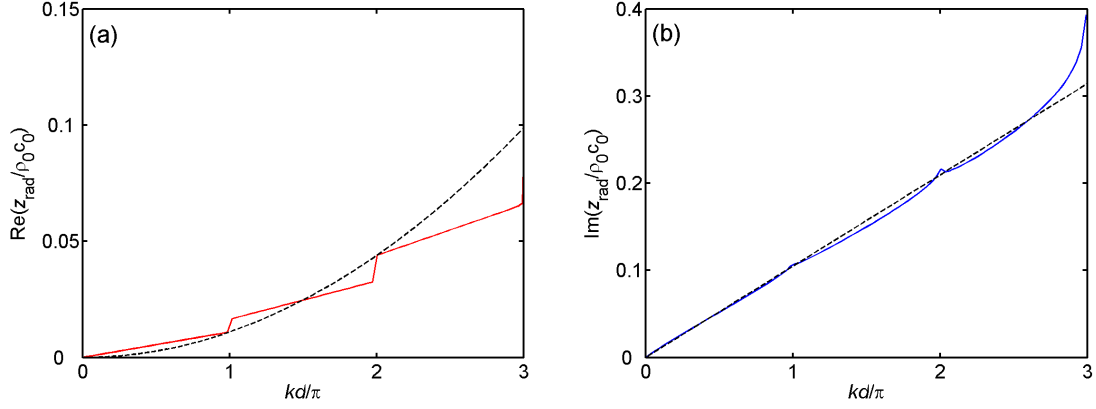
Figure 4.3: Radiation impedance of a bubble off-center between two parallel rigid plates and the resonance pattern for $d/R_0 = 30$, and with $b/d = 1/3$ (see Fig. 3.5). (a) Radiation resistance, (b) radiation reactance. Solid lines: bubble between two parallel rigid plates. Dashed lines: bubble in free space.

radiation resistance and reactance increase, and each new mode is introduced by a step (for the radiation resistance) or a spike (for the radiation reactance) at its cuton frequency. Notice that the resonance spikes/steps occur only where kd is a multiple of 2π (or when the plate separation d is an even multiple of a half wavelength), instead of at all integer multiples of π at which the acoustic resonances occur. This is because the bubble is located midway between the plates, and when the plate separation d is an odd multiple of a half wavelength there is a particle velocity antinode at the location of the bubble, and those modes are not excited. Once the bubble is moved off-center,[1] and not at locations that are distances $d/2$, $d/4$, $d/8$, etc., away from one of the plates, the spikes/steps for both radiation resistance and reactance occur when kd is an integer multiple of π, as can be seen in Fig. 4.3, where the bubble is located

---

[1]For this case, the summation in Eq. (4.9) is replaced by Eq. (3.18).

distance $d/3$ away from one of the plates.

In Eq. (4.9), the factor of jkR_0 multiplying the summation corresponds to the first term in the expansion of Eq. (4.7) for the image bubbles, and one can likewise keep higher-order terms. Results including the next higher-order term are now discussed. The first two terms in the expansion of Eq. (4.7) are $jkR_0(1-jkR_0)$. Replacing jkR_0 by $jkR_0(1-jkR_0)$ in Eq. (4.8), we obtain

$$\frac{z_{\mathrm{rad}}}{\rho_0 c_0} = jkR_0 + (kR_0)^2 - j2kR_0(1-jkR_0)\frac{R_0}{d}\ln(1-e^{-jkd}). \qquad (4.12)$$

Plots of Eq. (4.12) corresponding to Figs. 4.1–4.3 are shown in Figs. 4.4–4.6. No obvious differences are observed in the radiation reactance plots, but in the radiation resistance plots the spikes at the resonances become more pronounced when the next higher-order term is retained.
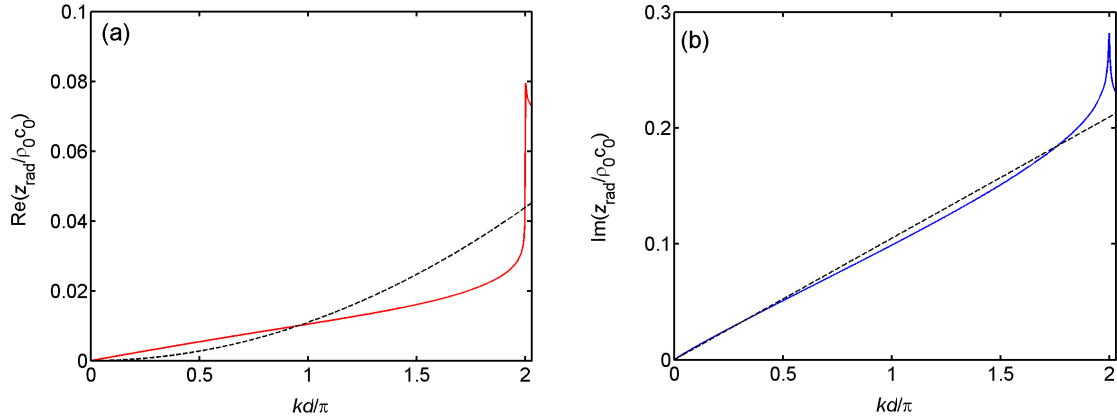
Figure 4.4: Radiation impedance of a bubble in the middle between two parallel rigid plates for $d/R_0 = 30$, obtained from Eq. (4.12). (a) Radiation resistance, (b) radiation reactance. Solid lines: bubble between two parallel rigid plates. Dashed lines: bubble in free space.

73
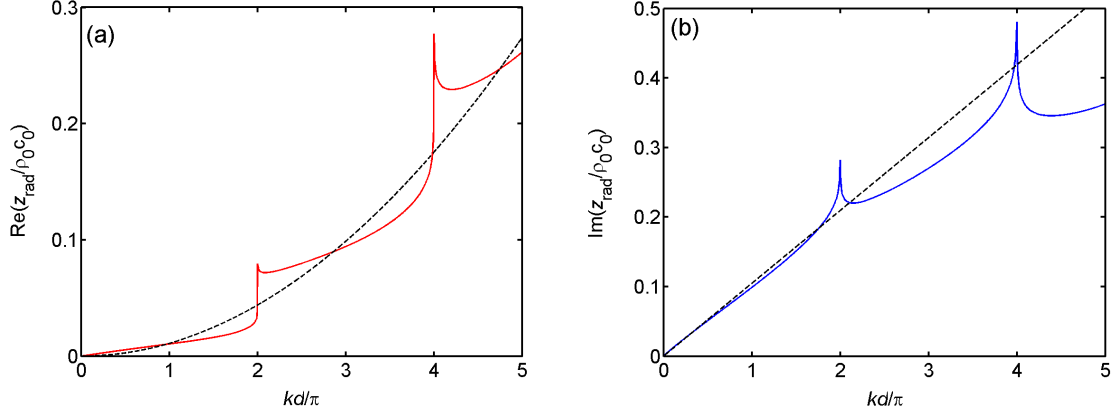
Figure 4.5: Radiation impedance of a bubble in the middle between two parallel rigid plates and the resonance pattern for $d/R_0 = 30$, obtained from Eq. (4.12). (a) Radiation resistance, (b) radiation reactance. Solid lines: bubble between two parallel rigid plates. Dashed lines: bubble in free space.
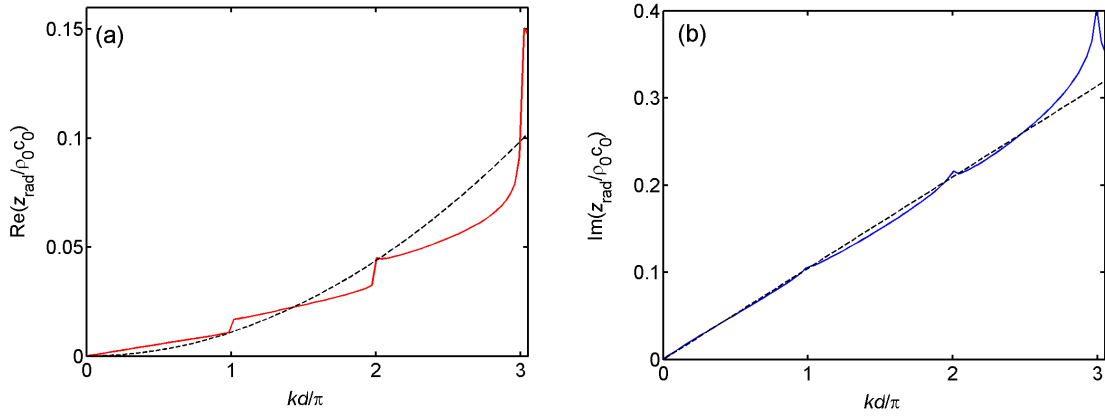
Figure 4.6: Radiation impedance of a bubble off-center between two parallel rigid plates and the resonance pattern for $d/R_0 = 30$ and with $b/d = 1/3$ (see Fig. 3.5), obtained from Eq. (4.9). (a) Radiation resistance, (b) radiation reactance. Solid lines: bubble between two parallel rigid plates. Dashed lines: bubble in free space.

74

4.1.2 Bubble in a Square Tube

For a bubble in a tube, comparison of Eqs. (3.28) and (4.6) shows that

$$\frac{z_{\text{rad}}^{\text{tube}}}{\rho_0 c_0} = jkR_0 + (kR_0)^2 + jkR_0^2 \sum_{l,m} \frac{e^{-jkr_{lm}}}{r_{lm}}, \tag{4.13}$$

where $z_{\text{rad}}^{\text{tube}}$ denotes the radiation impedance inside a tube. As before, the first two terms are the radiation impedance for a simple source in a free field, and the third term accounts for the effects from the reverberation field produced by the tube walls. For a square tube with side a we have $r_{lm} = a(l^2 + m^2)^{1/2}$ and Eq. (4.13) becomes

$$\frac{z_{\text{rad}}^{\text{sq}}}{\rho_0 c_0} = jkR_0 + (kR_0)^2 + j4kR_0 \frac{R_0}{a} \sum_{l=0}^{\infty} \sum_{m=1}^{\infty} \frac{e^{-j(l^2+m^2)^{1/2}ka}}{(l^2 + m^2)^{1/2}}, \tag{4.14}$$

where the superscript "sq" denotes square tube. The real and imaginary parts of the double summation in Eq. (4.14) account for the contributions to radiation damping and mass loading, respectively, due to the presence of the tube walls. To make the different contributions more clear, real and imaginary terms in Eq. (4.14) may be separated and regrouped as follows:

$$\frac{z_{\text{rad}}^{\text{sq}}}{\rho_0 c_0} = jkR_0 \left[1 + 4\frac{R_0}{a} \sum_{l=0}^{\infty} \sum_{m=1}^{\infty} \frac{\cos[(l^2 + m^2)^{1/2}ka]}{(l^2 + m^2)^{1/2}} \right]$$
$$+ (kR_0)^2 \left[1 + \frac{4}{ka} \sum_{l=0}^{\infty} \sum_{m=1}^{\infty} \frac{\sin[(l^2 + m^2)^{1/2}ka]}{(l^2 + m^2)^{1/2}} \right]. \tag{4.15}$$

Employing the expression Tolstoy and Tolstoy [48] obtained for the sine series, Eq. (3.37), we get

$$\frac{z_{\text{rad}}^{\text{sq}}}{\rho_0 c_0} = 2\pi \frac{R_0^2}{a^2} + jkR_0 \left[1 + 4\frac{R_0}{a} \sum_{l=0}^{\infty} \sum_{m=1}^{\infty} \frac{\cos[(l^2 + m^2)^{1/2}ka]}{(l^2 + m^2)^{1/2}} \right], \quad ka < 2\pi. \tag{4.16}$$

The first term in Eq. (4.16) is the radiation resistance, and it is independent of frequency (for $ka < 2\pi$). This term accounts for coupling of radiation from the bubble into the plane wave mode of the tube, the only propagating mode that is excited by a bubble in the center of the tube for $ka < 2\pi$, which is the condition under which Eq. (4.16) was obtained. It is therefore the only mode that can permit radiation when the bubble is in the center of the tube, and consequently the only mode that can contribute to the radiation resistance. This coupling into the plane wave mode acts as an impedance transformer due to conservation of volume velocity. The volume velocity of the bubble is $4\pi R_0^2 \dot{\xi}$, and the volume velocity in the tube may be expressed as $2a^2 u_{\mathrm{avg}}$, where u_{avg} is the average particle velocity across the tube, and the factor of two is due to the fact that sound is radiated in both directions. Equating these expressions and taking the ratio $u_{\mathrm{avg}}/\dot{\xi}$ yields $2\pi R_0^2/a^2$, which is the first term in Eq. (4.16). The second term in Eq. (4.16) is the radiation reactance.

The radiation resistance and reactance calculated from Eq. (4.15) are plotted in Fig. 4.7 for $a/R_0 = 30$. The dashed lines in Fig. 4.7 are again the results for a bubble in an unbounded liquid. As seen from Fig. 4.7(a), the radiation resistance of the bubble is independent of frequency in the range $ka < 2\pi$, with $\mathrm{Re}(z_{\mathrm{rad}}/\rho_0 c_0) \simeq$ 0.007 for $a/R_0 = 30$, associated with coupling into the plane wave mode. High radiation resistance corresponds to high damping and low quality factor, as observed in Fig. 3.11. From Fig. 4.7(b) we see that the radiation reactance is slightly lower than its value for free space over the region of interest, $ka < \pi$, which suggests that the mass loading on the bubble in a square tube is slightly lower than that in a free field. But as seen from Fig. 3.11, the resonance frequency for a bubble in a square

76

tube with $a/R_0 < 30$ is lower than its free field value. Therefore the downshift of the resonance frequency is not caused by larger mass loading. Instead, it is caused by the high damping in the system. Also, for $a/R_0 < 20$ the resonance peaks become difficult to identify because the system is overdamped. At $ka = 2\pi$ we see spikes in both the radiation resistance and reactance, where mode $(2,0)$ cuts on. For a bubble centered in the tube, mode $(2,0)$ is the first propagating nonplanar mode that can be excited. Modes $(1,0)$ and $(1,1)$ are not excited because they have velocity antinodes at the location of the bubble.

Plots of the real and imaginary parts of Eq. (4.15) for a rigid square tube, showing a larger number of propagating modes, are presented in Fig. 4.8 for a bubble located at the center. Similar to the cases where the bubble is located midway between the parallel plates, the symmetry renders some modes unexcited. If a bubble is located off-center (see Fig. 3.10), Eq. (4.13) with r_{lm} given by Eq. (3.32) is used instead of Eq. (4.15) to obtain the radiation impedance. Figure 4.9 is for a bubble located off-center with $x_s = -a/6$, and $y_s = -a/6$ (see Fig. 3.9). The cutoff frequencies for different modes in a square tube are given by $f_{lm} = (c_0/2a)\sqrt{l^2 + m^2}$ [60], and the values of ka/π for these modes can be calculated from $k_{lm}a/\pi = (l^2 + m^2)^{1/2}$. Table 4.1 gives the values of $k_{lm}a$ for the first six modes. [Note: Due to the symmetry of the square tube, modes (l, m) mode (m, l) are interchangeable.] When the bubble is located off-center, all six propagating modes for $ka/\pi \leq 3$ are excited, whereas for a bubble at the center, only two modes, $(2,0)$ and $(2,2)$, are excited. In general, for the bubble located at the center, since it is a velocity source, only those modes with an antinode at the center will be excited. Further, the symmetry about the x and

77

y axes of the source location causes the modes with either l or m odd to disappear. Only the mode with both l and m even are excited.
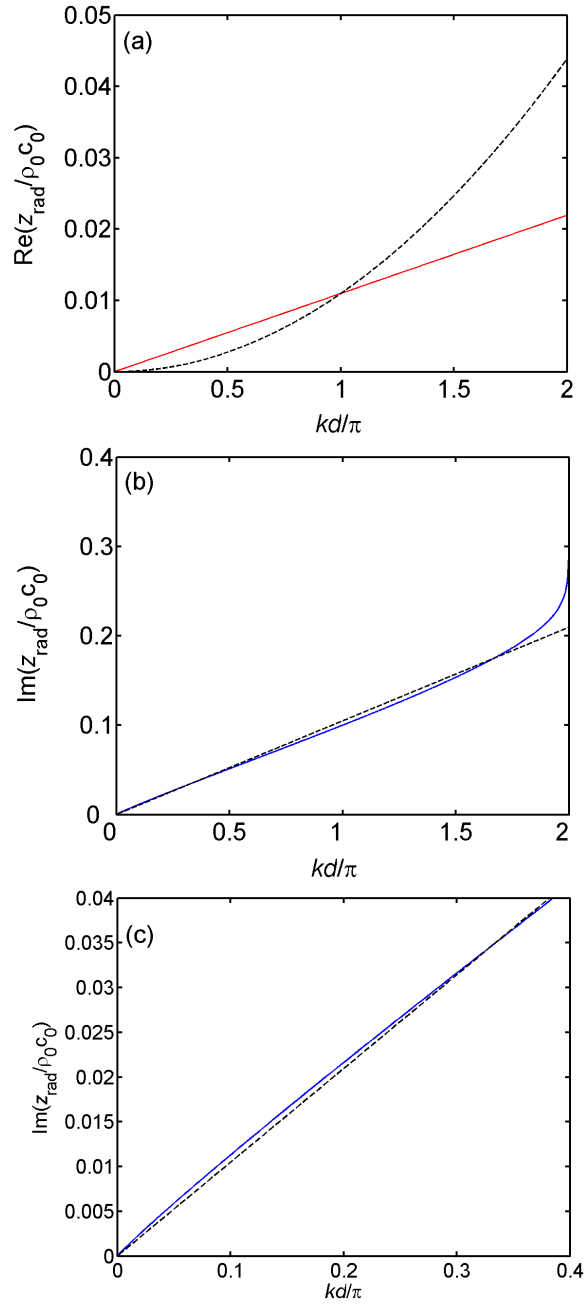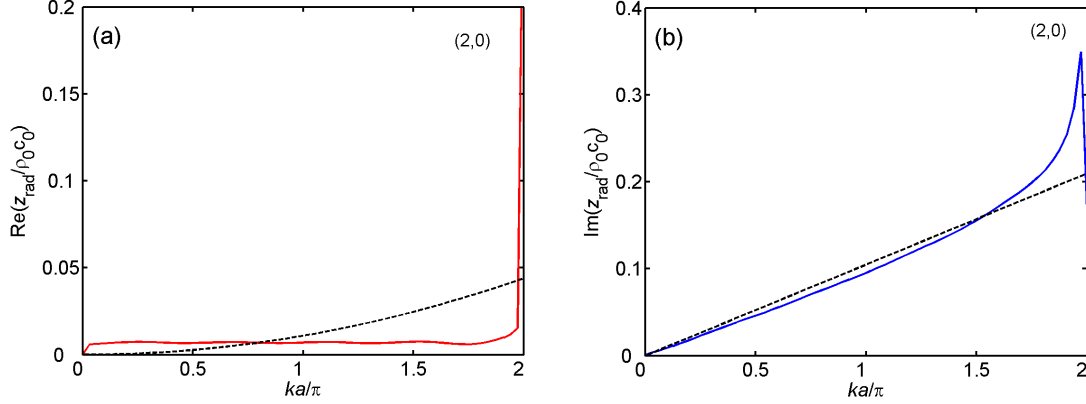

Figure 4.7: Radiation impedance of a bubble in the center of a rigid square tube for $a/R_0 = 30$, obtained from Eq. (4.15). (a) Radiation resistance, (b) radiation reactance. Solid lines: bubble in tube. Dashed lines: bubble in free space.

Mode	$k_{lm}a/\pi$
$(0,1)$	1.0
$(1,1)$	1.414
$(2,0)$	2.0
$(2,1)$	2.236
$(2,2)$	2.828
$(3,0)$	3.0

Table 4.1: Values of $k_{lm}a$ for the first six propagating modes in a square tube with $a/R_0 = 30$, $x_s = -a/6$, and $y_s = -a/6$ (see Fig. 3.9).

As in Eq. (4.12), we can keep the first two terms in the expansion of Eq. (4.7) for the images associated with rectangular tubes. Equation (4.13) then becomes

$$\frac{z_{\text{rad}}^{\text{tube}}}{\rho_0 c_0} = jkR_0 + (kR_0)^2 + jkR_0^2(1 - jkR_0)\sum_{l,m}\frac{e^{-jkr_{lm}}}{r_{lm}} \qquad (4.17)$$

78
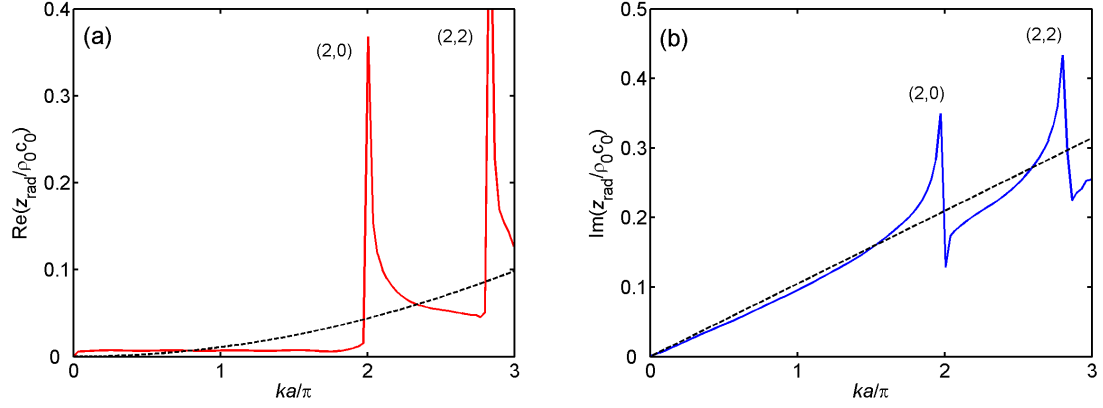
Figure 4.8: Radiation impedance of a bubble in the center of a rigid square tube showing the propagation modes for $a/R_0 = 30$, obtained from Eq. (4.15). (a) Radiation resistance, (b) radiation reactance. Solid lines: bubble in tube. Dashed lines: bubble in free space.
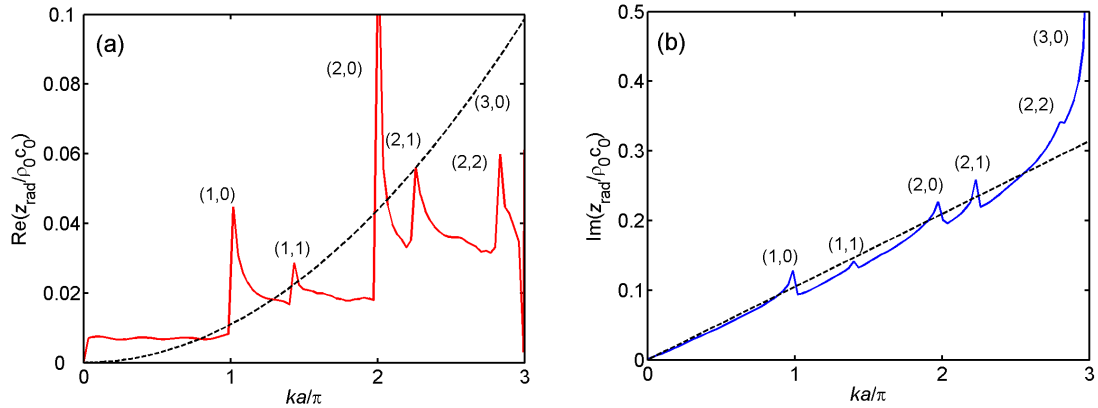
Figure 4.9: Radiation impedance of a bubble located off-center in a rigid square tube showing the propagation modes for $a/R_0 = 30$ with $x_s = -a/6$, and $y_s = -a/6$ (see Fig. 3.9), obtained from Eq. (4.13). (a) Radiation resistance, (b) radiation reactance. Solid lines: bubble between two parallel rigid plates. Dashed lines: bubble in free space.

or, for a square tube,

$$\frac{z_{\text{rad}}^{\text{sq}}}{\rho_0 c_0} = jkR_0 + (kR_0)^2 + j4kR_0\frac{R_0}{a}(1 - jkR_0)\sum_{l=0}^{\infty}\sum_{m=1}^{\infty}\frac{e^{-j(l^2+m^2)^{1/2}ka}}{(l^2+m^2)^{1/2}}\,. \qquad (4.18)$$

Plots of Eq. (4.18) corresponding to Figs. 4.7–4.9 are shown in Figs. 4.10–4.12. No obvious changes can be observed from the new set of plots. Due to $kR_0 \ll 1$, the second higher-order term has little effect on the results.
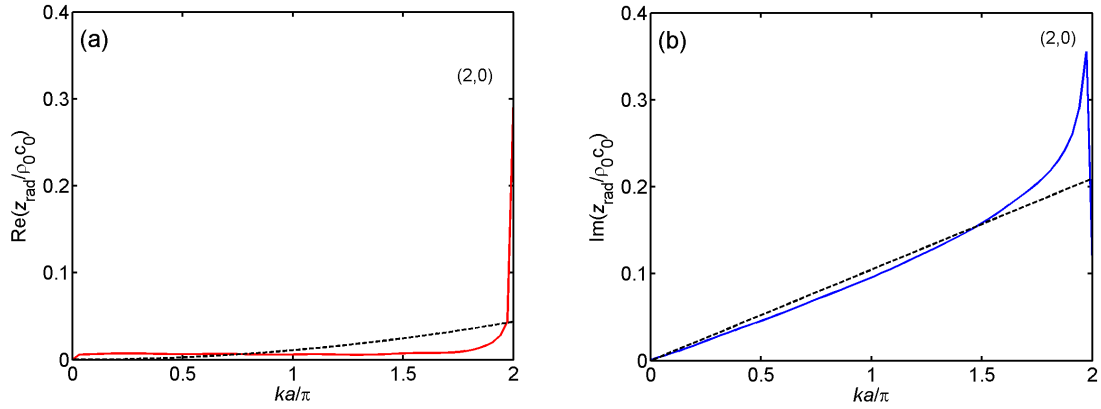
Figure 4.10: Radiation impedance of a bubble in the center of a rigid square tube, Eq. (4.18) for $a/R_0 = 30$, obtained from Eq. (4.18). (a) Radiation resistance, (b) radiation reactance. Solid lines: bubble in tube. Dashed lines: bubble in free space.

Dividing the first term of Eq. (4.16) by the second term of Eq. (4.13), the radiation resistance of a bubble in free field, we get

$$\frac{\text{Re}(z_{\text{rad}}^{\text{sq}})}{\text{Re}(z_{\text{rad}}^{\text{free}})} = \frac{2\pi}{(ka)^2}\,, \qquad (4.19a)$$

and therefore

$$\frac{\text{Re}(z_{\text{rad}}^{\text{sq}})}{\text{Re}(z_{\text{rad}}^{\text{free}})} \gg 1 \quad \text{for} \quad ka < 1. \qquad (4.19b)$$

80
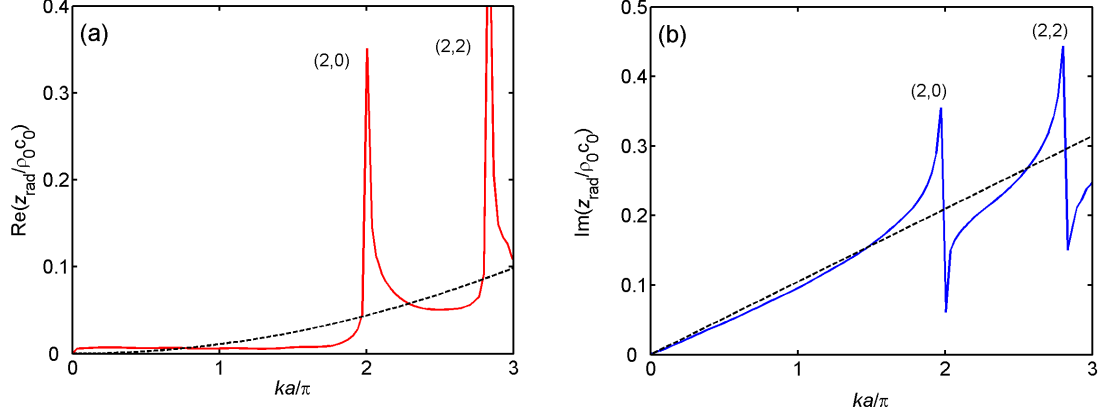
Figure 4.11: Propagating modes of a bubble in the center of a rigid square tube, Eq. (4.18) for $a/R_0 = 30$, obtained from Eq. (4.18). (a) Radiation resistance, (b) radiation reactance. Solid lines: bubble in tube. Dashed lines: bubble in free space.
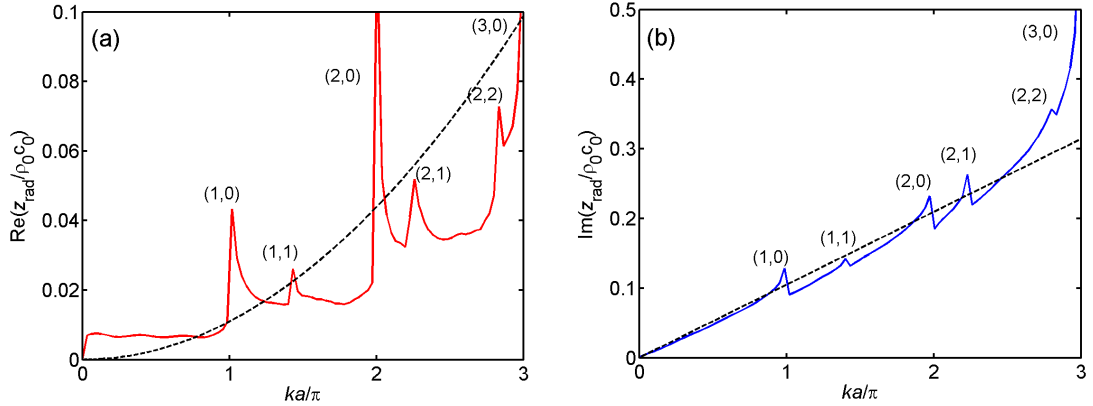
Figure 4.12: Radiation impedance of a bubble off center in a rigid square tube and the propagating modes for $a/R_0 = 30$ with $x_s = -a/6$, and $y_s = -a/6$ (see Fig. 3.9), obtained from Eq. (4.17). (a) Radiation resistance, (b) radiation reactance. Solid lines: bubble between two parallel rigid plates. Dashed lines: bubble in free space.

For $ka < 1$ there is thus a huge increase in the radiation resistance for a bubble in a square tube compared to that for a bubble in free space, the increase being proportional to $(1/ka)^2$.

Equation (4.16) can be further simplified by using the approximation of the cosine series given by Eq. (3.38):

$$\frac{z_{\mathrm{rad}}^{\mathrm{sq}}}{\rho_0 c_0} \simeq 2\pi \frac{R_0^2}{a^2} + jkR_0\left(1 - 4\frac{R_0}{a}\right), \quad ka/\pi \lesssim 1. \tag{4.20}$$

As seen from the imaginary part of Eq. (4.20), the radiation reactance (the effective mass loading on the bubble) is decreased only slightly compared to that of a bubble in a free field.

4.2 Normal Mode Solution of Morse and Ingard

Morse and Ingard [2] studied the radiation impedance of a simple source in a waveguide using a Green's function expressed in terms of normal modes, i.e., a series of eigenfunctions. The Green's function $g(\mathbf{r}|\mathbf{r}_s)$ is a solution of the following inhomogeneous wave equation for an unbounded medium:

$$\nabla^2 g(\mathbf{r}|\mathbf{r}_s) + k^2 g(\mathbf{r}|\mathbf{r}_s) = -\delta(\mathbf{r} - \mathbf{r}_s). \tag{4.21}$$

In rectangular coordinates $\delta(\mathbf{r} - \mathbf{r}_s) = \delta(x - x_s)\delta(y - y_s)\delta(z - z_s)$ is the Dirac delta function for three dimensions. The Green's function $g(\mathbf{r}|\mathbf{r}_s)$ is the spatial factor for a wave radiated by a simple time-harmonic source at location $\mathbf{r}_s$, and in free space it takes the form $g(\mathbf{r}|\mathbf{r}_s) = e^{jkR}/4\pi R$, where $R^2 = |\mathbf{r} - \mathbf{r}_s|^2 = (x - x_s)^2 + (y - y_s)^2 + (z - z_s)^2$. In this section alone, R also stands for the spherical radial coordinate in order

to be consistent with the notation used by Morse and Ingard. For calculation of the radiation impedance below, R will be set equal to the equilibrium bubble radius R_0 to evaluate the field at the bubble wall.

The boundary condition on the eigenfunctions Ψ_{lm} along the walls of the waveguide is

$$\frac{\partial \Psi_{lm}}{\partial n} = -jk_{lm}\beta\Psi_{lm}, \qquad (4.22)$$

where $\beta = \rho_0 c_0 / z_{\mathrm{wall}}$ is a normalized specific acoustic admittance and z_{wall} the wall impedance. The normal is directed into the wall, away from the interior of the waveguide. The eigenfunctions satisfy

$$\left(\frac{\partial^2}{\partial x^2} + \frac{\partial^2}{\partial y^2}\right)\Psi_{lm} = -\kappa_{lm}^2\Psi_{lm}, \qquad (4.23)$$

where κ_{lm} are the eigenvalues and

$$k_{lm} = \left[\left(\frac{\omega}{c_0}\right)^2 - \kappa_{lm}^2\right]^{\frac{1}{2}} \qquad (4.24)$$

are the corresponding propagation wavenumbers. Note that these k_{lm} are not the same as those used in the previous section, e.g., as in Table 4.1. The waveguide walls are assumed to be locally reactive, and therefore the eigenfunctions are orthogonal and satisfy the relation

$$\iint_S \Psi_{lm}\Psi_{l'm'}\,dx\,dy = S\Lambda_{lm}\delta_{ll'}\delta_{mm'}, \qquad (4.25)$$

where Λ_{lm} is the mean value of Ψ_{lm}^2 averaged over the waveguide cross-sectional area S, and δ_{lm} is the Kronecker delta.

83

The Green's function for an infinite waveguide with constant cross section, satisfying Eq. (4.21) and the boundary conditions on the walls, is expressed in terms of the eigenfunctions Ψ_{lm} as

$$g(x, y, z | x_s, y_s, z_s) = -\frac{j}{2S} \sum_{l,m} \frac{\Psi_{lm}(x,y)\Psi_{lm}(x_s,y_s)}{k_{lm}\Lambda_{lm}} e^{-jk_{lm}|z-z_s|}. \qquad (4.26)$$

Equation (4.26) is a general result that is applicable for arbitrary normally reactive wall impedances and arbitrary cross-sectional geometries.

For a rigid tube, the boundary condition is that the normal component of the particle velocity is zero at every point on the perimeter, or $\partial\Psi_{lm}/\partial n = 0$. In this case, the lowest propagating mode is the plane wave mode, also called the fundamental mode, for which the corresponding eigenvalue is $\kappa_{00} = 0$, and the corresponding eigenfunction is $\Psi_{00} = 1$, with $\Lambda_{00} = 1$. The eigenvalues κ_{lm} and the eigenfunctions Ψ_{lm} are both real for a rigid tube. Below the cutoff frequency of the lowest higher mode only the fundamental mode is propagated without attenuation; all higher modes are strongly attenuated evanescent waves. As the frequency is increased, successively higher modes start to propagate without attenuation.

Morse and Ingard [2] state that "For wavelengths of the same size as the duct dimensions, or longer" Eq. (4.26) may be approximated by

$$\begin{aligned} g \simeq \Bigg[&\frac{1}{4\pi R} - \frac{j}{2Sk} e^{-jk|z-z_s|} + \frac{|z-z_s|}{2S} \\ &- \sum_{l,m}^{N} \frac{\Psi_{lm}(x,y)\Psi_{lm}(x_s,y_s)}{2S\Lambda_{lm}} \left(\frac{je^{-jk_{lm}|z-z_s|}}{k_{lm}} + \frac{e^{-\kappa_{lm}|z-z_s|}}{\kappa_{lm}} \right) \Bigg] e^{j\omega t}, \qquad (4.27) \end{aligned}$$

where N is the nominal number of modes retained in the summation. The term $1/4\pi R$ in Eq. (4.27) is the free space Green's function at zero frequency, and factoring this

analytical expression out of Eq. (4.26) permits summing over a small number N of modes to obtain convergence. The second and third terms in Eq. (4.27) are associated with the plane wave mode. Although not stated by Morse and Ingard, Eq. (4.27) applies only to rigid tubes because of the terms for the plane wave mode

The pressure field in the tube is obtained directly from the Green's function. For a small source located at point $\mathbf{r}_s = (x_s, y_s, z_s)$ the pressure is [2]

$$P(\mathbf{r}|\mathbf{r}_s)e^{j\omega t} = jk\rho_0 c_0 U g(\mathbf{r}|\mathbf{r}_s)e^{j\omega t} , \qquad (4.28)$$

where U stands for the instantaneous value of the total flow of fluid (volume velocity) away from the center of the source, and therefore $U = 4\pi R_0^2 u_0$, where u_0 is the radial particle velocity on the surface of a small pulsating sphere of radius R_0. The mean pressure $j\omega\rho_0 U g$ on a small spherical source of radius R_0 $(kR_0 \ll 1)$ is thus

$$P \simeq \frac{\rho_0\omega}{2S}\left[\frac{jS}{2\pi R_0} + \frac{1}{k} + \sum_{l,m}^{N}\frac{\Psi_{lm}^2(x_s, y_s)}{\Lambda_{lm}}\left(\frac{1}{k_{lm}} - \frac{j}{\kappa_{lm}}\right)\right]4\pi R_0^2 u_0 e^{j\omega t} . \qquad (4.29)$$

Note that mode $(0,0)$ is separated out of the normal mode summation, thus l and m can not be zeros at the same time. The radiation impedance of the source is obtained by dividing by $u_0 e^{j\omega t}$ to obtain [2, Eq. (9.2.12)]

$$\frac{z_{\text{rad}}}{\rho_0 c_0} \simeq jkR_0\left[1 - 2\pi\frac{R_0}{S}\sum_{l,m}^{N}\frac{\Psi_{lm}^2(x_s, y_s)}{\Lambda_{lm}\kappa_{lm}}\right] + 2\pi\frac{R_0^2}{S}\left[1 + \sum_{l,m}^{N}\frac{k}{k_{lm}}\frac{\Psi_{lm}^2(x_s, y_s)}{\Lambda_{lm}}\right] . \qquad (4.30)$$

Comparison of Eq. (4.30) with Eq. (4.7) reveals that the leading term in the radiation reactance of a simple source in a tube is the same as the radiation reactance in a free field $(kR_0 \ll 1)$. Thus the presence of tube walls only reduces the mass loading on the source by a small amount that is proportional to the ratio of the

85

source radius R_0 to the mean dimension $\sqrt{S}$ of the tube cross section, and the exact amount is dependent on the location of the source. The same observation can be made from Eq. (4.20). For a small bubble centered in a square tube with side length a, this amount is approximately $4R_0/a$ for $ka < \pi$.

Comparison of Eq. (4.30) with Eq. (4.20) shows that the leading terms of the radiation resistance $2\pi R_0^2/S$ in both equations are the same. For small kR_0, the normalized radiation resistance for a source in a rigid tube approaches the constant value $2\pi R_0^2/S$ instead of going to zero. This is different from the behavior in a free field due to coupling with the plane wave mode. The real part of the second summation in Eq. (4.30) accounts for higher-order modes which propagate at the drive frequency and cause the resistance to vary with frequency. Contributions from the summations to the imaginary part of z_{rad} account for the deviation of the radiation reactance from the free field radiation reactance. As shown in Figs. 4.8 and 4.9, and later in Fig. 4.14, as the frequency is increased the radiation resistance and reactance increase stepwise, each new step corresponding to a new propagating mode.

Now consider specifically a rectangular cross section, as in Fig. 4.13, where the rectangle has breadth b in the x direction and depth d in the y direction. We assume a simple source is located at (x_s, y_s) and let the z axis run along one corner of the tube, such that the boundary conditions are

$$\frac{\partial p}{\partial x} = 0 \quad \text{at } x = 0, \quad x = b, \tag{4.31a}$$

$$\frac{\partial p}{\partial y} = 0 \quad \text{at } y = 0, \quad y = d. \tag{4.31b}$$

The eigenvalues, eigenfunctions, and normalization constant for the rectangular tube

are

$$\kappa_{lm} = \sqrt{(l\pi/b)^2 + (m\pi/d)^2}, \tag{4.32a}$$

$$\Psi_{lm} = \cos(l\pi x_s/b)\cos(m\pi y_s/d), \tag{4.32b}$$

$$\Lambda_{lm} = \frac{1}{\epsilon_l \epsilon_m}, \quad \epsilon_m = \begin{cases} 1 & m = 0 \\ 2 & m > 0 \end{cases}. \tag{4.32c}$$

Substitution into Eq. (4.30) with $S = bd$ yields

$$\frac{z_{\text{zad}}}{\rho_0 c_0} \simeq jkR_0 \left[1 - 2\frac{R_0}{bd} \sum_{l,m}^{N} \frac{\cos^2(l\pi x_s/b)\cos^2(m\pi y_s/d)}{\Lambda_{lm}\sqrt{(l\pi/b)^2 + (m\pi/d)^2}} \right]$$
$$+ 2\pi\frac{R_0^2}{bd} \left[1 + \sum_{l,m}^{N} \frac{k\cos^2(l\pi x_s/b)\cos^2(m\pi y_s/d)}{\Lambda_{lm}\sqrt{k^2 - (l\pi/b)^2 - (m\pi/d)^2}} \right]. \tag{4.33}$$

Equation (4.33) is applicable for an arbitrary source location in a rectangular (or square) tube. Shown in Fig. 4.13 is one specific example, where a simple source is located at $(x_s, y_s) = (b/4, d/10)$, with $d = (4/5)b$. The calculated radiation resistance and reactance for this case, based on Eq. (4.33), are shown in Fig. 4.14 by blue curves.

The red curves are obtained using the method of images, as follows. The radiation impedance of a simple source in a rectangular rigid tube, based on the method of images, is given by Eq. (4.13). The geometry of the source (bubble) location and the plane array of images are shown in Figs. 3.9 and 3.10, respectively. For the specific bubble position shown in Fig. 4.13, based on Fig. 3.9, the new coordinates are $x_s = -b/4$, $y_s = -2d/5$, and thus $d = (4/5)b$. These coordinates were chosen to coincide with those used in Fig. 9.10 of Morse and Ingard [2]. Equation (3.32) is used in Eq. (4.13) to obtain the plots shown as red lines in Fig. 4.14 for the radiation resistance and reactance.
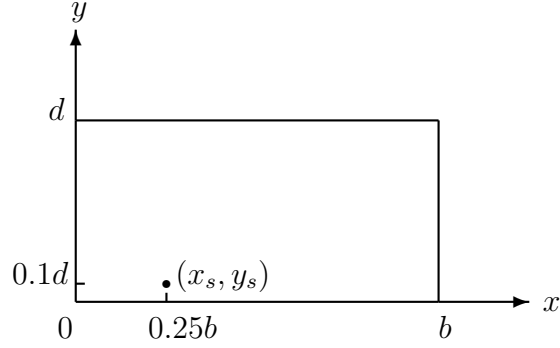
Figure 4.13: Coordinate system for an off-center bubble in a rectangular tube, with the z axis passing through the lower left corner of the tube, used as an example for the normal mode expansion approach.

For $ka < 3\pi$ there are six modes that propagate. The cutoff frequencies of these modes for a rectangular tube are given by $f_{lm} = (c_0/2)[(l/b)^2 + (m/d)^2]^{1/2}$. The values of $k_{lm}b/\pi$ for these these cutoff frequencies are given by $k_{lm}b/\pi = [l^2 + (mb/d)^2]^{1/2}$, which are listed in Table 4.2. Two modes are missing for this range of ka, $(2,0)$ and

Mode	$k_{lm}b/\pi$
$(1,0)$	1.0
$(0,1)$	1.25
$(1,1)$	1.6008
$(0,2)$	2.0
$(1,2)$	2.6926
$(3,0)$	3.0

Table 4.2: Values of kb for the first six propagating modes for a rectangular tube with $d = (4/5)b$, and $(x_s, y_s) = (b/4, d/10)$ (See Fig. 4.13), where b and d are sides of the rectangle.

$(2,1)$. The missing modes are due to the fact that the source is located distance $b/4$
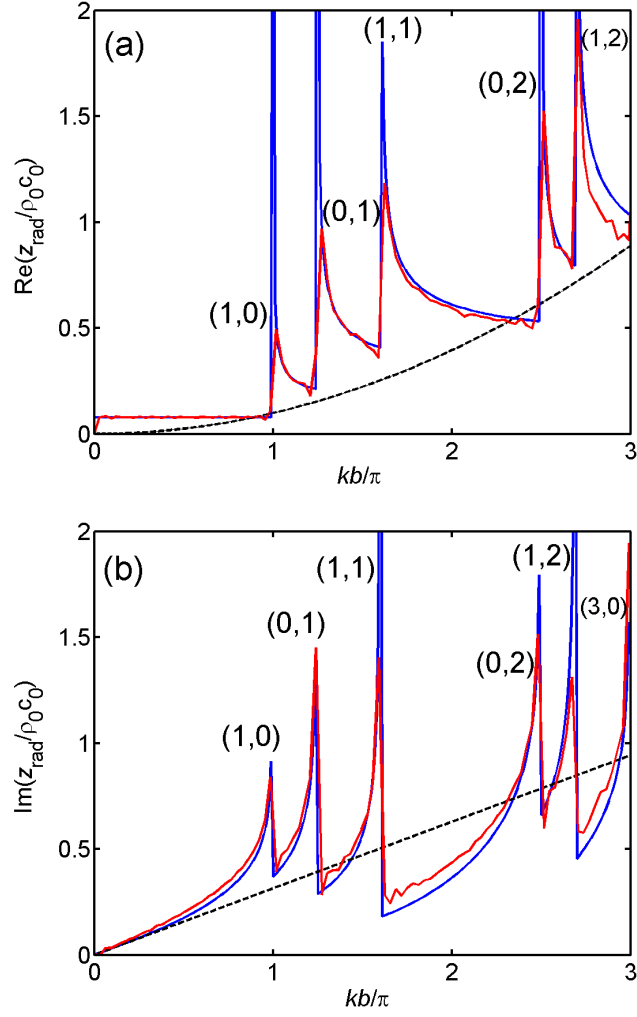
Figure 4.14: Comparison of (a) radiation impedance and (b) radiation reactance calculated using normal mode theory (blue lines) and the method of images (red lines). The black dashed lines are again the free field results. The bubble is positioned as shown in Fig. 4.13. The ordered pairs adjacent to resonance peaks are the mode numbers (l, m).

away from one wall, and these two modes have velocity antinodes at this location. From Fig. 4.14 we see that the red and blue curves overlap, and the two approaches are thus in excellent agreement.

Using Eq. (4.6), we can also calculate the frequency response of a bubble centered in a rectangular tube using normal mode theory. For this comparison we position the bubble in the center of a square tube. In Fig. 4.15, the red lines are the frequency response curves obtained using the method of images and the black lines are obtained from Eq. (4.6) with z_{rad} given by Eq. (4.33). The two approaches are in good agreement.
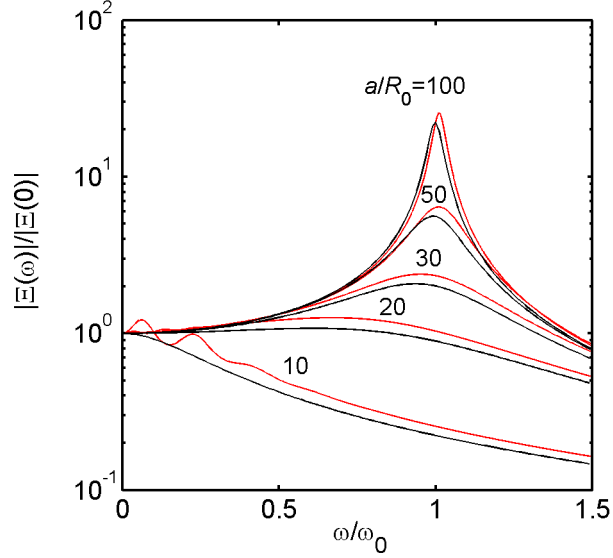
Figure 4.15: Comparison of frequency response of a bubble in the center of a square rigid tube calculated using the normal mode theory [Eq. (4.6), black lines] and the method of images [Eq. (3.35), red lines].

4.2.1 Differences between the Parallel-Plates Channel and a Tube

Because of cylindrical spreading between parallel plates, both the radiation resistance as well as the radiation reactance go to zero for small ka. The radiation efficiency is thus very poor for small ka. On the other hand, the restraint of the radial expansion of the flow by parallel plates increases the effective mass loading on the bubble, causing the resonance frequency to decrease. The radiation reactance increases as the plate separation decreases. For parallel plates, change in inertia is the dominant factor, and the damping is negligible. The dynamics of the bubble is thus mass controlled.

For a rigid tube, the plane wave mode is the only mode that can propagate for small ka, and the radiation resistance is constant in this region. In general, the resistance is proportional to $1/a^2$, and as a/R_0 decreases the damping experienced by the bubble increases according to R_0^2/S, where S is cross-sectional area of the tube. As observed in Figs. 3.11 and 4.15, the frequency response of a bubble in a rigid square tube is highly damped for narrow tubes, and for $a/R_0 < 20$ the resonance peak vanishes. In contrast, for a bubble between two parallel rigid plates we see a distinct resonance peak for a channel as narrow as 1.5 times the bubble diameter (see Fig. 3.2). On the other hand, the radiation reactance of a bubble in a square tube is slightly smaller than its value in a free field, suggesting less mass loading. As mentioned above, the resonance is barely noticeable for $a/R_0 < 20$ due to high damping. The slight downshift of the resonance frequencies for $a/R_0 = 30$ in Figs. 3.11 is just a manifestation of the damping. The dynamics of a bubble in a rigid tube is damping controlled.

91

4.3 Pressure Release Walls

In Chapter 3 we examined the frequency response of a bubble centered between two parallel plates, and in a square tube, with pressure release walls. Here we investigate the radiation impedance of a bubble in pressure release channels with the same geometries. Applying Eq. (3.19) to Eq. (4.9) and keeping the first two terms in the expansion of Eq. (4.7), we obtain the radiation impedance of a bubble centered between two parallel pressure release walls:

$$\frac{z_{\text{rad}}^{\text{pr}}}{\rho_0 c_0} = jkR_0 + (kR_0)^2 - j2kR_0(1 - jkR_0)\frac{R_0}{d}\ln(1 + e^{-jkd}), \qquad (4.34)$$

or, for low frequencies,

$$\frac{z_{\text{rad}}^{\text{pr}}}{\rho_0 c_0} = -2(kR_0)^2\frac{R_0}{d}\ln\left(2\cos\frac{kd}{2}\right) + jkR_0\left[1 - 2\frac{R_0}{d}\ln\left(2\cos\frac{kd}{2}\right)\right], \quad kd < \pi. \,(4.35)$$

The superscript "pr" in $z_{\text{rad}}^{\text{pr}}$ stands for pressure release walls. The radiation resistance and reactance are plotted in Fig. 4.16 for $d/R_0 = 30$. Again, the dashed lines are the free field results. From Eq. (4.35) we see that for $kd < \pi$ the radiation resistance is zero, which is also observed in Fig. 4.16(a). This means that for $d/R_0 < 224$ there is no radiation loss for an air bubble in water ($k_0 R_0 = 0.014$) when excited at resonance ($d/R_0 = \pi/k_0 R_0 = 224$). In other words, the quality factor is infinite for $d/R_0 < 224$. For $d/R_0 > 224$ the first propagating mode excited by the source cuts on and the quality factor recovers the value for a free field, those observations were made in Fig. 3.7. From Fig. 4.16(b) we notice that the radiation reactance of a bubble between free plates is lower than in a free field for $kd/\pi < 0.66$, which corresponds to smaller mass loading and higher resonance frequencies. For plate separations in
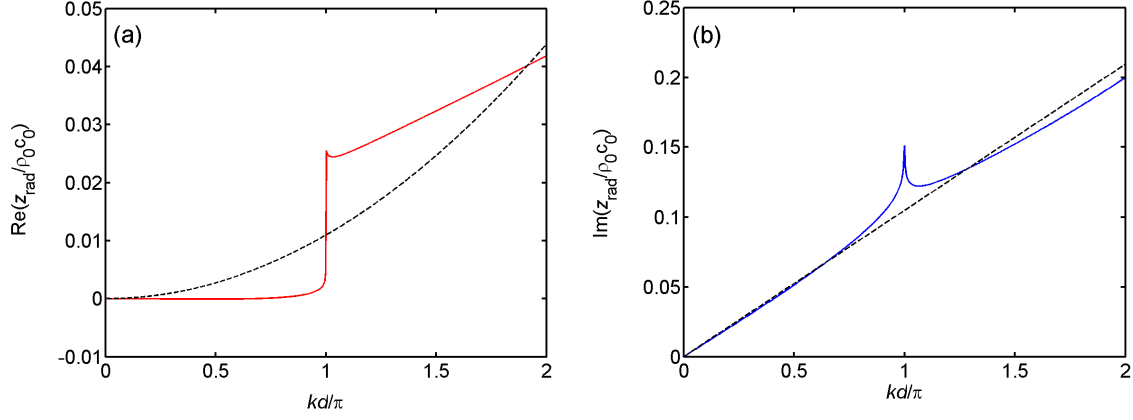
Figure 4.16: Radiation impedance of a bubble centered between two parallel pressure release plates for $d/R_0 = 30$. (a) Radiation resistance, (b) radiation reactance. Solid lines: bubble between two parallel free plates. Dashed lines: bubble in free space.

which we are interested, $3 \leq d/R_0 \leq 100$, we have $kd/\pi < 0.5$ for the frequency range $\omega \leq \omega_0$.

The crossover point $kd/\pi = 0.66$ where the radiation reactance exceeds the free field value is calculated as follows. Equating the first terms in Eqs. (4.34) and (4.35) yields $kd = 2\arccos(0.5) = 2\pi/3$, or $kd/\pi = 2/3$, independent of d/R_0.

The radiation resistance and reactance for two pressure release plates are plotted up to $kd = 5\pi$ in Fig. 4.17. As kd (e.g., the drive frequency) increases, both the radiation resistance and reactance increase stepwise corresponding to each new mode of propagation. Each step begins with a spike showing the resonance at that frequency. For this case, we notice that the resonance spikes occur only where values of kd are odd multiples of π (i.e., when the plate separation d is an odd multiple of a half wavelength), instead of all integer multiples of π at which the acoustic resonances occur. This is because the bubble is located midway between two pressure release

93
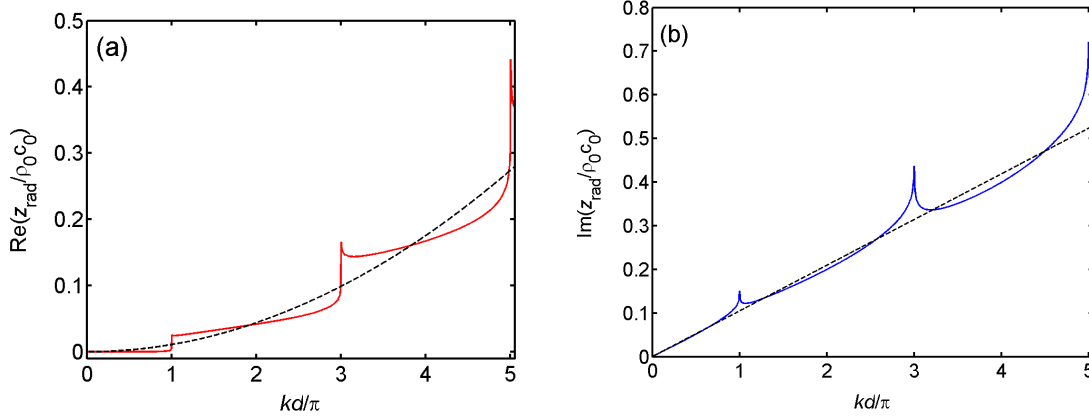
Figure 4.17: Radiation impedance of a bubble centered between two parallel free plates and the resonance pattern for $d/R_0 = 30$. (a) Radiation resistance, (b) radiation reactance. Solid lines: bubble between two parallel free plates. Dashed lines: bubble in free space.

plates, and when the plate separation d is an even multiple of a half wavelength, there is an antinode at the bubble location, and those modes are not excited. Once the bubble is moved off-center, and not at locations of $d/2$, $d/4$, $d/8$, etc., away from one of the plates, the spikes for both radiation resistance and reactance occur where kd is an integer multiple of π.

The pressure release boundary condition is now applied to a tube. Using the method of images, we write the summation in Eq. (4.13) as $\sum_{l,m}(-1)^{l+m}e^{-jkr_{lm}}/r_{lm}$ to obtain

$$\frac{z_{\mathrm{rad}}^{\mathrm{Ftube}}}{\rho_0 c_0} = jkR_0 + (kR_0)^2 + jkR_0^2\sum_{l,m}(-1)^{l+m}\frac{e^{-jkr_{lm}}}{r_{lm}}. \tag{4.36}$$

Here, only the first term in the expansion of Eq. (4.7) is retained since, as shown earlier, the second term has little effect on the results for a tube. For a square tube

94

with side length a we have $r_{lm} = a(l^2 + m^2)^{1/2}$ and Eq. (4.13) becomes

$$\frac{z_{\text{rad}}^{\text{Fsq}}}{\rho_0 c_0} = jkR_0 + (kR_0)^2 + j4kR_0 \frac{R_0}{a} \sum_{l=0}^{\infty} \sum_{m=1}^{\infty} (-1)^{l+m} \frac{e^{-j(l^2+m^2)^{1/2}ka}}{(l^2 + m^2)^{1/2}}, \qquad (4.37)$$

where F in the superscripts $z_{\text{rad}}^{\text{Ftube}}$ and $z_{\text{rad}}^{\text{Fsq}}$ indicates that the tube walls are free.

The normal mode expansion of the radiation impedance of a simple source at an arbitrary location inside a free tube of arbitrary cross section can be calculated by modifying Eq. (4.30) to account for pressure release boundary conditions. Specifically, for a rectangular tube with pressure release walls and with the geometry shown in Fig. 4.13, the boundary conditions are

$$p = 0 \quad \text{at } x = 0,\ b, \quad \text{and} \quad y = 0,\ d. \qquad (4.38)$$

The eigenvalues and eigenfunctions for this case are

$$\kappa_{lm} = \sqrt{(l\pi/b)^2 + (m\pi/d)^2}, \qquad (4.39a)$$

$$\Psi_{lm} = \sin(l\pi x_s/b) \sin(m\pi y_s/d), \qquad (4.39b)$$

$$\Lambda_{lm} = \frac{1}{\epsilon_l \epsilon_m}, \qquad (4.39c)$$

which are the same as in Eqs. (4.32) except with the cosines replaced by sines. For this case, however, neither l nor m can be zero. Substitution of Eqs. (4.39) into Eq. (4.30) with $S = bd$ thus yields, taking into account the absence of the plane wave mode,

$$\frac{z^{\text{pr}}}{\rho_0 c_0} \simeq jkR_0 \left[1 - 2\frac{R_0}{bd} \sum_{l,m}^{N} \frac{\sin^2(l\pi x_s/b) \sin^2(m\pi y_s/d)}{\Lambda_{lm} \sqrt{(l\pi/b)^2 + (m\pi/d)^2}} \right]$$

$$+ 2\pi \frac{R_0^2}{bd} \sum_{l,m}^{N} \frac{k \sin^2(l\pi x_s/b) \sin^2(m\pi y_s/d)}{\Lambda_{lm} \sqrt{k^2 - (l\pi/b)^2 - (m\pi/d)^2}}. \qquad (4.40)$$

95

The radiation resistance of a bubble in the center of a square tube with free walls, calculated using Eq. (4.40) with $a/R_0 = 10$, is plotted in Fig. 4.18(a). As seen from Fig. 4.18(a), for $ka < 1.414\pi$ the radiation resistance vanishes and the bubble experiences no damping. Since the plane wave mode is not supported by tubes with free surfaces, there can be no radiation before the first propagating mode cuts on. Neither l nor m can be zero, and therefore the first propagating mode is $(1, 1)$, for which the cutoff frequency is determined by $k_{11}a/\pi = (1^2 + 1^2)^{1/2} = 1.414$, or $a/R_0 = 1.414 \times \pi/k_0 R_0 = 317$. So only when the tube cross-sectional area satisfies $a/R_0 \geq 317$ does the bubble experience radiation loss. When $a/R_0 < 317$ there is no radiation damping and the quality factor is unbounded. This was observed in Fig. 3.17.

From Fig. 4.18(b) we observe that the radiation reactance for a source in a tube with free surfaces is smaller than that in free space for the typical values of ka encountered in bubble dynamics. The underlying physics is similar to that for a channel formed by two parallel free surfaces. The free surfaces of the tube provide the least resistance to the flow, and therefore the effective liquid inertia is less than that in free space. When the tube size is reduced, the liquid mass enclosed decreases, and thus the resonance frequency increases. This trend is also observed in Fig. 3.17, and also in Fig. 4.19 that follows.

The radiation impedance in a cylindrical tube was calculated recently by Hay et al. [61] using normal mode theory. Their impedance data were used in Eq. (4.6) to obtain the frequency responses for different sized cylindrical tubes as shown in Fig. 4.19(b). Figure 4.19(a) [note that Fig. 4.19(a) is a repetition of Fig. 3.17] shows

the frequency responses of a bubble in four different sized square tubes, where S is the area of the tube, and $\sqrt{S}/R_0 = 10, 20, 30, 100$. The cylindrical tubes are chosen to have the same cross-sectional areas as the square tubes.

Figure 4.19 shows again that when the tubes have the same cross-sectional areas, the dynamics of a bubble are the same for both the square tube and the cylindrical tube. This confirms what was observed in Fig. 3.11, that the cross-sectional shape of the tube does not affect the dynamics of the bubble. Again, Fig. 4.19 shows that the two approaches for radiation impedance produce almost identical results. The reason we use the method of images is that the nonlinearity of the bubble response is our focus, and the normal mode theory is less easily extended to the nonlinear regime. The agreement of the two approaches forms the basis for generalization of solutions obtained using the method of images to other tube geometries with finite wall impedance.
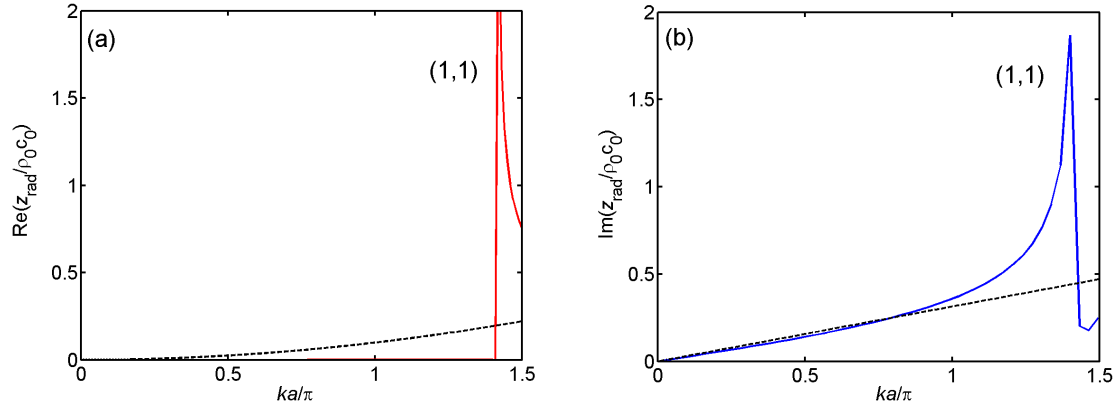
Figure 4.18: Radiation impedance of a bubble in the center of a free square tube with $a/R_0 = 10$. (a) Radiation resistance, (b) radiation reactance. Solid lines: bubble in tube. Dashed lines: bubble in free space.

97
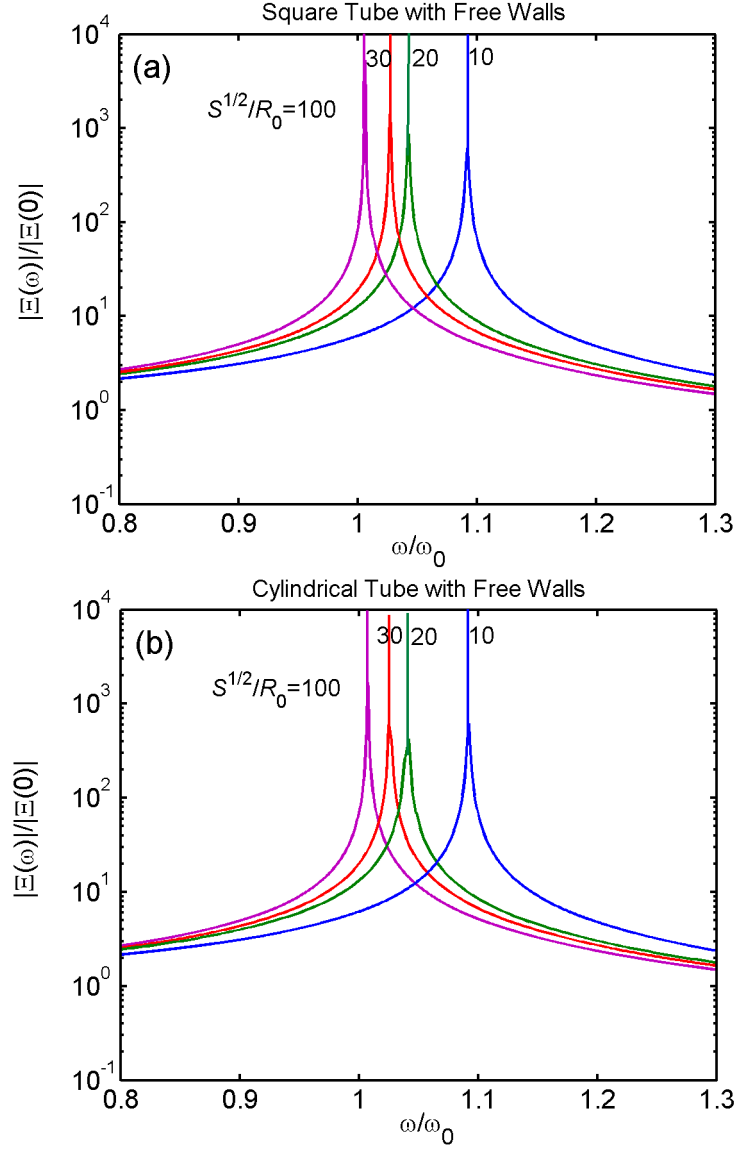
Figure 4.19: Frequency response of a bubble in the center of two equal-area tubes with free walls: (a) square tube, with plot generated from Eq. (3.35) based on the method of images, and (b) cylindrical tube, calculated using Eq. (4.6) with z_{rad} obtained by normal mode expansion.

Chapter 5

Weakly Nonlinear Oscillations

As the amplitude of the acoustic drive pressure increases, nonlinear effects in the bubble dynamics become significant. Chapters 5 and 6 are devoted to developing methodologies for handling the nonlinear terms and obtaining solutions for bubbles constrained by channel walls. The objective of the present chapter is to investigate the weakly nonlinear response of a confined bubble to an acoustic field with moderate drive amplitude (about 5% of atmospheric pressure). The model equations for a confined bubble, Eqs. (2.15) and (2.16), are expanded in terms of the perturbation of the bubble radius, and only terms of linear and quadratic order are retained. Solutions of the quadratic model equations are obtained in the frequency domain using the Newton-Raphson interation method. Frequency response curves for the first five harmonics are presented. Perturbation solutions for the frequency response are derived for the second harmonic and dc component. The numerical solutions obtained in the frequency domain are compared with the numerical solutions obtained in the time domain using a Runge-Kutta method.

5.1 Bubble between Parallel Plates

To obtain the model equation accounting for nonlinearity through quadratic order we substitute $R = R_0 + \xi$ in Eq. (2.15) to obtain

$$\ddot{\xi}(t) + \omega_0^2 \xi(t) - \frac{R_0}{c_0}\dddot{\xi}(t) + 2\frac{R_0}{d}\sum_{m=1}^{\infty}\frac{1}{m}\ddot{\xi}(t - md/c_0) = F(\xi) - \frac{p_{\text{ac}}(t)}{\rho_0 R_0}, \qquad (5.1)$$

where all quadratic terms, which are responsible for harmonic generation, are collected in the expression

$$F(\xi) = -\xi\ddot{\xi} - \frac{3}{2}\dot{\xi}^2 + \frac{1}{2}(3\gamma + 1)\omega_0^2\xi^2 + 2\frac{R_0}{c_0}(3\dot{\xi}\ddot{\xi} + \xi\dddot{\xi})$$
$$- 4\frac{R_0}{d}\sum_{m=1}^{\infty}\frac{1}{m}\left[\dot{\xi}^2\left(t - \frac{md}{c_0}\right) + \xi\left(t - \frac{md}{c_0}\right)\ddot{\xi}\left(t - \frac{md}{c_0}\right)\right]. \qquad (5.2)$$

The first two terms in Eq. (5.2) correspond to the quadratic terms on the left-hand side of Eq. (2.15). The third term accounts for the gas nonlinearity at quadratic order, and the fourth term contains the quadratic nonlinearity in the expansion of the compressibility term $\ddot{V}$. The summation contains the quadratic terms in the expansion of $\ddot{V}$ in Eq. (2.15), including the time delays due to liquid compressibility. Details involved in obtaining Eq. (5.1) from Eq. (2.15) are presented in Appendix C, as well as other intermediate steps for subsequent equations.

In Eq. (5.1), linear terms are grouped on the left-hand side, quadratic terms and the applied acoustic pressure on the right. If $F(\xi)$ is discarded, Eq. (5.1) reduces to Eq. (3.1). Like Eq. (3.1), Eq. (5.1) will also be solved in the frequency domain. The primary reason is that, as in the linear approximation, the summation in Eq. (5.2) can also be expressed in closed form in the frequency domain.

Begin by assuming a harmonic acoustic excitation at frequency ω:

$$p_{\text{ac}}(t) = \frac{1}{2}p_0 e^{j\omega t} + \text{c.c.} \qquad (5.3)$$

The response to this excitation is a full spectrum of harmonics of the drive frequency, plus a dc component. The perturbation of the bubble radius is thus expressed as the Fourier series expansion

$$\frac{\xi(t)}{R_0} = C_0 + \frac{1}{2}\sum_{n=1}^{N} C_n e^{jn\omega t} + \text{c.c.}, \qquad (5.4)$$

which is normalized by the equilibrium radius R_0 in order for the spectral amplitudes C_n to be dimensionless. The notation c.c. stands for complex conjugates, and C_0 is the dimensionless amplitude of the dc component. The summation is terminated with the Nth harmonic in anticipation of numerical solution. Before solving Eq. (5.1) for an arbitrary number of harmonics, we consider analytical solutions for the second harmonic and dc component.

5.1.1 Analytical Solution for the Second Harmonic and DC Component

Let the perturbation ξ include only the fundamental, the second harmonic, and the dc component:

$$\xi = \xi_1 + \xi_2 + \xi_0, \qquad (5.5)$$

where ξ_1 is $O(\epsilon)$, and ξ_2 and ξ_0 are $O(\epsilon^2)$. The perturbations are now expressed in the frequency domain as

$$\frac{\xi_1}{R_0} = \frac{1}{2}C_1(\omega)e^{j\omega t} + \text{c.c.}, \tag{5.6a}$$

$$\frac{\xi_2}{R_0} = \frac{1}{2}C_2(\omega)e^{j2\omega t} + \text{c.c.}, \tag{5.6b}$$

$$\frac{\xi_0}{R_0} = C_0. \tag{5.6c}$$

Substitution of Eq. (5.6b) into the left-hand side of Eq. (5.1), Eq (5.6a) into the right-hand side, and equating terms at the second harmonic yields

$$\frac{1}{2}C_2(\omega)\left[\omega_0^2 - 4\left(1 + 2\frac{R_0}{d}\sum_{m=1}^{\infty}\frac{e^{-j2mkd}}{m}\right)\omega^2 + j8\frac{R_0}{c_0}\omega^3\right]$$

$$= C_1^2(\omega)\left[\frac{3\gamma+1}{8}\omega_0^2 + \left(\frac{5}{8} + 2\frac{R_0}{d}\sum_{m=1}^{\infty}\frac{e^{-j2mkd}}{m}\right)\omega^2 - j2\frac{R_0}{c_0}\omega^3\right]. \tag{5.7}$$

After making use of Eq. (3.4) to write the summations in closed form and substituting $C_1(\omega) = \Xi(\omega)/R_0$ from Eq. (3.7) one obtains

$$\frac{C_2(\omega)}{C_2(0)} = \left(\frac{4}{3\gamma+1}\right)\frac{\Gamma(\omega)}{\Delta_1^2(\omega)\Delta_2(\omega)}, \tag{5.8}$$

where

$$\Delta_n(\omega) = 1 - n^2\left[1 - 2\frac{R_0}{d}\ln(1 - e^{-jnkd})\right]\frac{\omega^2}{\omega_0^2} + jn^3k_0R_0\frac{\omega^3}{\omega_0^3}, \tag{5.9}$$

$$\Gamma(\omega) = \frac{3\gamma+1}{4} + \left[\frac{5}{4} - 4\frac{R_0}{d}\ln(1 - e^{-j2kd})\right]\frac{\omega^2}{\omega_0^2} - j4k_0R_0\frac{\omega^3}{\omega_0^3}. \tag{5.10}$$

Likewise, the terms at zero frequency yield

$$\frac{C_0(\omega)}{C_0(0)} = \left(1 - \frac{1}{3\gamma+1}\frac{\omega^2}{\omega_0^2}\right)\frac{1}{|\Delta_1(\omega)|^2}. \tag{5.11}$$

102

Equations (5.8) and (5.11) have been normalized by the harmonic amplitudes at zero frequency, which are given by

$$C_0(0) = C_2(0) = \frac{3\gamma + 1}{4} \left(\frac{p_0}{3\gamma P_0} \right)^2. \tag{5.12}$$

Plots of the magnitudes of Eqs. (5.8) and (5.11) are shown in Fig. 5.1 for several values of the normalized plate separation d/R_0. The normalized frequency response for the second harmonic possesses two maxima. The primary, higher-frequency resonance occurs when the drive frequency matches the bubble resonance near $\omega = \omega_0$. The secondary, lower-frequency resonance occurs near $\omega = \omega_0/2$ because the second harmonic of the drive frequency, produced by the bubble, matches the bubble resonance. The frequency response of the dc component possesses one maximum and one minimum. The maximum occurs at the resonance of the bubble, and the minimum happens when $\omega = (3\gamma + 1)^{1/2}\omega_0 = 2.28\omega_0$, at which $C_0 = 0$.

Figure 5.2 displays the amplitudes of the resonance peaks in Figs. 3.2 and 5.1(a) versus plate separation using the metrics $Q_1 = |\Xi_1(\omega_r)/\Xi_1(0)|$, $Q_{2P} = |\Xi_2(\omega_r)/\Xi_2(0)|$, and $Q_{2S} = |\Xi_2(\omega_r/2)/\Xi_2(0)|$. Thus, Q_1 is the quality factor in linear theory, and it was presented previously in Eqs. (3.10)–(3.12). It is the amplitude at resonance relative to its value at zero frequency, and it is inversely proportional to damping. While the quantities Q_{2P} and Q_{2S} are defined in the same way for the second-harmonic amplitudes of the primary (P) and secondary (S) resonances, respectively, no specific connection to damping is intended. It is seen that Q_{2P} varies roughly as the square of Q_1, while apart from the oscillations for large plate separations the dependence of Q_{2S} on Q_1 is more nearly linear.
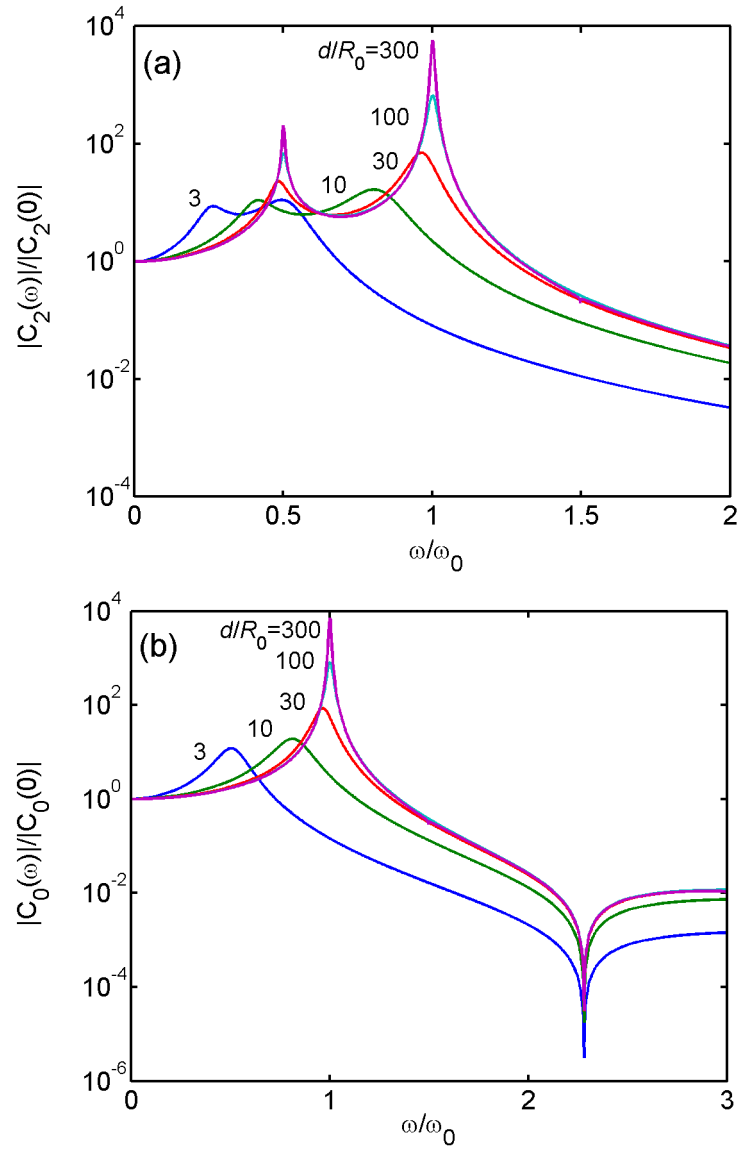
Figure 5.1: Frequency response of the for several different normalized plate separations d/R_0. (a) Second harmonic. (b) The dc component.

104
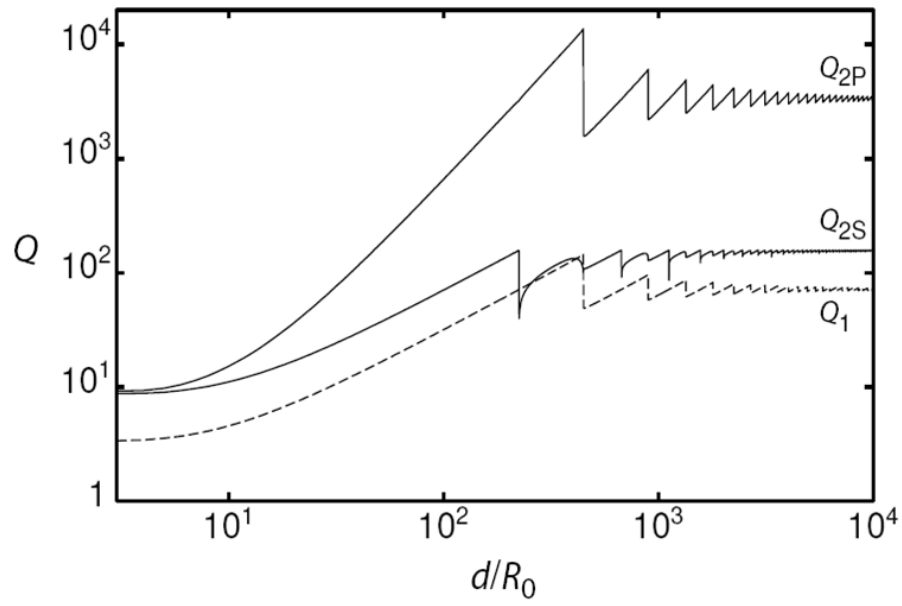
Figure 5.2: Relative amplitudes of the resonance peaks in the frequency responses at the fundamental and second harmonic frequencies.

5.1.2 Coupled Spectral Equations

In our numerical solutions of the quadratic model equation we include the effect of viscosity. The effect of viscosity on the dynamics of a bubble in a free field is given by the last term in Eq. (2.2), $4\mu\dot{R}/R$. Adding this term to Eq. (2.15), we have

$$R\ddot{R}+\frac{3}{2}\dot{R}^2 = \frac{1}{\rho}\left[P_0\left(\frac{R_0}{R}\right)^{3\gamma} - P_0 - 4\mu\frac{\dot{R}}{R} - p_{\rm ac}(t)\right] + \frac{\dddot{V}}{4\pi c_0} - \frac{1}{2\pi d}\sum_{m=1}^{\infty}\frac{1}{m}\ddot{V}\left(t - \frac{md}{c_0}\right),$$

(5.13)

and in place of Eq. (5.1) we now have

$$\ddot{\xi}(t) + \omega_0^2\xi(t) - \frac{R_0}{c_0}\dddot{\xi}(t) + 2\frac{R_0}{d}\sum_{m=1}^{\infty}\frac{1}{m}\ddot{\xi}(t - md/c_0) + \frac{4\mu}{\rho_0 R_0^2}\dot{\xi}(t) = F(\xi) - \frac{p_{\rm ac}(t)}{\rho_0 R_0^2}.$$

(5.14)

Substituting Eqs. (5.3) and (5.4) into (5.14), we obtain the following system of $N+1$ coupled nonlinear equations for the harmonic amplitudes:

$$\Delta_n C_n = \sum_{m=0}^{n} a_{mn}C_m C_{n-m} + \sum_{m=n+1}^{N} b_{mn}C_m C_{m-n}^* - \frac{p_0\delta_{1n}}{3\gamma P_0},$$

(5.15)

where the asterisk denotes complex conjugate, and the Kronecker delta ensures that the excitation frequency is ω. The coefficient of C_n is defined by

$$\Delta_n = 1 + jn\frac{4\mu}{\rho_0 R_0^2\omega_0}\frac{\omega}{\omega_0} - n^2\left[1 - 2\frac{R_0}{d}\ln(1 - e^{-jnkd})\right]\frac{\omega^2}{\omega_0^2} + jn^3 k_0 R_0\frac{\omega^3}{\omega_0^3},$$

(5.16)

which is the same as Eq. (5.9) except with viscosity included. The quality factor associated with viscosity alone is given by

$$\frac{1}{Q_{\rm vis}} = \frac{4\mu}{\rho_0 R_0^2\omega_0} = \frac{4\mu}{R_0\sqrt{3\gamma\rho_0 P_0}}.$$

(5.17)

The coefficients in the summations, which are derived in Appendix C, are defined by

$$a_{mn} = \frac{3\gamma+1}{4} + j\frac{m-n}{Q_{\rm vis}}\frac{\omega}{\omega_0} + (n-m)\left[\left(\frac{n}{2} + \frac{m}{4}\right) - 2n\frac{R_0}{d}\ln(1 - e^{-jnkd})\right]\frac{\omega^2}{\omega_0^2}$$
$$- j[n^3 + m^2(2m - 3n)]k_0 R_0\frac{\omega^3}{\omega_0^3},$$

(5.18)

$$b_{mn} = \frac{3\gamma + 1}{2} + j\frac{m}{Q_{\text{vis}}}\frac{\omega}{\omega_0} + \left[\frac{1}{2}(n^2 + mn - m^2) - 2n^2\frac{R_0}{d}\ln(1 - e^{-jnkd})\right]\frac{\omega^2}{\omega_0^2}$$
$$- jn^3 k_0 R_0 \frac{\omega^3}{\omega_0^3}. \tag{5.19}$$

The first summation in Eq. (5.15) accounts for sum frequency generation due to the quadratic nonlinearity, and the second summation accounts for difference frequency generation.

Alternatively, Eq. (5.16) can be expressed in terms of the radiation impedance as follows:

$$\Delta_n = 1 + j\left(\frac{1}{Q_{\text{vis}}} + \frac{z_{\text{rad}}(n\omega)}{k_0 R_0 \rho_0 c_0}\right)\frac{n\omega}{\omega_0}, \tag{5.20}$$

where $z_{\text{rad}}/\rho_0 c_0$ is given by Eq. (4.9). Likewise, Eqs. (5.18) and (5.19) become

$$a_{mn} = \frac{3\gamma + 1}{4} + j(m - n)\left[\frac{1}{Q_{\text{vis}}} + \frac{z_{\text{rad}}(n\omega)}{k_0 R_0 \rho_0 c_0}\right]\frac{\omega}{\omega_0} + (n - m)\left(\frac{m}{4} - \frac{n}{2}\right)\frac{\omega^2}{\omega_0^2}$$
$$- j(2m^3 - 3m^2 n + mn^2)k_0 R_0 \frac{\omega^3}{\omega_0^3}, \tag{5.21}$$

$$b_{mn} = \frac{3\gamma + 1}{2} + j\left[\frac{m}{Q_{\text{vis}}} - \frac{nz_{\text{rad}}(n\omega)}{k_0 R_0 \rho_0 c_0}\right]\frac{\omega}{\omega_0} - \frac{1}{2}[m^2 - mn + n^2]\frac{\omega^2}{\omega_0^2}. \tag{5.22}$$

The importance of writing Eqs. (5.20)–(5.22) in terms of radiation impedance is that the coupled system of Eqs. (5.15) is now easily generalized to account for all of the channels for which we derived the radiation impedance in Chapter 4, including those based on normal mode theory to account for arbitrary channel wall impedance.

Given p_0/P_0, ω/ω_0, d/R_0 and Q_{vis}, Eq. (5.15) is solved iteratively to find C_n using a Newton-Raphson iteration method. Comparisons will be made with direct numerical solutions of Eq. (2.15) in the time domain for the response in a free field,

and subsequently with the analytical solutions for the first and second harmonics and dc component derived in Section 5.1.1 for the response between parallel plates.

5.1.3   Numerical Solution and Verification of Procedure

Appendix C provides an introduction to the Newton-Raphson method for solving an equation with one independent variable. The method can also be generalized to multiple dimensions to solve a system of N nonlinear equations with N independent variables $\mathbf{x} = \{x_1, x_2, \ldots, x_N\}$ [63, Chapter 9]:

$$\mathbf{F} = \mathbf{0}, \quad \mathbf{F} = \{F_1(\mathbf{x}), F_2(\mathbf{x}), \ldots, F_N(\mathbf{x})\}. \tag{5.23}$$

In the neighborhood of $\mathbf{x}$, each of the functions F_i can be expanded in a Taylor series:

$$F_i(\mathbf{x} + \Delta\mathbf{x}) = F_i(\mathbf{x}) + \sum_{j=1}^{N} \frac{\partial F_i}{\partial x_j} \Delta x_j + O(\Delta\mathbf{x}^2), \quad i = 1, 2, \ldots, N, \tag{5.24}$$

or in matrix notation,

$$\mathbf{F}(\mathbf{x} + \Delta\mathbf{x}) = \mathbf{F}(\mathbf{x}) + \mathbf{J} \cdot \Delta\mathbf{x} + O[(\Delta\mathbf{x})^2], \tag{5.25}$$

where $\mathbf{J}$ is the Jacobian with

$$J_{ij} \equiv \frac{\partial F_i}{\partial x_j}, \quad i, j = 1, 2, \ldots, N. \tag{5.26}$$

By neglecting terms of order $(\Delta x)^2$ and higher and by setting $\mathbf{F}(\mathbf{x} + \Delta\mathbf{x}) = \mathbf{0}$, we obtain a set of linear equations for the corrections $\Delta\mathbf{x}$ that move each function closer to zero simultaneously, namely,

$$\Delta\mathbf{x} = -\mathbf{J}^{-1}\mathbf{F}. \tag{5.27}$$

The corrections are then added to the solution vector,

$$\mathbf{x}_{\text{new}} = \mathbf{x}_{\text{old}} + \Delta\mathbf{x}, \tag{5.28}$$

and the process of the iteration continues until it converges, i.e., until $\Delta\mathbf{x}$ is smaller than the accuracy desired in the solution, or until all $F_j(\mathbf{x})$ are sufficiently close to 0.

Similar to the one-dimensional Newton-Raphson method, the N-dimensional method generally converges quadratically provided an accurate starting value is given and the inverse of the Jacobian exists. One drawback of this procedure is that inversion of the matrix $\mathbf{J}$ is necessary for each iteration.

5.1.3.1 Weakly-Nonlinear and Fully-Nonlinear Solutions of the Rayleigh-Plesset Equation

Numerical solutions of Eq. (5.15), without the effects of the parallel plates and the radiation damping, are now compared with direct time-domain (Runge-Kutta) solutions of Eq. (2.15) for a bubble in a free field, or Eq. (2.1) without the effects of surface tension and vapor pressure, which are not needed for the purposes of the comparisons:

$$R\ddot{R} + \frac{3}{2}\dot{R}^2 = \frac{1}{\rho_0}\left[P_0 \left(\frac{R_0}{R}\right)^{3\gamma} - P_0 - 4\mu\frac{\dot{R}}{R} - p_{\text{ac}}(t) \right]. \tag{5.29}$$

Without the effects of the parallel plates and the radiation damping, Eq. (5.15) reduces to

$$\Delta'_n C_n = \sum_{m=0}^{n} a'_{mn} C_m C_{n-m} + \sum_{m=n+1}^{N} b'_{mn} C_m C^*_{m-n} - \frac{p_0 \delta_{1n}}{3\gamma P_0}, \tag{5.30}$$

109

where

$$\Delta'_n = 1 + \frac{jn}{Q_{\text{vis}}} \frac{\omega}{\omega_0} - n^2 \frac{\omega^2}{\omega_0^2}, \tag{5.31}$$

$$a'_{mn} = \frac{3\gamma + 1}{4} + j \frac{m - n}{Q_{\text{vis}}} \frac{\omega}{\omega_0} + \frac{1}{2}(n - m)\left(n + \frac{m}{2}\right) \frac{\omega^2}{\omega_0^2}, \tag{5.32}$$

$$b'_{mn} = \frac{3\gamma + 1}{2} + j \frac{m}{Q_{\text{vis}}} \frac{\omega}{\omega_0} + \frac{1}{2}(n^2 + mn - m^2) \frac{\omega^2}{\omega_0^2}. \tag{5.33}$$

With $N = \infty$, Eq. (5.30) is the quadratic approximation of Eq. (5.29) in the frequency domain.

Equations (5.30)–(5.33) resemble Eqs. (6)–(10) derived and solved by Kumar and Brennen [64], except that they included vapor pressure and surface tension. Without the surface tension terms, their Eqs. (6)–(10) are equivalent to our Eqs. (5.30)–(5.33), except that they did not include the dc component.

Comparisons of numerical solutions of Eqs. (5.29) and (5.30) serve two purposes. One is to validate the algebra underlying the derivation of Eqs. (5.15), (5.18) and (5.19). The other is to determine the domain of validity (i.e., the maximum drive pressure amplitude) in which the quadratic approximation (i.e., discarding all cubic and higher-order terms) underlying Eq. (5.15) is valid.

Given the drive pressure amplitude p_0/P_0, the excitation frequency ω/ω_0, and the viscosity parameter Q_{vis}, Eq. (5.30) is solved using the Newton-Raphson method for the first N harmonics and the dc component. Calculation of the Jacobian is described in Appendix C. Three excitation frequencies are chosen, $\omega/\omega_0 = 1/3, 1/2$, and 1. The drive pressure amplitude varies from $p_0/P_0 = 0.01$ to 0.2. We use $Q_{\text{vis}} = 10$ for all calculations. Once we have the C_n's, the harmonic amplitudes are substituted
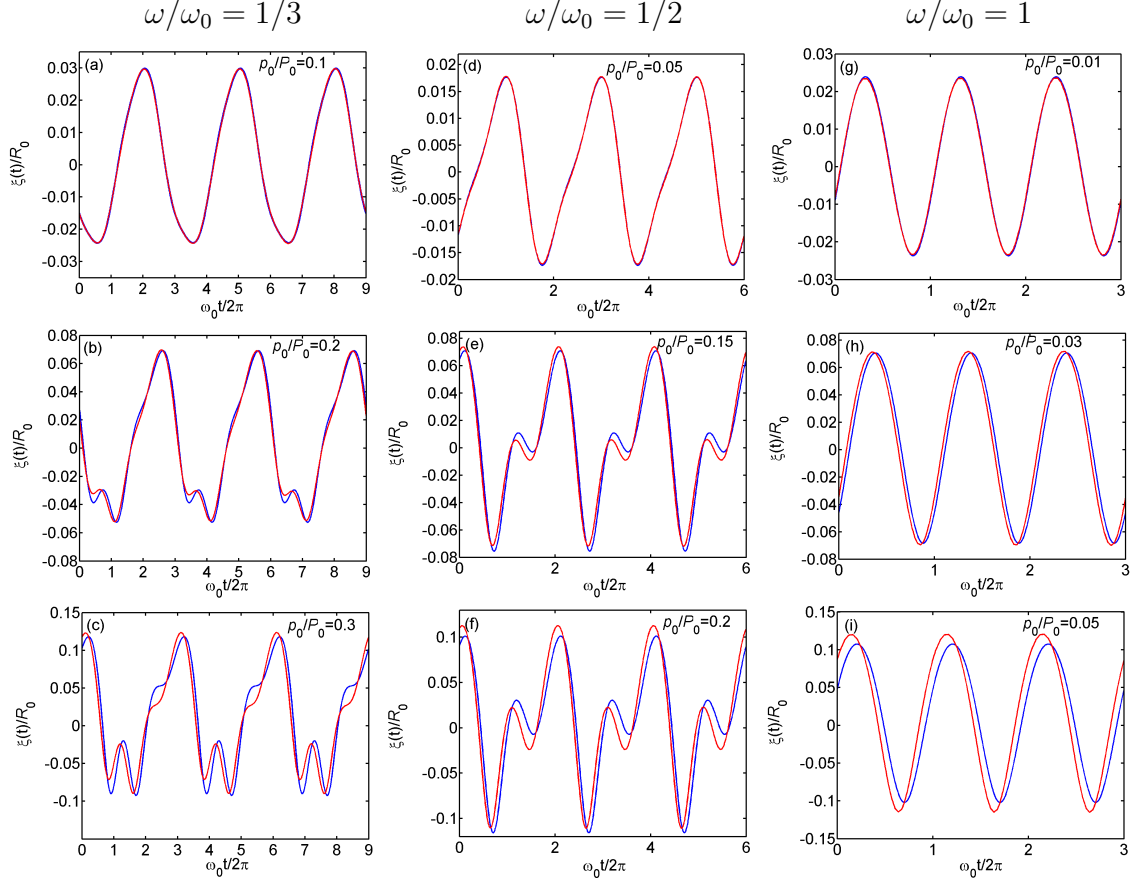
Figure 5.3: Time waveforms for bubble pulsation in a free field, calculated numerically in the frequency domain using a quadratic approximation of the nonlinearity [Eq. (5.30), blue lines] and in the time domain with full nonlinearity [Eq. (5.29), red lines]. Viscous losses are determined by $Q_{vis} = 10$.

111

back in Eq. (5.4) and summed up to obtain the time waveform. As explained later in this section, we use $N = 11$ for the calculations.

The weakly nonlinear solutions for $\xi(t)$ are compared in Fig. 5.3 with numerical solutions obtained by integrating Eq. (5.29) using a Runge-Kutta scheme for three excitation frequencies. The blue lines are the weakly nonlinear solutions obtained in the quadratic approximation, and the red lines are the numerical solutions obtained using the Runge-Kutta method. As illustrated in these figures, the quadratic approximation works quite well for sufficiently small drive amplitudes. It can also be seen that the limiting amplitude at which the quadratic approximation begins to fail is strongly dependent on the excitation frequency. As expected, the approximation begins to fail first (at around $p_0/P_0 = 0.05$) for $\omega/\omega_0 = 1$ (i.e., near resonance), whereas it works very well for $\omega/\omega_0 = 1/3$ up to $p_0/P_0 = 0.2$.

In terms of the bubble radius perturbation $\xi(t)$, the quadratic approximation is only valid for $|\xi| \lesssim 0.1R_0$. This inequality sets the upper limit on the magnitude of p_0/P_0. As seen from Fig. 5.3, the bubble has the strongest response around resonance, $\omega = \omega_0$, so the upper limit of the drive amplitude is largely determined by the oscillations of the bubble at resonance. From Fig. 5.3 it is seen that this limit is $p_0/P_0 = 0.05$. At this amplitude, the 5th harmonic is of order 10^{-7} and the 11th harmonic is of order 10^{-15} for $\omega/\omega_0 = 1$. At this drive frequency, with the combination of $p_0/P_0 = 0.05$ and $Q_{\text{vis}} = 10$, the number of harmonics to be included can be as small as 6 (the first 5 harmonics and the dc component) to achieve excellent agreement with the time domain solution. Including more harmonics has very little effect on the time waveforms shown in Fig. 5.3. The nonlinearity of the bubble oscillation is roughly

112

proportional to $Q_{vis}p_0$, the product of the drive pressure amplitude and the quality factor. As long as this product stays the same, the relative nonlinearity remains about the same, and the agreement of the two solutions is excellent. Increasing the product by increasing either the drive amplitude or the quality factor eventually leads to disagreement between the two solutions.

We included the first 11 harmonics in subsequent calculations. In the frequency response plots, only the first five harmonics (the dc component is included in Fig. 5.5) are presented.

5.1.3.2 Analytical and Numerical Solutions

As a second validation, the numerical solution of Eq. (5.15) obtained by the Newton-Raphson method is now compared to the analytical solutions. The frequency response of the fundamental, the second harmonic, and the dc component obtained numerically are compared with their analytical solutions given in Section 5.1.1. The frequency responses are generated by sweeping through the frequency range (say $0 \leq \omega/\omega_0 \leq 3$) in steps of $\Delta\omega/\omega_0 = 0.0025$. At each step, the solutions for C_n are collected. The final collection of C_n is plotted against ω/ω_0 to obtain the frequency responses. We included the first ten harmonics and the dc component in the calculations. Comparisons are made with and without viscosity included. For the former we chose $Q_{vis} = 10$, and for the latter we have $Q_{vis} = \infty$. To include viscosity in the analytical solutions, we replaced Eq. (5.9) by Eq. (5.16), and Eq. (5.10) by

$$\Gamma'(\omega) = \frac{3\gamma + 1}{4} + \left[\frac{5}{4} - 4\frac{R_0}{d}\ln(1 - e^{-j2kd})\right]\frac{\omega^2}{\omega_0^2} + \frac{1}{Q_{vis}}\frac{\omega^2}{\omega_0^2} - j4k_0R_0\frac{\omega^3}{\omega_0^3}. \quad (5.34)$$

113
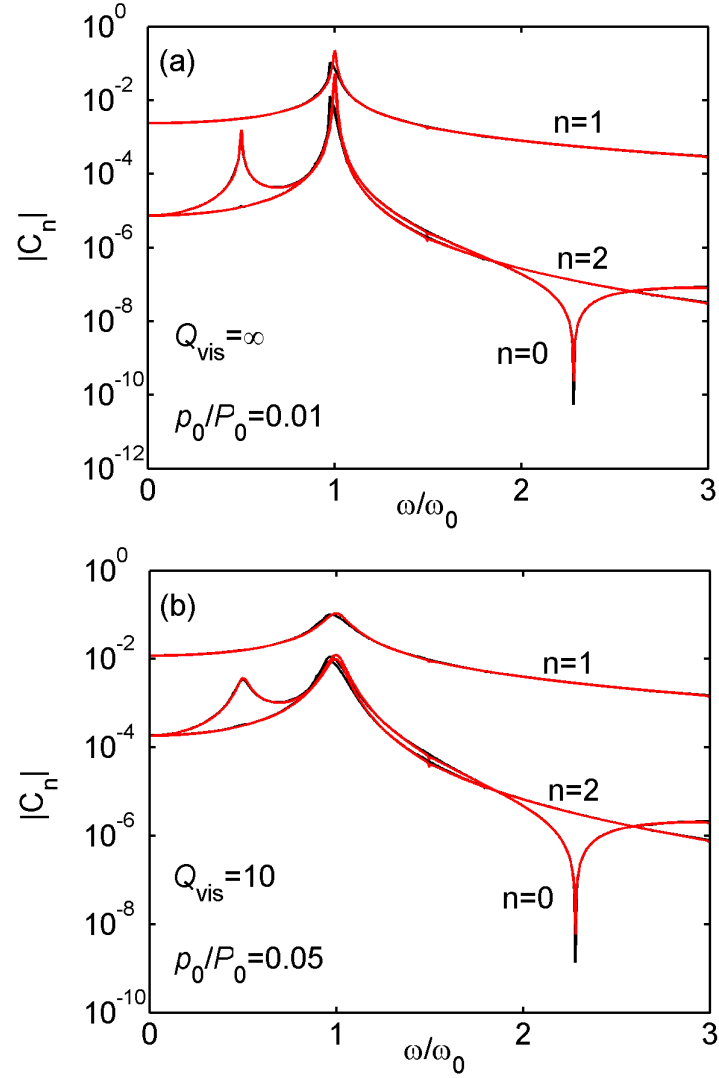
Figure 5.4: Comparison of numerical solutions (black lines) based on the Newton-Raphson method with analytical solutions (red lines) obtained by perturbation for $d/R_0 = 300$.

Figure 5.4 shows the comparisons between the numerical and the analytical solutions. Black curves are obtained from the numerical solutions using a Newton-Raphson method, and the red curves are obtained analytically using Eq. (5.8). In Fig. 5.4(b), with $Q_{\mathrm{vis}} = 10$, the two solutions match very well at the maximum drive amplitude, $p_0/P_0 = 0.05$. But when viscosity is neglected, the computer program for the Newton-Raphson method becomes unstable near resonance for $p_0/P_0 > 0.01$. As shown in Fig. 5.4(a), for drive amplitude $p_0/P_0 = 0.01$ and lower, the two results match very well.

5.1.4 Frequency Response

We now solve Eq. (5.15) for $0 \leq \omega/\omega_0 \leq 1.5$ at the maximum drive amplitude valid for the weakly nonlinear approximation. Equation (5.15) is solved using the Newton-Raphson method for the first ten harmonics and dc component. We again have $Q_{\mathrm{vis}} = 10$ for all calculations. If we set $d/R_0 = 300$, the results are basically the same as the free-field solution. Figure 5.5 displays two sets of frequency responses for the first five harmonics. The solid lines are from calculations that include the dc component (the dc component is the solid red line), while the dashed lines are based on calculations where the dc component is not included. We notice the following shifts in the resonance peaks. First, the resonance peaks for the curves including the dc component shift slightly lower in frequency than those without the dc component. This occurs because the mean radius of the bubble gets bigger. Second, the curves shift slightly upward because the drive frequency (based on the mean radius without dc generation) shifts to a higher relative frequency on the tuning curves.
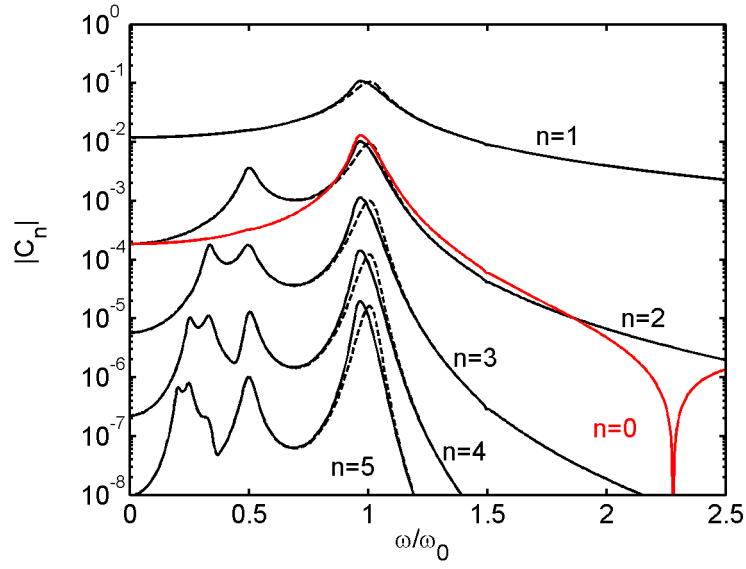
Figure 5.5: Frequency responses of the first five harmonics of the drive frequency, and including the dc component. The solid lines are the numerical solutions obtained with the dc component included in the calculations, and the dashed lines are the corresponding solutions obtained without taking the dc component into account. The parameter values are $p_0/P_0 = 0.05$, $d/R_0 = 300$ and $Q_{\mathrm{vis}} = 10$.

The curves labeled $n = 1$ are the magnitude of the response at the fundamental excitation frequency ω, the curves labeled $n = 2$ are the magnitude of the response at twice the excitation frequency, etc. We note that the fundamental component dominates all the other harmonics in amplitude, as it must for weak nonlinearity. Like the fundamental, the dc component, indicated by the red curve, also has a resonance peak at $\omega/\omega_0 = 1$. As observed from Fig. 5.1, the amplitude response at twice the drive frequency has two maxima, one at $\omega/\omega_0 = 1$, where the drive frequency matches the bubble resonance, and the other at $\omega/\omega_0 = 1/2$, where the second harmonic of the drive frequency matches the bubble resonance. There are three maxima in the amplitude response at three times the drive frequency. The first two exist for the reason explained above. The third happens at $\omega/\omega_0 = 1/3$, where the third harmonic of the drive frequency matches the bubble resonance. The same trend is observed for all higher harmonics.

The effect of plate separation on the amplitude responses of the first five harmonics is shown in Fig. 5.6. As for the fundamental, when the plate separation becomes narrower, all resonance peaks of all higher harmonics shift to lower frequencies, and the magnitudes of the peaks become smaller and broader. The overall physics underlying the response is as described in Chapter 3, namely, as plate separation decreases, the effective mass loading and radiation damping also increase, reducing the resonance frequencies and broadening the peak in the spectra of all harmonics.
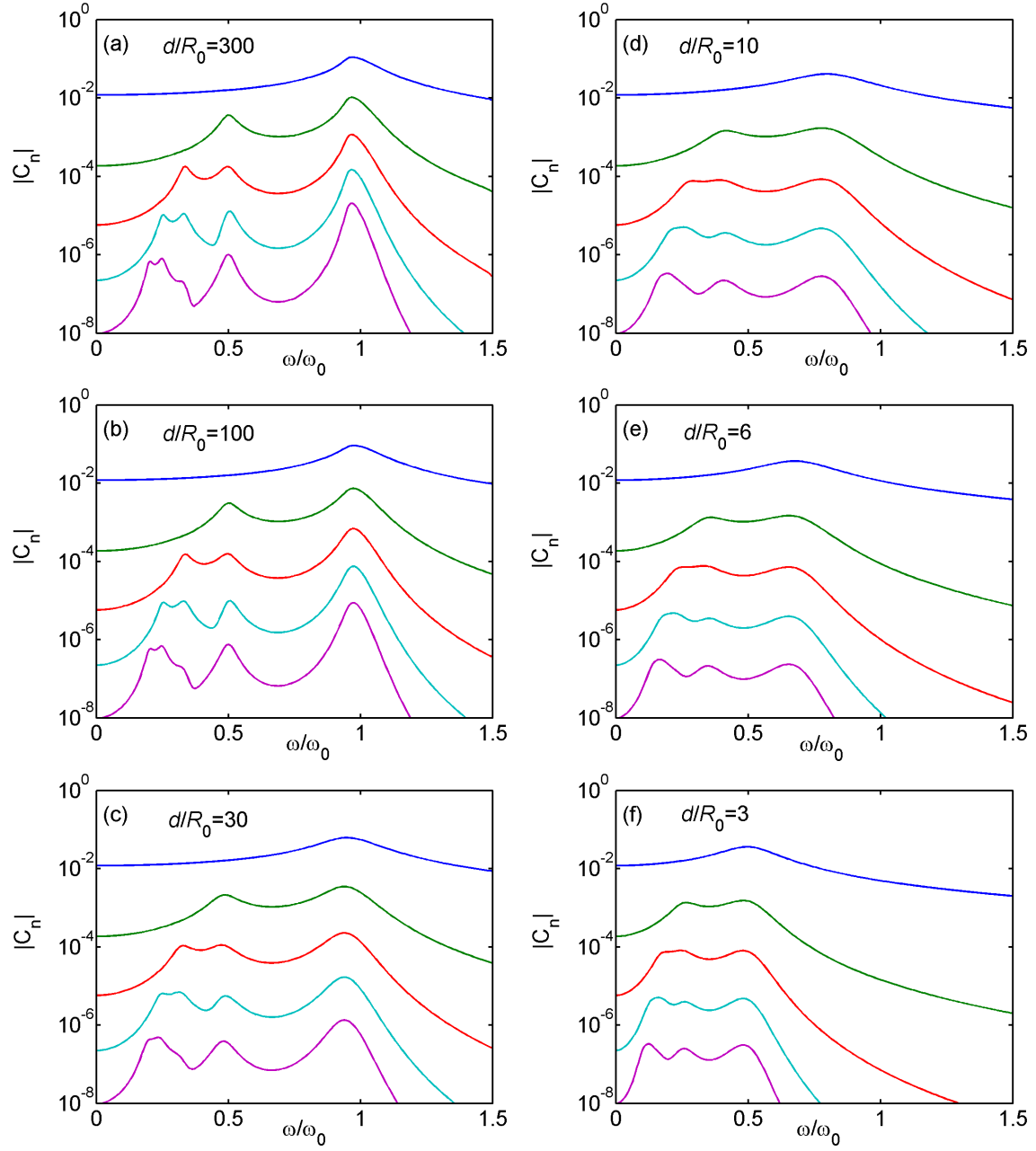
Figure 5.6: Frequency responses of the first five harmonics as functions of plate separation. The drive amplitude is $p_0/P_0 = 0.05$ and the viscosity parameter is $Q_{\mathrm{vis}} = 10$.

118

5.2 Quadratic Model for a Bubble in a Tube

We now substitute $R = R_0 + \xi$ in Eq. (2.16) to obtain, in place of Eq. (5.1),

$$\ddot{\xi}(t) + \omega_0^2 \xi(t) - \frac{R_0}{c_0}\dddot{\xi}(t) + R_0 \sum_{p,q} \frac{1}{r_{p,q}} \ddot{\xi}(t - r_{pq}/c_0) + \frac{4\mu}{\rho_0}\dot{\xi}(t) = F_{\text{duct}}(\xi) - \frac{p_{\text{ac}}(t)}{\rho_0 R_0^2}, \quad (5.35)$$

where

$$F_{\text{duct}}(\xi) = -\,\xi\ddot{\xi} - \frac{3}{2}\dot{\xi}^2 + \frac{\omega_0^2}{2}(3\gamma + 1)\xi^2 + 2\frac{R_0}{c_0}(3\dot{\xi}\ddot{\xi} + \xi\dddot{\xi})$$
$$-\,2R_0 \sum_{p,q} \frac{1}{r_{pq}} \left[\dot{\xi}^2(t - \frac{r_{pq}}{c_0}) + \xi(t - \frac{r_{pq}}{c_0})\ddot{\xi}(t - \frac{r_{pq}}{c_0})\right]. \quad (5.36)$$

Here in Eqs. (5.35)–(5.40), and only here, we have replaced the indices (l, m) with (p, q) in the summations over images to avoid conflict with the indices (m, n) used in the summations over frequencies. In the frequency domain we now have

$$\Delta_n^{\text{duct}} C_n = \sum_{m=0}^{n} a_{mn}^{\text{duct}} C_m C_{n-m} + \sum_{m=n+1}^{N} b_{mn}^{\text{duct}} C_m C_{m-n}^* - \frac{p_0 \delta_{1n}}{3\gamma P_0}, \quad (5.37)$$

where

$$\Delta_n^{\text{duct}} = 1 + j\frac{n}{Q_{\text{vis}}}\frac{\omega}{\omega_0} - n^2\left(1 + R_0 \sum_{p,q} \frac{e^{-jnkr_{pq}}}{r_{pq}}\right)\frac{\omega^2}{\omega_0^2} + jn^3 k_0 R_0 \frac{\omega^3}{\omega_0^3}, \quad (5.38)$$

$$a_{mn}^{\text{duct}} = \frac{3\gamma + 1}{4} + j\frac{m - n}{Q_{\text{vis}}}\frac{\omega}{\omega_0} + (n - m)\left[\left(\frac{n}{2} + \frac{m}{4}\right) + nR_0 \sum_{p,q} \frac{e^{-jnkr_{pq}}}{r_{pq}}\right]\frac{\omega^2}{\omega_0^2} \quad (5.39)$$
$$-\,j[n^3 + m^2(2m - 3n)]k_0 R_0 \frac{\omega^3}{\omega_0^3},$$

$$b_{mn}^{\text{duct}} = \frac{3\gamma + 1}{2} + j\frac{m}{Q_{\text{vis}}}\frac{\omega}{\omega_0} + \left[\frac{1}{2}(n^2 + mn - m^2) + n^2 R_0 \sum_{p,q} \frac{e^{-jnkr_{pq}}}{r_{pq}}\right]\frac{\omega^2}{\omega_0^2} \quad (5.40)$$
$$-\,jn^3 k_0 R_0 \frac{\omega^3}{\omega_0^3}.$$

119

Equations (5.38)–(5.40) also result from substituting Eq. (4.13), with k replaced everywhere by nk, into Eqs. (5.20)–(5.22). The summations in Eqs. (5.38)–(5.40) must be calculated numerically. Once the summations are calculated (for details refer to Appendix A), the Newton-Raphson method can be used to solve Eq. (5.37).

5.2.1   Frequency Response for a Bubble in a Tube

Using the same techniques outlined in Sec. 5.1.3.2 we can obtain the frequency responses at harmonics of the excitation frequency for a bubble centered in a tube with a triangular, square, or hexagonal cross section. Plots of the frequency responses of the first five harmonics are shown in Fig. 5.7 as the tube size decreases from $\sqrt{S}/R_0 = 100$ to 10, and the acoustic pressure amplitude is held constant at $p_0/P_0 = 0.05$. For each tube size, the response curves for all three cross-sections are plotted in each graph, black lines for the square tube, blue lines for the hexagonal tube, and red lines for the triangular tube. It can be seen that in all cases the curves are virtually indistinguishable. This shows that what was observed previously in the linear approximation, as shown in Fig. 3.11, extends to the nonlinear response of the bubble. It is the cross-sectional area of the tube, not its cross-sectional geometry, that primarily determines the dynamic response of a bubble located near the center of the tube. Figure 5.8 shows an expanded view of the three curves for the response at the fifth harmonic for a tube with $\sqrt{S}/R_0 = 10$. The frequency responses in Figs. 5.6 and 5.7 also confirm the difference between the dynamics of a bubble between plates and of a bubble in a tube that we observed in Sec. 4.2.1. Namely, the response of a bubble in a tube is damping controlled, and it is seen that the responses of the first

five harmonics are indeed heavily damped.
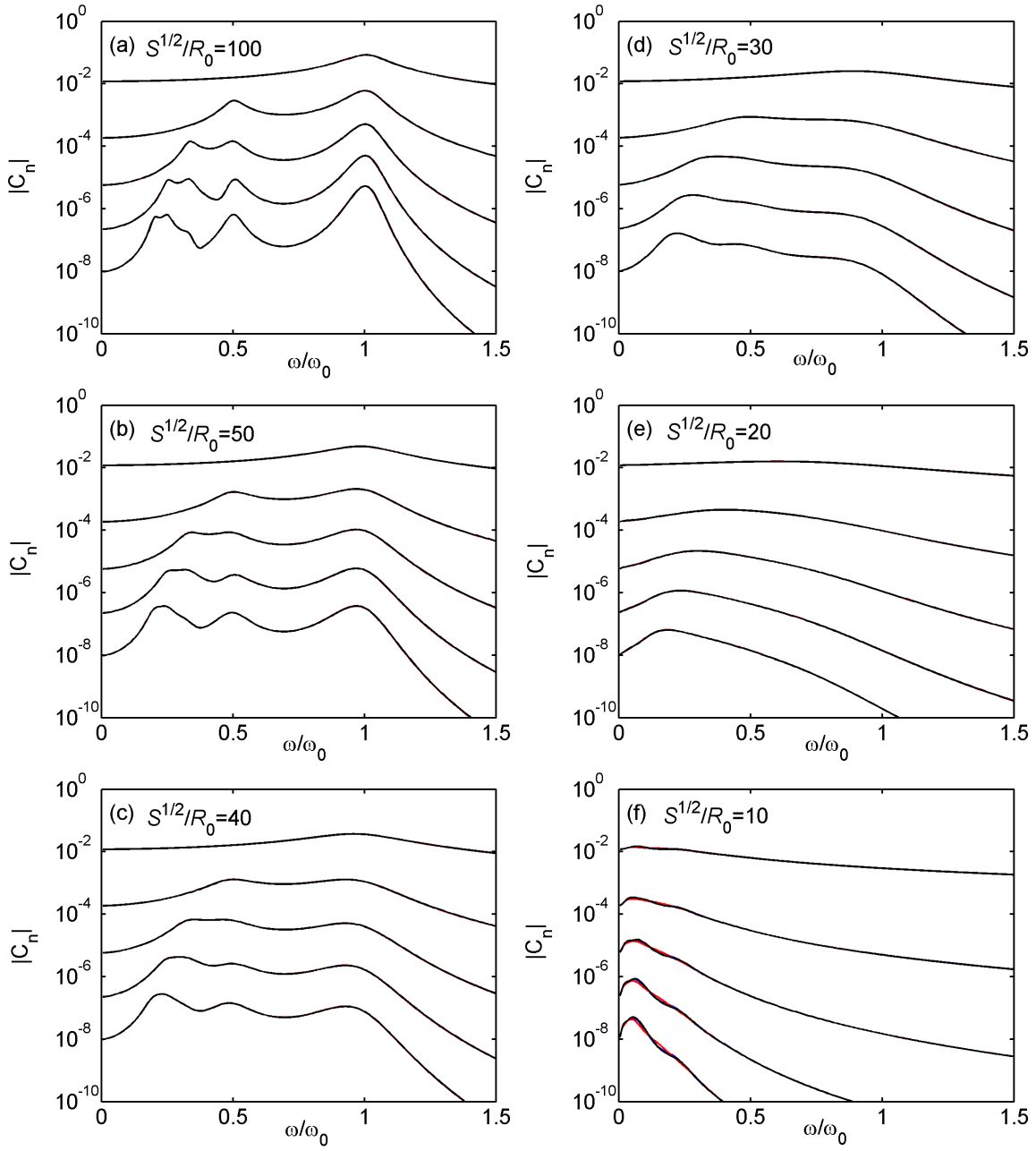
Figure 5.7: Harmonic frequency responses ($n = 1$ through $n = 5$) as functions of tube cross-sectional area. The drive amplitude is $p_0/P_0 = 0.05$ and the viscosity parameter is $Q_{\mathrm{vis}} = 10$. Three cross-sectional shapes are included: black lines for square, blue lines for hexagonal, and red lines for triangular.
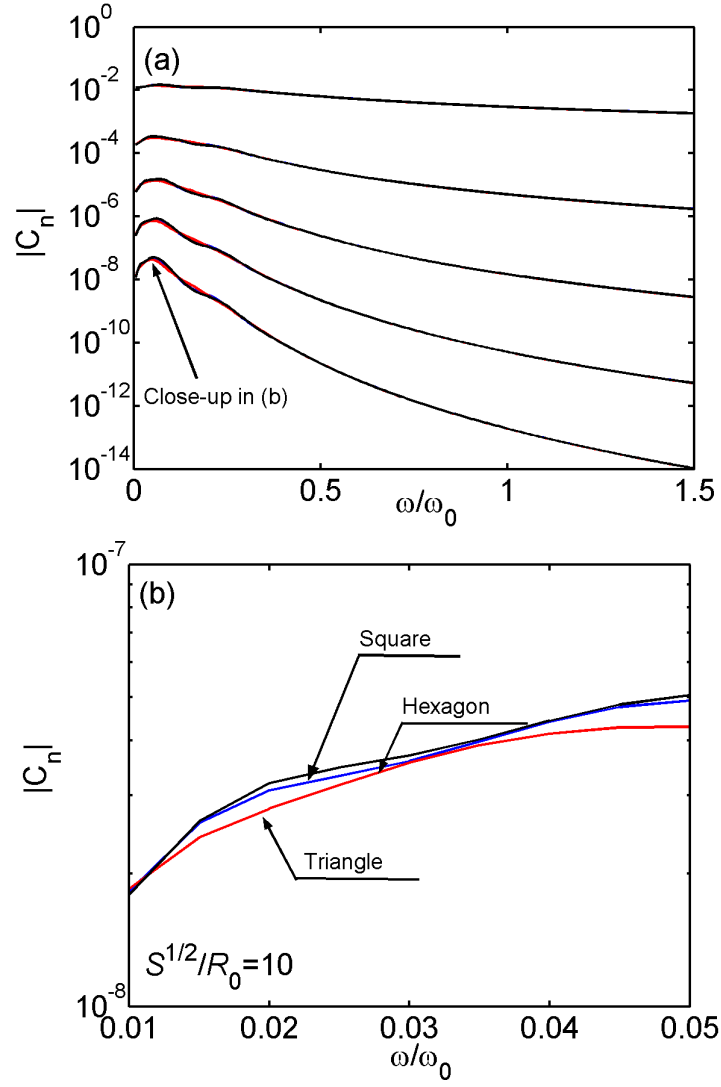
Figure 5.8: Expanded view of the three curves in Fig. 5.7(f) for square, hexagonal and triangular tubes: (a) normal view, (b) close-up. The drive amplitude is $p_0/P_0 = 0.05$, the tube dimension is $S^{1/2}/R_0 = 10$, and the viscosity parameter is $Q_{\mathrm{vis}} = 10$.

Chapter 6

Strongly Nonlinear Oscillations

In this chapter we investigate the fully nonlinear response of a bubble in a channel. A hybrid time-frequency domain method is developed for the purpose of modeling the dynamics of a bubble driven acoustically between two parallel plates [Eq. (2.15)] or in a tube [Eq. (2.16)] with the full nonlinearity taken into account. The same method can be extended directly to tubes with arbitrary shape and wall impedance provided an expression for the radiation impedance is available. We start with an overview of the method, and then validation is conducted by comparing solutions of the Rayleigh-Plesset equation obtained using this method with those obtained using a straightforward Runge-Kutta integration scheme. Solutions of Eqs. (2.15) and (2.16) are presented in the form of frequency responses of the first five harmonics. The fully nonlinear results are also compared to the weakly nonlinear solutions.

6.1 Hybrid Method

The model equation for a bubble between two parallel plates, Eq. (2.15), is used as an example to illustrate the hybrid method. The method can also be applied to solve the Rayleigh-Plesset equation [Eq. (5.29)] and the model equation for a bubble in a tube [Eq. (2.16)]. Equation (2.15) is repeated here with the effect of viscosity

included:

$$RR̈ + \frac{3}{2}\dot{R}^2 = \frac{1}{\rho_0}\left[P_0\left(\frac{R_0}{R}\right)^{3\gamma} - P_0 - 4\mu\frac{\dot{R}}{R} - p_{ac}(t)\right]$$

$$+ \frac{\dddot{V}}{4\pi c_0} - \frac{1}{2\pi d}\sum_{m=1}^{\infty}\frac{1}{m}\ddot{V}\left(t - \frac{md}{c_0}\right). \tag{6.1}$$

As discussed in previous chapters, the summation in Eq. (6.1) is history dependent, but it assumes a closed form in the frequency domain. Also, the third time derivative of V is easier to evaluate in the frequency domain. Thus it is preferable to transform the last two terms into the frequency domain. As shown below, the gas nonlinearity and the volume V itself are easier to calculate in the time domain, so a hybrid time-frequency method was developed to solve Eq. (6.1) as follows.

Begin by taking the Fourier transform of Eq. (6.1):

$$\mathcal{F}\left\{RR̈ + \frac{3}{2}\dot{R}^2 - \frac{1}{\rho_0}\left[P_0\left(\frac{R_0}{R}\right)^{3\gamma} - P_0 - 4\mu\frac{\dot{R}}{R} - p_{ac}(t)\right]\right\}$$

$$= \left[\frac{(j\omega)^3}{4\pi c_0} + \frac{(j\omega)^2}{2\pi d}\ln(1 - e^{-jkd})\right]\mathcal{F}\left(\frac{4}{3}\pi R^3\right), \tag{6.2}$$

where $\mathcal{F}$ is the Fourier transform operator. The terms multiplying the Fourier transform on the right-hand side account for the time derivatives of the bubble volume and the time delays due to the reflections. After making the substitution $R(t) = R_0 + \xi(t)$, linearizing the viscosity term, and converting to a discrete Fourier transform in which the applied pressure and radial displacement are expressed as in Eqs. (5.3) and (5.4)

(repeated here for convenience),

$$p_{\text{ac}}(t) = \frac{1}{2}p_0 e^{j\omega t} + \text{c.c.}, \tag{6.3}$$

$$\frac{\xi(t)}{R_0} = C_0 + \frac{1}{2}\sum_{n=1}^{N} C_n e^{jn\omega t} + \text{c.c.}, \tag{6.4}$$

we obtain for our model equation

$$\mathcal{F}_n\left\{ R_0\left(1+\frac{\xi}{R_0}\right)\ddot{\xi} + \frac{3}{2}\dot{\xi}^2 - \frac{1}{\rho_0}\left[P_0\left(1+\frac{\xi}{R_0}\right)^{-3\gamma} - P_0 - p_{\text{ac}}(t)\right] - \frac{\omega_0}{Q_{\text{vis}}}R_0\dot{\xi}\right\}$$
$$= V_0\left[\frac{(jn\omega)^3}{4\pi c_0} + \frac{(jn\omega)^2}{2\pi d}\ln(1-e^{-jnkd})\right]\mathcal{F}_n\left[\left(1+\frac{\xi}{R_0}\right)^3\right], \tag{6.5}$$

where V_0 is the equilibrium bubble volume. The subscript n on $\mathcal{F}$ indicates discretization in the frequency domain. It can be seen that the gas nonlinearity term $[1 + \xi(t)/R_0]^{-3\gamma}$ and the volume term $[1 + \xi(t)/R_0]^3$ are easier to evaluate in the time domain. Recall, e.g., from Eq. (5.15) that simple quadratic nonlinearity requires convolution in the frequency domain, and higher order nonlinearities are even more complicated to calculate numerically in the frequency domain.

Equation (6.5) is a system of coupled equations for the harmonic amplitudes C_n as we used in the quadratic approximation. However, unlike in the quadratic approximation, no explicit equations are obtained in the fully nonlinear regime. The Fourier transform in Eq. (6.5) is obtained numerically, and a fast Fourier transform (FFT) 'realft' from the Numerical Recipes [63] was used. Alternatively, Eq. (6.5) can

126

be expressed in terms of radiation impedance as follows:

$$\mathcal{F}_n\left\{R_0\left(1+\frac{\xi}{R_0}\right)\ddot{\xi}+\frac{3}{2}\dot{\xi}^2-\frac{1}{\rho_0}\left[P_0\left(1+\frac{\xi}{R_0}\right)^{-3\gamma}-P_0-p_{\mathrm{ac}}(t)\right]-\frac{\omega_0}{Q_{\mathrm{vis}}}R_0\dot{\xi}\right\}=$$
$$V_0\left\{\frac{(jn\omega)^3}{4\pi c_0}-\frac{\omega^2}{4\pi R_0}\left[n-jn^2k_0R_0\frac{\omega}{\omega_0}-\frac{z_{\mathrm{rad}}(\omega)}{jk_0R_0\rho_0c_0}\frac{\omega}{\omega}\right]\right\}F_n\left[\left(1+\frac{\xi}{R_0}\right)^3\right].$$
$$\text{(6.6)}$$

Equation (6.6) is the generalized form for all of the channels for which we derived radiation impedance in Chapter 4, including those based on normal mode theory to account for arbitrary channel wall impedance.

We solved Eq. (6.5) in the frequency domain using a Newton-Raphson iteration method. Embedded in each iteration is a loop that transforms $\xi(t)$ and its derivatives obtained in the frequency domain to the time domain where the arguments of the Fourier transforms in Eq. (6.5) are evaluated, and then transforms the results back to the frequency domain.

Given initial guesses for C_n, and the excitation pressure p_0 and quality factor Q_{vis}, we begin by obtaining ξ and its first and second time derivatives in the frequency domain. An inverse FFT is taken to obtain $\xi(t)$ and its derivatives in the time domain. Next, terms containing $\xi(t)$ and its derivatives [the arguments of the Fourier transforms in Eq. (6.5)] are calculated. A flow chart of the hybrid method is shown in Fig. 6.1. The operations just described account for the first two stages, F1 and T1. Blue and red colors are used to designate the frequency domain and the time domain, respectively.

Next, an FFT of the volume term $[1+\xi(t)/R_0]^3$ is taken, followed by calculations of the terms $(jn\omega)^3/(4\pi c_0)$ and $[(jn\omega)^2/(2\pi d)]\ln(1-e^{-jnkd})$. We thus obtain

127
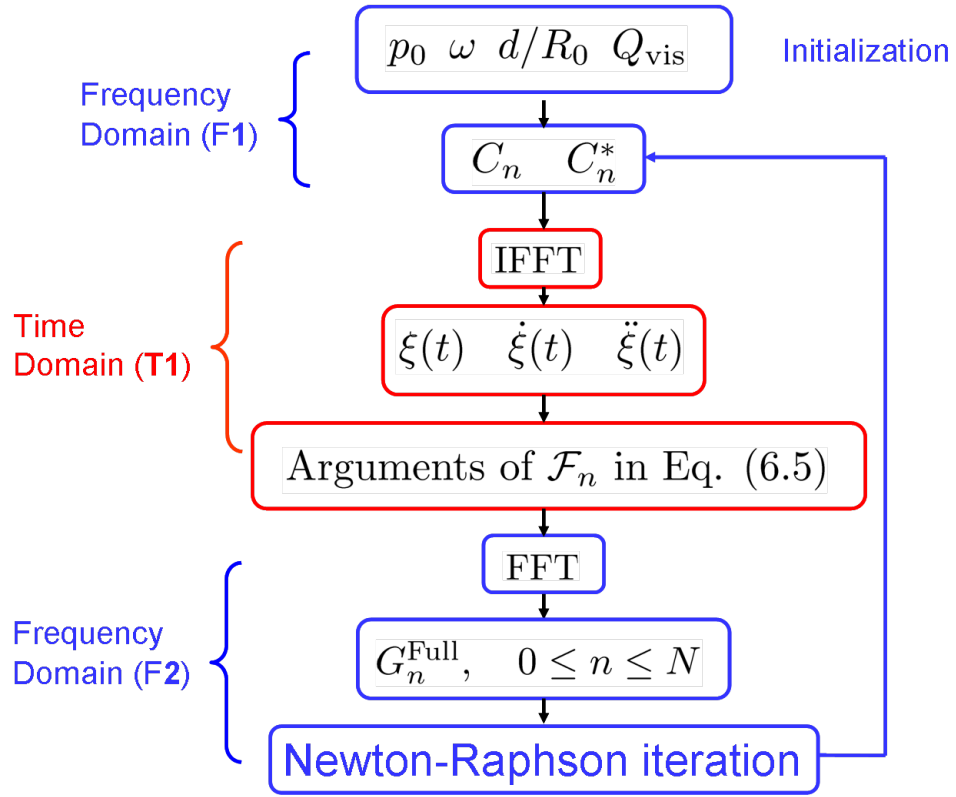
Figure 6.1: Flow chart of the hybrid method.

the spectral components of the pressure due to the radiation damping and reflections from the plates. Meanwhile, the expression on the left-hand side of Eq. (6.5) that is calculated in the time domain is transformed to the frequency domain using an FFT. A system of $N + 1$ coupled equations is thus obtained [Eq. (6.5)], which is converted to a system of $N + 1$ functions G_n^{Full} corresponding to F_n in Eq. (C.54). A Newton-Raphson iteration method from Numerical Recipes [63] called 'newt' is used to find the roots of these functions, and the iteration begins. These steps correspond to stage F2 in the flow chart. After each iteration, new values of C_n are obtained, and the functions G_n^{Full} are evaluated. When the values of G_n^{Full} fall within a given tolerance range, the iteration stops and the values of C_n are the solutions. Otherwise, the values of C_n are fed back to stage F1 and the iteration continues. The program aborts when calculation error occurs.

6.2 Validation of the Hybrid Method

Without the two terms accounting for the pressure on the bubble due to the radiation loss and the plates, Eq. (6.1) reduces to the Rayleigh-Plesset equation, Eq. (5.29). As a verification of the hybrid method, next we solve Eq. (6.5) without the two pressure terms [the right hand-side of Eq. (6.5) becomes zero], and the results are compared with the fully-nonlinear time-domain solutions of Eq. (5.29) by the Runge-Kutta method. Solutions of C_n obtained from the hybrid method are substituted into Eq. (6.4) to obtain ξ/R_0 so that the time waveforms from the two methods can be compared. The quality factor we used is $Q_{\text{vis}} = 10$, and the first 10 harmonics ($N = 10$) plus the dc component were included in the calculation.
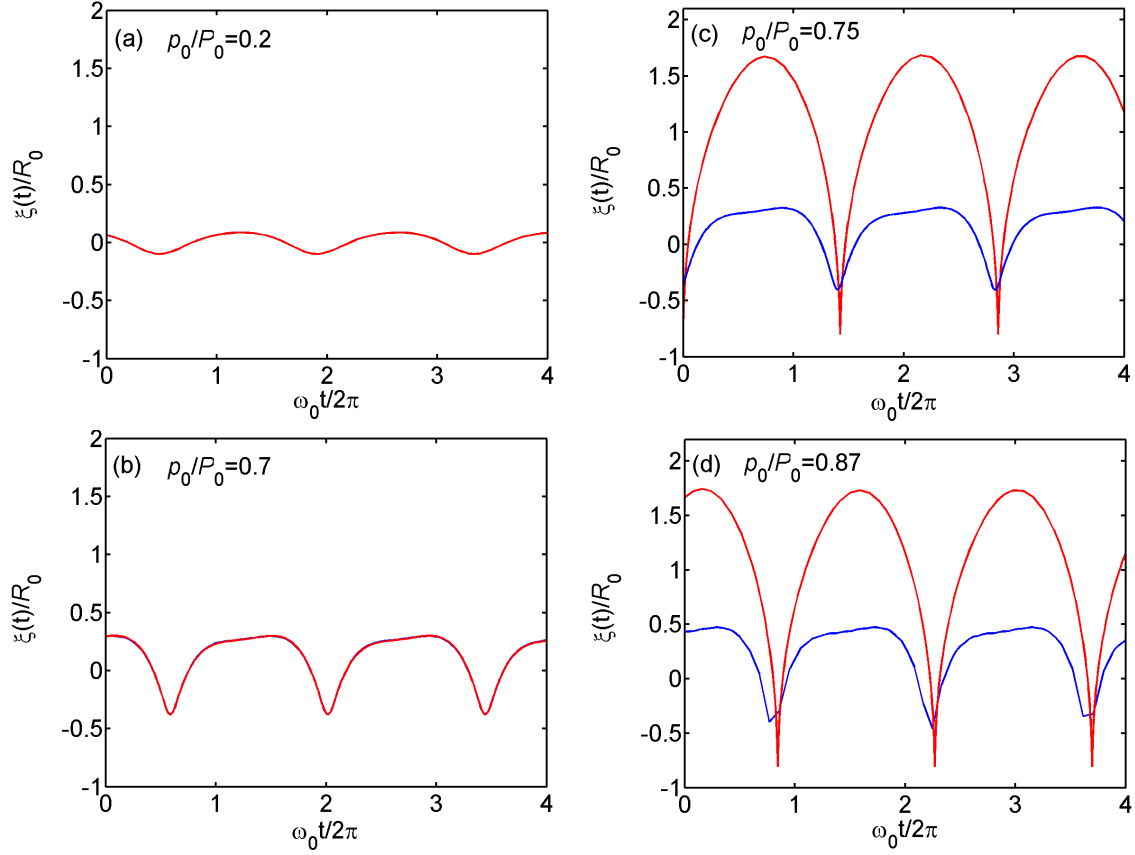
Figure 6.2: Time waveforms for bubble pulsation in a free field, calculated numerically in the frequency domain using the hybrid method (blue lines) and in the time domain with a Runge-Kutta method (red lines), for $Q_{\mathrm{vis}} = 10$, $\omega/\omega_0 = 0.7$.
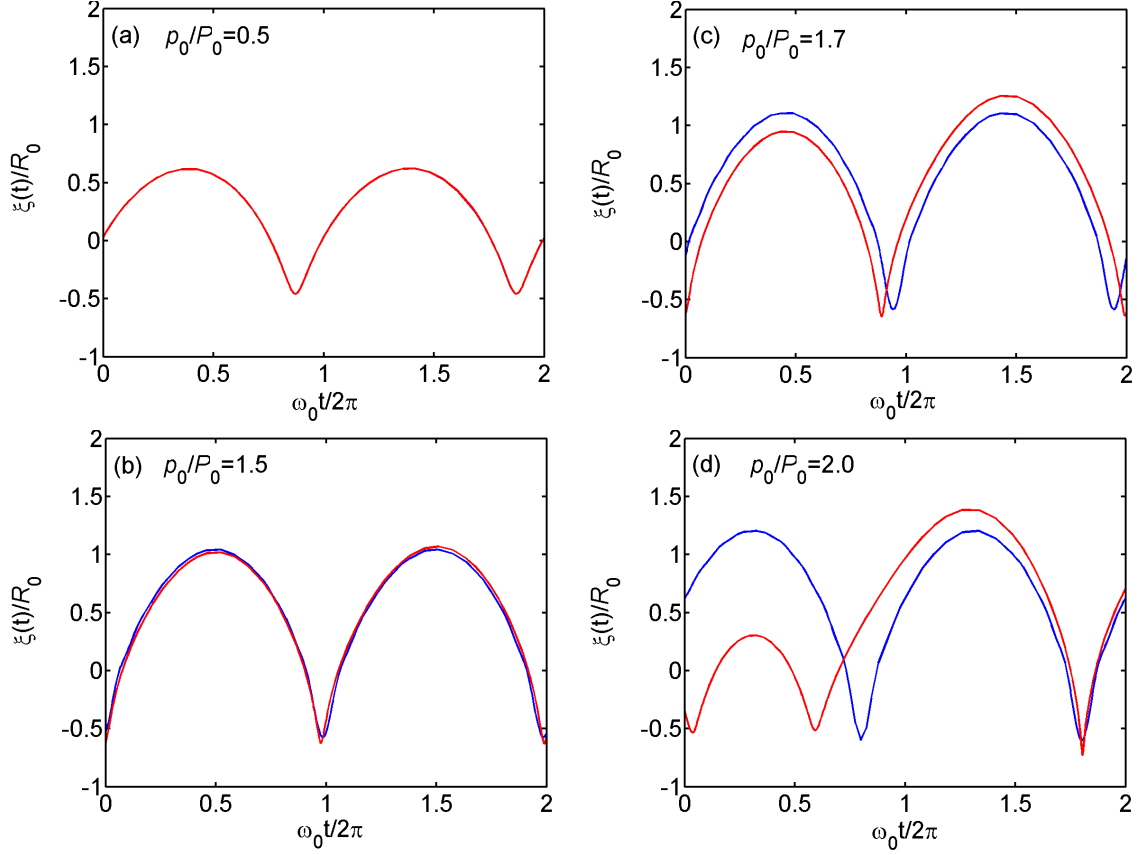
Figure 6.3: Time waveforms for bubble pulsation in a free field, calculated numerically in the frequency domain using the hybrid method (blue lines) and in the time domain with a Runge-Kutta method (red lines), for $Q_{\text{vis}} = 10$, $\omega/\omega_0 = 1$.

Figures 6.2 and 6.3 show two groups of comparisons for $\omega/\omega_0 = 0.7$ and $\omega/\omega_0 = 1$, respectively. The blue lines are results from the hybrid method and the red lines are obtained from the Runge-Kutta integration. It is observed that for low drive amplitudes ($p_0/P_0 \leq 0.7$ for $\omega/\omega_0 = 0.7$ and $p_0/P_0 \leq 0.15$ for $\omega/\omega_0 = 1$) the results from the two methods are almost identical. As the amplitude of the drive pressure increases, the two solutions start to show discrepancy. For $\omega/\omega_0 = 0.7$, at $p_0/P_0 = 0.87$ the maximum value of ξ/R_0 is about 2 from the Runge-Kutta solution, which means that at its maximum the bubble radius is three times its equilibrium value R_0, while the solution from the hybrid method shows $-0.5 \leq \xi/R_0 \leq 0.5$.

We see a drastic jump in the magnitudes of the Runge-Kutta solutions from Fig. 6.2(b) to 6.2(c), i.e., when the drive pressure changes from $p_0/P_0 = 0.7$ to $p_0/P_0 = 0.75$. More Runge-Kutta solutions were obtained for drive amplitudes in the range $0.7 \leq p_0/P_0 \leq 0.75$, and Fig. 6.4 shows the solutions for $p_0/P_0 = [0.70, 0.74, 0.75]$, from which we notice that the sudden increase in the response occurs in the range $0.74 < p_0/P_0 \leq 0.75$.

An expanded view of Fig. 6.3(d) is shown in Fig. 6.5. For $p_0/P_0 = 2$ the period of the Runge-Kutta solution at drive frequency $\omega = \omega_0$ is seen to be about twice that of the drive frequency, suggesting generation of the subharmonic at half the drive frequency(period doubling). Both the jump in the solutions and the generation of subharmonics are due to the nonlinear effects of the response at high drive amplitudes. Lauterborn [65] obtained numerical solutions of the Rayleigh-Plesset equation for increasing drive amplitudes for a wide range of drive frequencies. The frequency response curves obtained by Lauterborn are shown in Fig. 6.6, where the curves
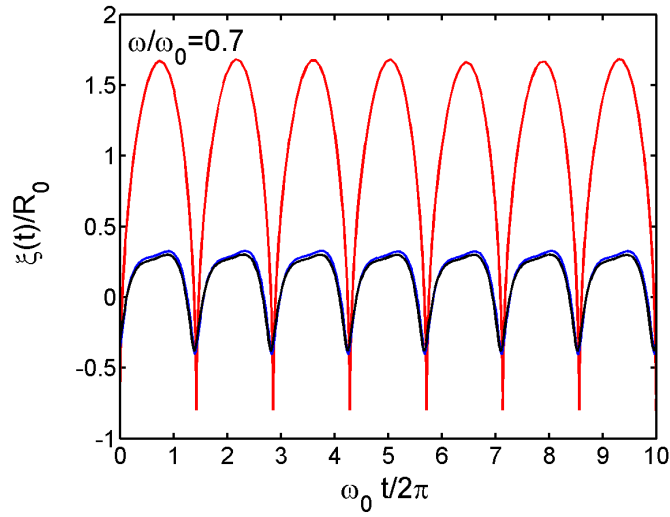
Figure 6.4: Comparison of Runge-Kutta solutions of the Rayleigh-Plesset equation for several drive amplitudes. Black line: $p_0/P_0 = 0.7$. Blue line: $p_0/P_0 = 0.74$. Red line: $p_0/P_0 = 0.75$.
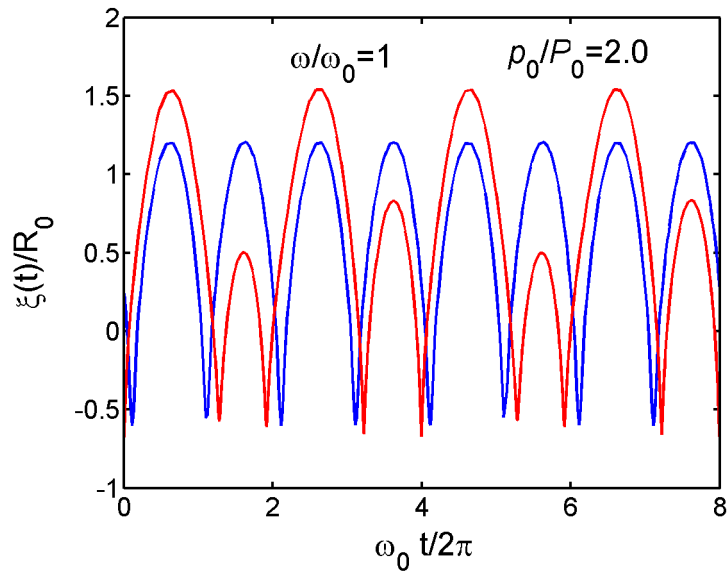
Figure 6.5: Expanded view of Fig. 6.3(d).

133

indicate the peak value of the time waveform. As the drive amplitude increases (indicated by the numbers to the left of the family of curves) the resonances begin to lean toward lower frequencies (indicating softening of the system "stiffness") until eventually a jump in the solution occurs (the discontinuities indicated by the dashed vertical lines). These jumps correspond to bifurcations or sudden transitions between two valid solutions for a given drive frequency. This distortion of the frequency response is a well-known property of nonlinear oscillations. One possible reason for the discrepancy in Fig. 6.2(c) between the Runge-Kutta time domain solution and the hybrid frequency domain solution could be that the two methods follow different branches of the bifurcating solutions, or it could be that the hybrid solution is not accurate since no subharmonic component is included.

A frequency response similar to Fig. 6.6 was obtained with the hybrid method, and it is shown in Fig. 6.7. For a given drive frequency the maximum deviation relative to the equilibrium radius is calculated based on an approximation given by Brennen [12, Eq. (4.22)], but without the dc term:

$$\frac{R_{\max} - R_0}{R_0} = \sum_{n=0}^{N} |C_n|. \tag{6.7}$$

The purpose of Eq. (6.7) is to capture the features in Fig. 6.6 qualitatively. This is done for convenience to avoid the computational burden of searching for peaks in highly nonlinear waveforms at every frequency and amplitude of the drive. Solutions for C_n for frequencies in the range $0.005 \leq \omega/\omega_0 \leq 1.5$ were obtained to generate Fig. 6.7. It may be inferred that failure of the Newton-Raphson method might be an indicator of a jump in the solution.

134
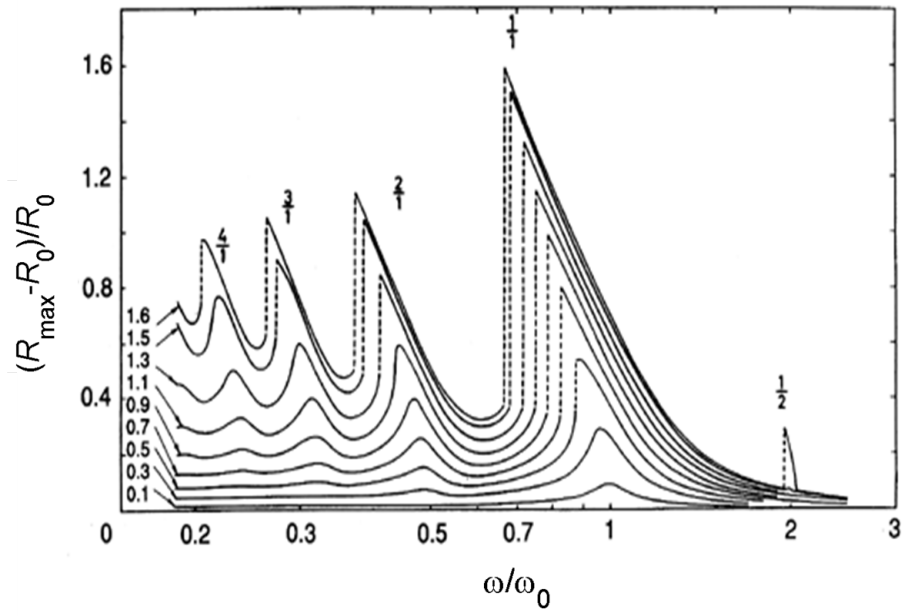
Figure 6.6: Frequency response of a bubble with $R_0 = 1$ μm in water at a mean ambient pressure of 1 bar. The amplitudes of the drive pressures (in bar) are labeled to the left of the curves. Adapted from Lauterborn [65].
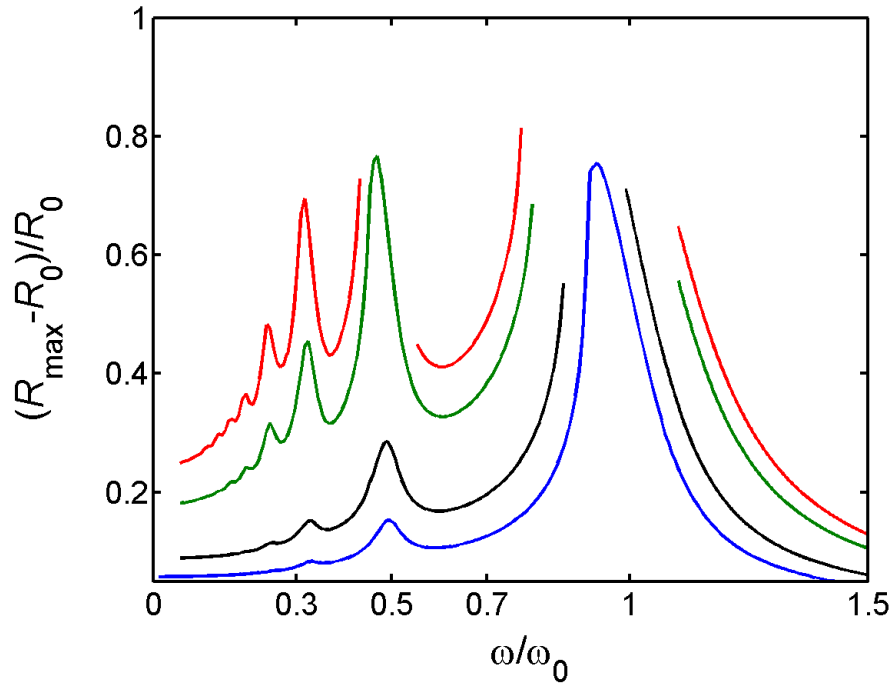
Figure 6.7: Frequency response of bubble radius. Blue curve: $p_0/P_0 = 0.21$. Black curves: $p_0/P_0 = 0.3$. Green curves: $p_0/P_0 = 0.5$. Red curves: $p_0/P_0 = 0.6$.

6.3 Subharmonics

Subharmonics are integer submultiples of the drive frequency, i.e., $\omega/2$, $\omega/3$, $\omega/4$, etc. To show the presence of subharmonics, spectral analysis of the Runge-Kutta solutions was performed for increasing drive amplitudes at drive frequency $\omega = \omega_0$. Figures 6.8 and 6.9 display the gradual increase of the subharmonic and its own harmonics. The plots show that at $p_0/P_0 = 1.67$ the subharmonic components become substantial, and for $p_0/P_0 > 1.8$ the subharmonic dominates the fundamental. Since no subharmonics are included in the hybrid method, the results from the two methods differ for high drive amplitudes. Table 6.1 provides the ratios of the amplitude of the subharmonic to that of the fundamental.

For the drive frequency $\omega = \omega_0$ we can see from Figs. 6.8 and 6.9 and Table 6.1 that the threshold for generation of subharmonics is $p_0/P_0 = 1.67$. As shown in Figs. 6.6 and 6.7 the resonance peaks lean to the left, and thus the thresholds for the subharmonics can be lower for drive frequencies around $\omega/\omega_0 = 0.88$.

To include subharmonics in the hybrid method, we rewrite the Fourier expansion as follows:

$$\frac{\xi(t)}{R_0} = C_0 + \frac{1}{2}\sum_{n=1}^{2N} C_n e^{jn\frac{1}{2}\omega t} + \text{c.c.} \tag{6.8}$$

For an example to examine the validity of the modified hybrid method, we take $\omega/\omega_0 = 2$ and $p_0/P_0 = 0.7$ and compare frequency spectra obtained from the Runge-Kutta method and the hybrid method. As is shown in Fig. 6.10, the two solutions are in excellent agreement. However, the modified hybrid method fails for most other
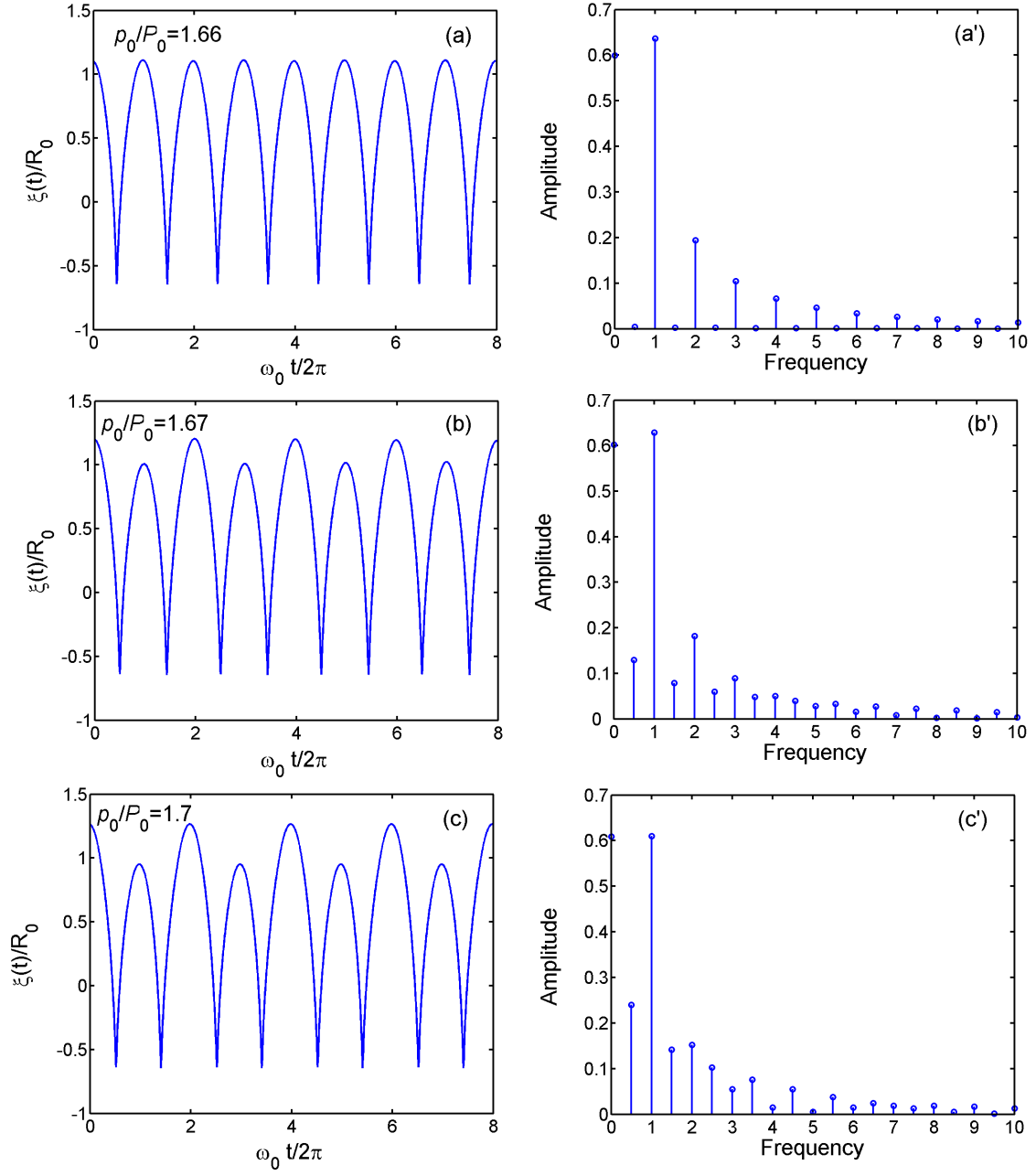
Figure 6.8: Time waveforms and frequency spectra obtained from Runge-Kutta solutions of Eq. (5.29) for different drive amplitudes with $\omega/\omega_0 = 1$. The drive amplitudes are $p_0/P_0 = 1.66, 1.67$ and 1.7. The viscosity parameter $Q_{\mathrm{vis}} = 10$ is included in the calculations.
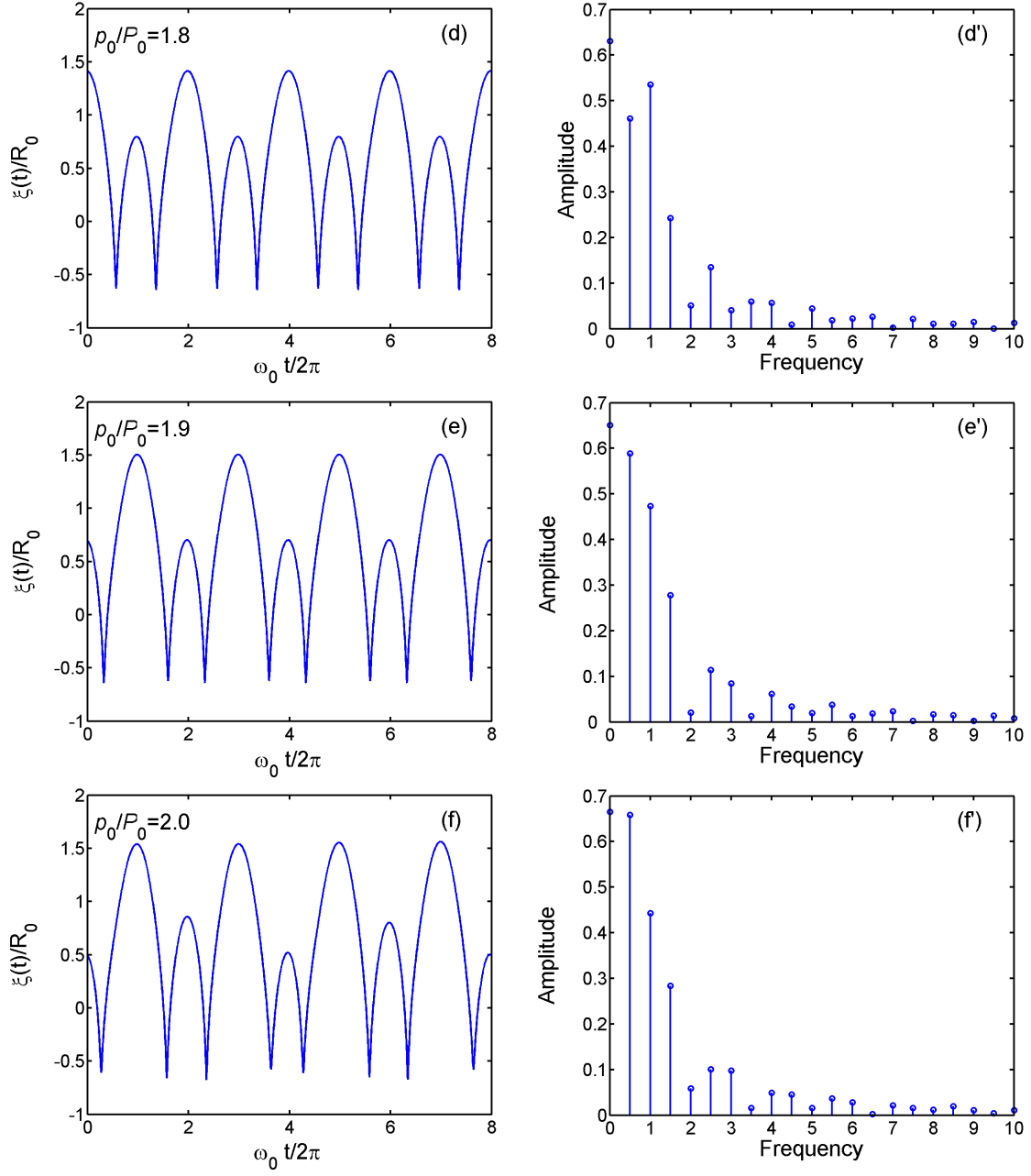
Figure 6.9: Continuation of Fig. 6.8, with $p_0/P_0 = 1.8, 1.9$ and 2.0.

p_0/P_0	$|C_{\frac{1}{2}}|/|C_1|$
1.60	1.9821×10^{-9}
1.65	4.0367×10^{-5}
1.66	0.0064
1.67	0.2053
1.68	0.2455
1.69	0.3275
1.7	0.3938
1.8	0.8616
1.9	1.2428
2.0	1.4860

Table 6.1: Values of the ratio $|C_{\frac{1}{2}}|/|C_1|$ for different drive amplitudes with drive frequency $\omega = \omega_0$.

drive frequencies. We were unable to solve this problem satisfactorily, and consequently we were restricted to acoustic drive amplitudes less than one atmosphere, but this still accommodates a reasonably large range of drive amplitudes. For example, it should be noted that $p_0 \sim P_0$ is the nominal cavitation threshold for a liquid. Therefore, in the following sections solutions are obtained using the hybrid method without subharmonics. As the threshold for generation of subharmonics for a bubble in confined channels is unknown, we seek solutions for fairly high drive amplitudes, i.e., $p_0/P_0 \sim 0.8$ for parallel plates and $p_0/P_0 \sim 1.1$ for tubes. The Newton-Raphson method used in the hybrid code fails to produce solutions for drive amplitudes above these two values.
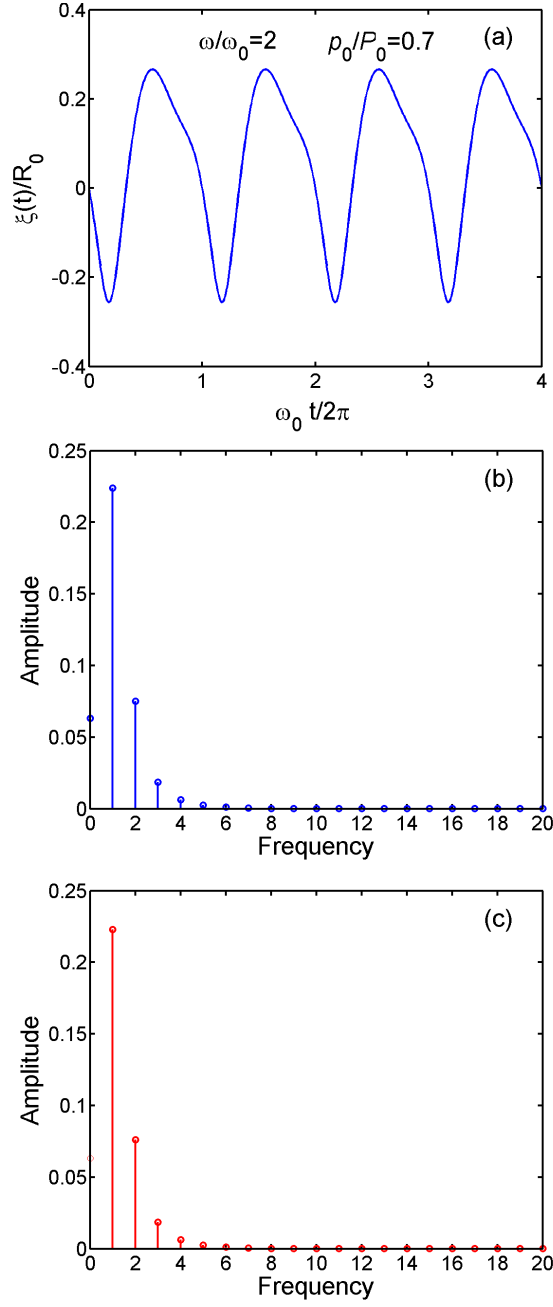
Figure 6.10: Comparison of the Runge-Kutta soluion and the hybrid solutions for drive frequency $\omega/\omega_0 = 2$ and drive pressure $p_0/P_0 = 0.7$. (a) Time waveform obtained using the Runge-Kutta method. (b) Spectrum obtained by taking an FFT of the time domain solution. (c) Spectral solution obtained using the hybrid method.

141

6.4   Bubble between Plates

In this section, solutions of Eq. (6.5) are presented for the time waveforms and the first five harmonics. The frequency responses are obtained numerically as outlined in Sec. 5.1.3.2. For low drive amplitudes the frequency responses are compared to the weakly nonlinear solutions obtained in the quadratic approximation in Chapter 5. Since for the weakly nonlinear regime we must have $p_0/P_0 \lesssim 0.05$, here we let $p_0/P_0 = 0.05$ and $Q_{\mathrm{vis}} = 10$. The drive frequency ranges up to $\omega/\omega_0 = 1.5$, and six values of plate separations are considered.

From Fig. 6.11 we can see that the two solutions agree quite well in general, especially for the fundamental and the second harmonic. Slight differences appear in the solutions for the third and higher harmonics. The good agreement of the two solutions first of all validates the hybrid method. Secondly, it also indicates that for low drive amplitudes, the weakly nonlinear approximation is appropriate.

Next, frequency responses for higher drive amplitudes are investigated. Four values of plate separations are considered. Figures 6.12–6.17 show the frequency response of the first five harmonics for four different plate separations. Higher drive amplitudes than what was indicated by Fig. 6.7 to be possible to model for unbounded liquid can be accommodated for bubbles in channels because the flow is constrained and the bubble oscillations are suppressed, e.g., $p_0/P_0 = 0.8$ in Fig.6.17(d). Therefore the narrower the channel, or the more constrained the flow (e.g., a bubble in a tube rather than between parallel plates), the higher the drive amplitude that can be used with the current version of the hybrid code.

Figure 6.11: Comparison of the fully-nonlinear solutions obtained using the hybrid method (solid lines) and the weakly-nonlinear solutions obtained in Chapter 5 using quadratic approximation (dashed lines) for the first five harmonics of a bubble between plates. The parameter values are $p_0/P_0 = 0.05$ and $Q_{\mathrm{vis}} = 10$.

The plots show that as the drive amplitude increases, the nonlinearity increases, as expected, causing the curves to move closer together. Also, as the drive amplitude increases, the resonance peaks become less pronounced. For narrow plate separations ($d/R_0 \leq 10$), for $p_0/P_0 \geq 0.6$ the harmonics display the strongest response in the region $0 < \omega/\omega_0 \leq 0.8$. To illustrate the progression of nonlinearity in the response (waveform distortion) with increase in drive amplitude, time waveforms at $\omega/\omega_0 = 0.5$ for $d/R_0 = 100$ and $\omega/\omega_0 = 0.3$ for $d/R_0 = 10$ are plotted in Figs. 6.13 and 6.16, corresponding to Figs. 6.12 and 6.15, respectively. As can be seen from Figs. 6.13 and 6.16, the oscillation of the bubble is rather violent for higher drive amplitudes.

6.5   Bubble in a Square Tube

In this section, the model equation for a bubble confined in a square tube is solved using the hybrid method. The solution procedure is similar to that for a bubble between plates, the only difference being that the summation in Eq. (2.16) has no closed-form solution in the frequency domain and must be calculated numerically. In the frequency domain this summation becomes $\sum_{l,m} e^{-jnkr_{lm}}/r_{lm}$, where r_{lm} is the distance between the bubble and an image with indices (l, m) and is given by Eq. (3.32). Substituting the negative of this summation for $\ln(1 - e^{jnkd})$ in Eq. (6.5)
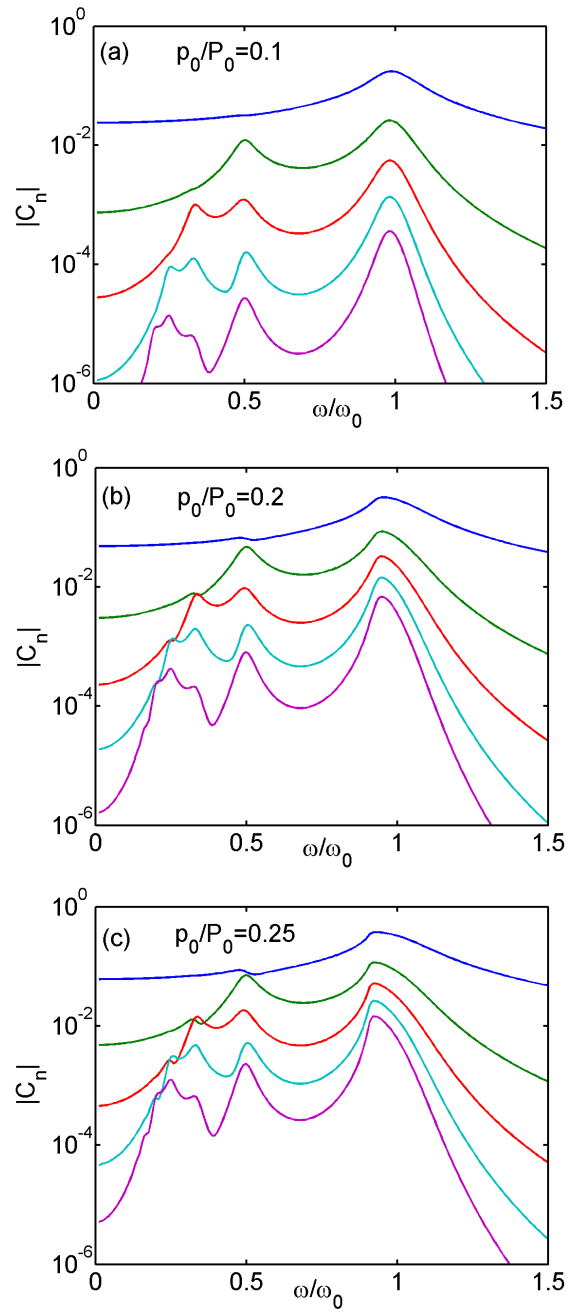
Figure 6.12: Harmonic frequency responses of a bubble centered between two rigid plates as functions of drive amplitude. The plate separation is $d/R_0 = 100$ and the viscosity parameter is $Q_{\mathrm{vis}} = 10$.
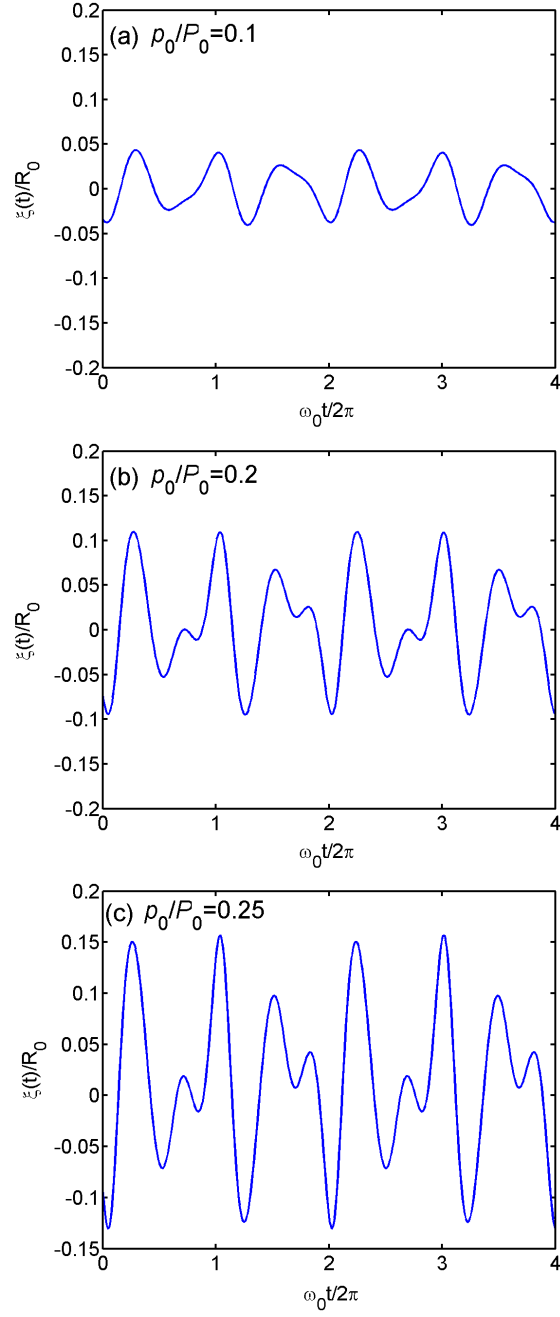
Figure 6.13: Corresponding time waveforms at $\omega/\omega_0 = 0.5$ for Fig. 6.12. The plate separation is $d/R_0 = 100$ and the viscosity parameter is $Q_{\mathrm{vis}} = 10$.

146
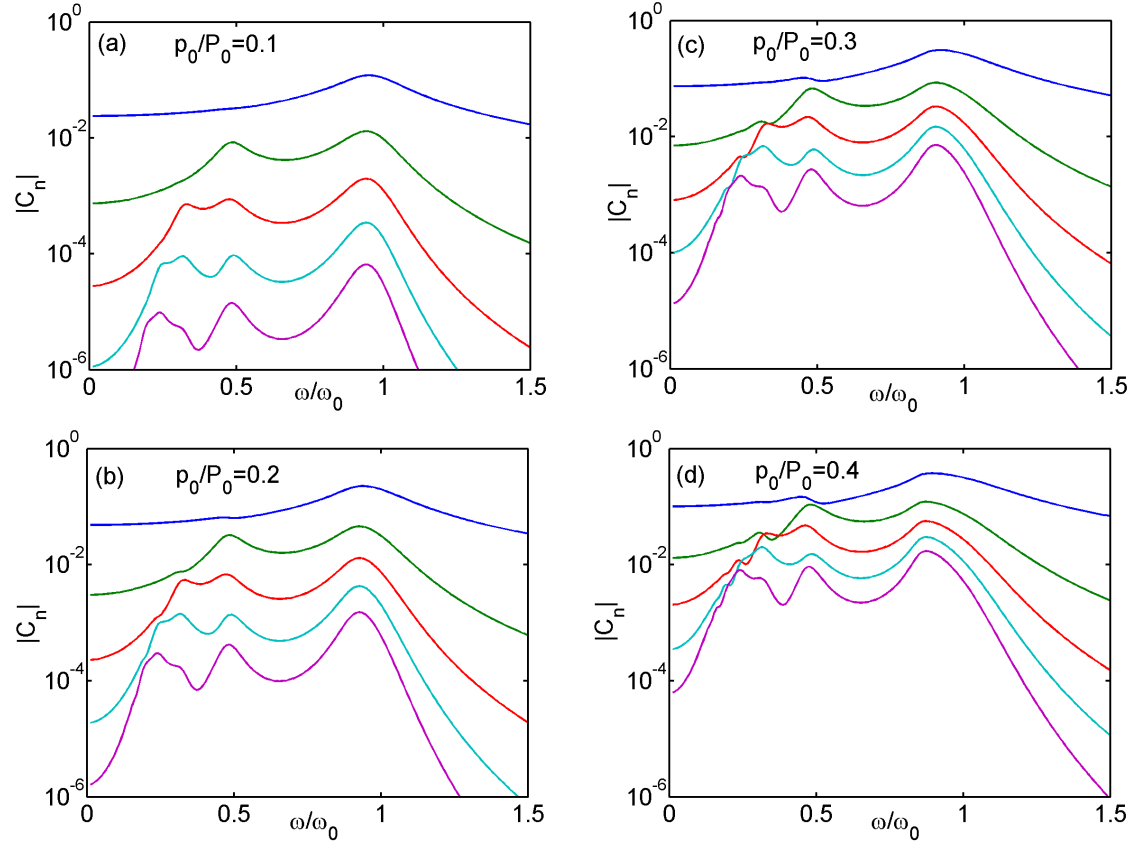
Figure 6.14: Harmonic frequency responses of a bubble centered between two rigid plates as functions of drive amplitude. The plates separation is $d/R_0 = 30$ and the viscosity parameter is $Q_{\mathrm{vis}} = 10$.
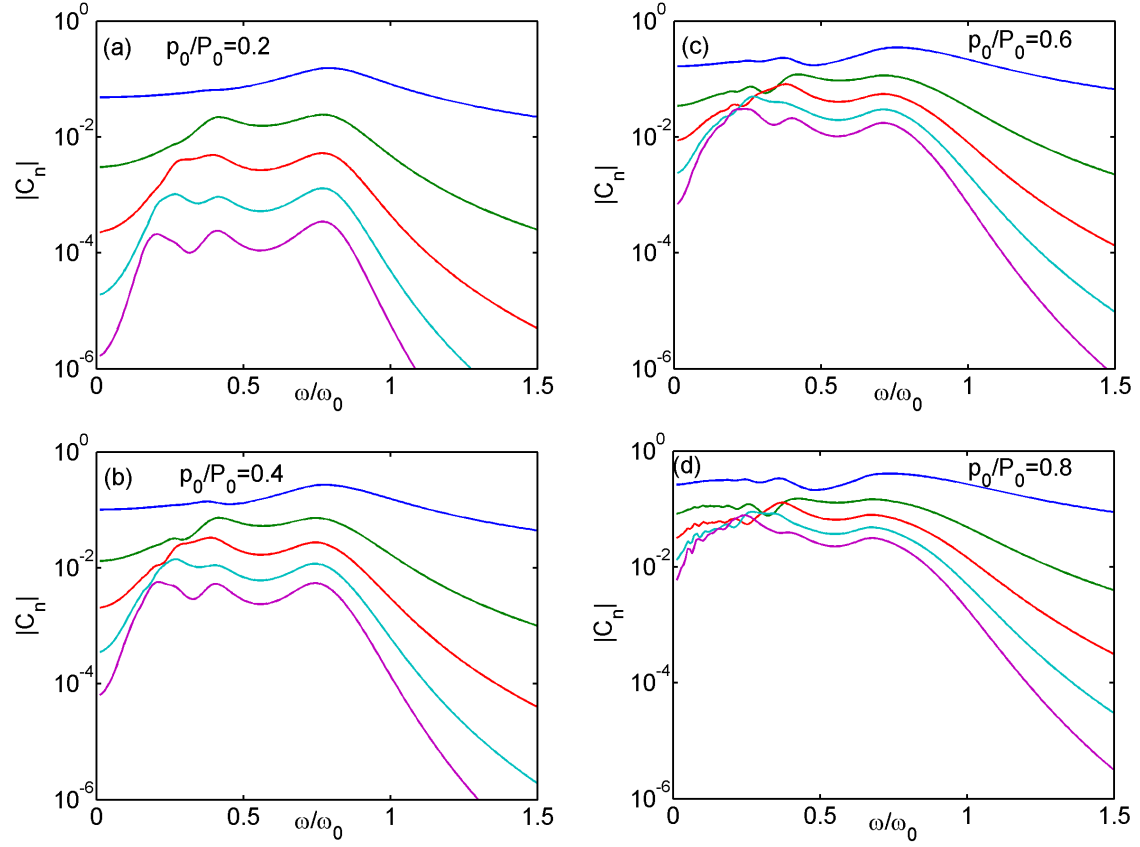
Figure 6.15: Harmonic frequency responses of a bubble centered between two rigid plates as functions of drive amplitude. The plate separation is $d/R_0 = 10$ and the viscosity parameter is $Q_{\mathrm{vis}} = 10$.
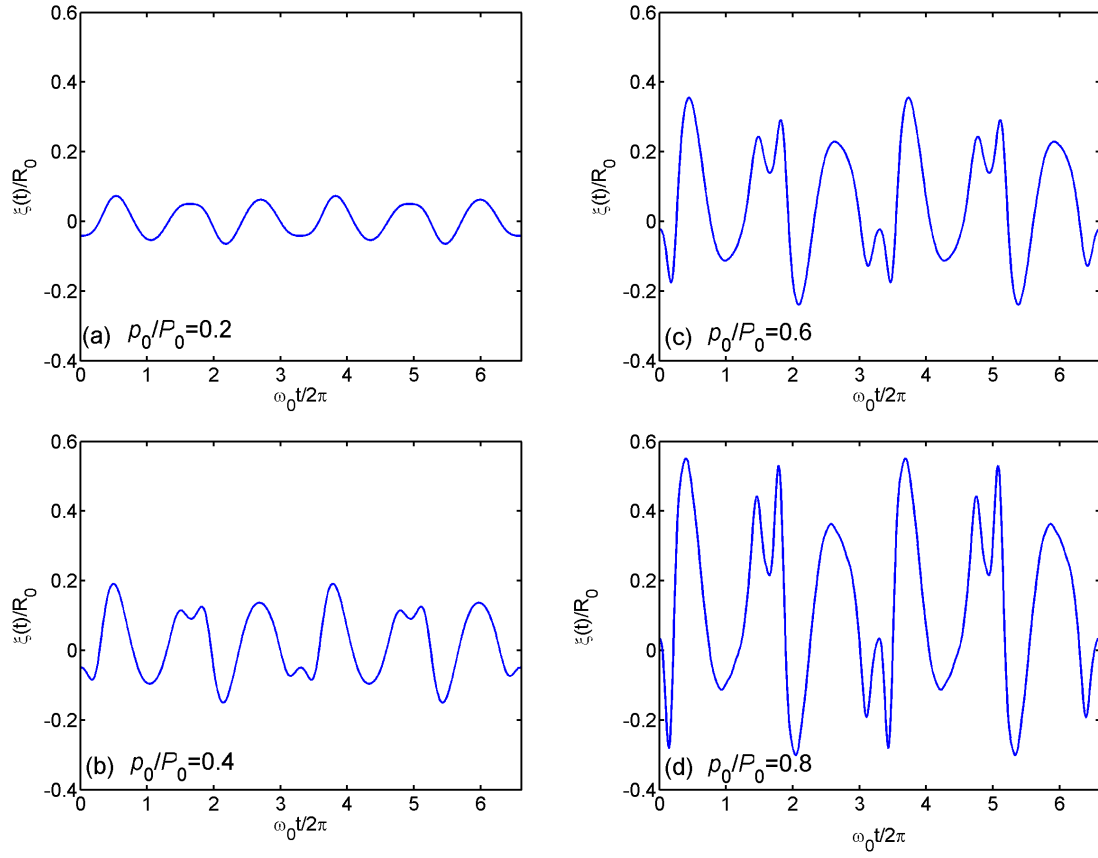
Figure 6.16: Corresponding time waveforms at $\omega/\omega_0 = 0.3$ for Fig. 6.15. The plate separation is $d/R_0 = 10$ and the viscosity parameter is $Q_{\text{vis}} = 10$.

149
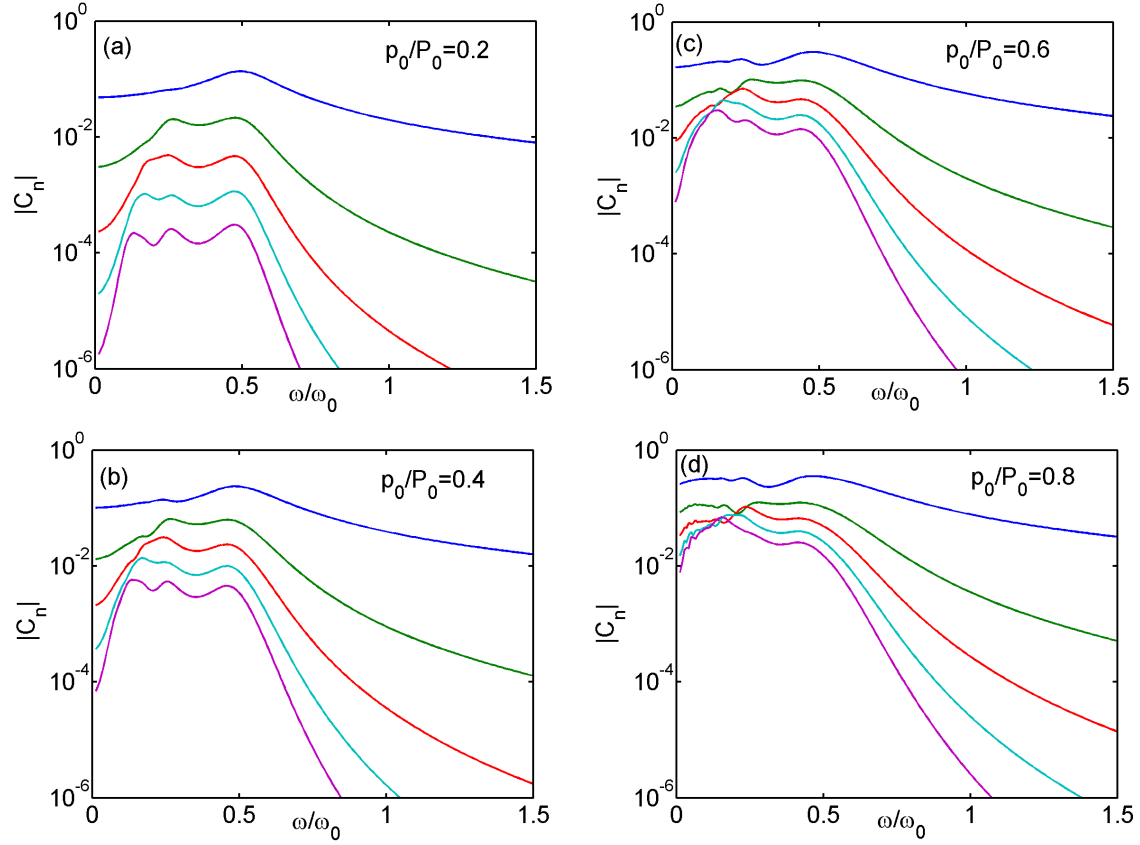
Figure 6.17: Harmonic frequency responses of a bubble centered between two rigid plates as functions of drive amplitude. The plate separation is $d/R_0 = 3$ and the viscosity parameter is $Q_{\mathrm{vis}} = 10$.

we obtain

$$\mathcal{F}_n\left\{R_0\left(1+\frac{\xi}{R_0}\right)\ddot{\xi}+\frac{3}{2}\dot{\xi}^2-\frac{1}{\rho_0}\left[P_0\left(1+\frac{\xi}{R_0}\right)^{-3\gamma}-P_0-p_{\mathrm{ac}}(t)\right]-\frac{\omega_0}{Q_{\mathrm{vis}}}R_0\dot{\xi}\right\}$$

$$=V_0\left[\frac{(jn\omega)^3}{4\pi c_0}-\frac{(jn\omega)^2}{4\pi}\sum_{l,m}\frac{e^{-jnkr_{lm}}}{r_{lm}}\right]\mathcal{F}_n\left[\left(1+\frac{\xi}{R_0}\right)^3\right]. \quad (6.9)$$

Alternatively, Eq. (6.9) can be obtained by substituting Eq. (4.13), with k replaced everywhere by nk, into Eq. (6.6).

The frequency responses for the first five harmonics are presented in Fig. 6.18. First we keep the drive amplitude low, $p_0/P_0 = 0.05$, and the fully-nonlinear solutions are compared to the weakly-nonlinear solutions. Shown in Fig. 6.18 are comparisons for the four tube sizes $a/R_0 = 100,\ 50,\ 30,\ 20$, where a is the length of a side of the square. From Fig. 6.18 we can see that we again obtain good agreement for the two solutions. Next, solutions for higher drive amplitudes are sought.

Figures 6.19–6.25 are frequency responses of a bubble in a square tube with five different cross-sectional areas, and the acoustic drive amplitude ranges from $p_0/P_0 = 0.1$ to $p_0/P_0 = 1.1$. For tubes with fairly large cross-sectional areas, $a/R_0 \geq 30$, the responses of the harmonics display similar trends as observed for parallel plates, the nonlinearity in the response dominates as the drive pressure gets high. For tubes of smaller cross-sectional areas ($a/R_0 \leq 20$), the responses of the harmonics are highly damped, which is consistent with observations from the quadratic nonlinear solutions. As was done for parallel plates, time waveforms at $\omega/\omega_0 = 0.5$ for $a/R_0 = 100$ and $\omega/\omega_0 = 0.3$ for $a/R_0 = 30$ are plotted in Figs. 6.20 and 6.23, corresponding to Figs. 6.19 and 6.22, respectively. From both the frequency responses
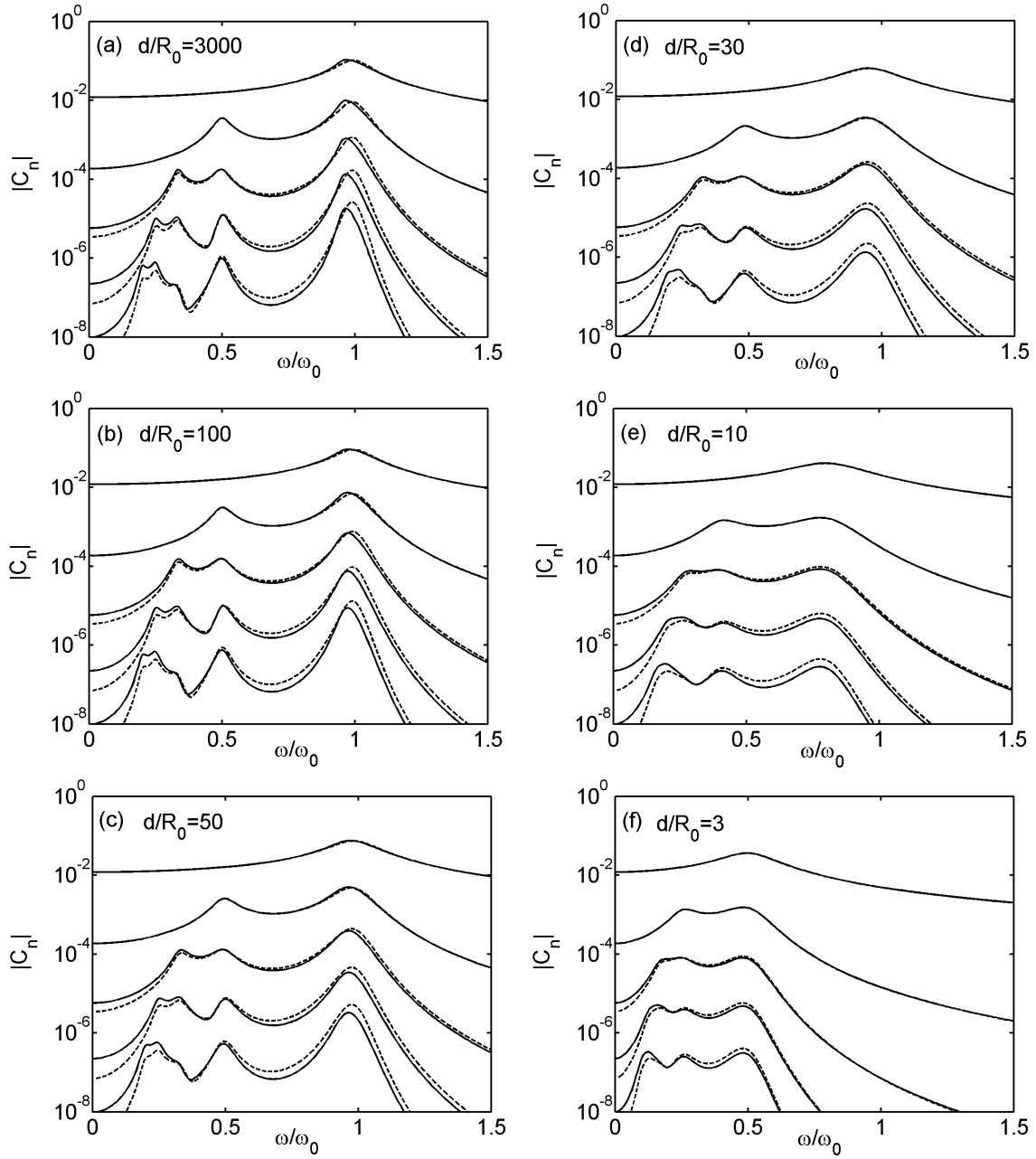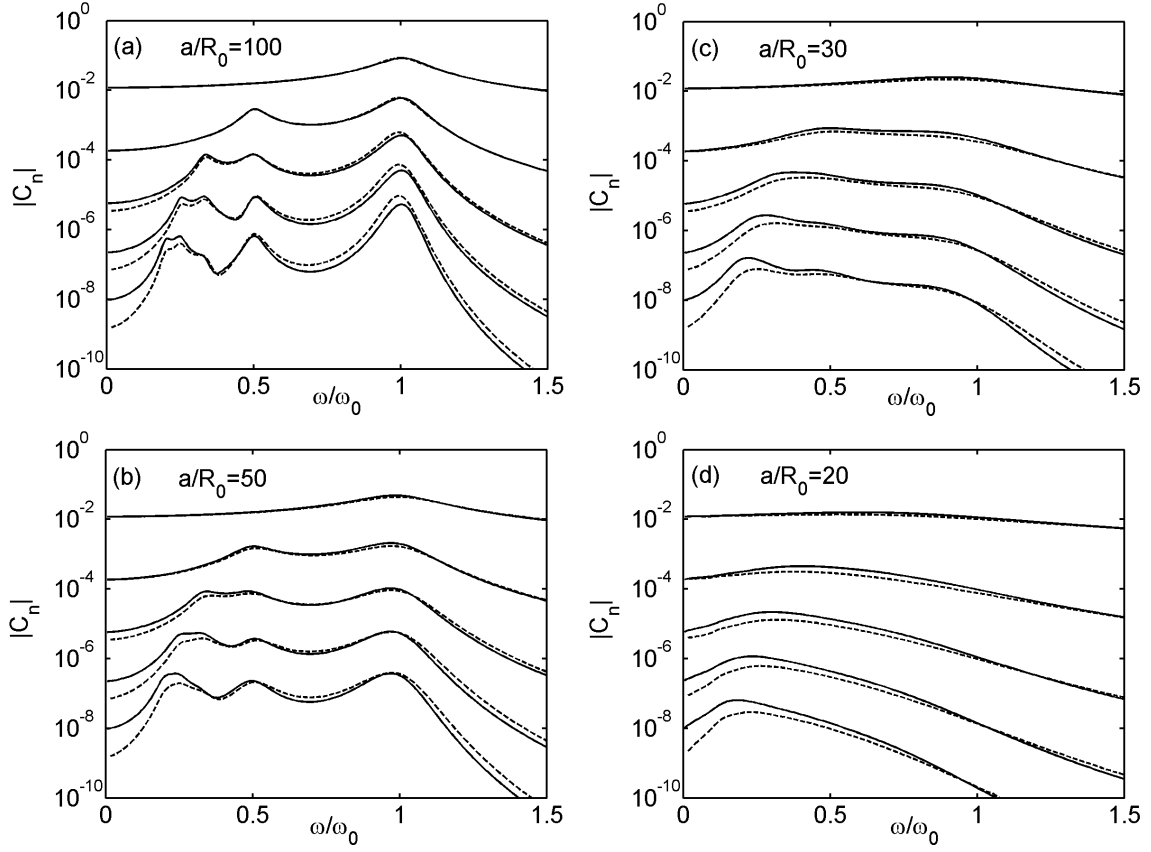
Figure 6.18: Comparison of the fully-nonlinear solutions obtained using the hybrid method (dashed lines) and the weakly-nonlinear solutions obtained in Chapter 5 using quadratic approximation (solid lines) for the first five harmonics of a bubble in a square duct. The parameter values are $p_0/P_0 = 0.05$ and $Q_{\mathrm{vis}} = 10$.
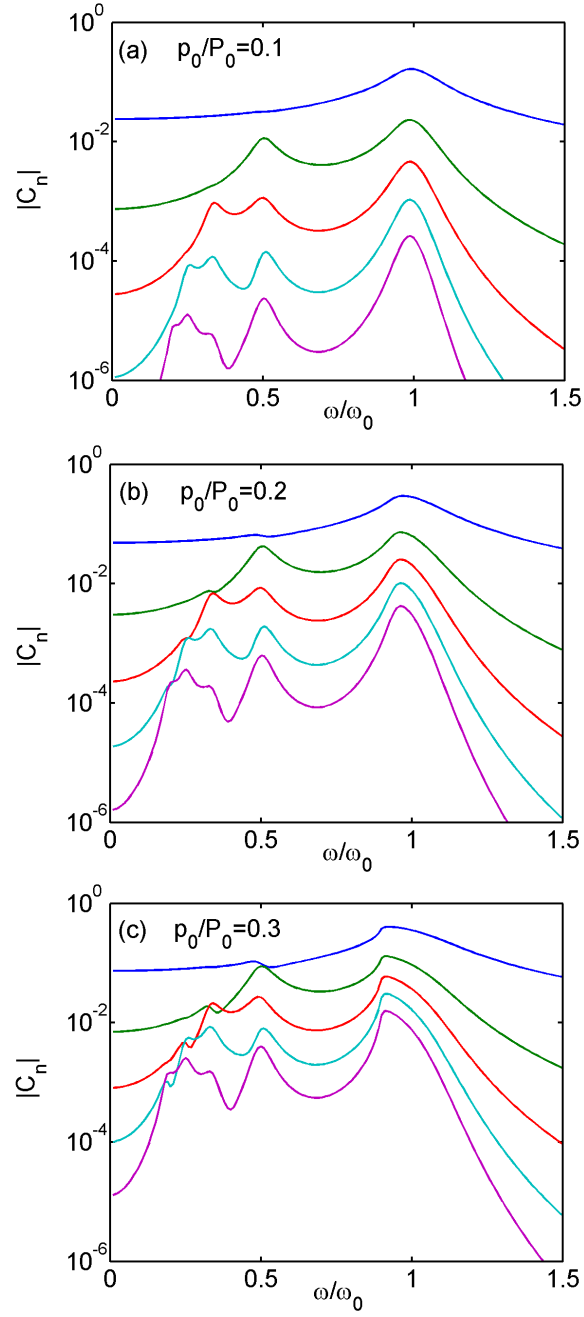
Figure 6.19: Harmonic frequency responses of a bubble centered in a square rigid tube as functions of drive amplitude. The parameter values are $a/R_0 = 100$ and $Q_{\mathrm{vis}} = 10$.
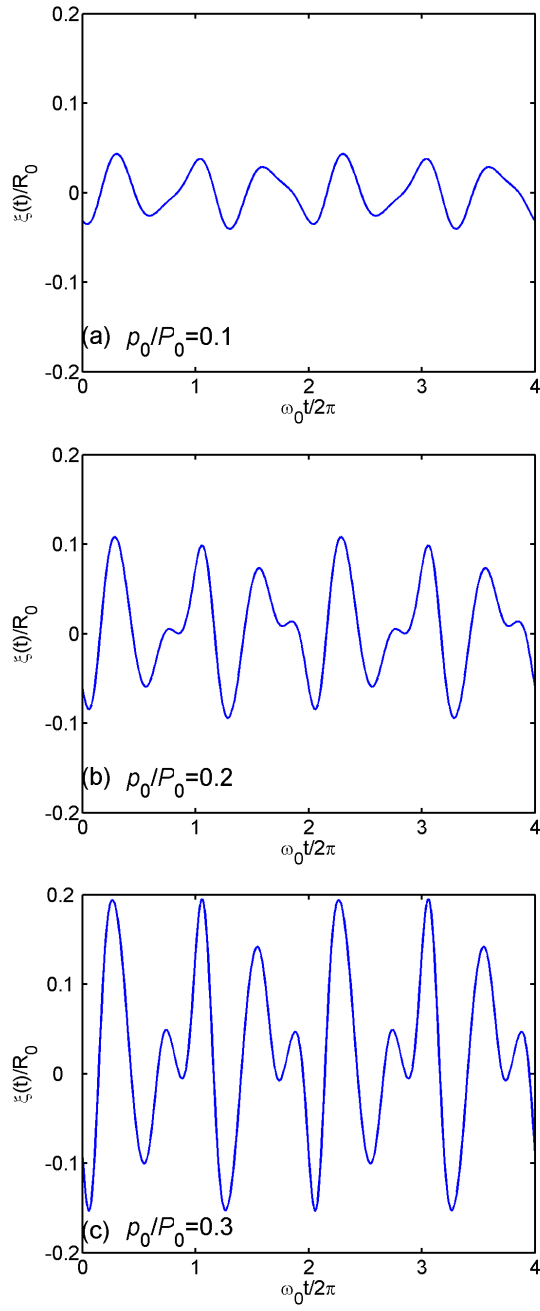
Figure 6.20: Corresponding time waveforms at $\omega/\omega_0 = 0.5$ for Fig. 6.19. The parameter values are $a/R_0 = 100$ and $Q_{\text{vis}} = 10$.

154
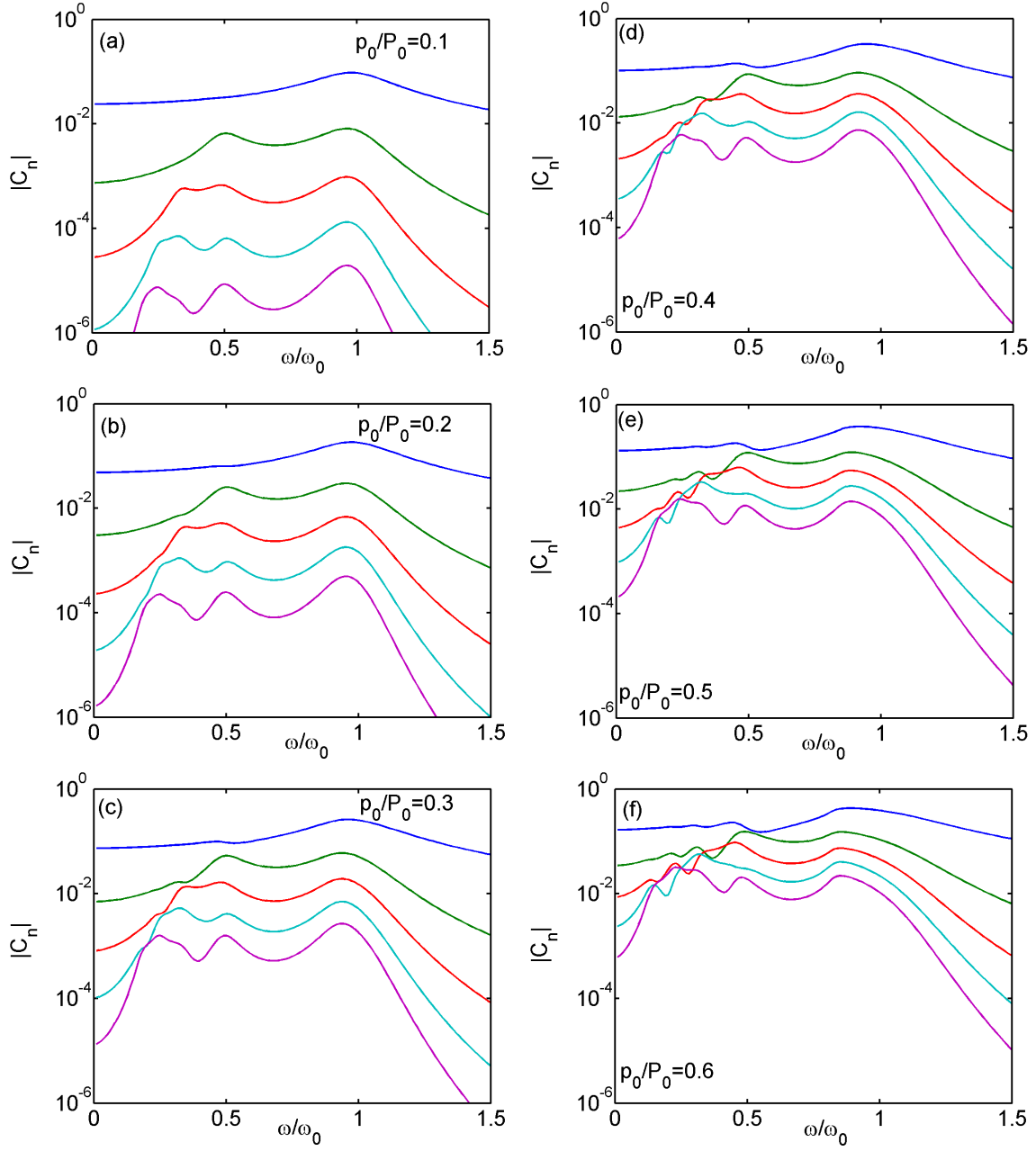
Figure 6.21: Harmonic frequency responses of a bubble centered in a square rigid tube as functions of drive amplitude. The parameter values are $a/R_0 = 50$ and $Q_{\text{vis}} = 10$.
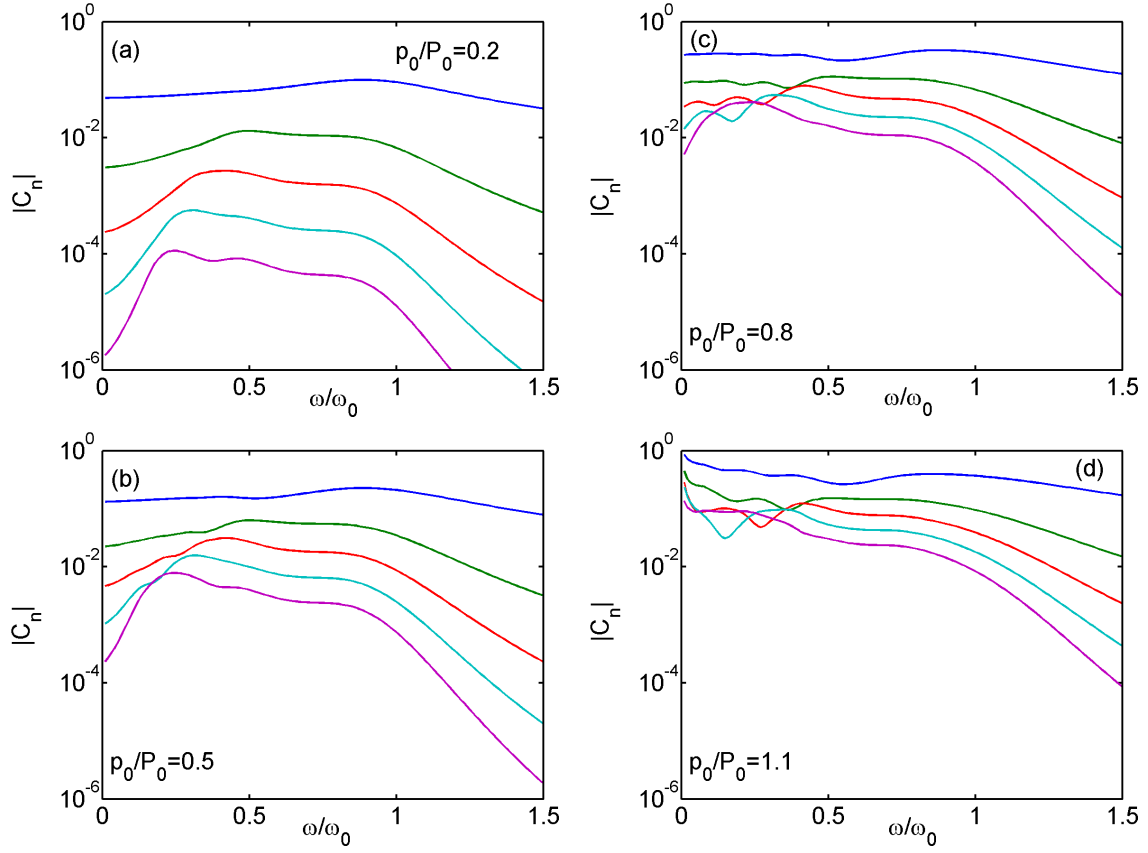
Figure 6.22: Harmonic frequency responses of a bubble centered in a square rigid tube as functions of drive amplitude. The parameter values are $a/R_0 = 30$ and $Q_{\mathrm{vis}} = 10$.
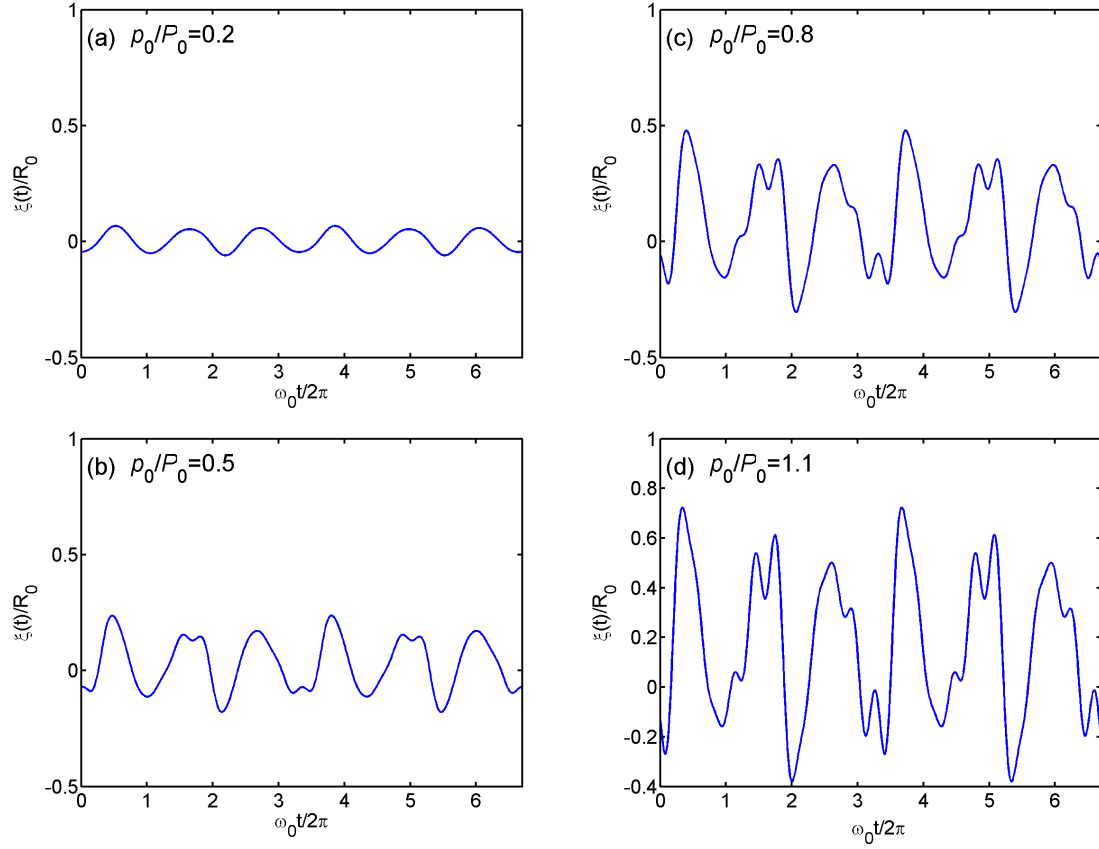
Figure 6.23: Corresponding time waveforms at $\omega/\omega_0 = 0.3$ for Fig. 6.22. The parameter values are $a/R_0 = 30$ and $Q_{\mathrm{vis}} = 10$.
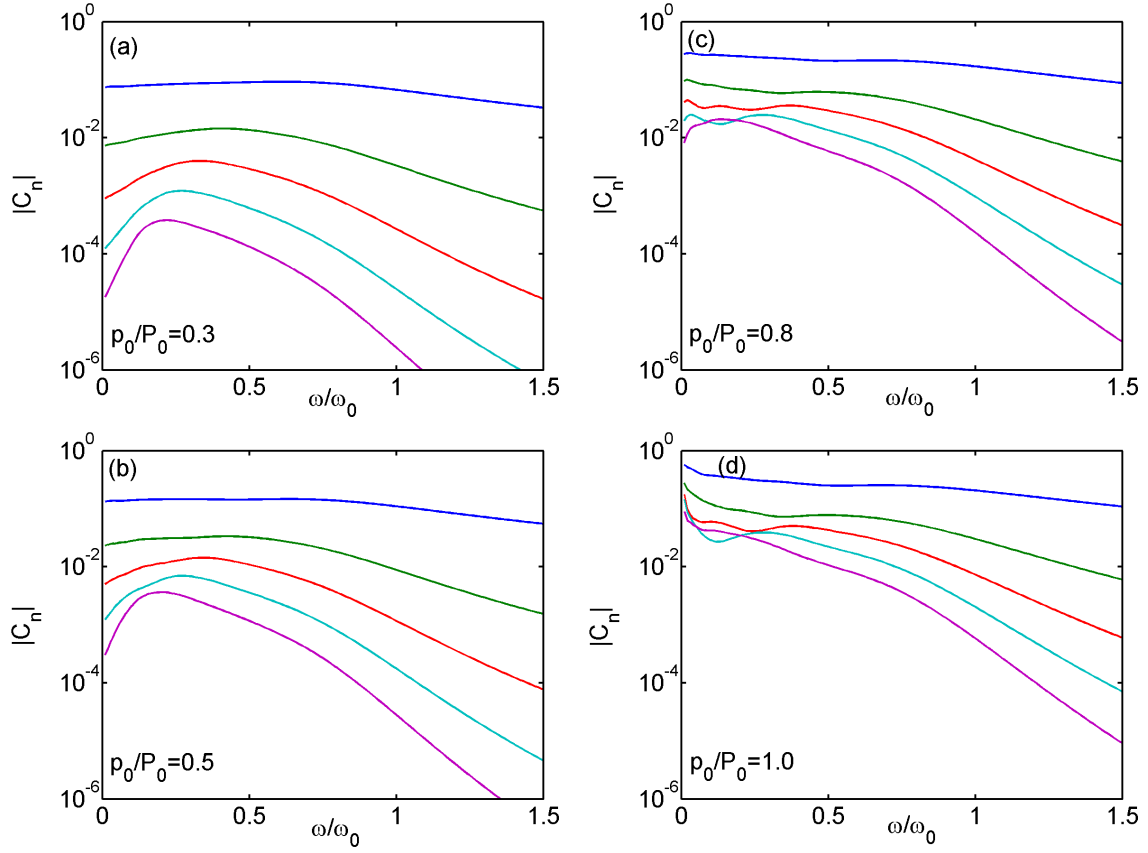
Figure 6.24: Harmonic frequency responses of a bubble centered in a square rigid tube as functions of drive amplitude. The parameter values are $a/R_0 = 20$ and $Q_{\text{vis}} = 10$.
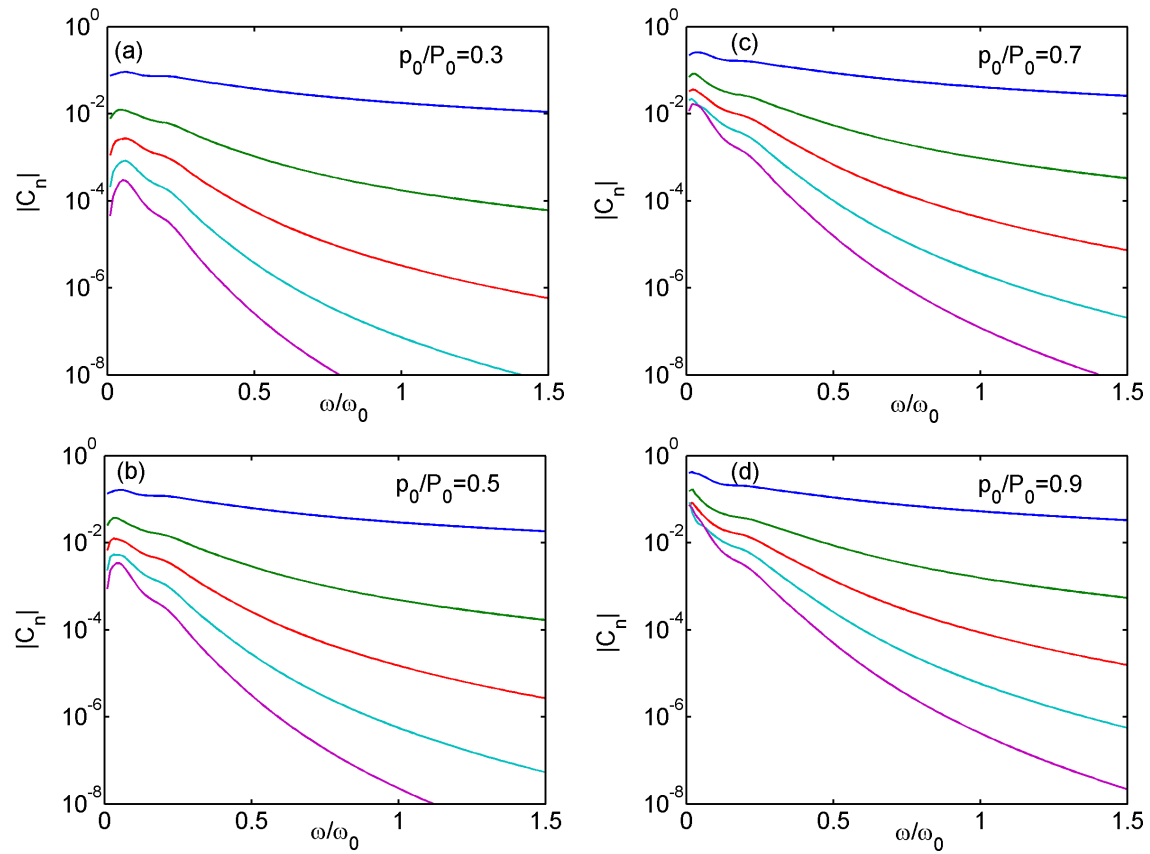
Figure 6.25: Harmonic frequency responses of a bubble centered in a square rigid tube as functions of drive amplitude. The parameter values are $a/R_0 = 10$ and $Q_{\mathrm{vis}} = 10$.

and the time waveforms, we note that the response of a bubble in a wide channel $(d/R_0 = 100)$ formed by two rigid parallel plates and in a wide rigid tube $(a/R_0 = 100)$ are very similar. Quantitatively, the response of bubble between plates with a separation $d/R_0 = 10$ is comparable to the response of a bubble in a tube with $a/R_0 = 30$. The responses of a bubble in channels for higher drive amplitudes (larger than half an atmosphere) are characterized by violent oscillations and rebounds. As the current solutions are obtained without including subharmonics (due to the fact that the threshold for subharmonic generation for a bubble in channels is unknown and the computer program including subharmonics does not work properly), we should be aware of the possibility that subharmonics could be generated in the responses for higher drive amplitudes (larger than half an atmosphere).

Chapter 7

Conclusion and Future Work

This dissertation covered a wide range of topics regarding the dynamics of a bubble in water-filled channels formed by parallel plates and tubes. A review of the literature showed that most mathematical models of a bubble in a confined region are numerical, and a frequently-used approximate analytical model is that of a short tube with rigid walls filled with an incompressible liquid. In the present work, analytical models that include liquid compressibility were derived. Linear and nonlinear responses of a bubble between parallel plates and in tubes of triangular, square, rectangle, and hexagonal cross sections were investigated. Radiation impedences of a bubble between plates and in rectangular or square tubes were also derived.

In Chapter 2, the equations of bubble dynamics that formed the basis for our models of a confined bubble were presented. The starting point was the Rayleigh-Plesset equation, which descibes the motion of the wall of a spherical bubble in an unbounded incompressible liquid. The Rayleigh-Plesset equation was modified to account for liquid compressibility in the manner of Ilinskii and Zabolotskaya [57] by including a term in bubble volume for radiation damping. The result was shown to be equivalent to an equation developed by Prosperetti [58] and also equivalent to the Keller-Miksis equation [59] at $O(1/c_0)$. When a bubble is part of a cluster

of bubbles, the radiation pressure from each neighboring bubble impinges upon it. This was accounted for in the manner of Hamilton et al. [52, Eq. (2)] by modeling each neighboring bubble as a monopole acoustic source at an arbitrary position, which yields an additional term in the Rayleigh-Plesset equation for each neighboring bubble. The same is done for all the bubbles in the cluster, and the result is a set of coupled equations describing the dynamics of every bubble in the cluster. A single bubble in a channel can be modeled using the cluster approach by invoking the method of images to satisfy the boundary conditions on the channel walls. Thus, the channel walls were replaced by an infinite series of image bubbles. For a bubble between infinite parallel plates, the image bubbles form an infinite line array. For a bubble in a tube of triangular, rectangular, square or hexagonal cross-section, an infinite planar array is formed. Model equations for each of these cases were derived from the bubble cluster model.

In Chapter 3, the model equations were solved in the linear approximation and the frequency response was obtained. For parallel plates, explicit expressions were derived for the frequency response, the resonance frequency, and the quality factor. For tubes of triangular, square, and hexagonal cross-sections, the frequency responses were found to be almost identical when the cross-sectional areas are the same. Both rigid and pressure release boundary conditions were investigated for parallel plates and a square tube. The rigid plates alter the ideal radial expansion of flow that occurs in an unbounded liquid, and thus the effective fluid inertia increases and the resonance frequency decreases as the plate separation decreases. On the other hand, the pressure release plates provide the least impedance to the liquid, and thus as the

162

plate separation decreases, less liquid is in motion, the effective fluid inertia decreases, and the resonance frequency increases. Finite wall impedance was considered for plates when $kd \gg 1$, or $d \gtrsim \lambda$. Off-center bubble positions were found to have little effect on the overall bubble dynamics. An approximate analytical expression for the frequency response of a bubble centered in a rigid square tube was derived. Frequency responses of a bubble confined in square and cylindrical tubes with equal cross-sectional areas and pressure release walls are compared, and the results agreed quite well.

Chapter 4 began with the derivation of the radiation impedance of a bubble between plates and in a square tube based on the method of images. The radiation resistance and reactance of a bubble centered or off-centered between plates and in tubes were compared to the corresponding values in a free field. The comparision again revealed that the radiation reactance for a bubble between rigid plates was larger than the value in a free field, and thus the resonance frequency is reduced in comparison to its free field value. The radiation resistance in the presence of rigid plates was larger than that in a free field, so the damping was increased. Constant radiation resistance was observed for a bubble in rigid tubes for $ka \leq \pi$. This is because radiation couples with the plane wave mode. As expected, cases which yielded high radiation resistance were found to correspond with highly damped regimes of the frequency response. Finally, the fundamental physical difference between confinement by plates and by tubes was determined. The dynamics of a bubble is mass controlled when confined between plates and resistance controlled when in a tube. The second part of Chapter 4 was devoted to a comparison of the radiation impedance obtained

for square and rectangular tubes by the method of images to that obtained by the normal mode expansion of Morse and Ingard [2], and excellent agreement was found.

In Chapter 5, a methodology was developed to solve the model equations in the quadratic approximation for the weakly nonlinear regime and solutions were obtained. The chapter began with a derivation of the model equation for plates at quadratic order, then the equation was solved in the frequency domain. Initially, analytical solutions were obtained for the fundamental, the second harmonic and the dc component. Finally, a full spectrum solution was obtained in the form of coupled equations of the harmonic amplitudes, which were generalized to channels with arbitrary cross-sections and wall impedance. A Newton-Raphson iteration method was used to solve the coupled spectral equations. To verify the validity of this solution method, the terms accounting for plate reflections and the radiation damping were eliminated and the results were compared to time domain solutions obtained with a Runge-Kutta method. The two results agreed quite well. Time waveforms were used to determine the range of drive amplitudes in which the quadratic approximation is valid, i.e. $|\xi|/R_0 \lesssim 0.1$, which sets the upper bound for the drive amplitude, $p_0/P_0 \leq 0.05$. Next, the frequency responses for a bubble between rigid plates and in a rigid tube were obtained and the first five harmonics plus the dc component were plotted. The weakly nonlinear response of the bubble was found to be similar to the linear response in that the cross-sectional area of the duct, not its cross-sectional geometry, primarily determines the dynamic response.

In Chapter 6, the model equations were solved with their full nonlinearity. A hybrid time-frequency domain method was developed specially for this case. The

164

chapter began with an overview of the method, followed by comparison of solutions of the Rayleigh-Plesset equaton obtained with this method and with the Runge-Kutta method. For $p_0/P_0 \simeq 1.5$ and at drive frequency $\omega = \omega_0$, only harmonics of the drive frequency were included in the hybrid method and the two solutions were in excellent agreement. For $p_0/P_0 \geq 1.7$ we observed poor agreement between the two methods. This was due to the omission of the subharmonics of the drive frequency in the hybrid method. It was found that for drive frequency $\omega = \omega_0$, the threshold for subharmonics was $p_0/P_0 \geq 1.67$. With subharmonics included we again obtained excellent agreement between the two methods. We studied the same cases reported in the previous chapters using the hybrid method for drive levels above the weakly nonlinear regime, but below the threshold for the generation of subharmonics. No qualitatively different results were observed in this fully-nonliniear regime.

Appendix A provides detailed accounts of the image counting strategy that was developed for triangular, rectangular, and hexagonal tubes. In Appendix B, the Newton-Raphson method was briefly reviewed. In Appendix C, detailed derivations of the analytical solutions for the second harmonic and the dc component, and for the coupled nonlinear equations for the harmonic amplitudes, were presented, as well as the derivation of the Jacobian.

Three aspects of this work should be carried forward. One is to perform a systematic parametric study of cylindrical tubes with arbitrary wall impedances using the generalized solutions provided in Chapters 5 and 6. The second possibility is to study bubbles of arbitrary shape by using spherical harmonic expansions. Finally, future experimental work should be focused on varifying the models and results

165

presented here.

Appendices

Appendix A

Image Counting Strategies

For harmonic motion, the summation in Eq. (3.1) can be expressed in closed form for a bubble centered between two parallel plates, as in Eq. (3.6). If the bubble is off-center, the symmetry in the image array is lost and an image counting strategy is needed to perform the summation. Also, no analytical expression is available for the summation in Eq. (3.26) for a bubble in a tube, and a strategy is needed to index those images. In this appendix the strategies for counting images will be discussed, first for a bubble located off-center between two parallel plates, then for a bubble in the center of a rectangular (or square), triangular, or hexagonal tube. For simplicity, only linear equations of motion are considered in this appendix, but the same approaches are used for the nonlinear equation of motion given by Eq. (5.35).

A.1 Bubble Off-Center between Parallel Plates

Without the symmetry for a centered bubble, Eq. (3.1) takes the form

$$\ddot{\xi}(t) + \omega_0^2 \xi(t) = \frac{R_0}{c_0} \dddot{\xi}(t) - R_0 \sum_m \frac{1}{d_m} \ddot{\xi}(t - d_m/c_0) - \frac{p_{\mathrm{ac}}(t)}{\rho_0 R_0} , \qquad (A.1)$$

and Eq. (3.3) becomes

$$\left[1 - \left(1 + R_0 \sum_m \frac{e^{-jkd_m}}{d_m} \right) \frac{\omega^2}{\omega_0^2} + jk_0 R_0 \frac{\omega^3}{\omega_0^3} \right] \Xi(\omega) = -\frac{p_1}{3\gamma P_0} . \qquad (A.2)$$

168

Figure A.1 shows the array of images. The black circle is the bubble and the rest
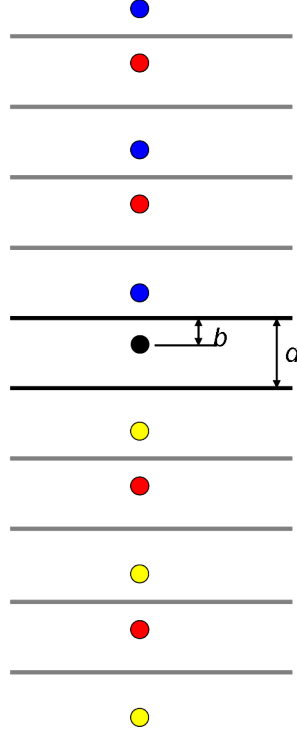
Figure A.1: Array of images for a bubble located off center between two parallel rigid plates. Black circle is the bubble, and colored circles are images.

are its images. Since no general symmetry is found in the images, they are grouped into three categories, designated by the colors red, blue and yellow, to facilitate the calculation of their distances from the bubble. The red group is symmetric about the bubble and extends infinitely in both directions, while the blue and yellow groups each form an infinite line array, one extending in one direction away from the bubble, and the other extending in the opposite direction. The distance from any image to

169

the bubble is given as follows:

$$
\left.\begin{array}{lll}
d_m^{\text{red}} = 2md, & \text{red} \\
d_m^{\text{blu}} = 2(d-b) + 2(m-1)d, & \text{blue} \\
d_m^{\text{yel}} = 2b + 2(m-1)d, & \text{yellow}
\end{array}\right\}. \tag{A.3}
$$

The superscripts indicate the colors of the images. There is no closed form for the summations, and instead we have

$$
\sum_{m=-\infty}^{\infty} \frac{e^{-jkd_m}}{d_m} = \sum_m \left(2\frac{e^{-jkd_m^{\text{red}}}}{d_m^{\text{red}}} + \frac{e^{-jkd_m^{\text{blue}}}}{d_m^{\text{blu}}} + \frac{e^{-jkd_m^{\text{yel}}}}{d_m^{\text{yel}}} \right). \tag{A.4}
$$

The coefficient 2 in front of the red image series accounts for the doubly infinite arrays in both the up and down directions. Substituting Eq. (A.3) in Eq. (A.4), we obtain

$$
\sum_{m=1}^{\infty} \frac{e^{-jkd_m}}{d_m} = \frac{1}{2d} \sum_{m=1}^{\infty} \left(\frac{2}{m} + \frac{e^{j2kb}}{m - b/d} + \frac{e^{j2k(d-b)}}{m - 1 + b/d} \right) e^{-j2mkd}. \tag{A.5}
$$

Equation (A.5) was used to obtain Eq. (3.18).

A.2 Rectangular Tube

The indexing for the images of a bubble in a rectangular (or square) tube is straightforward. The index for each row is l and the index for each column is m, with $l = m = 0$ for the cell where the bubble resides, as shown in Fig. A.2. As indicated, l increases or decreases by one for every row going upward or downward; m increases or decreases by one every column going right or left. The distance between an image and the bubble is then given in Eq. (3.32). The 4-fold symmetry is used to divide the grid into 4 regions. The highlighted region in Fig. A.2 is one of these 4 regions. Thus the summation over all the images can be written as

$$
4 \sum_{l=0}^{\infty} \sum_{m=1}^{\infty} \frac{e^{-j(l^2+m^2)^{1/2}ka}}{(l^2+m^2)^{1/2}} \tag{A.6}
$$

for a square tube.
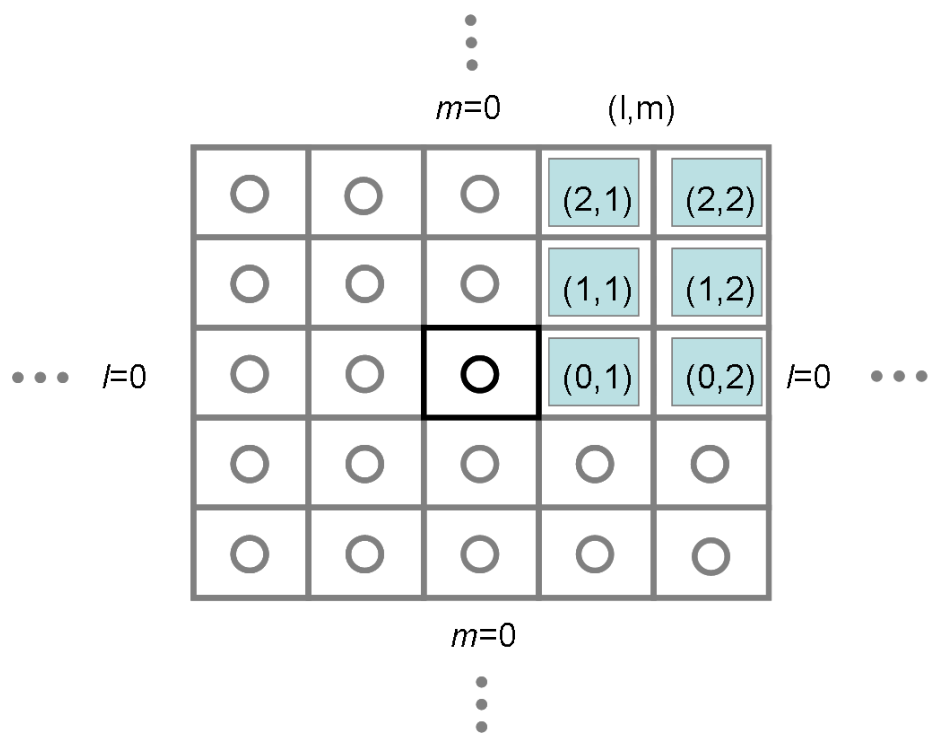
Figure A.2: Grid for images of a bubble centered in a rectangular (or square) tube showing indexing in one quadrant of the 4-fold symmetry.

A.3 Triangular Tube

Figure A.3 shows the infinite plane array of images of a bubble in the center of a triangular tube. Three symmetric regions are identified, the boundary of each highlighted by the red, blue and yellow images. We only need to sum over the images in one of the three regions, the result of which is multiplied by 3 to obtain the total contribution from the entire plane. Figure A.4 shows the details of the indexing scheme developed for one of the regions. The images are color coded by row in red, green, blue, and brown. The pattern repeats itself every four rows and every two columns. The rows are indexed by the integers l and l' and the columns by m. Starting from the row including the black bubble going upwards, l increases by one for every four rows (including the group of red, green, blue and brown rows). In other words, the first red, green, blue, and brown rows all have a same index $l = 1$, the second red, green, blue, and brown rows all have a same index $l = 2$, and so on. From the line including the bubble going downwards, a triangular region is formed. The rows for the triangular region are indexed by l', and l' increases by one downwards for every four rows. Starting from the column including the bubble going right, every two columns share the same index m. So for the first two columns they have the same index $m = 1$, then the next two columns have $m = 2$, and so on. Given the indices l

172
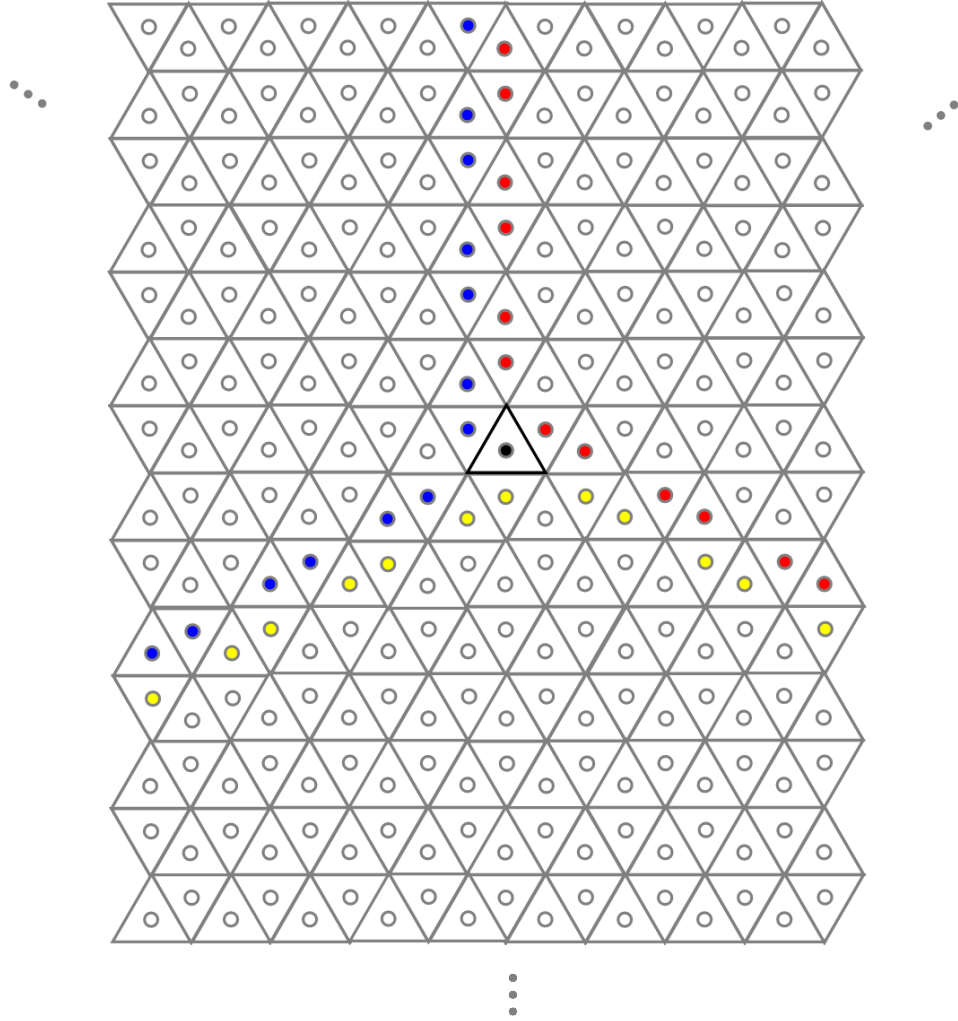
Figure A.3: Plane array of images for a bubble in a triangular tube. A 3-fold symmetry is used to group the images.

173
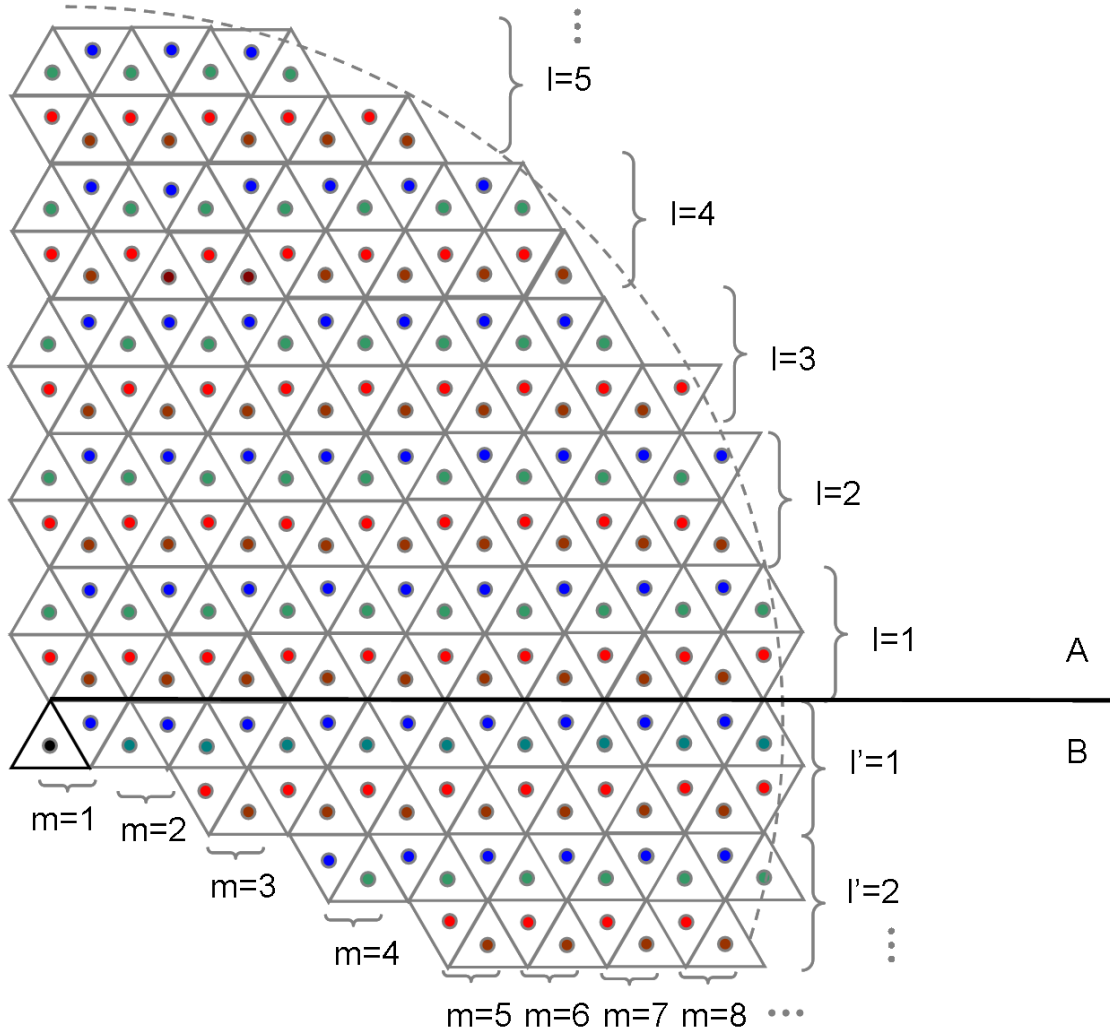
Figure A.4: Details of the indexing strategy for a triangular tube.

and m, we calculated the distance d_{lm} as follows. For region A

$$d_{lm}^{\text{red}} = \left(3l^2 - 2l + m^2 - 2m + \frac{4}{3}\right)^{\frac{1}{2}} s \qquad \text{red,} \qquad (\text{A.7})$$

$$d_{lm}^{\text{grn}} = \left(3l^2 + m^2 - 2m + 1\right)^{\frac{1}{2}} s \qquad \text{green,} \qquad (\text{A.8})$$

$$d_{lm}^{\text{blu}} = \left(3l^2 + l + m^2 - m + \frac{1}{3}\right)^{\frac{1}{2}} s \qquad \text{blue,} \qquad (\text{A.9})$$

$$d_{lm}^{\text{brn}} = \left(3l^2 - 3l + m^2 - m + 1\right)^{\frac{1}{2}} s \qquad \text{brown,} \qquad (\text{A.10})$$

and for region B

$$d_{l'm}^{\text{red}} = \left(3l'^2 - 4l' + m^2 + 2m + \frac{7}{3}\right)^{\frac{1}{2}} s \qquad \text{red,} \qquad (\text{A.11})$$

$$d_{l'm}^{\text{grn}} = \left(3l'^2 - 6l' + m^2 + 3\right)^{\frac{1}{2}} s \qquad \text{green,} \qquad (\text{A.12})$$

$$d_{l'm}^{\text{blu}} = \left(3l'^2 - 7l' + m^2 - m + \frac{13}{3}\right)^{\frac{1}{2}} s \qquad \text{blue,} \qquad (\text{A.13})$$

$$d_{l'm}^{\text{brn}} = \left(3l'^2 - 3l' + m^2 + 3m + 3\right)^{\frac{1}{2}} s \qquad \text{brown.} \qquad (\text{A.14})$$

In Sec. 3.2.1 we discussed how the summation in Eq. (3.26) was evaluated. We sum over images in a circular region of radius Ns_4, where N is a large number and s_4 is the length of a side of the square tube. The dashed line in Fig. A.4 indicates this region. In the computer code that calculates the summation, the distances between images and the bubble in a rectangular region ($l \leq 0.58N$, $m \leq N$) were calculated first, then images with distances larger than Ns_4 are eliminated before the summation.

A.4 Hexagonal tube

Figure A.5 is the grid for a bubble centered in a hexagonal tube. It possesses the 6-fold symmetry obtained by replicating the images colored red. The indexing

175

for the red images is shown in Fig. A.6. With s_6 denoting the length of a side of the hexagon, r the distance from the center to any side and R the distance from the center to a corner, we obtain for the distance from an image with indices (l, m) to the bubble $r_{lm} = \sqrt{3}(l^2 + lm + m^2)^{1/2}s_6$. The summation over all images is 6 times the summation over the red images.
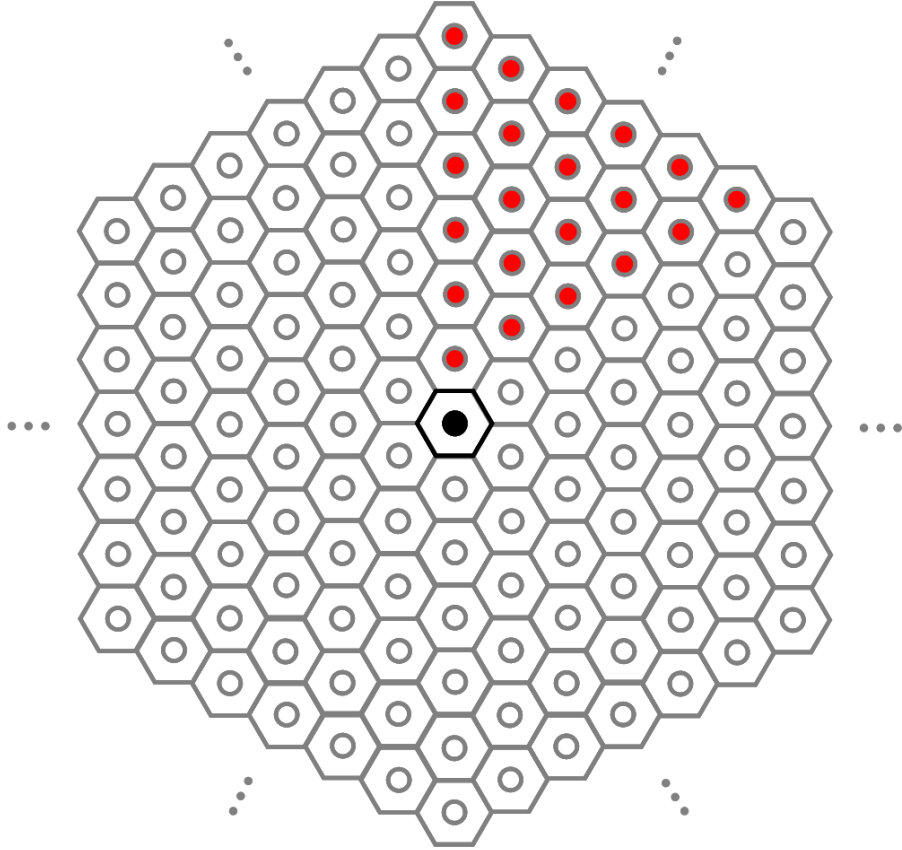
Figure A.5: Grid for images of a bubble centered in a hexagonal tube showing the 6-fold symmetry.

176
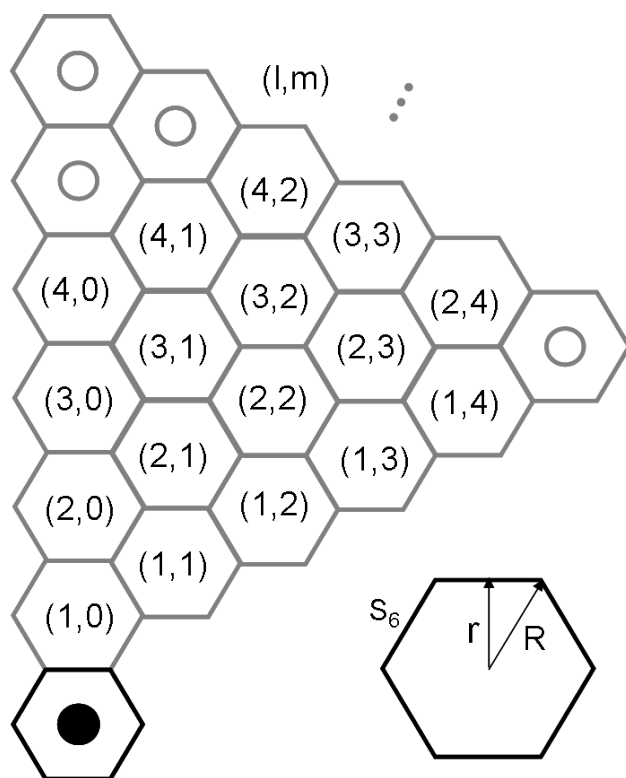
Figure A.6: Indexing for the images in one of the 6 symmetric triangular regions for a hexagonal tube.

Appendix B

Newton-Raphson Iteration Method

The Newton-Raphson method, also called Newton's method, is one of the most powerful and well-known root-finding algorithms. It is based on using linear approximations to solve equations. The iterative process to approximate one root of a function $f(x)$ is as follows [63].

Suppose the function $f(x)$ is twice continuously differentiable on a given interval $[a, b]$. Let $x_0 \in [a, b]$ be an approximation of the root x_r and expand $f(x)$ about the point x_0 in Taylor series to obtain

$$f(x_r) = f(x_0) + f'(x_0)(x_r - x_0) + \frac{1}{2}f''(x_0)(x_r - x_0)^2 + \cdots . \tag{B.1}$$

Keeping terms only to first order we get

$$f(x_r) \simeq f(x_0) + f'(x_0)(x_r - x_0). \tag{B.2}$$

Since by definition $f(x_r) = 0$, solve Eq. (B.2) to obtain

$$x_r \simeq x_0 - \frac{f(x_0)}{f'(x_0)}, \tag{B.3}$$

which is a better approximation of x_r than is x_0. This sets the stage for the iteration using Newton's method. The sequence $\{x_n\}$ is generated until it converges to root x_r:

$$x_n = x_{n-1} - \frac{f(x_{n-1})}{f'(x_{n-1})}. \tag{B.4}$$

178

With a good initial guess of the root, the algorithm can approach the root very quickly. Newton's method is powerful mainly because of its quadratic convergence rate. Expand $f(x)$ in a Taylor series about $x = x_n$ up to second order:

$$f(x_r) = f(x_n) + f'(x_n)E_n + \frac{1}{2}f''(x_n)E_n^2, \tag{B.5}$$

where $E_n = x_r - x_n$ is the error after the nth iteration. Since $f(x_r) = 0$, we obtain

$$f(x_n) + f'(x_n)E_n = -\frac{1}{2}f''(x_n)E_n^2. \tag{B.6}$$

With the assumption $f'(x) \neq 0$ for all x near the root x_r, so $f'(x_n) \neq 0$, Eq. (B.6) can be divided by $f'(x_n)$ to obtain

$$\frac{f(x_n)}{f'(x_n)} + \frac{f'(x_n)}{f'(x_n)}E_n = -\frac{f''(x_n)}{2f'(x_n)}E_n^2. \tag{B.7}$$

Rearrange the terms and simplify to get

$$E_n + \frac{f(x_n)}{f'(x_n)} = -\frac{f''(x_n)}{2f'(x_n)}E_n^2, \tag{B.8}$$

or

$$x_r - \left[x_n - \frac{f(x_n)}{f'(x_n)}\right] = -\frac{f''(x_n)}{2f'(x_n)}(x_r - x_n)^2. \tag{B.9}$$

Substitute Eq. (B.4) into Eq. (B.9) to obtain

$$E_{n+1} = -\frac{f''(x_n)}{2f'(x_n)}E_n^2. \tag{B.10}$$

Since $f'(x_n) = f'(x_r) + O(E_n)$ and $f''(x_n) = f''(x_r) + O(E_n)$, Eq. (B.10) becomes, to the same order,

$$E_{n+1} = -\frac{f''(x_r)}{2f'(x_r)}E_n^2. \tag{B.11}$$

179

Now take absolute values and obtain

$$|E_{n+1}| = -\frac{|f''(x_r)|}{|2f'(x_r)|}|E_n|^2.$$ (B.12)

The convergence rate is thus quadratic. Once in the neighborhood of the root, the significant digits approximately double with each step. This strong convergence property makes Newton's method efficient for any function whose derivative can be evaluated easily, and whose derivative is continuous and nonzero in the neighborhood of a root. However, the iteration procedure can be unstable near a horizontal asymptote and a local extremum, and Newton's method can fail for these cases. Also, a bad initial guess can cause the procedure to enter a nonconvergent cycle in which no solution can be achieved. Refer to Ref. [63] for further details.

Appendix C

Quadratic Approximation

This appendix includes two sections. The first section fills in the steps between Eq. (2.15) and its quadratic approximation in the frequency domain, Eq. (5.15). The steps for obtaining the analytical perturbation solution for the second harmonic, Eq. (5.8), are also included. The second section shows the details in obtaining the Jacobian for Eq. (5.15) when the Newton-Raphson iteration method is used to solve the nonlinear system of equations.

C.1 Derivation of the Quadratic Model Equation in the Frequency Domain

First we fill in the steps leading from Eq. (2.15) to Eq. (5.1) for a bubble between plates, and then the steps leading from Eq. (5.1) to the equations for the harmonics, Eq. (5.15). The same procedure applies to a bubble in a tube, Eq. (2.16), except no closed form for the summation is available.

Equation (2.15) is repeated here:

$$R\ddot{R} + \frac{3}{2}\dot{R}^2 = \frac{1}{\rho_0}\left[P_0\left(\frac{R_0}{R}\right)^{3\gamma} - P_0 - p_{\text{ac}}(t)\right] + \frac{\dddot{V}}{4\pi c_0} - \frac{1}{2\pi d}\sum_{m=1}^{\infty}\frac{1}{m}\ddot{V}(t-md/c_0). \quad \text{(C.1)}$$

Let $R = R_0 + \xi$, with $\dot{R} = \dot{\xi}$ and $\ddot{R} = \ddot{\xi}$, and let $V = \frac{4}{3}\pi R^3$, $V_0 = \frac{4}{3}\pi R_0^3$, to obtain

following expansion to quadratic order in ξ:

$$V = V_0 + 4\pi R_0^2 \xi + 4\pi R_0 \xi^2, \tag{C.2}$$

$$\dot{V} = 4\pi R_0^2 \dot{\xi} + 8\pi R_0 \xi \dot{\xi}, \tag{C.3}$$

$$\ddot{V} = 4\pi R_0^2 \ddot{\xi} + 8\pi R_0 \dot{\xi}^2 + 8\pi R_0 \xi \ddot{\xi}, \tag{C.4}$$

$$\dddot{V} = 4\pi R_0^2 \dddot{\xi} + 24\pi R_0 \dot{\xi}\ddot{\xi} + 8\pi R_0 \xi \dddot{\xi}. \tag{C.5}$$

The pressure term becomes

$$
\begin{aligned}
P_0 \left(\frac{R_0}{R}\right)^{3\gamma} - P_0 &= P_0 \left(1 + \frac{\xi}{R_0}\right)^{-3\gamma} - P_0 \\
&= P_0 \left[1 - 3\gamma \frac{\xi}{R_0} + \frac{3\gamma(3\gamma+1)}{2} \frac{\xi^2}{R_0^2} + \cdots\right] - P_0 \\
&= \frac{3\gamma P_0}{R_0}\xi + \frac{3\gamma(3\gamma+1)P_0}{2R_0^2}\xi^2.
\end{aligned} \tag{C.6}
$$

Now substitute in Eq. (C.1) to obtain

$$
\begin{aligned}
R_0\ddot{\xi} + \xi\ddot{\xi} + \frac{3}{2}\dot{\xi}^2 &+ 2\frac{R_0}{d}\sum_m \frac{1}{m}\left[\!\left[R_0\ddot{\xi} + 2\dot{\xi}^2 + 2\xi\ddot{\xi}\right]\!\right] - \frac{R_0}{c_0}(R_0\dddot{\xi} + 6\dot{\xi}\ddot{\xi} + 2\xi\dddot{\xi}) \\
&= -\frac{3\gamma P_0}{\rho_0 R_0}\xi + \frac{3\gamma(3\gamma+1)P_0}{2\rho_0 R_0^2}\xi^2 - \frac{p_{\mathrm{ac}}(t)}{\rho_0},
\end{aligned} \tag{C.7}
$$

where $[\![\cdot]\!]$ indicates evaluation at the delayed times $t - md/c_0$. Grouping linear terms on the left-hand side and the quadratic terms on the right-hand side, and dividing the equation by R_0, we get

$$
\begin{aligned}
\ddot{\xi}(t) + \omega_0^2 \xi(t) &- \frac{R_0}{c_0}\dddot{\xi}(t) + 2\frac{R_0}{d}\sum_{m=1}^{\infty}\frac{1}{m}\ddot{\xi}(t - md/c_0) \\
&= -\frac{1}{R_0}\left(\xi\ddot{\xi} + \frac{3}{2}\dot{\xi}^2\right) + \frac{\omega_0^2}{2R_0}(3\gamma+1)\xi^2 + \frac{2}{c_0}(3\dot{\xi}\ddot{\xi} + \xi\dddot{\xi}) \\
&\quad - \frac{4}{d}\sum_{m=1}^{\infty}\frac{1}{m}\left[\dot{\xi}^2(t - md/c_0) + \xi(t - md/c_0)\ddot{\xi}(t - md/c_0)\right] - \frac{p_{\mathrm{ac}}(t)}{\rho_0 R_0}, \tag{C.8}
\end{aligned}
$$

where $\omega_0^2 = 3\gamma P_0/\rho_0 R_0^2$. Equation (C.8) is the combined form of Eqs. (5.1) and (5.2).

The perturbation ξ can be expanded as follows to just include the fundamental, the second harmonic, and the dc component:

$$\xi = \xi_1 + \xi_2 + \xi_0, \tag{C.9}$$

where

$$\xi_1 = \frac{1}{2}A_1(\omega)e^{j\omega t} + \text{c.c.}, \tag{C.10a}$$

$$\xi_2 = \frac{1}{2}A_2(\omega)e^{j2\omega t} + \text{c.c.}, \tag{C.10b}$$

$$\xi_0 = A_0, \tag{C.10c}$$

and it is assumed that $|A_2| \ll |A_1|$, $|A_0| \ll |A_1|$. We may now solve Eq. (C.8) by successive approximations. In the first approximation, the solution for A_1 is obtained by setting the right-hand side of Eq. (C.8) to zero and substituting Eq. (C.10a) into the left-hand side. One thus obtains $A_1 = \Xi$, where Ξ is defined by Eq. (3.7). In the second approximation, Eq. (C.10b) or Eq. (C.10c) is substituted into the left-hand side and Eq. (C.10a) into the right-hand side.

For the second harmonic, the left-hand side becomes

$$
\begin{aligned}
\text{LHS} &= \frac{1}{2}A_2 e^{j2\omega t}\left(-4\omega^2 + \omega_0^2 + j8\omega^3\frac{R_0}{c_0} - 8\omega^2\frac{R_0}{d}\sum_{m=1}^{\infty}\frac{1}{m}e^{j2mkd}\right) + \text{c.c.} \\
&= \frac{1}{2}A_2 e^{j2\omega t}\left[\omega_0^2 - 4\omega^2 + j8\omega^3\frac{R_0}{c_0} + 8\omega^2\frac{R_0}{d}\ln(1 - e^{-j2kd})\right] + \text{c.c.} \\
&= \frac{1}{2}A_2 e^{j2\omega t}\omega_0^2\left\{1 - 4\left[1 - 2\frac{R_0}{d}\ln(1 - e^{-j2kd})\right]\frac{\omega^2}{\omega_0^2} + j8k_0 R_0\frac{\omega^3}{\omega_0^3}\right\} + \text{c.c.} \\
&= \frac{1}{2}A_2 e^{j2\omega t}\omega_0^2\Delta_2(\omega) + \text{c.c.}, \tag{C.11}
\end{aligned}
$$

183

where $\Delta_2(\omega)$ is defined in Eq. (5.9). On the right-hand side, retaining only terms containing the second harmonic, we have

$$\xi_1\ddot{\xi}_1 = -\frac{\omega^2}{4}A_1^2e^{j2\omega t} + \text{c.c.}, \tag{C.12a}$$

$$\dot{\xi}_1^2 = -\frac{\omega^2}{4}A_1^2e^{j2\omega t} + \text{c.c.}, \tag{C.12b}$$

$$\dot{\xi}_1\ddot{\xi}_1 = -j\frac{\omega^3}{4}A_1^2e^{j2\omega t} + \text{c.c.}, \tag{C.12c}$$

$$\xi_1\dddot{\xi}_1 = -j\frac{\omega^3}{4}A_1^2e^{j2\omega t} + \text{c.c.}, \tag{C.12d}$$

$$\xi_1^2 = \frac{1}{4}A_1^2e^{j2\omega t} + \text{c.c.}, \tag{C.12e}$$

$$\dot{\xi}_1^2\left(t-\frac{md}{c_0}\right) = -\frac{\omega^2}{4}A_1^2e^{j2\omega t}e^{-j2mkd} + \text{c.c.}, \tag{C.12f}$$

$$\xi_1\left(t-\frac{md}{c_0}\right)\ddot{\xi}_1\left(t-\frac{md}{c_0}\right) = -\frac{\omega^2}{4}A_1^2e^{j2\omega t}e^{-j2mkd} + \text{c.c.} \tag{C.12g}$$

Finally, the right-hand side becomes

$$\begin{aligned}
\text{RHS} &= A_1^2e^{j2\omega t}\left[\frac{5}{8}\frac{\omega^2}{R_0} - j2\frac{\omega^3}{c_0} + (3\gamma+1)\frac{\omega^2}{8R_0} - 2\frac{\omega^2}{d}\ln(1-e^{-j2kd})\right] + \text{c.c.} \\
&= \frac{\omega^2}{2R_0}A_1^2e^{j2\omega t}\left[\frac{5}{4}\frac{\omega^2}{\omega_0^2} - j4k_0R_0\frac{\omega^3}{\omega_0^3} + \frac{3\gamma+1}{4} - 4\frac{R_0}{d}\ln(1-e^{j2kd})\right] + \text{c.c.} \\
&= \frac{\omega^2}{2R_0}A_1^2e^{j2\omega t}\Gamma(\omega) + \text{c.c.}, \tag{C.13}
\end{aligned}$$

where $\Gamma(\omega)$ is defined in Eq. (5.10).

Equating LHS with RHS we get

$$\frac{\omega^2}{2}A_2e^{j2\omega t}\Delta_2(\omega) = \frac{\omega^2}{2R_0}A_1^2e^{j2\omega t}\Gamma(\omega), \tag{C.14}$$

or

$$A_2 = \frac{A_1^2}{R_0}\frac{\Gamma(\omega)}{\Delta_2(\omega)}. \tag{C.15}$$

The dimensionless amplitudes $C_1(\omega)$ and $C_2(\omega)$ defined in Eqs. (5.6a) and (5.6b) are thus

$$C_1(\omega) = \frac{C_1(0)}{\Delta_1(\omega)} = -\frac{p_0}{3\gamma P_0}\frac{1}{\Delta_1(\omega)}, \tag{C.16}$$

so

$$C_2(\omega) \equiv \frac{A_2}{R_0} = \left(\frac{p_0}{3\gamma P_0}\right)^2 \frac{\Gamma(\omega)}{\Delta_1^2(\omega)\Delta_2(\omega)}. \tag{C.17}$$

Equation (C.17) is equivalent to Eq. (5.8).

For the dc component, the left-hand side becomes

$$\text{LHS} = \omega_0^2 A_0, \tag{C.18}$$

which comes from the term $\omega_0^2 \xi$, and all other terms on the left-hand side are zeros after derivatives are taken. On the right-hand side, retaining only dc terms we have

$$\xi_1 \ddot{\xi}_1 = -\frac{\omega^2}{2}|A_1|^2, \tag{C.19a}$$

$$\dot{\xi}_1^2 = \frac{\omega^2}{2}|A_1|^2, \tag{C.19b}$$

$$\dot{\xi}_1 \ddot{\xi}_1 = 0, \tag{C.19c}$$

$$\xi_1 \dddot{\xi}_1 = 0, \tag{C.19d}$$

$$\xi_1^2 = \frac{\omega^2}{2}|A_1|^2, \tag{C.19e}$$

$$\dot{\xi}_1^2\left(t - \frac{md}{c_0}\right) = -\frac{\omega^2}{2}|A_1|^2, \tag{C.19f}$$

$$\xi_1\left(t - \frac{md}{c_0}\right)\ddot{\xi}_1\left(t - \frac{md}{c_0}\right) = \frac{\omega^2}{2}|A_1|^2. \tag{C.19g}$$

Finally, the right-hand side becomes

$$\text{RHS} = -\frac{\omega^2}{R_0}\left(-\frac{1}{2}|A_1|^2 + \frac{3}{4}|A_1|^2\right) + \frac{\omega_0^2}{2R_0}(3\gamma + 1)\frac{\omega^2}{2}|A_1|^2$$

$$= \frac{\omega_0^2}{4R_0}\left(3\gamma + 1 - \frac{\omega^2}{\omega_0^2}\right)|A_1|^2. \tag{C.20}$$

Equating LHS with RHS we get

$$A_0 = \frac{1}{4R_0}\left(3\gamma + 1 - \frac{\omega^2}{\omega_0^2}\right)|A_1|^2. \tag{C.21}$$

C.1.1 Coupled Nonlinear Equations for the Harmonics

Expressing ξ in the frequency domain using a Fourier expansion, we have

$$\xi(t) = \frac{1}{2}\sum_{n=-\infty}^{\infty}A_n e^{jn\omega t}. \tag{C.22}$$

Let α and β both be integers, such that the αth (and βth) order derivatives of ξ take the following form:

$$\frac{d^\alpha\xi}{dt^\alpha} = \frac{1}{2}\sum_{n=-\infty}^{\infty}(jn\omega)^\alpha A_n e^{jn\omega t}, \tag{C.23}$$

so

$$\left(\frac{d^\alpha\xi}{dt^\alpha}\right)\left(\frac{d^\beta\xi}{dt^\beta}\right) = \frac{1}{4}\sum_{l=-\infty}^{\infty}(jl\omega)^\alpha A_l e^{jl\omega t}\sum_{m=-\infty}^{\infty}(jm\omega)^\beta A_m e^{jm\omega t}$$

$$= \frac{1}{4}(j\omega)^{\alpha+\beta}\sum_{l=-\infty}^{\infty}\sum_{m=-\infty}^{\infty}l^\alpha m^\beta A_l A_m e^{j(l+m)\omega t}$$

$$= \sum_{n=-\infty}^{\infty}\frac{1}{4}(j\omega)^{\alpha+\beta}\left[\sum_{m=-\infty}^{\infty}m^\alpha(n-m)^\beta A_m A_{n-m}\right]e^{jn\omega t}$$

$$\triangleq \sum_{n=-\infty}^{\infty}\frac{1}{4}(j\omega)^{\alpha+\beta}S_n(\alpha,\beta)e^{jn\omega t}, \tag{C.24}$$

186

where $l + m = n$,

$$S_n(\alpha, \beta) = \sum_{m=-\infty}^{\infty} m^\alpha (n-m)^\beta A_m A_{n-m}, \tag{C.25}$$

and it can be seen that $S_n(\alpha, \beta) = S_n(\beta, \alpha)$. The summation in Eq. (C.8) can be rewritten as follows:

$$\sum_{m=1}^{\infty} \frac{1}{m} \ddot{\xi}\left(t - \frac{md}{c_0}\right) = \sum_{m=1}^{\infty} \frac{1}{m} \frac{1}{2} \sum_{n=-\infty}^{\infty} (-n^2\omega^2) A_n e^{j(n\omega t - mnkd)}$$

$$= -\frac{\omega^2}{2} \sum_{n=-\infty}^{\infty} n^2 A_n e^{jn\omega t} \sum_{m=1}^{\infty} \frac{1}{m} e^{-jmnkd}$$

$$= \frac{\omega^2}{2} \sum_{n=-\infty}^{\infty} n^2 A_n e^{jn\omega t} \ln(1 - e^{-jnkd}). \tag{C.26}$$

Now the left-hand side of Eq. (C.8) becomes

$$\text{LHS} = \frac{1}{2} \sum_{n=-\infty}^{\infty} A_n e^{jn\omega t} \left[-(n\omega)^2 + \omega_0^2 + 2\frac{R_0}{d}(n\omega)^2 \ln(1 - e^{-jnkd}) + j(n\omega)^3 \frac{R_0}{c_0} \right]$$

$$= \frac{\omega^2}{2} \sum_{n=-\infty}^{\infty} A_n e^{jn\omega t} \left[1 - \frac{(n\omega)^2}{\omega_0^2} + 2\frac{R_0}{d} \frac{(n\omega)^2}{\omega_0^2} \ln(1 - e^{-jnkd}) + jk_0 R_0 \frac{(n\omega)^3}{\omega_0^3} \right]$$

$$= \frac{\omega^2}{2} \sum_{n=-\infty}^{\infty} A_n e^{jn\omega t} \Delta_n, \tag{C.27}$$

where

$$\Delta_n = 1 - n^2 \left[1 - 2\frac{R_0}{d} \ln(1 - e^{-jnkd}) \right] \frac{\omega^2}{\omega_0^2} + jn^3 k_0 R_0 \frac{\omega^3}{\omega_0^3}. \tag{C.28}$$

187

Equation (C.28) is equivalent to Eq. (5.31) when the viscous term in the latter is omitted. For the right-hand side, term by term we have

$$\xi\ddot{\xi} = \frac{1}{4}\sum_{n=-\infty}^{\infty}(j\omega)^2 S_n(0,2)e^{jn\omega t}, \tag{C.29}$$

$$\dot{\xi}^2 = \frac{1}{4}\sum_{n=-\infty}^{\infty}(j\omega)^2 S_n(1,1)e^{jn\omega t}, \tag{C.30}$$

$$\dot{\xi}\ddot{\xi} = \frac{1}{4}\sum_{n=-\infty}^{\infty}(j\omega)^3 S_n(1,2)e^{jn\omega t}, \tag{C.31}$$

$$\xi\dddot{\xi} = \frac{1}{4}\sum_{n=-\infty}^{\infty}(j\omega)^3 S_n(0,3)e^{jn\omega t}, \tag{C.32}$$

$$\xi^2 = \frac{1}{4}\sum_{n=-\infty}^{\infty}S_n(0,0)e^{jn\omega t}, \tag{C.33}$$

$$\sum_{m=1}^{\infty}\frac{1}{m}\dot{\xi}^2\left(t-\frac{md}{c_0}\right) = -\frac{\omega^2}{4}\sum_{n=-\infty}^{\infty}S_n(1,1)e^{jn\omega t}\sum_{m=1}^{\infty}\frac{e^{-jnmkd}}{m} \tag{C.34}$$

$$= \frac{\omega^2}{4}\sum_{n=-\infty}^{\infty}S_n(1,1)e^{jn\omega t}\ln(1-e^{-jnkd}), \tag{C.35}$$

$$\xi\left(t-\frac{md}{c_0}\right)\ddot{\xi}\left(t-\frac{md}{c_0}\right) = -\frac{\omega^2}{4}\sum_{n=-\infty}^{\infty}S_n(0,2)e^{jn\omega t}e^{-jnmkd}. \tag{C.36}$$

Substitute all the above equations into the right-hand side of Eq. (C.8) to obtain

$$\text{RHS} = \sum_{n=-\infty}^{\infty}e^{jn\omega t}\left\{\frac{\omega^2}{4R_0}\left[S_n(0,2)+\frac{3}{2}S_n(1,1)\right]-\frac{j\omega^3}{2c_0}[S_n(0,3)+3S_n(1,2)]\right.$$
$$\left.+(3\gamma+1)\frac{\omega_0^2}{8R_0}S_n(0,0)-\frac{\omega^2}{d}[S_n(0,2)+S_n(1,1)]\ln(1-e^{-jnkd})\right\}-\frac{p_0e^{j\omega t}}{2\rho_0 R_0}. \tag{C.37}$$

Now define

$$Z_n = \frac{3\gamma + 1}{4R_0} S_n(0,0) + \frac{1}{2R_0}\left[S_n(0,2) + \frac{3}{2}S_n(1,1)\right]\frac{\omega^2}{\omega_0^2}$$
$$- \frac{2}{d}\ln(1 - e^{-jnkd})[S_n(0,2) + S_n(1,1)]\frac{\omega^2}{\omega_0^2}$$
$$- jk_0[S_n(0,3) + 3S_n(1,2)]\frac{\omega^3}{\omega_0^3} - \frac{\delta_{1n}p_0}{\rho_0 R_0 \omega_0^2}, \tag{C.38}$$

where δ_{lm} is the Kronecker delta and thus

$$\text{RHS} = \frac{\omega^2}{2}\sum_{n=-\infty}^{\infty} e^{jn\omega t} Z_n. \tag{C.39}$$

Equating the LHS to the RHS and we get

$$\frac{\omega^2}{2}\sum_{n=-\infty}^{\infty} \Delta_n A_n e^{jn\omega t} = \frac{\omega^2}{2}\sum_{n=-\infty}^{\infty} e^{jn\omega t} Z_n, \tag{C.40}$$

or

$$\Delta_n A_n = Z_n. \tag{C.41}$$

Equation (C.25) is now expanded as follows:

$$S_n(\alpha, \beta) = \sum_{m=-\infty}^{\infty} m^\alpha (n-m)^\beta A_m A_{n-m}$$
$$= \delta_{\alpha 0} n^\beta A_0 A_n + \delta_{\beta 0} n^\alpha A_0 A_n$$
$$+ \left(\sum_{m=-\infty}^{-1} + \sum_{m=1}^{n-1} + \sum_{m=n+1}^{\infty}\right) m^\alpha (n-m)^\beta A_m A_{n-m}, \tag{C.42}$$

where

$$\sum_{m=-\infty}^{-1} m^\alpha (n-m)^\beta A_m A_{n-m} = \sum_{m=\infty}^{n+1} (n-l)^\alpha l^\beta A_{n-l} A_l$$
$$= \sum_{m=n+1}^{\infty} (n-l)^\alpha l^\beta A_l A_{l-n}^*$$
$$= \sum_{m=n+1}^{\infty} (n-m)^\alpha m^\beta A_m A_{m-n}^*. \tag{C.43}$$

189

Thus

$$S_n(\alpha, \beta) = \sum_{m=0}^{n} m^\alpha (n-m)^\beta A_m A_{n-m}$$

$$+ \sum_{m=n+1}^{\infty} [m^\alpha (n-m)^\beta + m^\beta (n-m)^\alpha] A_m A_{m-n}^*, \qquad (\text{C.44})$$

where the first summation accounts for sum frequency generation, the second for difference frequency generation. If we are only interested in the first N harmonics, the upper limit ∞ in $S_n(\alpha, \beta)$ is replaced by N. Now let $C_n = A_n/R_0$ and $Q_n = S_n/R_0^2$, such that Eq. (C.41) becomes

$$\Delta_n C_n = \frac{3\gamma + 1}{4} Q_n(0,0) + \frac{1}{2}\left[Q_n(0,2) + \frac{3}{2}Q_n(1,1)\right]\frac{\omega^2}{\omega_0^2}$$

$$- \frac{R_0}{d}\ln(1 - e^{-jnkd})[Q_n(0,2) + Q_n(1,1)]\frac{\omega^2}{\omega_0^2}$$

$$- jk_0 R_0[Q_n(0,3) + 3Q_n(1,2)]\frac{\omega^3}{\omega_0^3} - \frac{\delta_{1n}p_0}{3\gamma P_0}. \qquad (\text{C.45})$$

From Eq. (C.44) we get

$$Q_n(0,2) = \sum_{m=0}^{n} (n-m)^2 C_m C_{n-m} + \sum_{m=n+1}^{\infty} [(n-m)^2 + m^2] C_m C_{n-m}^*, \qquad (\text{C.46})$$

$$Q_n(0,3) = \sum_{m=0}^{n} (n-m)^3 C_m C_{n-m} + \sum_{m=n+1}^{\infty} [(n-m)^3 + m^3] C_m C_{n-m}^*, \qquad (\text{C.47})$$

$$Q_n(1,1) = \sum_{m=0}^{n} m(n-m) C_m C_{n-m} + \sum_{m=n+1}^{\infty} 2m(n-m) C_m C_{n-m}^*, \qquad (\text{C.48})$$

$$Q_n(1,2) = \sum_{m=0}^{n} m(n-m)^2 C_m C_{n-m}$$

$$+ \sum_{m=n+1}^{\infty} [m(n-m)^2 + m^2(n-m)] C_m C_{n-m}^*. \qquad (\text{C.49})$$

190

The first two terms on the right-hand side of Eq. (C.45) can be rewritten as follows:

$$\frac{3\gamma+1}{4}Q_n(0,0) + \frac{1}{2}\left[Q_n(0,2) + \frac{3}{2}Q_n(1,1)\right]\frac{\omega^2}{\omega_0^2}$$

$$= \sum_{m=0}^{n}\left\{\frac{3\gamma+1}{4} + \frac{1}{2}\left[(n-m)^2 + \frac{3}{2}m(n-m)\right]\frac{\omega^2}{\omega_0^2}\right\}C_mC_{n-m}$$

$$+ \sum_{m=n+1}^{\infty}\left\{\frac{3\gamma+1}{2} + \frac{1}{2}\left[(n-m)^2 + m^2 + 3m(n-m)\right]\frac{\omega^2}{\omega_0^2}\right\}C_mC_{m-n}^*$$

$$= \sum_{m=0}^{n}\left[\frac{3\gamma+1}{4} + \frac{1}{2}(n-m)\left(n+\frac{m}{2}\right)\frac{\omega^2}{\omega_0^2}\right]C_mC_{n-m}$$

$$+ \sum_{m=n+1}^{\infty}\left[\frac{3\gamma+1}{2} + \frac{1}{2}(n^2 + mn - m^2)\right]\frac{\omega^2}{\omega_0^2}C_mC_{m-n}^*. \tag{C.50}$$

The remaining coefficients in Eq. (C.45) become

$$Q_n(0,2) + Q_n(1,1) = \sum_{m=0}^{n}[(n-m)^2 + m(n-m)]C_mC_{n-m}$$

$$+ \sum_{m=n+1}^{\infty}[(n-m)^2 + m^2 + 2m(n-m)]C_mC_{m-n}^*$$

$$= \sum_{m=0}^{n}n(n-m)C_mC_{n-m} + \sum_{m=n+1}^{\infty}n^2C_mC_{m-n}^*, \tag{C.51}$$

and

$$Q_n(0,3) + 3Q_n(1,2) = \sum_{m=0}^{n}[(n-m)^3 + 3m(n-m)^2]C_mC_{n-m}$$

$$+ \sum_{m=n+1}^{\infty}[(n-m)^3 + m^3 + 3m(n-m)^2 + 3m^2(n-m)]C_mC_{m-n}^*$$

$$= \sum_{m=0}^{n}[n^3 + m^2(2m-3n)]C_mC_{n-m} + \sum_{m=n+1}^{\infty}n^3C_mC_{m-n}^*. \tag{C.52}$$

Equation (C.45) thus becomes, exactly,

$$\Delta_n C_n = \sum_{m=0}^{n} a_{mn} C_m C_{n-m} + \sum_{m=n+1}^{\infty} b_{mn} C_m C_{m-n}^* - \frac{p_0 \delta_{1n}}{3\gamma P_0}, \qquad \text{(C.53)}$$

which is equivalent to Eq. (5.15) after truncating the Fourier expansion to N harmonics. The coefficients Δ_n, a_{mn} and b_{mn} are given by Eqs. (5.16), (5.18) and (5.19), respectively, omitting the viscous terms.

C.2 Jacobian Matrix

To solve Eq. (C.53) using the Newton-Raphson iteration method, we need the Jacobian of the function $\mathbf{F}(C_1, \cdots, C_N)$, where $\mathbf{F} = (F_1, \cdots, F_N)$ and

$$F_n = \frac{p_0 \delta_{1n}}{3\gamma P_0} + \Delta_n C_n - \sum_{m=0}^{n} a_{mn} C_m C_{n-m} - \sum_{m=n+1}^{N} b_{mn} C_m C_{m-n}^*, \qquad \text{(C.54)}$$

where we now acknowledge truncation of the Fourier expansion at the Nth harmonic for the purpose of numerical calculations. With $F_n = F_n^{\mathrm{r}} + jF_n^{\mathrm{i}}$ expressed in real and

imaginary parts, Eq. (C.54) becomes

$$
\begin{aligned}
F_n &= \frac{p_0 \delta_{1n}}{3\gamma P_0} + (\Delta_n^{\mathrm{r}} + j\Delta_n^{\mathrm{i}})(C_n^{\mathrm{r}} + jC_n^{\mathrm{i}}) \\
&\quad - \sum_{m=0}^{n} (a_{mn}^{\mathrm{r}} + ja_{mn}^{\mathrm{i}})(C_m^{\mathrm{r}} + jC_m^{\mathrm{i}})(C_{n-m}^{\mathrm{r}} + jC_{n-m}^{\mathrm{i}}) \\
&\quad - \sum_{m=n+1}^{N} (b_{mn}^{\mathrm{r}} + jb_{mn}^{\mathrm{i}})(C_m^{\mathrm{r}} + jC_m^{\mathrm{i}})(C_{m-n}^{*\mathrm{r}} + jC_{m-n}^{*\mathrm{i}}), \\
&= \frac{p_0 \delta_{1n}}{3\gamma P_0} + (\Delta_n^{\mathrm{r}} C_n^{\mathrm{r}} - \Delta_n^{\mathrm{i}} C_n^{\mathrm{i}}) + j(\Delta_n^{\mathrm{i}} C_n^{\mathrm{r}} + \Delta_n^{\mathrm{r}} C_n^{\mathrm{i}}) \\
&\quad - \sum_{m=0}^{n} \left\{ \left[a_{mn}^{\mathrm{r}}(C_m^{\mathrm{r}} C_{n-m}^{\mathrm{r}} - C_m^{\mathrm{i}} C_{n-m}^{\mathrm{i}}) - a_{mn}^{\mathrm{i}}(C_m^{\mathrm{i}} C_{n-m}^{\mathrm{r}} + C_m^{\mathrm{r}} C_{n-m}^{\mathrm{i}}) \right] \right. \\
&\quad \left. + j \left[a_{mn}^{\mathrm{i}}(C_m^{\mathrm{r}} C_{n-m}^{\mathrm{r}} - C_m^{\mathrm{i}} C_{n-m}^{\mathrm{i}}) - a_{mn}^{\mathrm{i}}(C_m^{\mathrm{i}} C_{n-m}^{\mathrm{r}} + C_m^{\mathrm{r}} C_{n-m}^{\mathrm{i}}) \right] \right\} \\
&\quad - \sum_{m=n+1}^{N} \left\{ \left[b_{mn}^{\mathrm{r}}(C_m^{\mathrm{r}} C_{n-m}^{\mathrm{r}} + C_m^{\mathrm{i}} C_{n-m}^{\mathrm{i}}) - b_{mn}^{\mathrm{i}}(C_m^{\mathrm{i}} C_{n-m}^{\mathrm{r}} - C_m^{\mathrm{r}} C_{n-m}^{\mathrm{i}}) \right] \right. \\
&\quad \left. + j \left[b_{mn}^{\mathrm{i}}(C_m^{\mathrm{r}} C_{n-m}^{\mathrm{r}} + C_m^{\mathrm{i}} C_{n-m}^{\mathrm{i}}) + b_{mn}^{\mathrm{r}}(C_m^{\mathrm{i}} C_{n-m}^{\mathrm{r}} - C_m^{\mathrm{r}} C_{n-m}^{\mathrm{i}}) \right] \right\}. \quad \text{(C.55)}
\end{aligned}
$$

Therefore

$$
\begin{aligned}
F_n^{\mathrm{r}} &= \frac{p_0^{\mathrm{r}} \delta_{1n}}{3\gamma P_0} + (\Delta_n^{\mathrm{r}} C_n^{\mathrm{r}} - \Delta_n^{\mathrm{i}} C_n^{\mathrm{i}}) \\
&\quad - \sum_{m=0}^{n} \left[a_{mn}^{\mathrm{r}}(C_m^{\mathrm{r}} C_{n-m}^{\mathrm{r}} - C_m^{\mathrm{i}} C_{n-m}^{\mathrm{i}}) - a_{mn}^{\mathrm{i}}(C_m^{\mathrm{i}} C_{n-m}^{\mathrm{r}} + C_m^{\mathrm{r}} C_{n-m}^{\mathrm{i}}) \right] \\
&\quad - \sum_{m=n+1}^{N} \left[b_{mn}^{\mathrm{r}}(C_m^{\mathrm{r}} C_{n-m}^{\mathrm{r}} + C_m^{\mathrm{i}} C_{n-m}^{\mathrm{i}}) - b_{mn}^{\mathrm{i}}(C_m^{\mathrm{i}} C_{n-m}^{\mathrm{r}} - C_m^{\mathrm{r}} C_{n-m}^{\mathrm{i}}) \right], \quad \text{(C.56)}
\end{aligned}
$$

and

$$F_n^i = \frac{p_0^i \delta_{1n}}{3\gamma P_0} + (\Delta_n^i C_n^r + \Delta_n^r C_n^i)$$

$$- \sum_{m=0}^{n} \left[a_{mn}^i (C_m^r C_{n-m}^r - C_m^i C_{n-m}^i) - a_{mn}^i (C_m^i C_{n-m}^r + C_m^r C_{n-m}^i) \right]$$

$$- \sum_{m=n+1}^{N} \left[b_{mn}^i (C_m^r C_{n-m}^r + C_m^i C_{n-m}^i) + b_{mn}^r (C_m^i C_{n-m}^r - C_m^r C_{n-m}^i) \right]. \qquad \text{(C.57)}$$

The Jacobian $\mathbf{J}(C_1^r, \ldots, C_N^r, C_1^i, \ldots, C_N^i, C_0)$ is obtained by taking partial derivatives of the real and imaginary parts of $\mathbf{F}$ with respect to real and imaginary parts of $\mathbf{C}$. Including the dc component, the matrix will be $2(N+1)$ by $2(N+1)$. When taking partial derivatives with respect to C_n^r, we treat C_m^r as constant for all m not equal to n, and C_m^i constant for any m, including C_0. The $2(N+1)$ by $2(N+1)$ Jacobian is defined as follows:

$$\mathbf{J} = \begin{vmatrix} \frac{\partial F_1^r}{\partial C_1^r} & \cdots & \frac{\partial F_1^r}{\partial C_N^r} & \frac{\partial F_1^r}{\partial C_1^i} & \cdots & \frac{\partial F_1^r}{\partial C_N^i} & \frac{\partial F_1^r}{\partial C_0} \\ \frac{\partial F_1^i}{\partial C_1^r} & \cdots & \frac{\partial F_1^i}{\partial C_N^r} & \frac{\partial F_1^i}{\partial C_1^i} & \cdots & \frac{\partial F_1^i}{\partial C_N^i} & \frac{\partial F_1^i}{\partial C_0} \\ \vdots & \cdots & \vdots & \vdots & \cdots & \vdots & \vdots \\ \frac{\partial F_N^r}{\partial C_1^r} & \cdots & \frac{\partial F_N^r}{\partial C_N^r} & \frac{\partial F_N^r}{\partial C_1^i} & \cdots & \frac{\partial F_N^r}{\partial C_N^i} & \frac{\partial F_N^r}{\partial C_0} \\ \frac{\partial F_N^i}{\partial C_1^r} & \cdots & \frac{\partial F_N^i}{\partial C_N^r} & \frac{\partial F_N^i}{\partial C_1^i} & \cdots & \frac{\partial F_N^i}{\partial C_N^i} & \frac{\partial F_N^i}{\partial C_0} \\ \frac{\partial F_0}{\partial C_1^r} & \cdots & \frac{\partial F_0}{\partial C_N^r} & \frac{\partial F_0}{\partial C_1^i} & \cdots & \frac{\partial F_0}{\partial C_N^i} & \frac{\partial F_0}{\partial C_0} \end{vmatrix}.$$

Equation (C.53) can also be solved using Numerical Recipes [63], in which case the Jacobian is obtained numerically.

Bibliography

[1] H. N. Oğuz and A. Prosperetti. The natural frequency of oscillation of gas bubbles in tubes. *J. Acoust. Soc. Am.*, 103:3301–3308, 1998.

[2] P. M. Morse and K. U. Ingard. *Theoretical Acoustics*, Chapter 9. McGraw-Hill, New York, 1968.

[3] M. Minnaert. On musical air-bubbles and the sounds of running water. *Phil. Mag.*, 16:235–248, 1933.

[4] A. Shima. Studies on bubble dynamics. *Shock Waves*, 7:33–42, 1997.

[5] Lord Rayleigh. On the pressure developed in a liquid during the collapse of a spherical cavity. *Phil. Mag.*, 34:94–98, 1917.

[6] W. H. Besant. *A Treatise on Hydrostatics and Hydrodynamics*, chapter 158. Cambridge University Press, Deighton, Bell, London, 1859.

[7] R. T. Knapp, J. W. Daily, and F. G. Hammitt. *Cavitation*. McGraw-Hill, New York, 1970.

[8] F. G. Hammitt. *Cavitation and Multiphase Flow Phenomena*. McGraw-Hill, New York, 1980.

[9] W. H. Isay. *Kavitation*. Schiffahrts-Verlag Hansa C. Schroedter and Co., Hamburg, 1981.

[10] F. R. Young. *Cavitation.* McGraw-Hill, New York, 1989.

[11] T. G. Leighton. *The Acoustic Bubble.* Academic, San Diego, 1994.

[12] C. E. Brennen. *Cavitation and Bubble Dynamics.* Oxford University Press, Oxford, 1995.

[13] H. Becher and P. N. Burns. *Handbook of Contrast Echocardiography.* Springer-Verlag, Berlin, 2000.

[14] P. N. Burns, J. E. Powers, S. D. Hope, V. Uhlendorf, and T. Fritzsch. Harmonic imaging: principles and preliminary results. *Angiology*, 47:S63–S74, 1996.

[15] S. P. Qin and K. W. Ferrara. The natural frequency of nonlinear oscillation of ultrasound contrast agents in microvessels. *Ultrasound in Medicine and Biology*, 33:1140–1148, 2006.

[16] M. Fechheimer, J. F. Boylan, S. Parker, J. E. Sisken, G. L. Patel, and S. G. Zimmer. Transfection of mammalian cells with plasmid DNA by scrape loading and sonication loading. *Proc. Natl. Acad. Sci. U.S.A.*, 84:8463–8467, 1987.

[17] D. L. Miller and R. L. Thomas. The role of cavitation in the induction of cellular DNA damage by ultrasound and lithotripter shock waves *in vitro*. *Ultrasound Med. Biol.*, 22:681–687, 1996.

[18] S. Bao, B. D. Thrall, and D. L. Miller. Transfection of a reporter plasmid into cultured cells by sonoporation *in vitro*. *Ultrasound Med. Biol.*, 23:953–959, 1997.

[19] J. Liu, T. N. Lewis, and M. R. Prausnitz. Non-invasive assessment and control of ultrasound-mediated membrane permeabilization. *Pharm. Res.*, 15:918–924, 1998.

[20] C. Chaussy and G. J. Fuchs. Current state and future developments if non-invasive treatment of human urinary stones with extracorporeal shock wave lithotripsy. *J. Urol.*, 141:782–792, 1989.

[21] W. Sass, H. P. Dreyer, S. Kettermann, and J. Seifert. The role of cavitational activity in fragmentation processes by lithotripters. *J. Stone Dis.*, 4:193–207, 1992.

[22] Ch. Renner and J. Rassweiler. Treatment of renal stones by extracorporeal shock wave lithotripsy. *Nephron*, 81:71–81, 1999.

[23] S. Zhu, F. H. Cocks, G. M. Preminger, and P. Zhong. The role of stress waves and cavitation in stone comminution in shock wave lithotripsy. *Ultrasound Med. Biol.*, 28:661–671, 2002.

[24] Yu. A. Pishchalnikov, O. A. Sapozhnikov, M. R. Bailey, J. C. Williams Jr., R. O. Cleveland, T. Colonius, L. A. Crum, A. P. Evan, and J. A. McAteer. Cavitation bubble cluster activity in the breakage of kidney stones by lithotripter shockwaves. *J. Endourol.*, 17:435–446, 2003.

[25] A. Gelet, J. Y. Chapelon, R. Bouvier, C. Pangaud, and Y. Lasne. Local control of prostate cancer by transrectal high intensity focused ultrasound therapy: preliminary results. *The Journal of Urology*, 161:156–162, 1999.

[26] A. Blana, B. Walter, S. Rogenhofer, and W. F. Wieland. High-intensity focused ultrasound for the treatment of localized prostate cancer: 5-year experience. *Urology*, 63:297–300, 2004.

[27] Y. T. Hu, S. Qin, T. Hu, K. W. Ferrara, and Q. Jiang. Asymmetric oscillation of cavitation bubbles in a microvessel and its implications upon mechanisms of clinical vessel injury in shock-wave lithotripsy. *Int. J. Non-Linear Mech.*, 40:341–350, 2005.

[28] D. M. Skyba, R. J. Price, A. Z. Linka, T. C. Shalak, and S. Kaul. Direct *in vivo* visualization of intravascular destruction of microbubbles by ultrasound and its local effects on tissue. *Circulation*, 98:290–293, 1997.

[29] D. Dalecki, C. H. Raeman, S. Z. Child, D. P. Penney, R. Mayer, and E. L. Carstensen. The influence of contrast agents on hemorrhage produced by lithotripter fields. *Ultrasound Med. Biol.*, 23:1435–1439, 1997.

[30] S. Z. Child, C. L. Hartman, L. A. Schery, and E. L. Carstensen. Lung damage from exposure to pulsed ultrasound. *Ultrasound Med. Biol.*, 16:817–825, 1990.

[31] A. F. Tarantal and D. R. Canfield. Ultrasound-induced lung hemorrhage in the monkey. *Ultrasound Med. Biol.*, 20:65–72, 1994.

[32] P. Zhong, Y. Zhou, and S. Zhu. Dynamics of bubble oscillation in constrained media and mechanisms of vessel rupture in SWL. *Ultrasound Med. Biol.*, 27:119–134, 2001.

[33] E. Sassaroli and K. Hynynen. Forced linear oscillations of microbubbles in blood capillaries. *J. Acoust. Soc. Am.*, 115:3235–3243, 2004.

[34] E. Sassaroli and K. Hynynen. Resonance frequency of microbubbles in small blood vessels. In *Proceedings of the 2004 IEEE International UFFC Joint 50th Anniversary Conference*, pages 1465–1468, 2004.

[35] E. Sassaroli and K. Hynynen. Resonance frequency of microbubbles in small blood vessels: A numerical study. *Phys. Med. Biol.*, 50:5293–5305, 2005.

[36] C. F. Caskey, D. E. Kruse, P. A. Dayton, T. K. Kitano, and K. W. Ferrara. Microbubble oscillations in tubes with diameters of 12, 25, and 195 microns. *Appl. Phys. Lett.*, 88:033902, 2006.

[37] S. P. Qin and K. W. Ferrara. Acoustic response of compliable microvessels containing ultrasound contrast agents. *Phys. Med. Biol.*, 51:5065–5088, 2006.

[38] S. P. Qin, Y. T. Hu, and Q. Jiang. Oscillatory interaction between bubbles and confining microvessels and its implications on clinical vascular injuries of shock-wave lithotripsy. *IEEE Trans. Ultrason. Ferroelec. Freq. Control.*, 53:1322–1329, 2006.

[39] X. M. Chen and A. Prosperetti. Thermal processes in the oscillations of gas bubbles in tubes. *J. Acoust. Soc. Am.*, 104:1389–1398, 1998.

[40] T. Ye and J. L. Bull. Direct numerical simulations of micro-bubble expansion in gas embolotherapy. *ASME J. Biomech. Eng.*, 126:745–759, 2004.

[41] T. Ye and J. L. Bull. Microbubble expansion in a flexible tube. *ASME J. Biomech. Eng.*, 128:554–563, 2006.

[42] B. Krasovitski and E. Kimmel. Gas bubble pulsation in a semiconfined space subjected to ultrasound. *J. Acoust. Soc. Am.*, 109:891–898, 2001.

[43] T. G. Leighton, D. G. Ramble, A. D. Phelps, C. L. Morfey, and P. P. Harris. Acoustic detection of gas bubbles in a pipe. *Acta Acust.*, 84:801–814, 1998.

[44] T. G. Leighton, P. R. White, C. L. Morfey, J. W. L. Clarke, G. J. Heald, H. A. Dumbrell, and K. R. Holland. The effect of reverberation on the damping of bubbles. *J. Acoust. Soc. Am.*, 112:1366–1376, 2002.

[45] V. Twersky. Multiple scattering of waves and optical phenomena. *J. Opt. Soc. Am.*, 52:145–171, 1962.

[46] E. A. Zabolotskaya. Interaction of gas bubbles in a sound field. *Sov. Phys. Acoust.*, 30:365–368, 1984.

[47] D. E. Weston. Acoustic interaction effects in arrays of small spheres. *J. Acoust. Soc. Am.*, 39:316–322, 1966.

[48] I. Tolstoy and A. Tolstoy. Line and plane arrays of resonant monopole scatterers. *J. Acoust. Soc. Am.*, 87:1038–1043, 1990.

[49] C. Feuillade. Scattering from collective modes of air bubbles in water and the physical mechanism of superresonances. *J. Acoust. Soc. Am.*, 98:1178–1190, 1995.

[50] A. A. Doinikov. Mathematical model for collective bubble dynamics in strong ultrasound fields. *J. Acoust. Soc. Am.*, 116:821–824, 2004.

[51] A. A. Doinikov, R. Manasseh, and A. Ooi. Time delays in coupled multibubble systems (L). *J. Acoust. Soc. Am.*, 117:47–50, 2005.

[52] M. F. Hamilton, Yu. A. Ilinskii, G. D. Meegan, and E. A. Zabolotskaya. Interaction of bubbles in a cluster near a rigid surface. *Acoust. Res. Lett. Online*, 6:207–213, 2005.

[53] Yu. A. Ilinskii, Mark F. Hamilton, and E. A. Zabolotskaya. Bubble interaction dynamics in Lagrangian and Hamiltonian mechanics. *J. Acoust. Soc. Am.*, 121:786–795, 2007.

[54] J. Cui, M. F. Hamilton, P. S. Wilson, and E. A. Zabolotskaya. Bubble pulsations between parallel plates. *J. Acoust. Soc. Am.*, 119:2067–2073, 2006.

[55] J. Cui, M. F. Hamilton, P. S. Wilson, and E. A. Zabolotskaya. Bubble dynamics in constrained media. In A. A. Atchley, V. W. Sparrow, and R. M. Keolian, editors, *Proceedings of the 17th International Symposium on Nonlinear Acoustics*, pages 229–232, New York, 2006. American Institute of Physics.

[56] M. S. Plesset. The dynamics of cavitation bubbles. *J. Appl. Mech.*, 16:277–282, 1949.

[57] Yu. A. Ilinskii and E. A. Zabolotskaya. Cooperative radiation and scattering of acoustic waves by bubbles in liquid. *J. Acoust. Soc. Am.*, 92:2837–2841, 1992.

[58] A. Prosperetti. The equation of bubble dynamics in a compressible liquid. *Physics of Fluids*, 30:3626–3628, 1987.

[59] J. B. Keller and M. Miksis. Bubble oscillations of large amplitude. *J. Acoust. Soc. Am.*, 68:628–633, 1980.

[60] D. T. Blackstock. *Fundamentals of Physical Acoustics*. Wiley-Interscience, New York, 2000.

[61] T. A. Hay, T. Y. Cheung, M. F. Hamilton, and Yu. A. Ilinskii. Frequency response of bubble pulsations in tubes with arbitrary wall impedance. *J. Acoust. Soc. Am.* (A), 123:3220, 2008.

[62] M. Abramowitz and I. A. Stegun, editors. *Handbook of Mathematical Functions with Formulas, Graphs, and Mathematical Tables*. Dover, New York, 1972.

[63] W. H. Press, S. A. Teukolsky, W. T. Wetterling, and B. P. Flannery. *Numerical Recipes in Fortran 77*, Chapter 9. Cambridge University Press, New York, 1992.

[64] S. Kumar and C. E. Brennen. Some nonlinear interactive effects in bubbly clouds. *J. Fluid Mech.*, 253:565–591, 1993.

[65] W. Lauterborn. Numerical investigation of nonlinear oscillations of gas bubbles in liquids. *J. Acoust. Soc. Am.*, 59:283–293, 1976.

Vita

Jianying Cui Atkisson was born in Taiyuan, China on October 25, 1972 (or September 19, 1972 on the Chinese lunar calendar), the daughter of Hong Cui and Aiqing Liang. She graduated from Taiyuan University of Technology in China with a Bachelor of Arts degree in English in 1996 and a Bachelor of Science degree in Mechanical Engineering in 1997. In 1999 she came to the United States to study at University of Nevada, Las Vegas, where she graduated with a Master of Science degree in Mechanical Engineering in 2001. She transferred to The University of Texas at Austin in 2002 to study acoustics. In her spare time, she draws.

Permanent address: 3919 Knollwood
San Antonio, Texas 78247

This dissertation was typeset with LaTeX[†] by the author.

_____

[†]LaTeX is a document preparation system developed by Leslie Lamport as a special version of Donald Knuth's TeX Program.